Portofoliu de lucrări

1. Iftimiciuc M., Lache, S., Vandepitte, D., **Velea, M.N.**, 2022, Bending performance of a sandwich beam with sheet metal pyramidal core, Materials Today Communications 31, 103490, **FI 3.7**.
2. Iftimiciuc M., Lache, S., Wennhage, P., **Velea, M.N.**, 2020, Structural performance analysis of a novel pyramidal cellular core obtained through a mechanical expansion process, Materials, Vol. 13, ISSN 1996-1944, Elsevier, **FI 3.057**.
3. **Velea, M.N.**, Lache, S., 2019, Energy absorption of all-PET 2nd order hierarchical sandwich structures under quasi-static loading conditions, Thin-Walled Structures, Vol. 138, pp. 117-123, ISSN 0263-8231, Elsevier, **FI 5.7**.
4. **Velea, M.N.**, Schneider, C., Lache, S., 2016, Second-order hierarchical sandwich structure made of self-reinforced polymers by means of a continuous folding process, Materials & Design, Vol. 102, pp. 313-320, ISSN 0261-3069, Elsevier, **FI 7.6**.
5. Schneider, C., **Velea, M.N.**, Kazemahvazi, S., Zenkert, D., 2015, Compression properties of novel thermoplastic carbon fibre and poly-ethylene terephthalate fibre composite lattice structures, Materials & Design, Vol. 65, pp.1110-1120, ISSN 0261-3069, Elsevier, **FI 7.6**.
6. **Velea, M.N.**, Wennhage, P., Zenkert, D., 2014. Multi-objective optimisation of vehicle bodies made of FRP sandwich structures. Composite Structures, Vol. 111, pp.75-84, ISSN 0263-8223, Elsevier, FI **6.3**.
7. **Velea, M.N.**, Wennhage, P., Lache, S., 2012. Out-of-plane effective shear elastic properties of a novel cellular core for sandwich structures. Materials & Design, Vol. 36, pp.679-686, ISSN 0261-3069, Elsevier, **FI 7.6**.

8. **Velea, M.N.**, Lache, S., 2011. In-plane effective elastic properties of a novel cellular core for sandwich structures. Mechanics of Materials, Vol. 43, No.7, pp. 377-388, ISSN 0167-6636, Elsevier, **FI 3.4**.
9. **Velea, M.N.**, Lache, S., Roșca I.C., 2016, Damping characteristics identification of self-reinforced poly-ethylene terephthalate, Proceedings of the Romanian Academy, Series A, Vol. 17, No.4/2016, pp. 336-343.

Data

02.12.2024

Marian Nicolae Velea,

Materials Today Communications 31 (2022) 103490

Contents lists available at ScienceDirect

Materials Today Communications

journal homepage: www.elsevier.com/locate/mtcomm

Bending performance of a sandwich beam with sheet metal pyramidal core

Mihaela Iftimiciuc [a], Simona Lache [a], Dirk Vandepitte [b], Marian Nicolae Velea [a,*]

[a] Department of Mechanical Engineering, Transilvania University of Brasov, Romania
[b] Department of Mechanical Engineering, KU Leuven, Belgium

ARTICLE INFO

Keywords:
Pyramidal cellular core. Four-point bending. Mechanical expansion. Finite element model

ABSTRACT

Metallic sandwich structures with pyramidal cellular cores have proven to be highly effective in the industry of advanced lightweight materials thanks to their high strength-to-weight ratios. This paper presents the investigation of the bending performance of a sandwich structure based on a novel pyramidal cellular core. The effective bending and shear stiffness are investigated using numerical and experimental approaches. Furthermore, the finite element model created for the four-point bending scenario is in good agreement with the experimental one and can be subsequently used for further product development. This represents a cost-efficient method used for structural optimisation and may lead to improved mechanical properties and higher lightweight capabilities. The study includes a comparison to other existing periodic core topologies which shows that the investigated pyramidal structure has high potential to be used for the construction of sandwich panel assemblies.

1. Introduction

The efforts exerted in reducing toxic emissions and greenhouse gases have significantly influenced the research and development of advanced lightweight structures. The motivation behind the extensive research conducted up to the present is the need to comply with the strict environmental regulations adopted all over the world considering fuel economy [1,2]. In this regard, sandwich panels have become an attractive solution within the aerospace, naval and automotive industries where high stiffness and strength-to-weight ratios are required [3–5]. In addition, they provide a wide range of multifunctional behaviours, offering a very good absorption of impact energy as well as an efficient control of acoustic noise and vibrations [6–9].

The out-of-plane mechanical properties of sandwich assemblies have been extensively studied in the past years in order to design geometries which can be subjected to complex loading scenarios. Stochastic cellular structures represent a popular alternative to heavy monolithic constructions. Their bending performances have been successfully improved by embedding different reinforcing elements into the foam core (resin columns, ribs from composite materials, corrugated cores etc.). Despite this, the most common problem of these sandwich structures remains the bonding of the components [10–12].

Closed cell cores also represent a good option for increasing flexural properties of sandwich assemblies. Arbaoui et al. [13] has analysed the performance of a honeycomb-based sandwich panel and has proven that a multi-layer configuration is effective in increasing the flexural performances of sandwich panels. Yuan Shi et al. [14] has developed a closed cell composite sandwich panel manufactured through a liquid silicon infiltration process, with excellent bending stiffness and strength at significantly low densities. Nonetheless, a major drawback is represented by the complex manufacturing process which translates in high overall costs.

Sandwich structures with open cell cores have been gaining popularity among the lightweight core solutions due to their topological versatility. There are also some disadvantages for such low-density structures represented occurrence of node fracture during die forming which can significantly reduce the overall mechanical properties [16–18]. Lu Zhang et al. [15] has designed a ceramic composite pyramidal core with excellent lightweight properties and high flexural performance obtained through precursor infiltration pyrolysis (PIP). An important shortcoming of this core is represented by the poor quality of the bond between the face sheets and core which failed during loading for all the investigated configurations.

In this regard, the authors propose a new metallic pyramidal core for the construction of sandwich panels. Obtained through a sheet metal deformation process, the corrugated structure has the advantage of reducing the material loss during manufacturing while providing a high adhesion surface and thus significantly simplifying the assembly process of the associated sandwich panel [19].

The objective of the present paper is to evaluate the bending

* Correspondence to: 29 Eroilor Blvd, 500036 Brașov, Romania.
E-mail address: marian.velea@unitbv.ro (M.N. Velea).

https://doi.org/10.1016/j.mtcomm.2022.103490
Received 27 July 2021; Received in revised form 13 March 2022; Accepted 3 April 2022
Available online 6 April 2022
2352-4928/© 2022 Elsevier Ltd. All rights reserved.

performance of a sandwich beam which contains the novel pyramidal core, mentioned above. Overall bending and shear stiffness in a four-point bending configuration are predicted using finite element simulation and both properties are also measured experimentally. The results are further compared to other types of sandwich beams based on different core topologies to highlight the structural performance of the cellular configuration.

2. Cellular core and manufacturing process

The pyramidal corrugated core can be obtained from any ductile metallic sheet (e.g. aluminium alloys, stainless steels etc.) through a continuous manufacturing process as described in [19]. This results in a pyramidal corrugated structure with a bi-directional expansion on both *Ox* and *Oy* axes, Fig. 1.

The constructive parameters defining the cellular core, Fig. 1a) are: g – thickness of the base material, l_o – length of the strut, c – base of the cell's strut, l_1 – distance between two consecutive perforations, R – radius of the perforations, A – expansion angle of the structure, B – inclination angle of the strut.

The interdependence between them lead to the computation of the bulk dimensions of the unit cell; t – width of the expanded structure, h – height of the unit cell, and w – length of the expanded unit cell [19].

The lightweight characteristic of a corrugated core can be evaluated through its relative density (ρ_r) represented by the ratio between the volume of base material (V_m) from which the cellular core is manufactured and the volume of the resulting structure $(V_s = wth)$ [20,21].

The lightweight characteristic of a corrugated core can be evaluated through its relative density (ρ_r) represented by the ratio between the volume of base material (V_m) from which the cellular core is manufactured and the volume of the resulting structure (V_s) [20,21].

$$\rho_r = \frac{V_m}{V_s} \tag{1}$$

Relative density of the pyramidal core shown in Fig. 1 is computed using Eq. (2).

$$\rho_s = \frac{4cg(l_0 + l_1 + 2R) - zgl_1 - 8glR - 4\pi gR^2}{wth} \tag{2}$$

where z is the thickness of the cutting tool.

3. Bending and shear stiffness of the sandwich assembly

3.1. Sandwich beam theory

In traditional beam theory, Fig. 2, bending stiffness of a simple homogeneous beam is determined as the value of the Young's modulus E, multiplied by the second moment of area of the beam, equation (3) [20].

For a sandwich beam, Fig. 3, where the elastic modulus of the core along the z axis is not constant, equation (3) can be rewritten as:

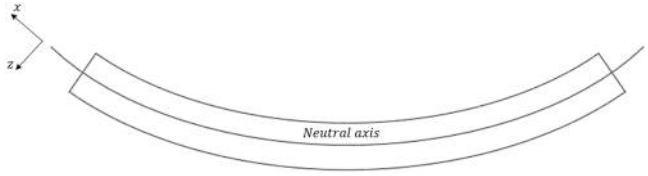

Fig. 2. Simple homogeneous beam subjected to bending loading.

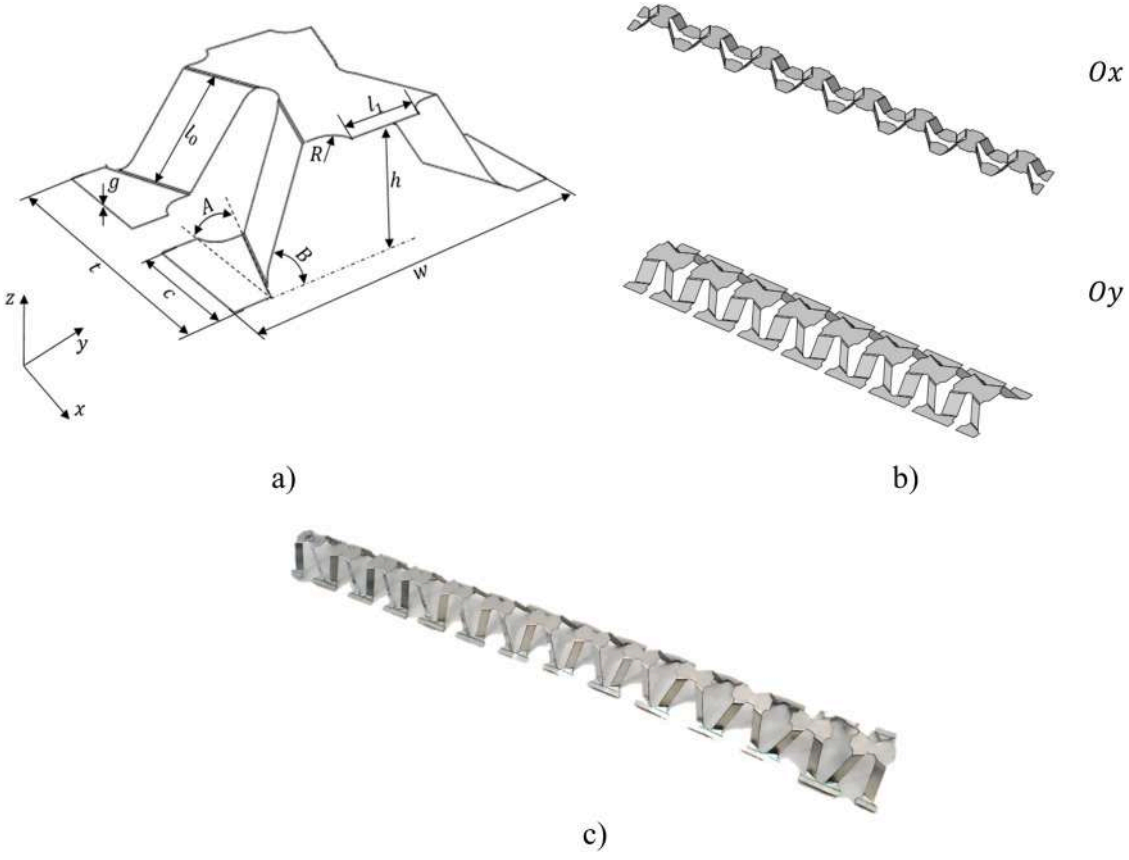

Fig. 1. The schematic representation of the pyramidal cellular core: a) the unit cell and its parameters: b) the resulting core and its expansion directions; c) a strip of the mechanically expanded core (O_y direction) [19].

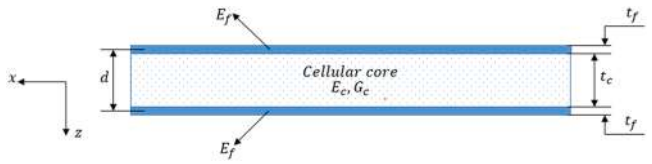

Fig. 3. Schematic representation of a sandwich beam ($z = 0$ at the mid-section of the core).

$$D = \int E z^2 dz \tag{4}$$

By considering Eq. (4) and assuming a symmetric sandwich beam where the two face sheets have the same thickness, t_f, the bending stiffness becomes [23]:

$$D = \int_{-t_f-\frac{t_c}{2}}^{-\frac{t_c}{2}} E_f z^2 dz + \int_{-\frac{t_c}{2}}^{\frac{t_c}{2}} E_c z^2 dz + \int_{\frac{t_c}{2}}^{\frac{t_c}{2}+t_f} E_f z^2 dz \tag{5}$$

Taking into consideration that $d = t_f + t_c$ and after integration, Eq. (5) becomes:

$$D = \frac{E_f t_f{}^3}{6} + \frac{E_f t_f d^2}{2} + \frac{E_c t_c{}^3}{12} = 2D_f + D_0 + D_c \tag{6}$$

where:

E_f – Young's modulus of the face sheet material;.
E_c – Young's modulus of the core material;.
t_f – face sheet thickness;.
t_c – thickness of the core;.
D_f – the bending stiffness of the two face sheets;.
D_0 – the Steiner contribution to bending stiffness;.
D_c – the bending stiffness of the core.

The shear stiffness of a sandwich beam, considering the assumptions that $t_f \ll t_c$ and $E_c \ll E_f$, can be defined with the following equation:

$$S = \frac{Gd^2}{t_c} \tag{7}$$

where: G – the shear modulus of the core.

Both D and S given by Eq. (6) and Eq. (7) are measures per unit width of the beam.

For the bending performances of a sandwich beam to be determined it has to be subjected to a bending loading scenario. Three-point bending (3PB) has been proven effective for computing the stiffness of a sandwich beam [23,24] but in the case of a pyramidal corrugation with a significant distance between two successive adhesion surfaces, a four-point bending (4PB) setup is deemed more appropriate.

4PB has a constant shear force P in the entire region between the outer and inner supports and a constant bending moment in the mid-span. This lowers the risk of local failure due to indentation of the face sheets and it helps in achieving a broader understanding of the core behaviour and its mechanical properties [25,26].

In order to determine the bending and shear stiffness of the sandwich beam, the four-point bending set-up described in Fig. 4 is considered.

Having determined the relation between the imposed displacement w_1 , the resulting deflection w_2 and the measured load P, the bending and shear stiffnesses can be computed according to the sandwich beam theory, by using Eqs. (8) and (9) [21,22]:

$$D = \frac{PL_1{}^2(L_2 - L_1)}{16 w_2} \tag{8}$$

$$S = \frac{12DP(L_2 - L_1)}{12 w_1 D L_2 - P\left(L_1{}^3 - 3L_1{}^2 L_2 + 2L_2{}^3\right)} \tag{9}$$

An effective way for evaluating the structural performance of a sandwich beam is to determine the specific bending and shear stiffness, according to Eqs. (10) and (11):

$$D_m = \frac{D}{m} \tag{10}$$

$$S_m = \frac{S}{m} \tag{11}$$

where:

$$m = \left(2\rho_{s_{sk}} t_f + \rho_r \rho_{s_c} t_c\right) L_2 b$$

with: t_f - thickness of the skins, t_c – thickness of the core, ρ_r – relative density of the cellular core, $\rho_{s_{sk,c}}$ – density for the base material of the face sheets and core respectively, b – width of the sandwich beam, L_2 – active length of the sandwich beam.

3.2. Numerical identification and finite element model

The finite element model for the four-point bending analysis of the sandwich beam is presented in Fig. 5, where the sandwich beam consisting in two lateral faces (marked 3 and 5) and a cellular core (marked 4) is subjected to a four-point bending loading scenario between support rollers (marked 6 and 7) and the loading rollers (marked 1 and 2).

Components are modelled using 4-node structural shell elements, S4R. This is a reduced integration element with 6 DOFs for each node, 3 translations and 3 rotations. The element count for each individual model is different since it is influenced by the number of unit cells contained in the core and by the width and length of the sandwich beam. The average number of elements for the O_y and O_x direction is 110.000 and 130.000, respectively. The number of elements over beam width and length is 22 respectively 270, the number of elements in one pyramid cell is on average 8500. The number of elements for a single roller is 2000.

Components marked 1, 2, 6 and 7 representing the rollers are modelled as analytical rigid bodies. The main feature of such a component is the inability to sustain deformation and its position in space is defined by a single reference point. For the support rollers, all DOFs are restricted while for the loading rollers an imposed displacement is applied on the perpendicular direction of the face sheets. The deflection at midspan is registered at a node on the top sandwich face sheets in the symmetry plane and the corresponding reaction force is taken from the bottom cylinders. The contact areas between the sandwich components (core and face sheets) are modelled as a node-to-surface contact with a perfectly bonded option. The contact between the support and loading rollers with the sandwich face sheets is

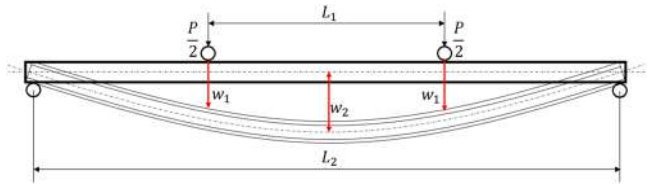

Fig. 4. Schematic representation of the four-point bending setup.

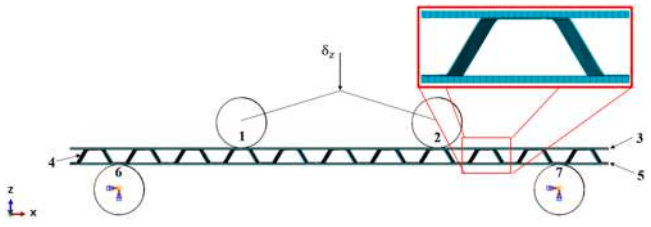

Fig. 5. Four-point bending setup for the numerical model.

modelled as a surface contact with a theoretical friction coefficient of 0.17 corresponding to a dry, in air steel-to-steel interaction. A simplified contact was considered sufficient at this stage of the research since slight variations of the friction coefficient are not expected to have a significant influence on the overall results. The elastic and plastic properties of the core material are defined in the model according to Table 1. The face sheets are manufactured from mild carbon steel with the elastic modulus $E_s = 111$ GPa and the yield strength $\sigma_y = 143.3$ MPa.

A thorough investigation of the material properties used for the manufacturing of the pyramidal core and face sheets of the sandwich panel was not deemed necessary at this point of the research since the properties of the investigated structure are highly influenced by systematic defects of the manufacturing process. This suggests that the parameters controlling the mechanical expansion are the key factor in controlling the geometric imperfections rather than slight variations of the base material properties.

The yield stress – plastic strain curve of the material model is shown in Fig. 6.

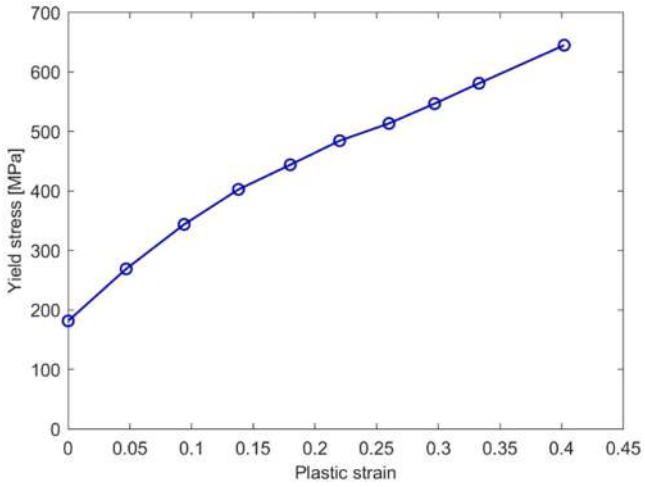

Fig. 6. Yield Stress – Plastic Strain data for stainless-steel type 304 [25] used for defining the plasticity behaviour.

3.3. Geometric imperfections

When computing the bending and shear stiffness of sandwich assemblies with periodic cellular cores, especially in the out-of-plane direction, simulation results are usually higher than experimental values. This is caused by the imperfections in the cellular structure due to undesired variations of the geometric parameters which can occur during the manufacturing process [22].

Including the initial geometric imperfections of the corrugated core into the numerical model may lead to more realistic solutions and evaluation of the mechanical properties of the sandwich assembly.

Geometric imperfections are defined as perturbations of the initial geometry. A common approach to define the geometric imperfections is the superposition of buckling eigenmodes onto the initial geometry before load application. The first step consists in performing a linear buckling analysis to establish the most probable collapse modes. The evaluation of the buckling shapes enables the choice of the modes which generate the most critical imperfections (the lowest buckling modes are assumed to provide the best approximation).

The distorted nodal coordinates can be furtherly imposed onto the geometry to create a perturbation of the mesh by using a scaling factor, using Eq. (12):

$$\Delta x_i = \sum_{i=1}^{M} \omega_i \phi_i \tag{12}$$

where:

Δx_i – represents the distorted nodal coordinates; M – the number of buckling shapes; ϕ_i – is the i^{th} mode shape and ω_i – is the associated scaling factor [28].

For the finite element model of the sandwich beam under study, the geometric imperfections of the core are considered. Due to its complex topology, the struts of the unit cell are most likely to sustain deformation during the manufacturing process. Thus, a linear buckling simulation is performed on the standalone core and the first 20 deformation shapes are computed. By analysing the eigenmodes, and due to their similarity in shape and eigenvalues, the first buckling mode is considered to have the highest probability in generating critical initial deformation, Fig. 7.

A scaling factor of 0.1 is applied. This generates a perturbation of the initial core geometry which allows the nodes affected by the loading case to translate in the direction set by the eigenmode by 10% of the value of the initial displacement U_i.

Table 1
Mechanical properties of stainless-steel type 304 [27].

Young's Modulus [MPa]	Poisson's coefficient
187000	0.29
Yield Stress [MPa]	**Plastic strain**
181.5	0
269	0.047
343.8	0.094
402.5	0.138
444	0.18
484.4	0.22
513.5	0.26
546.8	0.297
581	0.333
645	0.402

3.4. Experimental procedure

The objective of the experimental investigation is to validate the numerical model for the computation of bending and shear stiffness of the sandwich beams constructed with the proposed pyramidal cellular core. To ensure the reproducibility of the bending behaviour, three samples for each configuration were subjected to experimental testing.

3.5. Manufacturing of specimens

The cellular core is manufactured from a stainless-steel type 304 metallic sheet with a 0.25 mm thickness. The perforated profile is obtained on a Maxiem 1530 water jet cutting machine which is equipped with 20 HP hydraulic pump and can sustain a constant water pressure of 3500 bar.

The face sheets are obtained from mild carbon steel metal sheet with a thickness of 1.5 mm and with the elastic properties as listed in Section 3. The cellular core is bonded to the face sheets using Araldite 2015, an epoxy based bi-component adhesive produced by Huntsman. The adhesive is applied using a manual glue gun with a mixing nozzle to keep

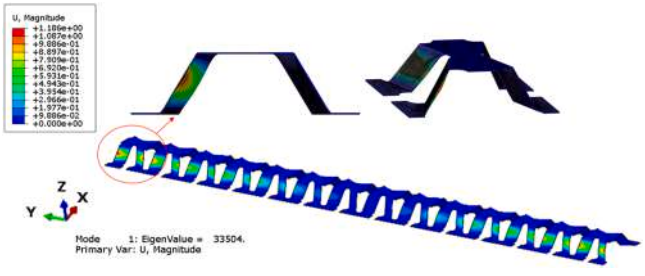

Fig. 7. Buckling mode 1 for the investigated core.

the mixing percentage as recommended by the manufacturer, Fig. 8a). The resulting sandwich assembly is depicted in Fig. 8b). The position of the sandwich beams during the experimental procedure, for all the configurations considered for the study, is shown in Fig. 8c).

3.6. Investigation of geometric configurations

Different geometric configurations of the cellular core are obtained by varying the radius of the perforations $R = [3–5]$ mm, which results in a variation of the expansion angle A. Parameters $B = 60°$, $l_1 = 10$ mm, $l_0 = 15$ mm and $c = 15$ mm are kept constant. Both expansion directions of the cellular core, x and y, are taken into consideration when manufacturing the samples. This leads in obtaining six configurations named C1X ÷ C3X and C1Y ÷ C3Y respectively, Table 2.

Since the core of the sandwich panel is represented by a pyramidal corrugation, the dimensions for the shear- and mid- spans are chosen in consideration to the specimen's configurations so that the loading rollers come in contact with the face sheets correspond to the middle of the top and bottom adhesion surfaces of the pyramidal cell in order premature bending effects of the face sheets, Fig. 9.

3.7. Experimental protocol

The four-point bending tests are performed on an Instron 2985 testing unit, they are displacement controlled with a constant cross-head speed of 1 mm/min and an imposed displacement of 3 mm. Applied load is measured using a 30 kN load cell.

Digital Image Correlation (DIC) is carried out in order to register the deflection at midspan, w_2, throughout the experimental procedure. The optical equipment consists of one high speed camera connected to the data acquisition computer of the test rig with an image recording at a frame rate of 10 images per second. That system ensures the synchronous recording of the analogue data (e.g. displacement, registered load) for each registered image.

The maximum deflection at midspan, w_2, is later determined on the slope of the load-displacement graph in the elastic regime and it is computed as: $w_2 = h_1 - h_0$, with the help of the images registered

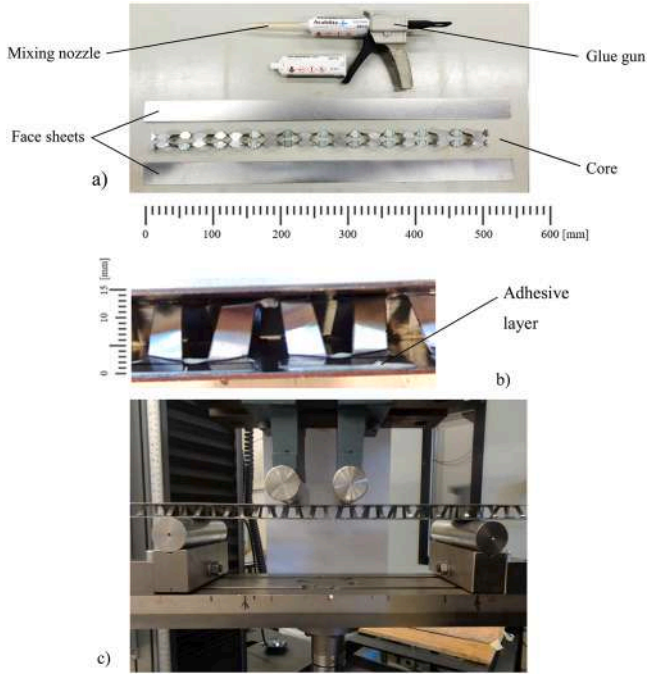

Fig. 8. (a) Component elements of the sandwich assembly; b) assembled sandwich structure; c) position of the sandwich beam in the testing unit.

Table 2
Experimental configurations and dimensions of the samples for the four-point bending tests.

Config.	Beam length [mm]	Beam width [mm]	Beam height [mm]	Expansion angle, A [°]	Loading span, L_1 [mm]	Support span, L_2 [mm]
C1X	533	37.9	18.09	21.8	183	419
C1Y	525	45.09	18.15	21.8	180	416
C2X	550	37.77	18.56	28.1	95	343
C2Y	535	50.94	18.82	28.1	104	364
C3X	568	38.28	19.12	33.7	61	366
C3Y	550	54.86	19.49	33.7	73	381

during the experiment and depicted in Fig. 10. The value for h_1 is registered following a point marked in white on the bottom face sheets of the sandwich beam.

4. Results

The stiffness of the sandwich beams subjected to four-point bending can be computed analytically with the help of Eq. (7) with respect to the dimensions and mechanical properties of the core and face sheets; the value of the core stiffness, E_c, was previously determined as follows: $E_{C1X} = E_{C1Y} = 15.4MPa$; $E_{C2X} = E_{C2Y} = 9.08MPa$ and $E_{C3X} = E_{C3Y} = 5.43MPa$ [17].

The results for the specific bending stiffness with respect to the total mass of the sandwich beam are shown in Table 3.

The specific shear stiffness of the sandwich beam cannot be computed analytically since the shear modulus of the standalone core has not yet been determined.

It should be noted that in a sandwich configuration the pyramidal core provides only point-wise support for both face sheets. The span between successive struts may be much larger than face sheet thickness which implies that face sheets develop bending behaviour at the scale of this span. Upper and lower face sheets may exhibit a global deflection pattern to which a local pattern is superposed. As a result, the conditions of constant curvature are not entirely fulfilled in a four-point bending setup which may lead to an overestimation of beam bending stiffness. An analytical prediction of sandwich stiffness for this configuration is not realistic and formula (7) is only indicative, which makes the replacement with finite element calculations a necessity. Worth mentioning is that the shear deformation is significant only in the case of a short shear span, otherwise local effects are usually encountered.

Four-point bending tests provide values for the load (P), displacement (w_1) and deflection at midspan (w_2) for each of the specimens considered during the experimental procedure. Table 4 presents a comparison between the experimental and numerical results. The value for the displacement (w_1) is the same for both models, experimental and numerical, in order to ensure an accurate correlation for the bending stiffness and strength.

As expected, the experimental values registered for the maximum load are slightly lower than the numerical ones. The numerical model does not take into consideration the thickness of the adhesive layer used to assemble the sandwich beam, which is transposed into a difference in height of the sandwich beam. This results in slightly lower values in the case of the numerical model as opposed to the samples subjected to testing. However, in the conditions defined by the present setup, this would not have a significant influence on the structural performance.

In addition to this, the potential geometric imperfections of the sandwich face sheets are not taken into consideration for the numerical model. This aspect has an influence on the values for the deflection at midspan which are lower for the samples subjected to experimental testing as opposed to the numerical model.

Considering the values in Table 3 and using them into Eqs. (8) and (9), the bending and shear stiffness of the sandwich beams can be computed.

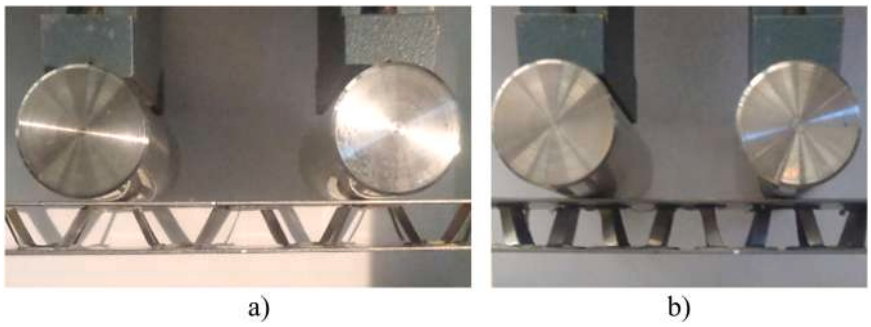

Fig. 9. Placement of loading rollers: a) configuration C2X; b) configuration C2Y.

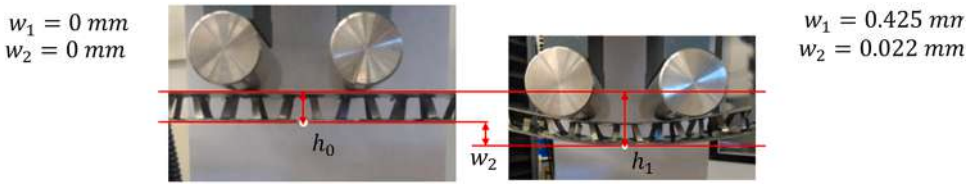

Fig. 10. Method for extracting the value of w_2: h_0 – the initial position of the sandwich beam; h_1 – the position of the beam corresponding to the given displacement for each configuration.

Table 3
Analytical calculation of the specific bending stiffness (ratio of stiffness over beam mass).

Config.	D_m [kNm^2/kg]
C1X	4.94
C1Y	3.95
C2X	7.05
C2Y	7.1
C3X	2.12
C3Y	1.76

Table 4
Numerical and experimental results for the four-point bending loading.

	Experimental results			Numerical (FEA) results	
Config.	Load [N]	w_2 [mm]	w_1 [mm]	Load [N]	w_2 [mm]
C1X	70.31	0.022	0.425	81.45	0.021
C1Y	44.04	0.021	0.246	77.19	0.023
C2X	33.59	0.003	0.3	51.91	0.004
C2Y	42.12	0.0034	0.25	73.32	0.005
C3X	27.18	0.004	0.27	32.07	0.005
C3Y	24.12	0.0052	0.25	30.77	0.006

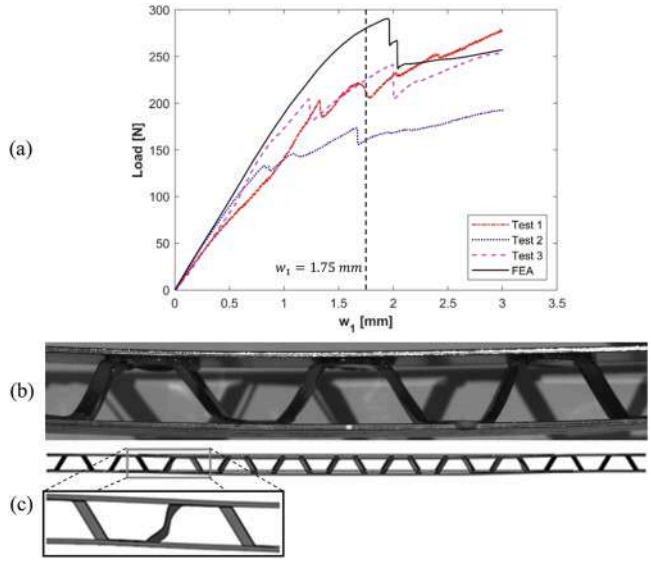

Fig. 11. (a) Load-Displacement plot for the C1X configuration under four-point bending; (b) Experimental deformation for $w_1 = 1.75$ mm; (c) FE model deformation for $w_1 = 1.75$ mm.

Figs. 11 –16 show the values for the bending and shear stiffness for all the configurations subjected to experimental testing (C1X-C3X and C1Y-C3Y) as well as the comparison with the numerical values resulted from finite element simulation.

The bending performance is defined on the elastic regime of the load-displacement curves and the values for the w_1 and w_2 displacements were registered and computed in the midspan, thus, the DIC system was focused on that region alone. The deformed shapes of the entire beam represent the prediction of the finite element models and are super-imposed onto the un-deformed shapes. The values for the applied displacement, w_1 are mentioned on the each figure and are specifically defined for every configuration. The details highlighted show the buckling shapes of the struts of the unit cells in the shear span.

The comparative study shows that both models, numerical and experimental, exhibit the same trend. Although deviations between the sets of physical and virtual experiments are occurring for some configurations, it is considered that the phenomena which are observed in both models correlate well.

5. Discussions

Since the dimensions of the shear- and mid- spans are chosen in consideration with the topology of the core, due to the registered differences between values, Table 3, the most relevant comparison with respect to the performance of the sandwich beam can be outlined according to the two expansion directions defined by the main axes of the corrugation: x and y.

The bending performance of the sandwich beam strongly depends on the expansion direction of the corrugation due to the position of the strut determined by the value of the expansion angle A. The slenderness of the strut (determined by the value of the perforation radius, R) as well as the

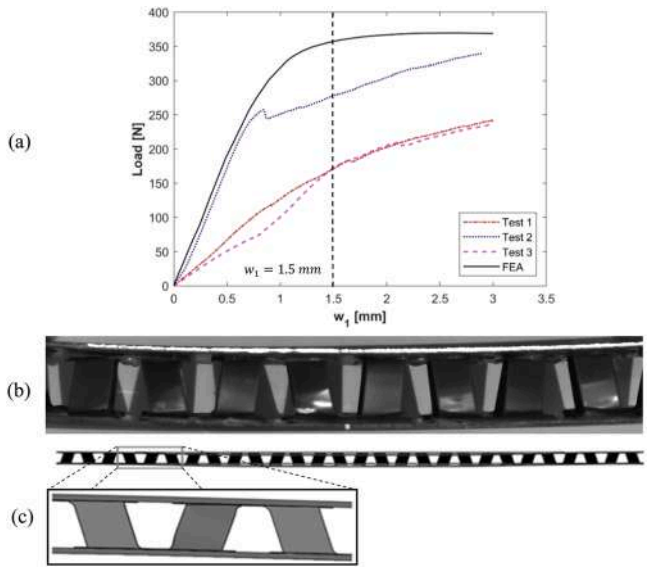

Fig. 12. (a) Load-Displacement plot for the C1Y configuration under four-point bending; (b) Experimental deformation for $w_1 = 1.5$ mm; (c) FE model deformation for $w_1 = 1.5$ mm.

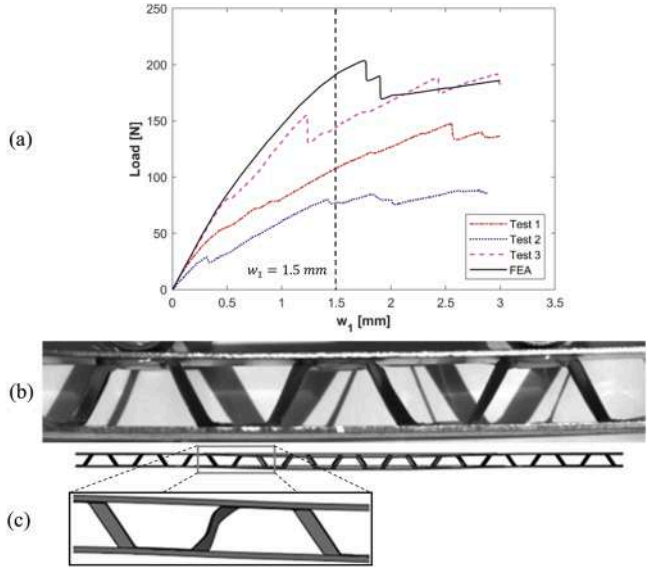

Fig. 13. (a) Load-Displacement plot for the C2X configuration under four-point bending; (b) Experimental deformation for $w_1 = 1.5$ mm; (c) FE model deformation for $w_1 = 1.5$ mm.

distance between the top and bottom adhesion surfaces (given by the length of the unit cell of the core) also have a significant influence on the structural performance of the assembly.

Analysis of the graphs in Figs. 11–16 reveals a difference between the experimental and FE curves. A noticeable difference was registered for the configurations defined by the *y* axis. This could be due to the fact the struts of the pyramidal core are more susceptible to geometrical imperfections when the diplacement is exerted on a transversal direction. The error introduced by the geometric imperfections could be influenced by the value of the radius of the perforation, *R*, which defines the slenderness of the strut as well as by the bending moment of the adhesion surfaces. For the C1Y and C2Y configurations at least one of the load-displacement curves registered experimentally was similar to the one obtained using the FE computation as shown in Figs. 12 and 14. For the C3Y configuration, the experimental results were different than the

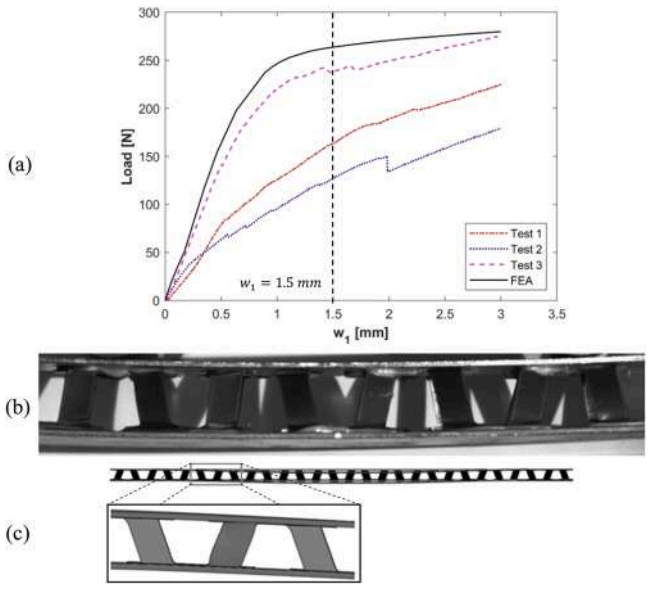

Fig. 14. (a) Load-Displacement plot for the C2Y configuration under four-point bending; (b) Experimental deformation for $w_1 = 1.5$ mm; (c) FE model deformation for $w_1 = 1.5$ mm.

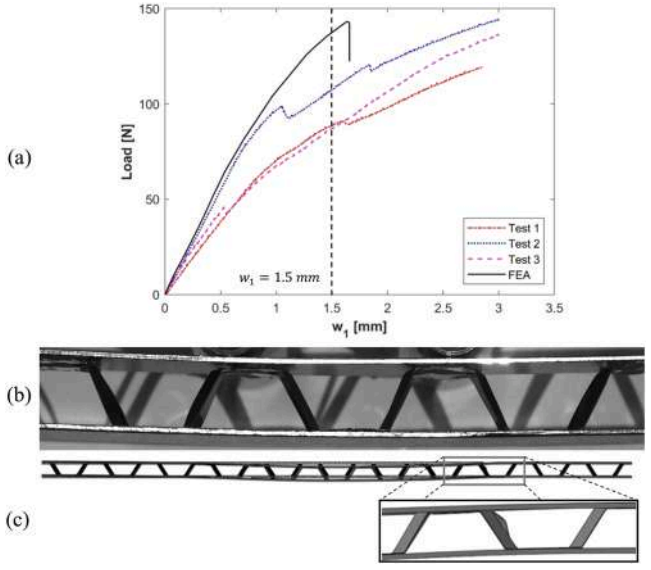

Fig. 15. (a) Load-Displacement plot for the C3X configuration under four-point bending; (b) Experimental deformation for $w_1 = 1.5$ mm; (c) FE model deformation for $w_1 = 1.5$ mm.

FE model suggesting that the expansion process is harder to control when the slenderness of the strut is increased, Fig. 16.

Another reason for the difference registered between the FE and experimental results is due to the fact that for some of the tested samples, a premature failure in the adhesive layer was observed prior to core failure (e.g. sample 1 for the C2X configuration), Fig. 17.

Since the process of mechanical expansion does not involve forming the core between two flat supports (e.g. cold forming in moulds) geometric imperfections are likely to appear. If the values of the geometric parameters are not respected accordingly, planarity deviations of two or more adjacent adhesion surfaces may occur. Fig. 17 a) shows the planarity deviation of two successive adhesion surfaces (marked A and B). The purpose of the adhesive layer is to maintain the connection between the core and face sheets so that the distance between the two

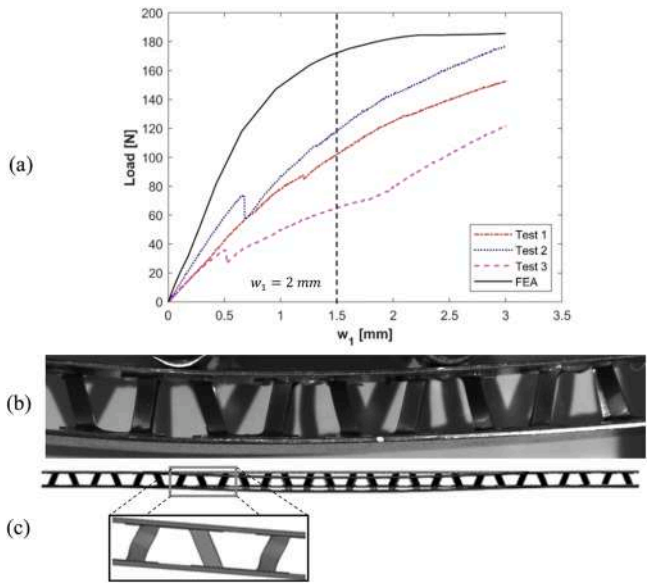

Fig. 16. (a) Load-Displacement plot for the C3Y configuration under four-point bending; (b) Experimental deformation for $w_1 = 2$ mm; (c) FE model deformation for $w_1 = 2$ mm.

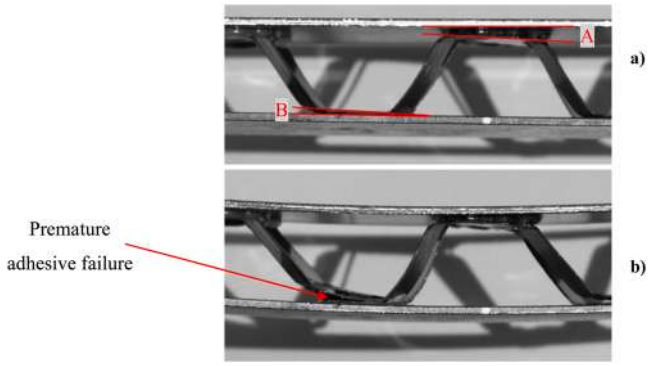

Fig. 17. a) Planarity variations of two successive adhesion surfaces; b) Regions of adhesive failure.

would be constant throughout the loading process. If the four struts of one-unit cell do not have the same height the condition cannot be accomplished. This results in an inconsistent load transfer between the components of the beam which may lead to a premature failure, Fig. 17 b). For the C2X configuration, sample one registered a premature adhesive failure at a displacement $w_1 = 0.23$ mm. This is translated in a change in trend of the load-displacement curve of the tested sample.

However, adhesive failure is observed only in some regions of the contact between the core and face sheets. In addition, for each of the configurations there is at least one sample with values for the bending and shear stiffnesses similar to the FE models. Furthermore, since the bending performance was defined on the elastic regime the fracture of the adhesive layer was not regarded since it would not have a significant influence on the overall mechanical properties of the sandwich assembly.

With respect to bending behaviour, the sandwich beam is more susceptible to deformation on the direction corresponding to the *y* axis as opposed to the *x* axis for the C1 and C3 configurations. A significant difference with respect to the specific bending stiffness is registered for the C1 configuration with a value of 4.68 kNm^2/kg for case C1X as opposed to 3.47 kNm^2/kg for case C1Y.

A decrease of the same magnitude is found for the C3 configuration, with a drop in value of approximately 25% for C3Y configuration in comparison to C3X.

However, the C2 configuration shows a completely different behaviour. In terms of specific bending stiffness, the two configurations register the same value of 6.5 kNm^2/kg. This shows that the geometric parameters of the unit cell for this configuration generate a more homogeneous core with similar bending behaviour on both of the in-plane directions.

In terms of specific shear stiffness, for the C1Y configuration an improvement of approximately 16% can be observed for the shear stiffness when compared to C1X. This is due to the fact that in the *y* direction the core becomes more compact and the inclined position of the struts offers the structure the capacity to better sustain shear stresses. The same trend is observed for the C2 configuration with a value of 287.18 N/kg for C2X and 341.97 N/kg for C2Y.

However, the same behaviour is not observed for the C3 configuration, where the shear stiffness for the *y* direction is reduced approximately by 35% as opposed to the *x* axis.

This suggests that, together with the decrease of the slenderness of the strut, the beam becomes more prone to shear failure.

In the C3 configuration, a significant difference between the numerical and experimental values is encountered. This suggests that, as the radius of the perforation ($R = 5mm$) increases, the corrugation becomes more susceptible to geometric imperfections through the strut's width during the mechanical deformation process. This variation together with the large span between two adjacent struts translates in a decrease of the mechanical performances of the structure.

Structural performance of the proposed sandwich cores is further compared with a selection of sandwich beams based on different core types. The comparative results for the sandwich configurations with respect to the specific bending and shear stiffness are presented in Figs. 18 and 19. The similarity of the specific bending stiffness in the case of C2X and C2Y places this configuration as the best candidate for future investigation and optimisation which might lead to a further improvement in mechanical performance. The possibility that the density can be further reduced may be considered.

The sandwich beams based on the proposed pyramidal core show high potential for the industry of advanced lightweight structures with a significant improvement in bending stiffness when compared to state-of-the-art honeycomb structure by an order of magnitude. All the investigated configurations show a significantly reduced density compared to the Honeycomb [21] and the Expasym developed by Velea et al. [21].

The highest bending stiffness is registered for the C2X and C2Y configurations with a value of 6.5 kNm^2/kg. They are seconded by the foam based core HB1F, presented by Fubin Zhang et al. [29], with a

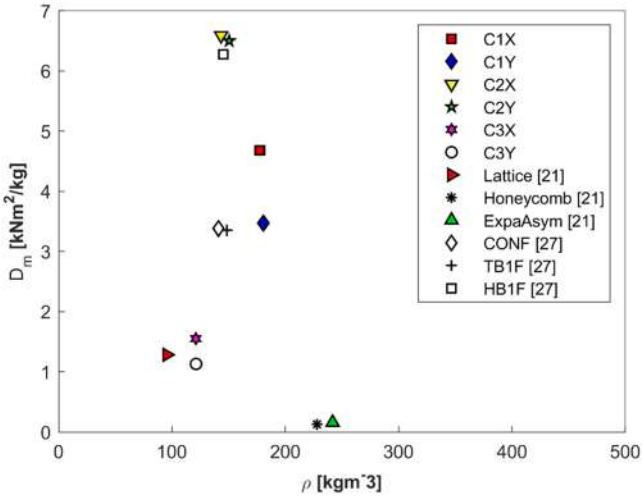

Fig. 18. Specific bending stiffness as function of core density for the beams subjected to study.

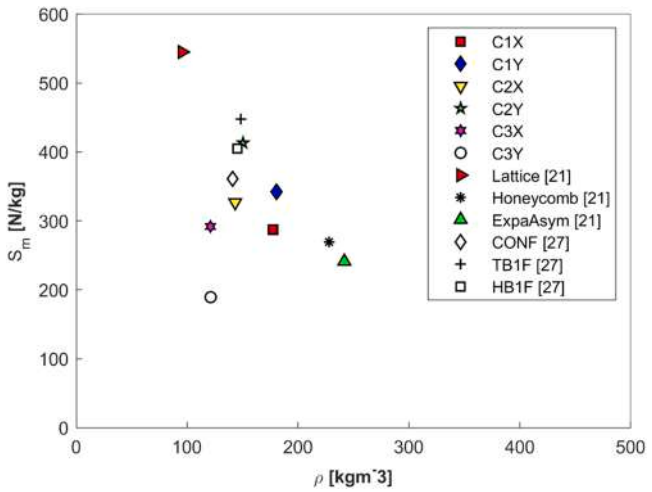

Fig. 19. Specific shear stiffness as a function of core density for the sandwich beams subjected to study.

slight decrease in performance but with the same density. Structures CONF and HB1F from the same author have the same lightweight capabilities and mechanical performances similar to the C1Y configuration and considerably lower that the C1X.

Considering the bending behaviour, the lowest performance, with an effective stiffness of 1.15 kNm^2/kg, is registered for the C3Y case. Even though this ranks above some of the configurations used in the comparative study, it is still exceeded by the lattice-based assembly with improved mechanical properties and a density of 95.3 kg/m^3. The C3X configuration presents a slightly improved bending stiffness but at the same time has a higher density.

The presence of the expansion angle *A* proves to have a positive influence on the mechanical performance. Further optimisation of the pyramidal core may lead to a reduced density while maintaining/increasing its mechanical properties.

The specific shear stiffness as a function of core density is illustrated in Fig. 19. The structural performance with respect to density is similar for most of the structures subjected to study. The highest performance for the shear stiffness is registered for the C2Y configuration with a maximum value of 341.07 N/kg. The newly developed cellular core is ranked above most of the structures considered throughout the comparative study. Its shear performance is still exceeded by the lattice corrugation [21], with a value of 545 N/kg for a density of 95.36 kg/m^3. An optimisation of the geometric parameters of the pyramidal core is expected to lead to an improvement of the bending performance of the associated beam. This could be the subject for further research and a good starting point is to consider the expansion angle, *A*, independent from the radius of the perforation, *R*.

The foam core-based beam TB1F [29] also shows slightly higher performances, with a value of 405.14 N/kg but with the same lightweight characteristics as the C2Y configuration. The advantages of the sandwich core under study are its open topology and multifunctional potential.

Configuration C3Y ranks lower in shear performance than the ExpaAsym and the honeycomb, but with a significant reduction in density.

Bending and shear stiffness may further be increased by replacing the stainless-steel core material with a low density one (e.g., aluminium) and the face sheets material from mild steel to carbon fibre reinforced composites. This is expected to translate into a significant decrease in density, which is a topic of interest for further investigations.

The novelty brought by the investigated pyramidal structure is represented by the versatility of the topology of the core. By variating a single parameter, from the multitude that define the representing unit cell, a total number of six configurations were obtained, shown in Fig. 20.

The load bearing feature of the pyramidal corrugation is represented by the inclined member of the strut. Its slenderness, defined by the radius of the perforation, *R*, has a direct influence on the density and mechanical properties of the sandwich assembly.

The study of the bending performance for these configurations has led to a high level of understanding the behaviour of the pyramidal core in complex loading scenarios. The experimental and numerical investigations have shown that the sandwich structure is more prone to have higher bending stiffness when exploited on the *x* direction of expansion but has a better capacities in sustaining shear loads on the direction defined by the *y* axis.

Furthermore, the slenderness of the struts has a high influence in reducing the overall bending stiffness and strength, as suggested by configurations C3X and C3Y, but in terms of complex loading scenarios, the structural performance is mainly influenced by the combination of the defining parameters of the unit cell rather than a single one, as shown by the similarity of the values obtained for the C2 configuration, Table 5.

6. Conclusions

The main objective of this research is to assess the bending performance of a sandwich beam based on a pyramidal cellular core, made out of sheet metal through a mechanical deformation process. The bending and shear stiffness are computed with the help of a finite element model which is validated through physical experiments.

The following conclusions can be drawn regarding the proposed sandwich configurations:

- The present sandwich structure has the potential to compete with concepts based on other cellular topologies.
- The C2 geometrical configuration proves to be the best candidate for future investigations and optimisations in order to reach the maximum potential of the sandwich assembly based on the pyramidal corrugation. The ratio between the defining parameters of the unit cell provide an efficient load transfer between the core and the face sheets resulting in a structurally stable sandwich beam on both directions of expansion.
- The internal angle *A* proves to have a positive influence on the mechanical performance of the pyramidal structure compared to a similar topology but with an expansion angle equal to zero (A=0°).
- Increased overall bending and shear stiffness together with weight reduction may also be achieved by replacing the material of the core and face sheets with low-density materials (e.g. aluminium, carbon fibre reinforced composites etc.).
- Another possibility of improving the performances of the sandwich structure would be considering the expansion angle, *A,* independent from the perforation radius *R*.

CRediT authorship contribution statement

Iftimiciuc Mihaela: Writing – original draft, Methodology, Investigation, Validation. **Simona Lache:** Writing – review & editing, Supervision. **Dirk Vandepitte:** Writing – review & editing, Resources. **Marian Nicolae Velea:** Conceptualization, Supervision, Methodology, Validation.

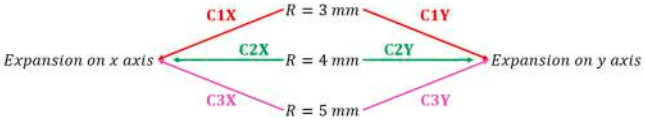

Fig. 20. Forming algorithm of the investigated configurations.

Table 5
shows the comparison between the numerical values resulted from the finite element simulations and the values measured during the experiments, for the bending and shear stiffness.

	D_m [kNm^2/kg]	S_m [kN/kg]
	3.0	0.221
C1X	4.63	0.227
	4.51	0.224
D_m **– average**	**4.05**	**0.224**
D_m **– FEA**	**4.68**	**0.287**
	1.49	0.151
C1Y	3.23	0.313
	1.28	0.129
D_m **– average**	**2.01**	**0.198**
D_m **– FEA**	**3.47**	**0.341**
	4.25	0.258
C2X	3.41	0.237
	6.04	0.301
D_m **– average**	**4.57**	**0.266**
D_m **– FEA**	**6.29**	**0.326**
	3.22	0.197
C2Y	4.03	0.271
	5.56	0.392
D_m **– average**	**4.27**	**0.286**
D_m **– FEA**	**6.5**	**0.412**
	1.27	0.236
C3X	1.38	0.245
	1.33	0.241
D_m **– average**	**1.32**	**0.241**
D_m **– FEA**	**1.55**	**0.291**
	0.83	0.141
C3Y	0.96	0.165
	0.81	0.126
D_m **– average**	**0.87**	**0.144**
D_m **– FEA**	**1.13**	**0.189**

Declaration of Competing Interest

The authors declare that they have no known competing financial interests or personal relationships that could have appeared to influence the work reported in this paper.

Acknowledgements

This work is part of a doctoral research stage funded by the Department of Mechanical Engineering from Transilvania University of Brasov, Romania and the Department of Mechanical Engineering from KU Leuven, Belgium.

References

[1] Regulation (EU) 2019/631 of the European Parliament and of the Council of 17th of April 2019 setting CO2 emission performance standards for new passenger cars and for new light commercial vehicles and repealing Regulations (EC) No 443/2009 and (EU) No 510/2011.
[2] Rohit Rajpal, K.P. Lijesh, K.V. Gangadharan, Parametric studies on bending stiffness and damping ratio of Sandwich structures, Addit. Manuf. 22 (2018) 583–591.
[3] Giuseppe Petrone, Vincenzo D'Alessandro, Francesco Franco, Sergio De Rosa, Numerical and experimental investigations on the acoustic power radiated by Aluminium Foam Sandwich panels, Composite Structures 2014. 118: p. 170–177.
[4] S. Vignesh Iyer, Ritam Chatterjee, M. Ramya, E. Suresh, K. Padmalabhan, A comparative of the three- and four-point bending of rigid foam core glass/epoxy face sheet sandwich composites, Mater. Today. Proc. 5 (2018) 12083–12090.
[5] Amin Farrokhabadi, Seyed Ahmad Taghizadeh, Hamidreza Madadi, Hossein Norouzi, Ahmad Ataei, Experimental and numerical analysis of novel multi-layer sandwich panels under three point bending load, Compos. Struct. 250 (2020), 112631.
[6] Seyed Ahmad Taghizadeh, Mohsen Naghdinasab, Hamidreza Madadi, Amin Farrokhabadi, Investigation of novel multi-layer sandwich panels under quasi-static indentation loading using experimental and numerical analyses, Thin Walled Struct. 160 (2021), 107326.
[7] Bin Han, Zhi-Jia Zhang, Qian-Cheng Zhang, Qi Zhang, Tian Jian Lu, Bing-Heng Lu, Recent advances in hybrid lattice-cored sandwiches for enhanced multifunctional performance, Extrem. Mech. Lett. 10 (2017) 58–69.
[8] Yang Suna, Li-cheng Guoa, Tian-shu Wang, Liao-jun Yaoa, Xin-yang Suna, Bending strength and failure of single-layer and double-layer sandwich structure with graded truss core, Compos. Struct. 226 (2019), 111204.
[9] H.N.G. Wadley, Multifunctional periodic cellular metals, Philos. Trans. R. Soc. 364 (2006) 31–68.
[10] D.Y. Seong, C.G. Jung, D.Y. Yang, K.J. Moon, D.G. Ahn, Quasi-isotropic bending responses of metallic sandwich plates with bi-directionally corrugated cores, Mater. Des. 31 (2010) 2804–2812.
[11] R.A.W. Mines, S. Tsopanos, Y. Shen, R. Hasan, S.T. McKown, Drop weight impact behaviour of sandwich panels with metallic micro lattice cores, Int. J. Impact Eng. 60 (2013) 120–132.
[12] Gregory W. Kooistra, Haydn N.G. Wadley, Lattice truss structures from expanded metal sheet, Mater. Des. 28 (2007) 507–514.
[13] J.E. Shafizadeh, et al., Evaluation of the in-service performance behavior of honeycomb composite sandwich structures, J. Mater. Eng. Perform. 8 (6) (1999) 661–668.
[14] Douglas T. Queheillalt, Haydn N.G. Wadley, Titanium alloy lattice truss structures, Mater. Des. 30 (2009) 1966–1975.
[15] David J. Sypek, Cellular truss core sandwich structures, Appl. Compos. Mater. 12 (2005) 229–246.
[16] Min-Geun Lee, Gyeong-Deuk Ko, Junye Song, Ki-Ju Kang, Compressive characteristics of a wire-woven cellular metal, Mater. Sci. Eng. A 539 (2012) 185–193.
[17] Vikram S. Tochukwu George, Deshpande, N.G.Wadley Haydn, Mechanical response of carbon fiber composite sandwich panels with pyramidal truss cores, Compos. Part A 47 (2013) 31–40.
[18] Zhunli Tan, Lishuo Bai, Bingzhe Bai, Bing Zhao, Zhiqiang Li, Hongliang Hou, Fabrication of lattice truss structures by novel super-plastic forming and diffusion bonding process in a titanium alloy, Mater. Des. 92 (2016) 724–730.
[19] Mihaela Iftimiciuc, Simona Lache, Per Wennhage, Marian Nicolae Velea, Structural performance analysis of a novel pyramidal cellular core obtained through a mechanical expansion process, Materials 13 (19) (2020) 42–64.
[20] Marian N. Velea, Simona Lache, In-plane effective elastic properties of a novel cellular core for sandwich structures, Mech. Mater. 43 (2011) 377–388.
[21] Marian N. Velea, Simona Lache, Numerical simulations of the mechanical behavior of various periodic cellular cores for sandwich panels, Procedia Eng. 10 (2011) 287–292.
[22] Marian Nicolae Velea. Lightweight cellular Structures – Design, Modelling and Analysis-. Brasov: Editura Universitati Transilvania din Brasov; 2011.
[23] Craig A. Steeves, Optimizing sandwich beams for strength and stiffness, J. Sandw. Struct. Mater. 14 (5) (2012) 573–595.
[24] Zhendong Li, Zhonggang Wang, Xinxin Wang, Wei Zhou, Bending behavior of sandwich beam with tailored hierarchical honeycomb cores, Thin Walled Struct. 157 (2020), 107001.
[25] D. Zenkert, The Handbook of Sandwich Construction, EMAS, Worcestershire, 1997.
[26] Gang Zhou, Hiu Ling Leung, Ben Robinson, Can Zheng, New method for the evaluation of residual compressive strengths of sandwich panels via four-point bending, Mech. Mater. 136 (2019), 103075.
[27] Ju Chen, Ben Young, Stress–strain curves for stainless steel at elevated temperatures, Eng. Struct. 28 (2006) 229–239.
[28] ABAQUS, 2017. Geometric imperfections, Abaqus analysis user's manual. Dassault Systémes.
[29] Fubin Zhang, Weiqing Liub, Hai Fang, Zhemin Jia, Flexural behavior of composite sandwich beams with different kinds of GFRP ribs in flatwise and edgewise positions, Compos. Part B 156 (2019) 229–239.

materials

MDPI

Article

Structural Performance Analysis of a Novel Pyramidal Cellular Core Obtained through a Mechanical Expansion Process

Mihaela Iftimiciuc [1], Simona Lache [1], Per Wennhage [2] and Marian Nicolae Velea [1,*]

[1] Department of Mechanical Engineering, Transilvania University of Brasov, 500036 Brasov, Romania; mihaela.iftimiciuc@unitbv.ro (M.I.); slache@unitbv.ro (S.L.)

[2] Department of Engineering Mechanics, KTH Royal Institute of Technology, SE-100 44 Stockholm, Sweden; wennhage@kth.se

* Correspondence: marian.velea@unitbv.ro; Tel.: +40-723-676-387

Received: 24 August 2020; Accepted: 18 September 2020; Published: 24 September 2020

Abstract: Stiff and strong yet lightweight cellular structures have become widely designed and used as cores for the construction of sandwich panels to reach high stiffness and strength to weight ratios. A low-density pyramidal cellular core has been proposed for investigation in this work. The novel core is manufactured from stainless steel sheet type 304 through a mechanical expansion procedure which is described in detail. The out-of-plane stiffness and strength performance is estimated by an analytical model which is successfully validated through experimental tests. A comparative study with other existing cellular core configurations made from other materials indicates an average performance behavior for the investigated structure. However, potential for a further structural performance increase is observed and discussed

Keywords: pyramidal cellular core; out-of-plane compression; mechanical expansion; analytical model

1. Introduction

Over the past few decades, the use of periodic cellular cores for sandwich structures has become a widely used approach in the context of structural weight reduction and energy saving. The concept has been proven to provide increased stiffness and strength as well as impact energy absorption capabilities, in industries such as aerospace, automotive and naval [1].

Honeycomb cellular cores are the most common choice when it comes to high-performance applications, but the associated manufacturing process remains complex [2,3]. In addition to this, due to their closed-cell structure, they trap moisture, which may lead to internal corrosion and face sheet de-bonding [4]. The intensive research conducted in this field proposes a wide range of low-density cellular cores developed as an alternative to the honeycomb. These range from simple manufactured structures and low structural performance ones to more sophisticated manufacturing procedures and high-performance ones, depending on the targeted application [3]. On the one hand, the corrugated structures represent one of the cores easiest to manufacture, but this does not provide the best solution with respect to stiffness and strength to weight ratios. However, methods for improving their structural behavior have been proposed by considering the hierarchical structure concept [5,6].

On the other hand, lattice-truss cellular cores have been considered more and more in recent years, due to their increased structural performance [7–9]. These also offer the possibility of integrating multifunctional characteristics due to the open-space geometry; however, most of the corresponding manufacturing methods are not attractive for bulk and mass production. Research has been carried out to simplify the manufacturing process of pyramidal lattice structures [10] and triangular corrugated structures [11,12] where solutions have been proposed for structures made of thermoplastic composites.

More recently, additive manufacturing technologies bring total freedom with respect to the cellular configuration, however not yet to the type of material that can be used [13–16]. In addition, additive manufacturing is not yet cost effective for bulk and mass production.

Within this context, a novel pyramidal cellular core is obtained within this study. The stiffness and strength of the newly developed structure is evaluated both theoretically and experimentally in out-of-plane compression. The results obtained are evaluated through a comparison with other types of cellular configurations.

2. Cellular Structure and Its Manufacturing Principle

The cellular structure developed in this research is derived from one that is perforated trapezoidal corrugated, with an addition of an internal angle A, as shown in Figure 1.

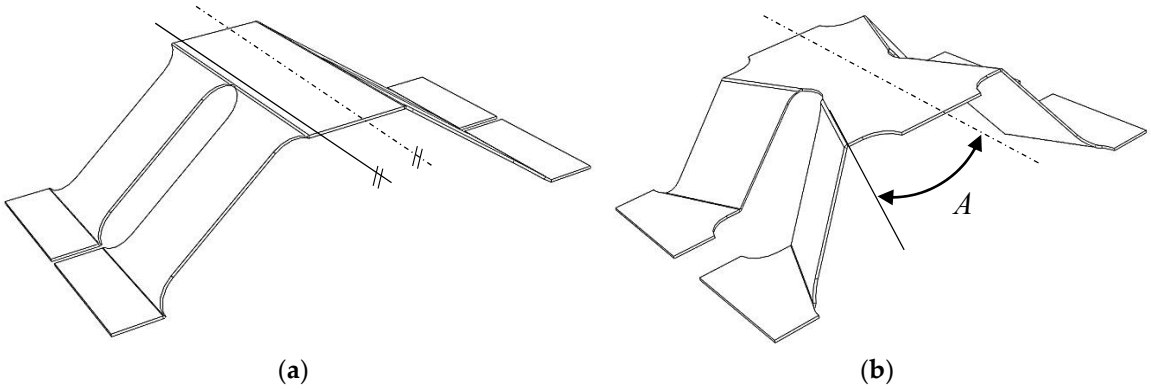

Figure 1. Schematic representation of the cellular structure: (**a**) perforated trapezoidal corrugation; (**b**) mechanically expanded perforated trapezoidal corrugation resulting in a pyramidal structure.

In a continuous manufacturing process, Figure 2, the stages can be described as follows: a series of specific perforations are generated on a flat sheet metal resulting in a profile numbered 1, 2 (zone I). Successively, a pattern of bends, numbering 3, is performed with the purpose of better guidance of the expansion process (zone II). The sheet metal is then fixed at one end (points O_1 and O_2) while at the opposite end a specific displacement U_x is applied along the direction of expansion. The expansion process is stopped when the cells reach the desired inclination angle B. An example of the manufactured mechanically expanded perforated corrugated structure is shown in Figure 3.

The interdependence of the geometric parameters for the investigated pyramidal structure are indicated in Table 1.

Table 1. Interdependence between geometric parameters for the investigated topology.

Geometric Parameter	Expression
Expansion angle	$A = arctan\left(\frac{2R}{c}\right)$
Length of the unit cell	$w = 2l_1 + 2l_o cos(B) + ctan(A) + 2R$
Width of the unit cell	$t = 2c + z + l_0 \sin(B) \tan(A)$
Height of the unit cell	$h = 2g + l_0 sin(B)$

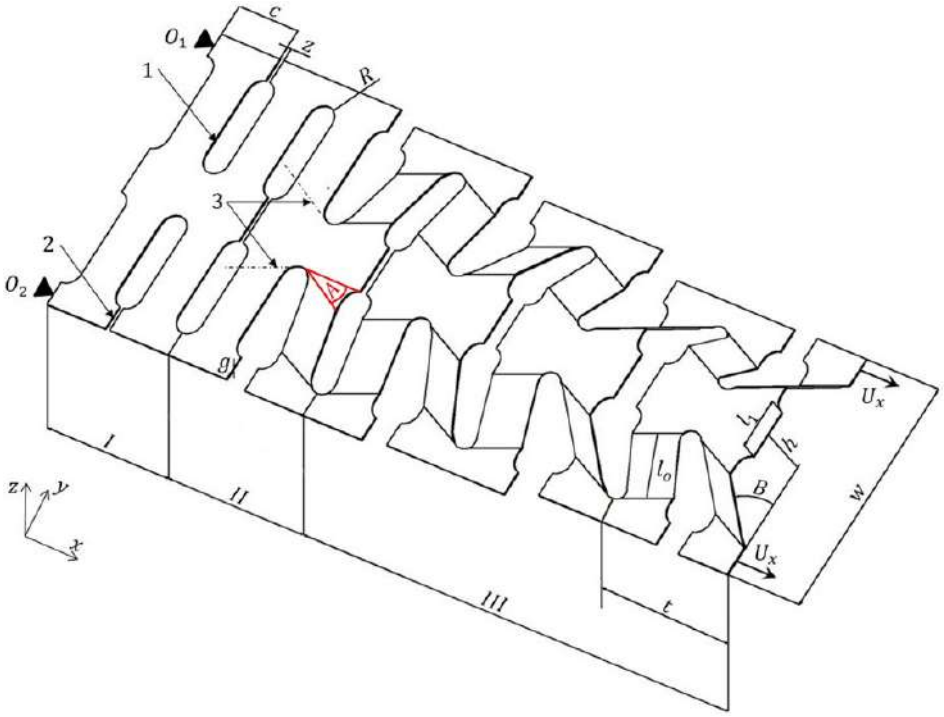

Figure 2. Key steps in the manufacturing process of the pyramidal cellular structure. The parameters defining the structure are: c—base of the cell's arm, z—thickness of the cutting tool, R—radius of the perforation, g—thickness of the base material, A—expansion angle of the structure, t—width of the expanded structure, l_o—strut length, l_1—distance between the perforations, h—height of the expanded unit cell, B—inclination of the strut, and w—length of the expanded unit cell.

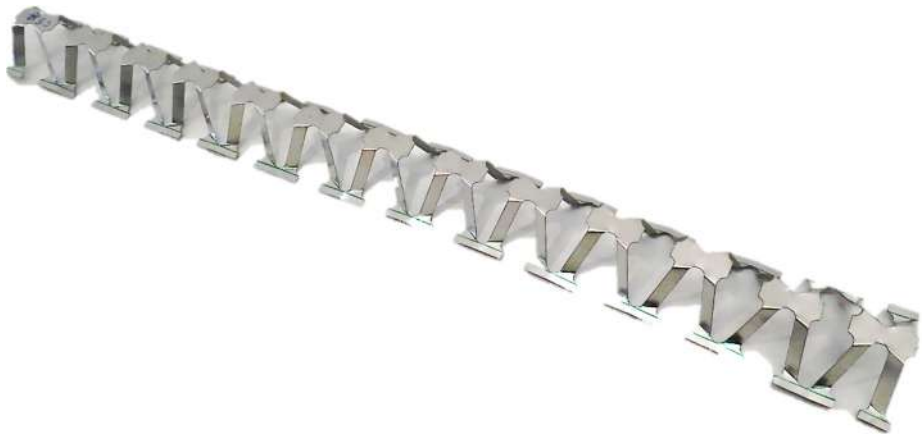

Figure 3. A strip of mechanically expanded perforated corrugated structure—pyramidal cellular structure.

3. Analytical Model for Stiffness and Strength in Out-of-Plane Compression

Due to the symmetric topology of the structure, a quarter of the unit cell has been taken into consideration for developing the analytical model, as shown in Figure 4. It consists of two segments, representing the free members influenced by the external forces acting on the system. The loads and boundary conditions consist of applying a uniformly distributed line pressure p on segment 1–2 while setting to zero all DOF's in point 3. The line pressure imposed on the model in the z direction generates the vertical displacement δ_z.

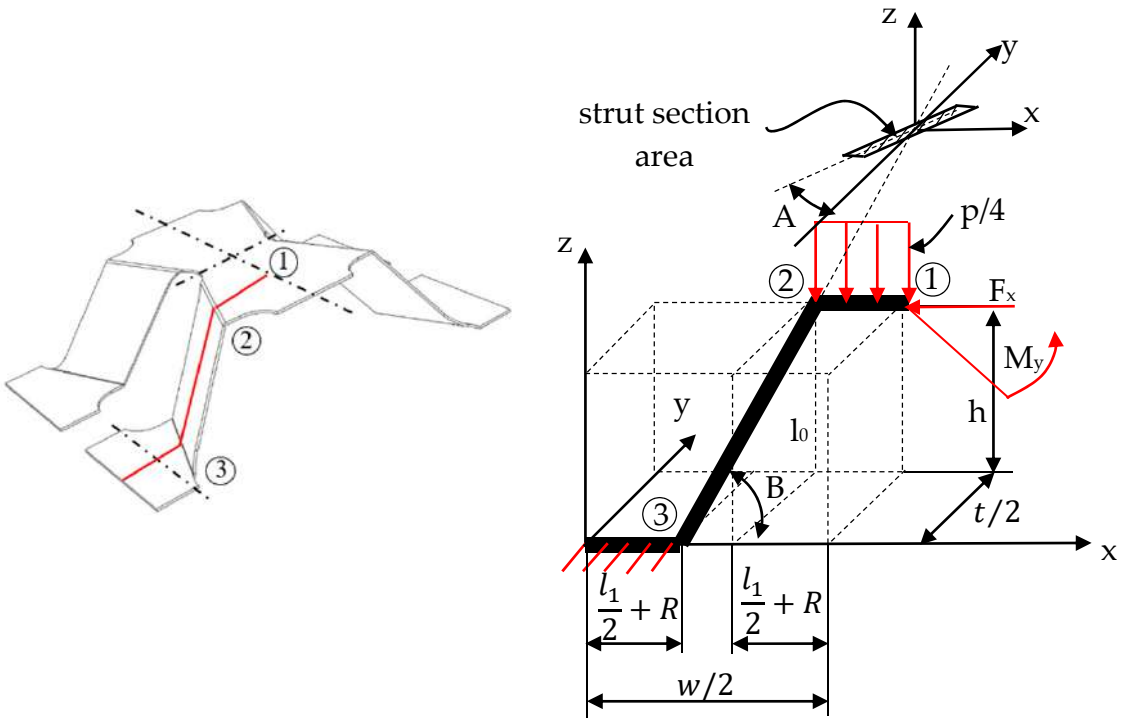

Figure 4. Quarter of unit cell under out-of-plane compression loading.

The resulting displacement δ_z is calculated based on Castigliano's second theorem [17] which states that, for linear elastic deformations, the displacement δ_j of the point of application j of the force F_j along the direction of F_j can be determined as:

$$\delta_j = \frac{\partial U}{\partial F_j} \tag{1}$$

where U is the strain potential energy stored in a volume V of a body in equilibrium conditions, and can expressed as [18]:

$$U = \int_V \frac{\sigma\varepsilon}{2} dV + \int_V \frac{\tau\gamma}{2} dV \tag{2}$$

where σ is the normal stress, τ is the shear stress, ε is the normal strain and γ represents the shear strain.

When the inner forces consist of bending moments and tangential forces, by considering that the material complies with Hooke's law ($\sigma = E \cdot \varepsilon$), Equation (2) becomes:

$$U = \int_V \frac{\sigma^2}{2E} dV + \int_V \frac{\tau^2}{2G} dV \tag{3}$$

For a Euler beam of length l, Equation (3) may be rewritten as:

$$U = \int_l \frac{M^2}{2EI} dx + \int_l \frac{T^2}{2GA} dx \tag{4}$$

By replacing U from Equation (4) to Equation (1), we obtain:

$$\delta_j = \frac{\partial}{\partial F_j} \int_l \frac{M^2}{2EI} dx + \frac{\partial}{\partial F_j} \int_l \frac{T^2}{2GA} dx \tag{5}$$

This equivalent model formulation was successfully applied to several types of corrugations [19,20] and to expanded hexagonal structures [21].

For the pyramidal structure (Figure 4), the calculated displacement δ_z is:

$$\delta_z = p\left(\frac{2R+l_1}{32Gcg} - \frac{12{l_0}^2\left(\frac{\cos(B)\left(R+\frac{l_1}{2}\right)\left(\frac{R}{2}+\frac{l_1}{4}\right)}{32} + \frac{\cos(B)\left(R+\frac{l_1}{2}\right)\left(\frac{R}{4}+\frac{l_1}{8}\right)}{8}\right) + \frac{{l_0}^3\cos(B)^2\left(R+\frac{l_1}{2}\right)}{4} + +3l_0\left(R+\frac{l_1}{2}\right)\left(\frac{R}{2}+\frac{l_1}{4}\right)\left(\frac{R}{4}+\frac{l_1}{8}\right)}{Eg^3(2R-c)}\right) + \frac{12{l_0}^2\left(\frac{M_y\cos(B)}{8} + \frac{F_x\cos(A)\sin(B)\left(\frac{R}{4}+\frac{l_1}{8}\right)}{2} + 12l_0M_y\left(\frac{R}{4}+\frac{l_1}{8}\right) + F_x{l_0}^3\cos(A)\cos(B)\sin(B)\right)}{Eg^3(2R-c)} - \frac{3M_y\left(R+\frac{l_1}{2}\right)^2}{2Ecg^3} - \frac{F_xl_0\cos(A)\cos(B)\sin(B)}{4Gg(2R-c)} \quad (6)$$

where:

$$M_y = \frac{p2E\left(6R^2g^2\left(cl_1+2cl_0-{l_1}^2\right)+4R^3g^2(c-3l_1)+Rg^2\left(12\cos(B){l_0}^2c-12cl_0l_1-{l_1}^3+6c{l_1}^2\right)-8R^4g^2\right)}{96(ERg^2(2c-4Rl_1+2cl_0+cl_1)+Gl_0(2c{l_0}^216R^2l_0+8Rcl_0-8Rl_0l_1+4cl_0l_1))} + \frac{pG\left(8Rl_0l_1\left(3c{l_0}^2-l_0{l_1}^2+3cl_0l_1\right)-64R^2{l_0}^2+24R^2l_0\left(c{l_0}^2+2l_0{l_1}^22cl_0l_1\right)+cl_0l_1\left(4l_0l_1+6{l_0}^2l_1\right)\right)}{96(ERg^2(2c-4Rl_1+2cl_0+cl_1)+2Gl_0{}^2(cl_016R^2+4Rc-4Rl_1+2cl_1))}$$

$$F_x = \frac{p2Eg^2\cos(B)(2R(2R-c+l_1)-(2cl_0-cl_1))}{8\cos(A)\sin(B)((Eg^2(2Rc-4R^2-2Rl_1+2cl_0+cl_1))+2G(c{l_0}^3-8R^2{l_0}^2+4Rcl_0{}^2-4Rl_0{}^2l_1+2cl_0{}^2l_1))} + \frac{pG\left(-16R^4l_0-8R^3l_0(3l_1+c+4l_0\cos(B))-4R^2l_0\left(8\cos(B)l_0l_1-4\cos(B)l_0c+3{l_1}^2-3cl_1\right)\right)}{8\cos(A)\sin(B)((Eg^2(2Rc-4R^2-2Rl_1+2cl_0+cl_1))+2G(c{l_0}^3-8R^2{l_0}^2+4Rcl_0{}^2-4Rl_0{}^2l_1+2cl_0{}^2l_1))} + \frac{pG\left(-2Rl_0\left(2\cos(B)cl_0{}^2-4\cos(B)l_0{l_1}^2+8\cos(B)cl_0l_1-3{l_1}^2+3c{l_1}^2\right)\right)}{8\cos(A)\sin(B)((Eg^2(2Rc-4R^2-2Rl_1+2cl_0+cl_1))+2G(c{l_0}^3-8R^2{l_0}^2+4Rcl_0{}^2-4Rl_0{}^2l_1+2cl_0{}^2l_1))}$$

The effective strain is therefore obtained as:

$$\varepsilon_z = \frac{\delta_z}{h} \quad (7)$$

where h is representing the height of the structure (Table 1).

The effective stress acting on the structure is calculated as:

$$\sigma_z = \frac{pl_1}{A_s} \quad (8)$$

where $A_s = wt/4$ represents the compressive area of the structure, with w and t detailed in Table 1.

The effective stiffness parameter is further on calculated as:

$$E_z = \frac{\sigma_z}{\varepsilon_z} \quad (9)$$

By substituting Equations (7) and (8) into Equation (9), it yields the expression for the out-of-plane compressive stiffness.

The out-of-plane compressive strength model of the investigated structure is developed by assuming the Euler buckling failure mode of the struts. The critical buckling load of the strut can be written as:

$$F_{cr} = \frac{\pi^2EI_{2-3}}{4(0.6l_0)^2} \quad (10)$$

where I_{2-3} represents the cross-section moment of inertia of the strut.

An effective length factor of 0.6 was used as being the average value between fixed-fixed condition (0.5) and fixed-pinned condition (0.7). This assumption was made to approximate the influence of the perforation radius R at the ends of the struts.

The out-of-plane compressive strength can be evaluated by the following equation:

$$\sigma_z = \frac{F_z}{A_s} \quad (11)$$

where $F_Z = \frac{F_{cr}2\cos(A)}{\sin(B)}$ and $A_s = wt/4$.

Eventually, Equation (11) becomes:

$$\sigma_z = \frac{2\frac{\pi^2 E I_{2-3} \cos A}{(0.6 l_0)^2}}{wt \sin B} \tag{12}$$

4. Experimental Approach

The experimental investigation aims to validate the analytical model defined for computing the strength and stiffness of the pyramidal cellular structure.

4.1. Manufacturing of Specimens

The specimens for the pyramidal structure were created by using a stainless-steel type 304 ($E = 187,000$ MPa) sheet metal with a thickness of 0.25 mm.

The perforations were generated on a water jet cutting machine Maxiem 1530, Figure 5a, equipped with a 20 HP hydraulic pump, which can sustain a constant water pressure of 3500 bar.

(**a**) (**b**)

Figure 5. (**a**) Manufacturing method of the perforated profile (**b**) specimens used for the experimental testing.

The expansion angle A was marked and the bend lines required for initiating the expansion process were applied on the perforated profile, Figure 5b. The unit cells were afterwards expanded at the gauge dimensions, calculated using the equations presented in Table 1.

4.2. Investigated Geometric Configurations

The investigated geometric configurations of the pyramidal cellular structure were obtained by varying the parameter $R = [3,\ 4,\ 5]$ mm resulting in the variation of the expansion angle A (Figure 2) while keeping constant the parameters $B = 60°$, $l_1 = 10$ mm, $l_0 = 15$ mm and $c = 15$ mm, thus resulting in a number of three configurations named C1 ÷ C3, shown in Table 2.

Table 2. Configurations and dimensions of the samples for the compression tests.

Config.	w [mm]	t [mm]	h [mm]	B [°]	A [°]
C1	47	37	13.3	60	21.8
C2	51	38	13.3	60	28.1
C3	54	39	13.3	60	33.7

After expanding the unit cells, they were individually glued to 1 mm thickness steel plates to fix the movement of the struts during compression, therefore limiting the influence of the edge effects. The adhesive used was a bi-component, epoxy based one, Araldite 2015, produced by Huntsman.

4.3. Experimental Protocol

The compression tests were performed on an Instron 3360 testing unit and were displacement driven with a constant crosshead speed of 3 mm/min. The load was measured using a 5 kN load cell. The compressive stress was calculated by dividing the measured load by the surface area of the unit cell $\left(w \times t \text{ mm}^2\right)$. The compressive strain was computed by dividing the crosshead displacement by the core initial height.

The out-of-plane elastic modulus was determined on the slope of the stress-strain curve as $E_z = \sigma_z / \varepsilon_z$.

5. Results

The out-of-plane compression tests have provided values for the strength (σ_z) and effective elastic modulus (E_z) for a single unit cell with the strut inclination angle equal to 60°. A comparison between experimental and analytical results is presented in Table 3.

Table 3. Analytical and experimental results for the out-of-plane compression.

Config	Analytic		Experimental	
	E_z [*MPa*]	σ_z [*MPa*]	E_z [*MPa*]	σ_z [*MPa*]
C1	15.4	0.33	15.153	0.286
C2	9.08	0.22	9.04	0.196
C3	5.43	0.13	5.05	0.12

As expected, the registered experimental values for the maximum strength and stiffness are slightly lower than the theoretical ones, since the analytical model does not take into consideration the geometric imperfections of the cell's struts obtained during the manufacturing process.

In addition, the value for the bend radii, depicted in Figure 1 numbered 3, is equal to zero, while, in the case of the experimental testing, the bends performed have had a radius up to 1 mm. This radius contributes in avoiding the crack propagation in the sheet metal during the expansion process.

Figures 6–8 show the values for stiffness and strength for the samples as well as the mean value for all the configurations subjected to experimental testing (C1, C2 and C3).

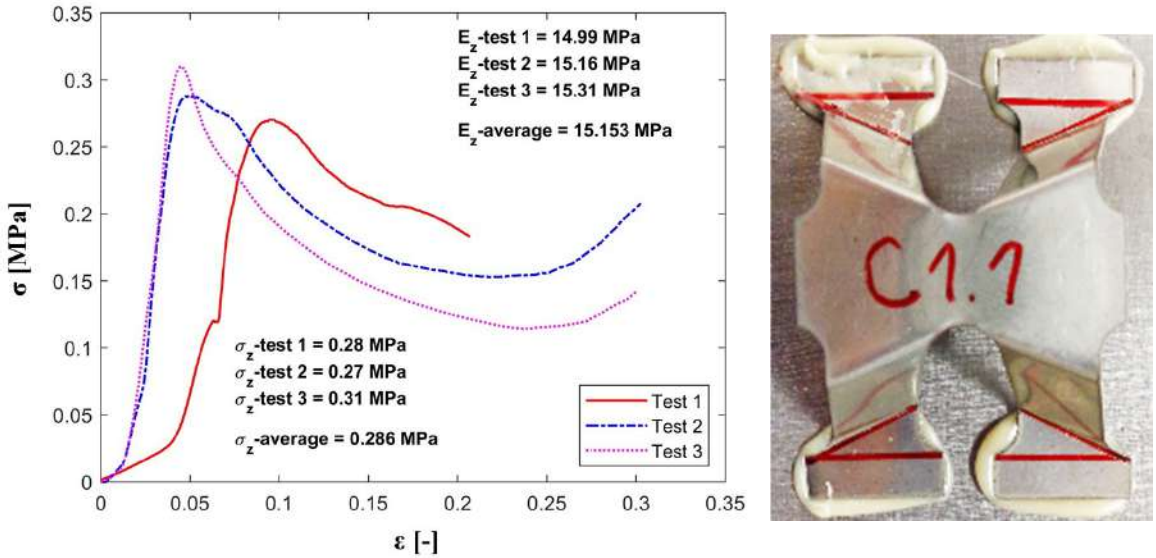

Figure 6. Stress-strain plot for the C1 configuration under out-of-plane compression.

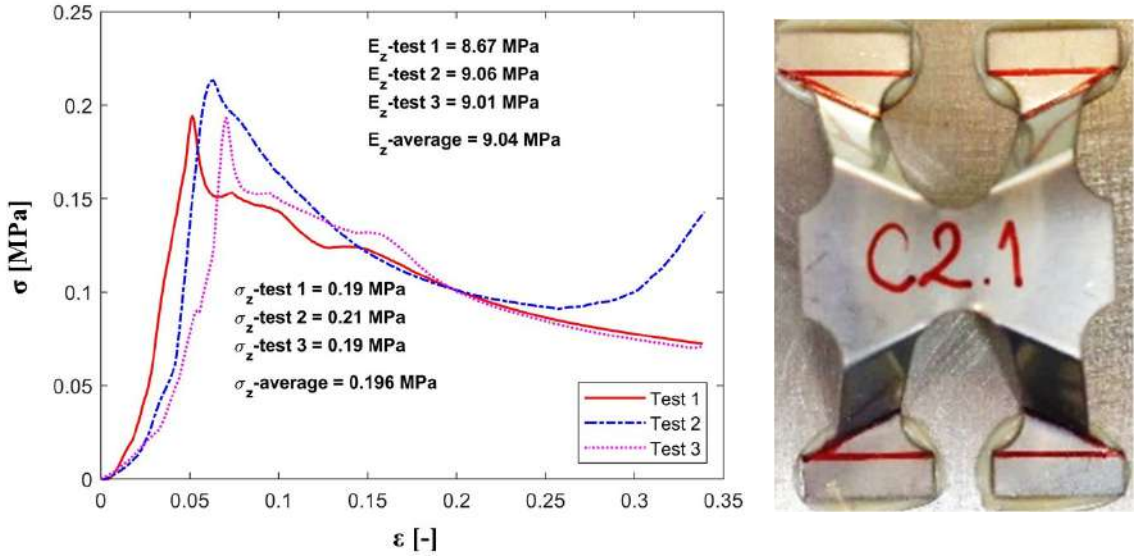

Figure 7. Stress-strain plot for the C2 configuration under out-of-plane compression.

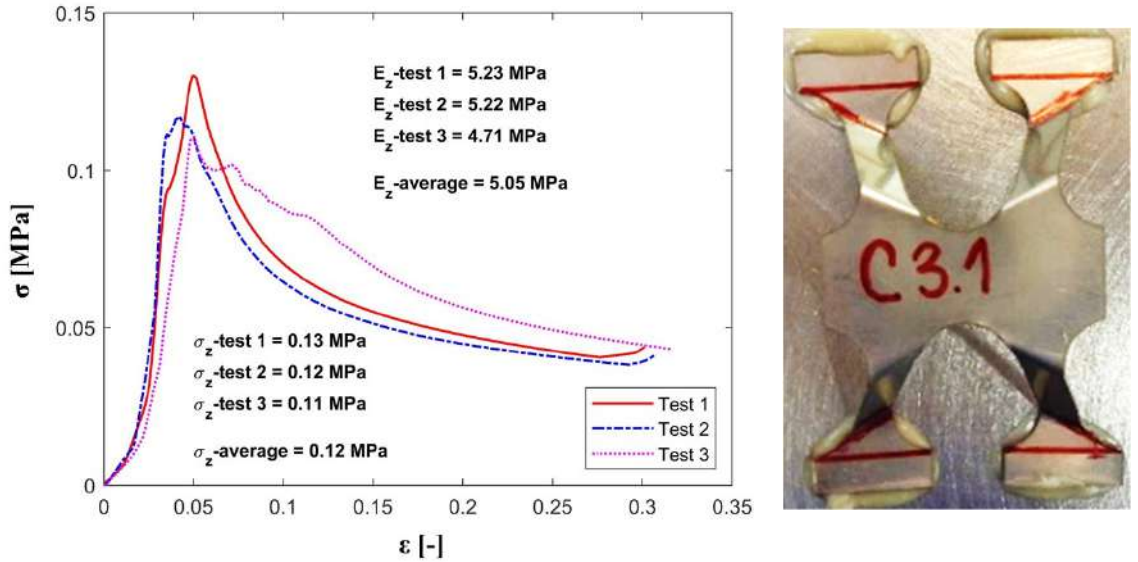

Figure 8. Stress-strain plot for the C3 configuration under out-of-plane compression.

The comparative study shows that both models, analytical and experimental, follow the same path which outlines that the analytical model was successfully validated through the experimental testing.

6. Parametric Study

Based on the validated analytical model, the out-of-plane mechanical properties can be studied while varying the geometric parameters.

Figure 9 shows the evolution of the specific compressive stiffness and strength, E_z/ρ and σ_z/ρ, for the investigated structure. The fixed parameters of the structure were $l_0 = 15$ mm, $c = 15$ mm, $l_1 = 10$ mm while the strut inclination angle varied in the range of [0°–90°]. The radius of the perforation was different for each of the tested configurations; $R = 3$ mm for C1, $R = 4$ mm for C2 and $R = 5$ mm for C3. The expansion angle differed between the three configurations as well since its value is dependent on the perforation radius.

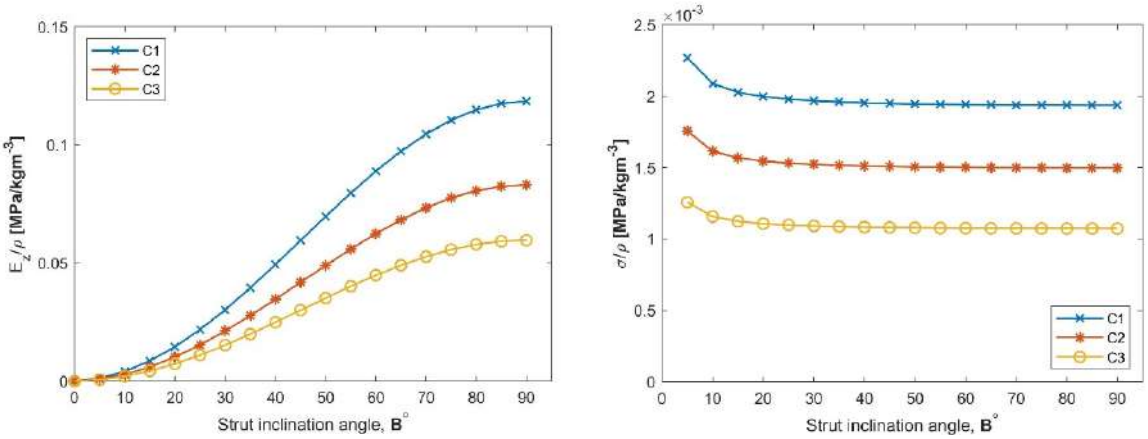

(**a**) (**b**)

Figure 9. (**a**) Normalized compression stiffness and (**b**) normalized compression strength for the configurations subjected to study.

On the one hand, as expected, the stiffness of the pyramidal structure is significantly influenced by an increase of the strut inclination angle B, Figure 9a. On the other hand, it results that the specific stiffness will decrease with the increase of the perforation radius R (which turns into an increase of the angle A).

The strength of the structure, Figure 9b, decreases together with an increase of the perforation radius, R, and, therefore, with an increase of the angle A. The difference between the three configurations is caused by the slenderness of the cell's strut. The highest values are recorded by the C1 configuration, where the radius of the perforation has the lowest value, $R = 3$ mm.

7. Discussion

The typical out-of-plane nominal stress-strain response for the pyramidal structure is shown in Figure 10. It can be observed that the structure exhibits typical characteristics of corrugated cellular structures: a region of elastic response (I), peak strength (1) followed by a plastic region represented by a drop in flow typical to Euler's buckling of the struts (II). The graph ends with a hardening region associated with core densification (III) [22].

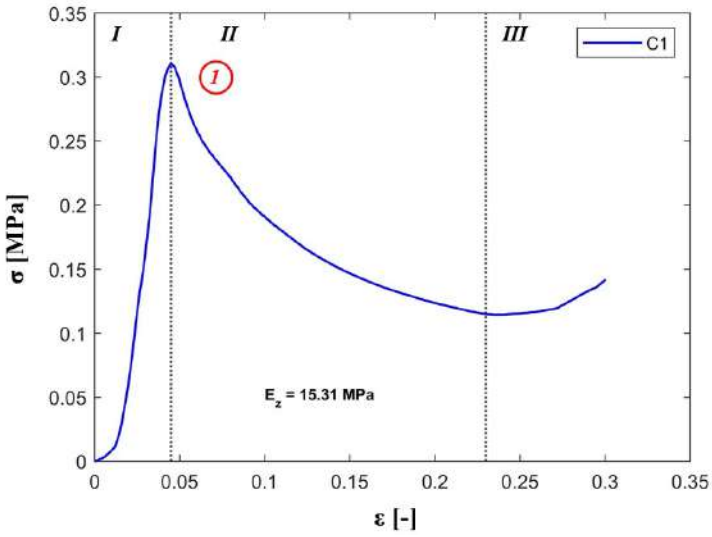

Figure 10. Stress-strain flow and characteristics of the investigated pyramidal cellular structure.

Analyzing the results presented in Table 3, it can be concluded that E_z decreases proportionally with the increase in value of the radius of the perforation, the major reason being the resulting slenderness of the cell's strut.

Having the out-of-plane stiffness of the investigated structure defined and validated, its performance has been compared with a selection of different core types, as shown in Figure 11.

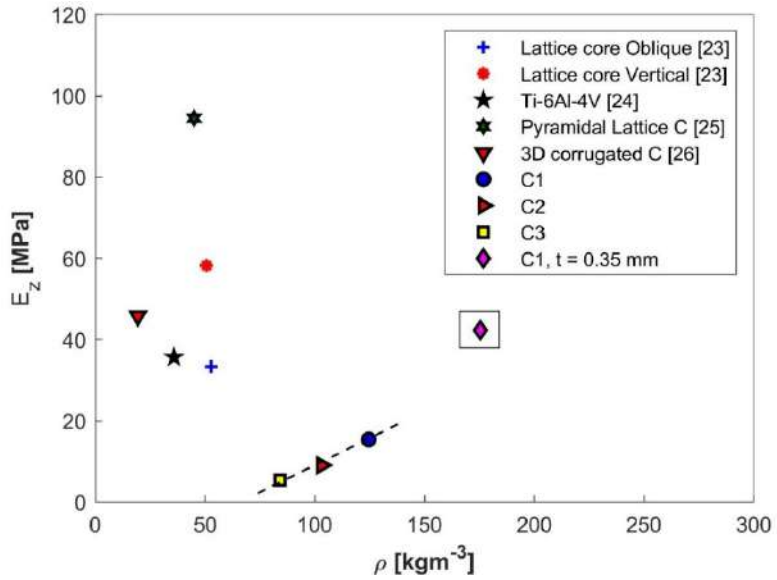

Figure 11. Out-of-plane stiffness as function of core density for several types of cellular structures.

The pyramidal structure did not show better compressive stiffness performance as compared to the other structures taken into consideration. Despite this, it is relevant to mention that the thickness of the base material was 0.25 mm, significantly reduced from the other studied structures (e.g., 0.9 mm for the carbon fiber/epoxy lattice core oblique and lattice core vertical developed by J. Xiong et al. [23] and 0.635 for the titanium alloy structure presented by Queheillalt and Wadley [24]). The reduced thickness of the parent material made the pyramidal structure more susceptible to buckling. However, by taking into consideration a base material thickness to 0.35 mm and computing the new value based on Equation (9), the stiffness of the structure became 42.36 MPa for a density of 175 kg·m^{-3}, marked in the rectangle on the graph. Through this configuration, the novel structure reached half the stiffness value compared to that of the pyramidal lattice C developed by Ming Li et al. [25] with a significantly higher density. The possibility of maintaining/increasing the stiffness while reducing the structure's density could be obtained by further applying both perforating and embossing operations on the struts in order to increase their second moment of inertia or by replacing the stainless steel with a low density material (e.g., aluminum).

The out-of-plane strength as a function of core density is illustrated in Figure 12. The highest performance with respect to strength has been registered for the C1 configuration with a maximum stress of 0.33 MPa. As a result, the newly developed structure is ranked above the lattice core oblique corrugation with a value of 0.32 and the 3D corrugated C presented by Jian Xiong et al. [26] but at a higher density.

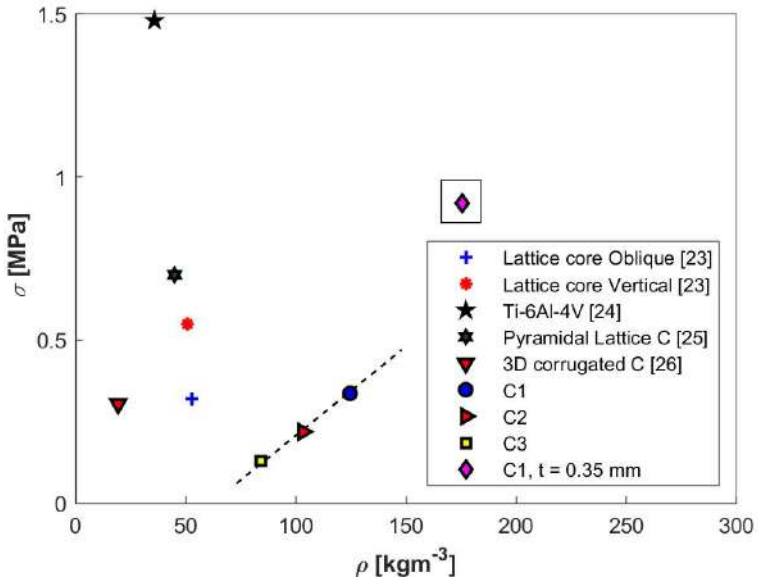

Figure 12. Strength as function of core density for several types of cellular structures.

If the material thickness used for the C1 configuration is increased from 0.25 mm to 0.35 mm, this brings the investigated structure to a compression strength of 0.92 MPa with a density of 175 kg·m^{-3}. Perforating and embossing operations on the struts may be a solution for increasing compressive strength performance.

The value of the internal angle A has been considered to be a function of the radius R (Table 1). This assumption turned out to be a limitation with respect to the performance of the structure (both stiffness and strength) because to increase the angle A, one needs to increase the value of R, which results in a slender strut. Further investigations should consider the angle A independent from the radius R.

In the current study, the mechanical behavior of the structure was linked to the characteristics of the material the structure was made of. Therefore, for different values of E and G (longitudinal and transversal stiffness moduli), the structural behavior will change accordingly. Furthermore, the developed model has been proven to work for the investigated geometry. If a bigger or a smaller scale are considered, additional effects might have to be investigated. Temperature effects are also not taken into consideration within this study, but it is a topic of interest for further investigations. In particular, the behavior of the adhesive should be considered if the temperature varies significantly.

8. Conclusions

The main purpose of this research was to evaluate the mechanical properties of a novel pyramidal cellular core obtained through a mechanical expansion process for the construction of sandwich panels. A theoretical model has been developed to define the out-of-plane compressive behavior. Expressions for computing the maximum strength, and stiffness were defined with the help of the developed analytical model which was validated through experimental testing.

The following conclusions can be drawn regarding the proposed pyramidal structure:

- The present pyramidal cellular core has the potential to compete with other cellular core concepts
- A decreased internal angle A increases both the out-of-plane stiffness and out-of-plane strength, but increases the core density
- Increased overall structural performance (both stiffness and strength) may be achieved by considering the angle A independent from the radius R.
- The specific stiffness and strength behavior can be improved by using low-density materials or by increasing the second moment of inertia of the struts, for example through embossing operations.

Author Contributions: M.I. manufactured the specimens, did the experiments, and developed the analytical model. P.W. supervised the experimental tests and reviewed the article. S.L. supervised the work and reviewed the article. M.N.V. wrote the paper together with M.I. M.N.V. reviewed the analytical model. All authors have read and agreed to the published version of the manuscript.

Funding: This research received no external funding.

Acknowledgments: This work has been part of a doctoral research stage funded by Transilvania University of Brasov through a research grant at the Lightweight Structures Laboratory from the Royal Institute of technology, KTH Sweden. The technical support of the Lightweight Structures group members at the Royal Institute of technology—KTH is acknowledged.

Conflicts of Interest: The authors declare no conflict of interest.

References

1. Wadley, H.N. Multifunctional periodic cellular metals. *Philos. Trans. R. Soc. A Math. Phys. Eng. Sci.* **2005**, *364*, 31–68. [CrossRef] [PubMed]
2. Bitzer, T.N. *Honeycomb Technology: Materials, Design, Manufacturing, Applications and Testing*; Springer Science & Business Media: Dordrecht, The Netherlands, 1997.
3. Wadley, H.; Fleck, N.A.; Evans, A.G. Fabrication and structural performance of periodic cellular metal sandwich structures. *Compos. Sci. Technol.* **2003**, *63*, 2331–2343. [CrossRef]
4. Shafizadeh, J.E.; Seferis, J.C.; Chesmar, E.F.; Geyer, R. Evaluation of the In-Service Performance Behavior of Honeycomb Composite Sandwich Structures. *J. Mater. Eng. Perform.* **1999**, *8*, 661–668. [CrossRef]
5. Kooistra, G.W.; Deshpande, V.; Wadley, H.N.G. Hierarchical Corrugated Core Sandwich Panel Concepts. *J. Appl. Mech.* **2007**, *74*, 259–268. [CrossRef]
6. Kazemahvazi, S.; Tanner, D.; Zenkert, D. Corrugated all-composite sandwich structures. Part 2: Failure mechanisms and experimental programme. *Compos. Sci. Technol.* **2009**, *69*, 920–925. [CrossRef]
7. Rashed, M.; Ashraf, M.; Mines, R.; Hazell, P. Metallic microlattice materials: A current state of the art on manufacturing, mechanical properties and applications. *Mater. Des.* **2016**, *95*, 518–533. [CrossRef]
8. Feng, L.J.; Wu, L.Z.; Yu, G.C. An Hourglass truss lattice structure and its mechanical performances. *Mater. Des.* **2016**, *99*, 581–591. [CrossRef]
9. Fan, H.; Sun, F.; Yang, L.; Jin, F.; Zhao, D. Interlocked hierarchical lattice materials reinforced by woven textile sandwich composites. *Compos. Sci. Technol.* **2013**, *87*, 142–148. [CrossRef]
10. Schneider, C.; Velea, M.; Kazemahvazi, S.; Zenkert, D. Compression properties of novel thermoplastic carbon fibre and poly-ethylene terephthalate fibre composite lattice structures. *Mater. Des.* **2015**, *65*, 1110–1120. [CrossRef]
11. Velea, M.; Schneider, C.; Lache, S. Second order hierarchical sandwich structure made of self-reinforced polymers by means of a continuous folding process. *Mater. Des.* **2016**, *102*, 313–320. [CrossRef]
12. Velea, M.N.; Lache, S. Energy absorption of all-PET 2nd order hierarchical sandwich structures under quasi-static loading conditions. *Thin Walled Struct.* **2019**, *138*, 117–123. [CrossRef]
13. Liu, W.; Song, H.W.; Wang, Z.; Wang, J.; Huang, C. Improving mechanical performance of fused deposition modeling lattice structures by a snap-fitting method. *Mater. Des.* **2019**, *181*, 108065. [CrossRef]
14. Beharic, A.; Egui, R.R.; Yang, L. Drop-weight impact characteristics of additively manufactured sandwich structures with different cellular designs. *Mater. Des.* **2018**, *145*, 122–134. [CrossRef]
15. Wei, K.; Yang, Q.; Yang, X.; Tao, Y.; Xie, H.; Qu, Z.; Fang, D. Mechanical analysis and modeling of metallic lattice sandwich additively fabricated by selective laser melting. *Thin Walled Struct.* **2020**, *146*, 106189. [CrossRef]
16. Pollard, D.; Ward, C.; Herrmann, G.; Etches, J. The manufacture of honeycomb cores using Fused Deposition Modeling. *Adv. Manuf. Polym. Compos. Sci.* **2017**, *3*, 21–31. [CrossRef]
17. Castigliano, C.A. *Intorno ai Sistemi Elastici*; Politecnico di Torino: Torino, Italy, 1873.
18. Reddy, J.N. *Energy Principles and Variational Methods in Applied Mechanics*, 2nd ed.; John Wiley & Sons, Inc.: Hoboken, NJ, USA, 2002.
19. Bartolozzi, G.; Pierini, M.; Orrenius, U.; Baldanzini, N. An equivalent material formulation for sinusoidal corrugated cores of structural sandwich panels. *Compos. Struct.* **2013**, *100*, 173–185. [CrossRef]
20. Bartolozzi, G.; Baldanzini, N.; Pierini, M. Equivalent properties for corrugated cores of sandwich structures: A general analytical method. *Compos. Struct.* **2014**, *108*, 736–746. [CrossRef]

21. Velea, M.; Lache, S. In-plane effective elastic properties of a novel cellular core for sandwich structures. *Mech. Mater.* **2011**, *43*, 377–388. [CrossRef]
22. Queheillalt, D.T.; Wadley, H.N. Cellular metal lattices with hollow trusses. *Acta Mater.* **2005**, *53*, 303–313. [CrossRef]
23. Xiong, J.; Ma, L.; Vaziri, A.; Yang, J.; Wu, L. Mechanical behavior of carbon fiber composite lattice core sandwich panels fabricated by laser cutting. *Acta Mater.* **2012**, *60*, 5322–5334. [CrossRef]
24. Queheillalt, D.T.; Wadley, H.N. Titanium alloy lattice truss structures. *Mater. Des.* **2009**, *30*, 1966–1975. [CrossRef]
25. Li, M.; Wu, L.; Ma, L.; Wang, B.; Guan, Z. Mechanical Response of All-composite Pyramidal Lattice Truss Core Sandwich Structures. *J. Mater. Sci. Technol.* **2011**, *27*, 570–576. [CrossRef]
26. Xiong, J.; Ma, L.; Wu, L.; Wang, B.; Vaziri, A. Fabrication and crushing behavior of low density carbon fiber composite pyramidal truss structures. *Compos. Struct.* **2010**, *92*, 2695–2702. [CrossRef]

© 2020 by the authors. Licensee MDPI, Basel, Switzerland. This article is an open access article distributed under the terms and conditions of the Creative Commons Attribution (CC BY) license (http://creativecommons.org/licenses/by/4.0/).

Thin-Walled Structures 138 (2019) 117–123

Contents lists available at ScienceDirect

Thin-Walled Structures

journal homepage: www.elsevier.com/locate/tws

Full length article

Energy absorption of all-PET 2nd order hierarchical sandwich structures under quasi-static loading conditions

Marian N. Velea, Simona Lache*

Transilvania University of Brasov, Department of Mechanical Engineering, Romania

ARTICLE INFO

Keywords:
Hierarchical sandwich structure
Thermoplastic composites
Self-reinforced polymers
Specific energy absorption

ABSTRACT

The impact performance of lightweight structures represents an important design criterion in modern applications. Within this framework, the self-reinforced PET (poly-ethylene terephthalate) materials prove to exhibit large deformations till failure, which enables them to be proper candidates for impact energy absorption. Apart from the advantages offered by the lightweight characteristics, they are made of recyclable materials, an additional reason for their consideration in engineering applications. In this paper, the behavior of a hierarchical sandwich structure made out of self-reinforced PET (matrix & fibre) combined with PET foam is numerically investigated with respect to the specific energy absorption (SEA) capacity in out-of-plane quasi-static loading conditions. The numerical model of the structure is developed and its behavior is firstly validated through experimental tests. The specific energy absorption is further on determined for several geometric configurations of the hierarchical sandwich structure and compared with the behavior of other cellular structures found in the technical literature. A competitive behavior is observed with respect to impact energy absorption.

1. Introduction

Apart from high strength and stiffness to weight ratios, the specific energy absorption (SEA) capacity of lightweight structures and, more specifically, of sandwich structures represents a major interest from an impact protection perspective [1–3]. Several constructive solutions were proposed in order to reach higher SEA performance criteria. In general, the cellular cores of the sandwich structures are the components that count when it comes to impact performance. Whether these cellular structures are made of metallic materials [4–6], CFRP [7–10] or a combination of several materials [8,11,12] formed into simple [13,14] or complex shapes [15–22], it is always a matter of finding the proper type and arrangement of material(s) that offer the highest absorbed impact energy to weight ratio. A consistent review with respect to the SEA performance of thin-walled tubes having different cross sections, filled or not with stochastic foams, is done by Baroutaji et al. [23]. A critical review done by Barthelat [24] emphasizes the benefits of using the so called architectured materials with respect to impact energy absorption.

Recently, the self-reinforced poly-ethylene terephthalate (SrPET) material [25–27] has been investigated and used for manufacturing different cellular topologies for sandwich structures [28,29]. Kazemahvazi et al. [30] and Schneider et al. [31] proved that these materials pose higher ductility compared to conventional glass and carbon reinforced plastics, which make them appropriate for impact protection applications [32], apart from the obtained lower life cycle environmental impact [33].

An all-PET 2nd order hierarchical sandwich structure has been previously proposed [29] based on a simple manufacturing route (i.e. folding of a single sheet of material which has monolithic and sandwich sections distributed in an alternate way). This structure is herein investigated based on a validated FE model, with respect to the specific energy absorption under quasi-static loading conditions, for several geometric configurations. A comparison of the specific energy absorption for the investigated structure is made with the state of the art cellular structures found in the literature.

2. The shape and constituent materials of the structures

The investigated second order hierarchical sandwich structure is obtained through a continuous flow of operations described in detail by Velea et al. [29]. Essentially, the structure is obtained by folding an already consolidated plate which contains alternate monolithic and sandwich sections (Fig. 1). The 2nd order sandwich hierarchy results without adding other plates as face sheets, this being an important advantage of the proposed manufacturing method. A mechanical inter-

* Correspondence to: Transilvania University of Brasov, 29 Eroilor Blvd, 500036 Brașov, Romania.
E-mail address: slache@unitbv.ro (S. Lache).

https://doi.org/10.1016/j.tws.2019.01.039
Received 2 July 2018; Received in revised form 15 January 2019; Accepted 30 January 2019
Available online 07 February 2019
0263-8231/ © 2019 Elsevier Ltd. All rights reserved.

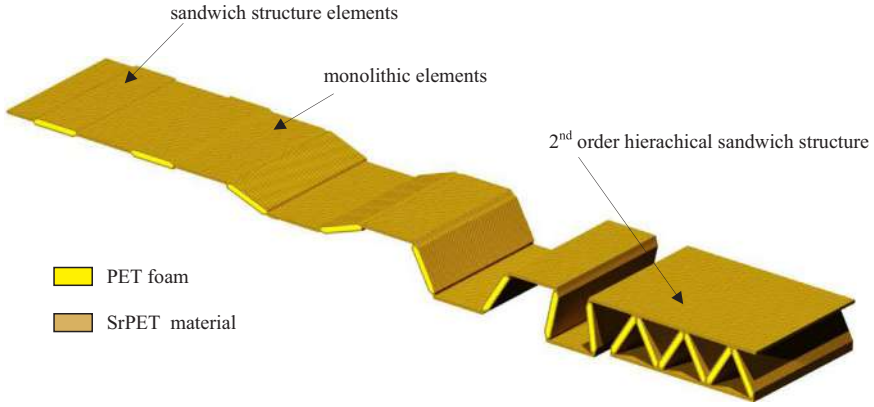

Fig. 1. Manufacturing principle of the 2nd order hierarchical sandwich structure.

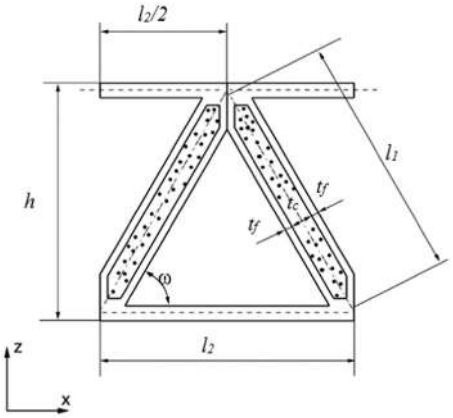

Fig. 2. The unit cell of the investigated all-PET 2nd order hierarchical sandwich structure and its geometric parameters [29]. The dotted area represents the PET structural foam. Geometric parameters: l_1 – length of the sandwich section, l_2 – length of the monolithic section, h – height of the sandwich unit cell, t_c – thickness of the PET foam, t_f – thickness of the face sheets, ω – folding angle.

locking results at the end of the sandwich struts, due to the folding procedure, which excludes the classical in-plane interface between the face sheets and the core structure in general. The structure is made out of poly-ethylene terephthalate matrix reinforced with poly-ethylene terephthalate fibres (SrPET) and poly-ethylene terephthalate foam (PET), Figs. 2 and 3.

Details on the SrPET material characteristics were previously published by Schneider et al. [25,34]. The foam used for creating the specimens is an ArmaForm PET AC with a density of 100 kg m^{-3} [35]. The connection of the sandwich struts elements is made by the local melting, pressing and cooling of the PET, guided through the alignment of the monolithic elements, without adding other joining material.

3. Numerical investigation

The numerical investigation is performed based on a validated FE model developed in Abaqus commercial software in order to extract the force - displacement curve in out-of-plane compression quasi-static loading conditions for 10 geometric configurations. Based on these results and by following the resulted deformation modes, an evaluation of the absorbed energy capacity can be performed.

3.1. Geometry and mesh type

The geometric configurations investigated numerically are shown in Table 1, where the corrugation angle ω is kept constant at 60°, as well as the width of the specimens, $w = 40$ mm.

The layers of SrPET material are modelled as shells while the PET foam is modelled as solid, Fig. 4. 8-node linear solid elements, type C3D8R, with reduced integration and hourglass control are used for the discretization of the foam geometry (Fig. 5). The shell geometry is meshed with 4-node linear elements, type S4R, also with reduced integration and hourglass control (Fig. 5).

3.2. Boundary conditions, interactions and constraints

The bottom and side surfaces of the unit cell are constrained, as shown in Fig. 6, in order to avoid the edge effects. An imposed displacement is applied on point A, Fig. 6, which is connected by means of a kinematic coupling constraint to the top surface of the structure. Along the simulation history, the reaction force is recorded on the same point A. The imposed displacement δ is calculated, for each geometric

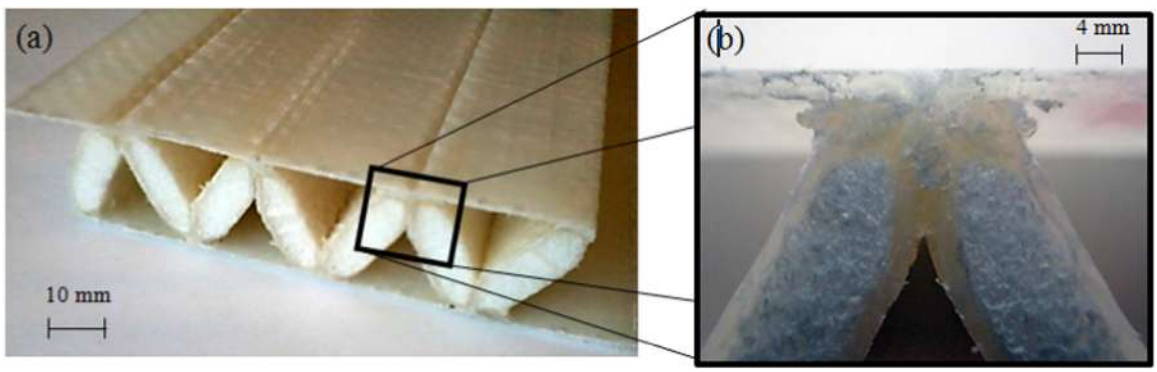

Fig. 3. (a) The all-PET 2nd order hierarchical sandwich structure (b) Cross section within the joining area – no additional material is used for the joining procedure; the joint is done by locally melting the PET on the face sheets, pressing and cooling [29].

Table 1
The investigated geometric configurations.

Configuration	t_f [mm]	t_c [mm]	l_1 [mm]	l_2 [mm]	h [mm]	ρ [kg m^{-3}]
I	0.45	7.1	24	25.8	23.64	232
II	0.9	6.2	25	27.6	25.94	346
III	0.45	7.1	81	80.8	70.99	23
IV	0.9	6.2	82	84.6	75.31	41
V	0.45	4.2	34	34.8	31.16	75
VI	0.9	8.5	35	36.6	33.74	254
VII	0.45	4.2	56	56.8	50.21	29
VIII	0.9	8.5	57	58.6	52.79	105
IX	0.45	4.2	100	96.8	84.85	10
X	0.9	8.5	97	98.6	87.43	39

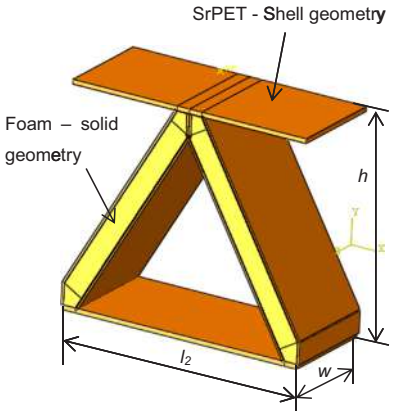

Fig. 4. Type of geometry of the components (foamPET and SrPET).

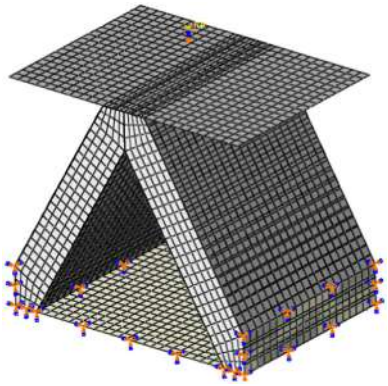

Fig. 5. Discretization of the geometry with finite elements.

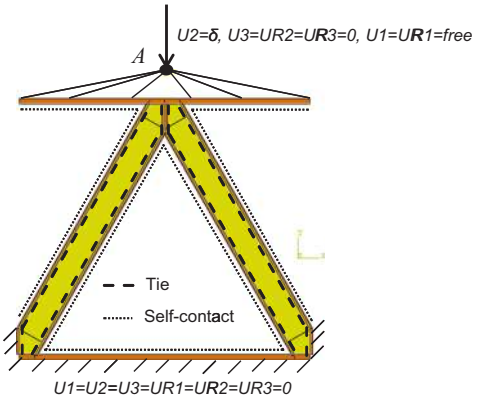

Fig. 6. The applied boundary conditions and constraints.

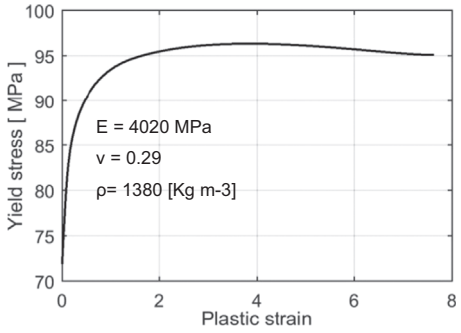

Fig. 7. Plastic material behavior of the SrPET material considered within the FE model.

configuration, in order to obtain $\varepsilon = \delta/h = 0.1$, where h represents the initial height of the structure.

The foam (solid elements) is connected to the SrPET face sheet (shell elements) through a tie constraint, Fig. 6. A self-contact is defined by using the surface to surface discretization method [36] in order to avoid penetration of the surfaces during the out of plane compression of the structure (see Fig. 6).

3.3. Materials' properties

The elastic and plastic material data considered in the numerical model for the SrPET material are shown in Fig. 7 and they are established according to the measurements published by Schneider et al. [25] and by Kazemahvazi et al. [34].

The data describing the elastic and plastic material behavior for the PET foam material is shown in Fig. 8 and it is based on the producer's technical sheet [35] correlated with the experiments carried out by Costas et al. [12].

3.4. Validation of the FE model

The developed FE model is validated by comparing the experimentally obtained stress-strain curves for the geometric configurations I, II, III and IV (see Table 1) and the corresponding analytical solution, both obtained by Velea et al. [29], with the ones numerically obtained herein, from Figs. 9–12. Based on the numerically obtained force-displacement curves, the stress σ is obtained by dividing the measured force F to the area of the unit cell ($w \cdot l_2$), while the strain ε is given by the δ/h ratio, where δ represents the imposed displacement and h is the initial height of the unit cell (see Fig. 4), similar to Harris et al. in [37].

Fig. 9 shows that, for case I, the peak strength is twice compared to the numerical and analytical results, the latter two being very close in value (3% difference). This major difference between the experiments and both the numerical and analytical solutions can be explained by a high sensitivity on the manufacturing method of the specimens (i.e.

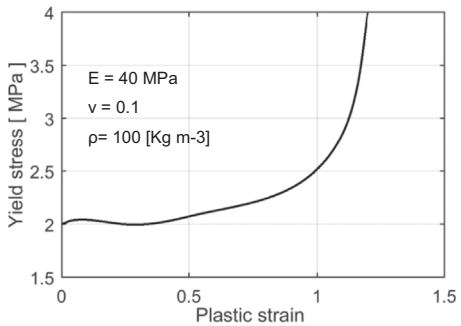

Fig. 8. Plastic material behavior of the PET foam considered within the FE model.

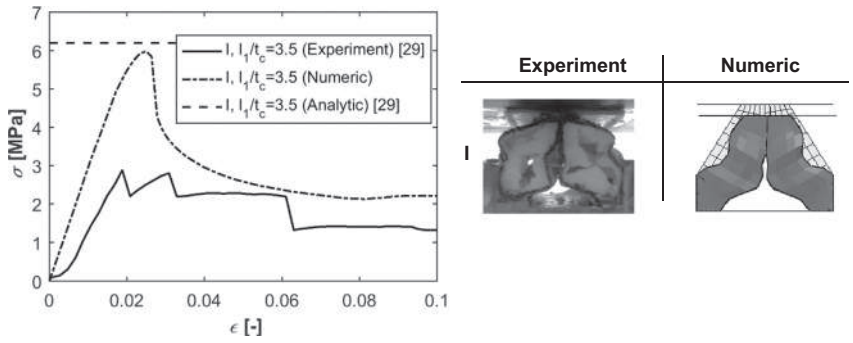

Fig. 9. The obtained numerical results compared with the experimental results and analytical calculations [29] for case I (Table 1).

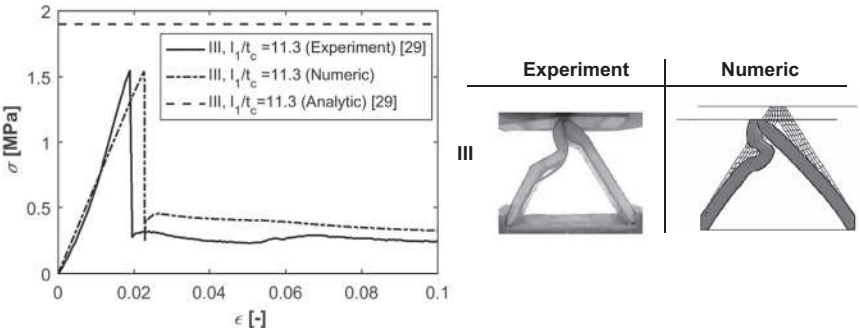

Fig. 10. The obtained numerical results compared with the experimental results and analytical calculations [29] for case III (Table 1).

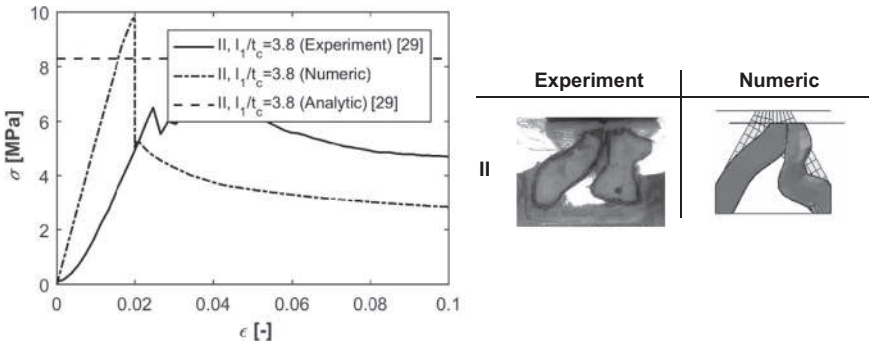

Fig. 11. The obtained numerical results compared with the experimental results and analytical calculations [29] for case II (Table 1).

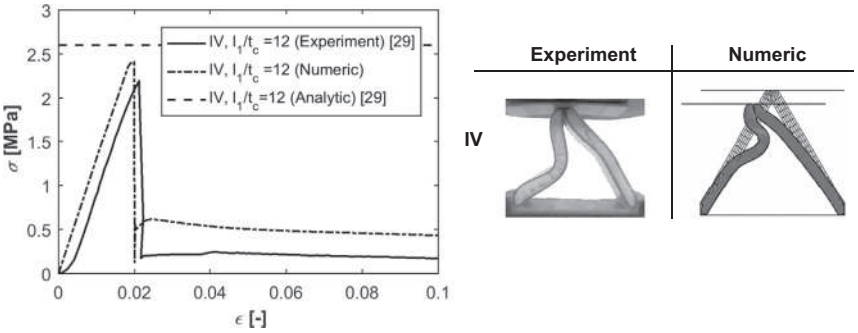

Fig. 12. The obtained numerical results compared with the experimental results and analytical calculations [29] for geometric configurations IV (Table 1).

band saw cutting, at moderate speed, in order not to melt de PET under friction) where the foam suffered at the edges a premature crack at the interface with the SrPET face sheet. In addition, as shown in [29], the failure mode for this geometric case was the local buckling which is initiated by the above mentioned premature crack. However, since both analytical and numerical results are close to each other, it is expected that an ideal manufactured sample will have a similar experimental behavior. In terms of stiffness, a slightly higher value is obtained numerically, as expected. The post-failure region of the numerical model is comparable with the experimental curve.

When looking at case III, Fig. 10, the maximum strength is very well predicted by the numerical model compared to the experiments. The analytical solution is a bit higher but still within acceptable limits (1% difference). The numerical estimated stiffness is slightly lower

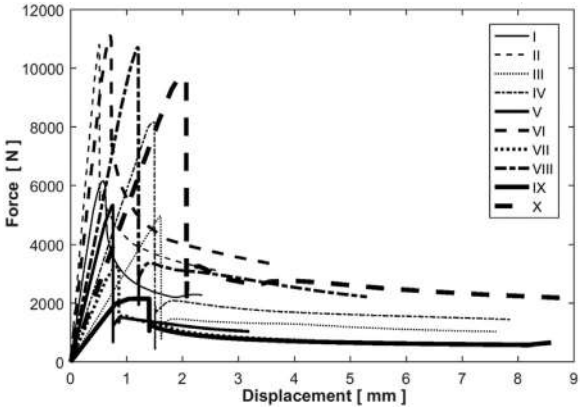

Fig. 13. Force - displacement curve for the investigated geometric configurations.

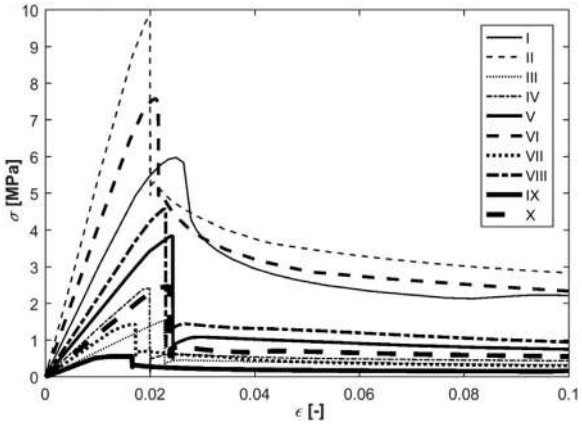

Fig. 14. Strain - Stress curve for the investigated geometric configurations.

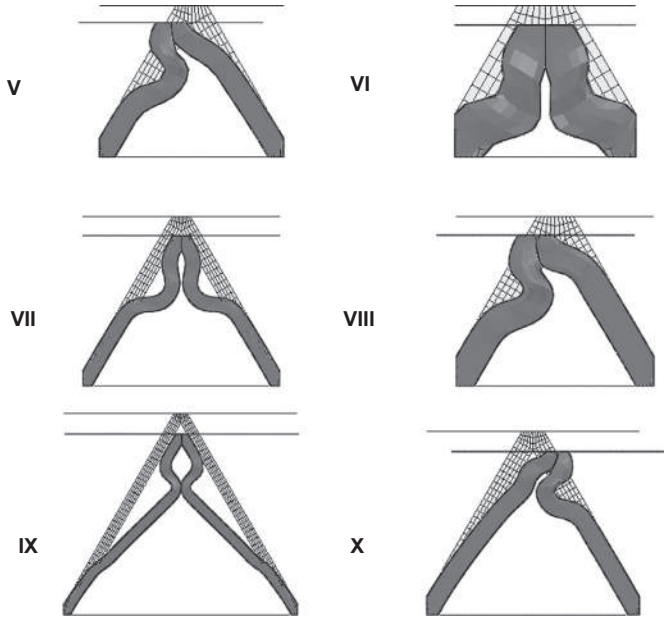

Fig. 15. The deformed shapes of the structures (V to X) for $\varepsilon = 0.1$.

compared to the experiments. The post-failure region of the numerical model fits very well the experimental curve. The failure of the core is initiated by local buckling.

Fig. 11 shows that pretty scattered solutions are obtained for case II, for the maximum strength point of view. We certainly have the same

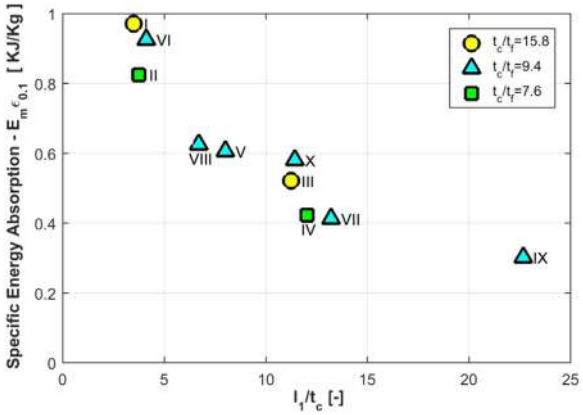

Fig. 16. The resulted E_m in terms of the geometric parameters of the investigated structure.

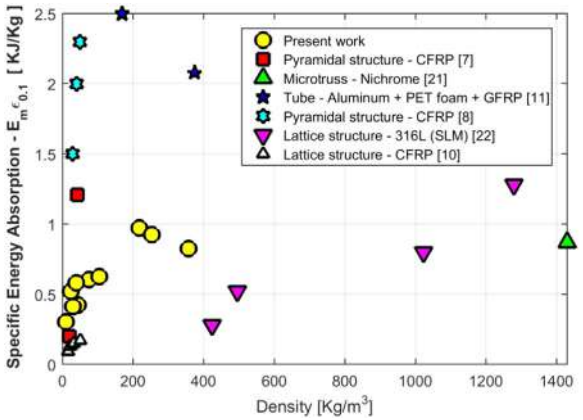

Fig. 17. Comparison of the specific energy absorption E_m for different proposed cellular structures for $\varepsilon = 0.1$.

influence of the manufacturing method, similar to case I, that gives a difference of approximately 45% between the experimental and numerical results. However, the difference is not as big as in the case I because the thickness of the SrPET material is doubled (0.9 mm instead of 0.45 mm) which increased the stiffness of the strut and therefore being more stable when cutting the specimens. The analytically obtained value is however close to the numerical one (15% difference). The structure fails, in this case, by shear buckling.

For case IV, Fig. 12, there is an almost perfect correlation between the numerical, analytical and experimental results. The observed failure mode is shear buckling followed by general buckling.

It is therefore concluded that the FE model predicts very well the experimental behavior for case II and IV; these results are also strengthened by the analytical results. Differences exist for cases I and III, at higher l_1/t_c ratios, where the structure is denser and where there is a major influence of the manufacturing method on its experimental assessed behavior.

Based on the validated FE models for geometric cases I, II, III, and IV, additional geometric cases V to X, Table 1, have been investigated in quasi-static loading conditions in order to extract the force - displacement curve, Fig. 13.

By having the force - displacement data, and by taking into consideration the size of the specimens, Table 1, for each investigated case, the Stress - Strain relationship is reached, Fig. 14.

The corresponding deformed shapes of the geometric configurations V, VI, VII, VIII, IX and X, at $\varepsilon = 0.1$ are shown in Fig. 15.

4. Specific energy absorption

Several quantitative criteria exist for the evaluation of the energy absorption capacity [1,38]. One of the most used refers to the determination of the specific energy absorption capacity E_m [KJ/Kg], which is the absorbed energy per unit mass. Thus, the specific energy absorption capacity of a structure is calculated as the ratio between the absorbed energy E_{abs} and its mass m, Eq. (1).

$$E_m = SEA = \frac{E_{abs}}{m}, \tag{1}$$

where,

$$E_{abs} = \int_0^{\delta_{max}} F(\delta)d\delta, \tag{2}$$

with: m – mass of the structure; F – measured force; δ – crushing distance

It is known that higher values for the reaction forces are obtained at higher strain rates when compared to a quasi-static loading [15,39,40], meaning that higher SEA capacity results as the strain rate is increasing. Therefore, the current SEA estimation, based on quasi-static-loading conditions, allows obtaining the lower boundary for the energy absorption capacity.

The energy absorption E_{abs} and the corresponding specific energy absorption E_m is calculated herein for $\varepsilon = 0.1$. This condition results from the need of a comparison base between the investigated geometric cases (see Fig. 13, where the compression depth differs from one geometric case to the other) and the other types of cellular structures from the technical literature. Fig. 16 shows that, for the investigated hierarchical sandwich structure, the specific energy absorption E_m increases while the l_1/t_c ratio decreases. For the same t_c/t_f ratio, the specific energy absorption E_m increases twice for the case I (232 kg m^{-3}) compared to the case III (23 kg m^{-3}). The same behavior is similar for the case II (346 kg m^{-3}) compared to the case IV (41 kg m^{-3}), which indicates, as expected, an increase of the E_m values with the density. The value of the E_m doubles while the density of the structure is ten times increased. Another observation is that the E_m is increasing by 20% while doubling the thickness t_f of the face sheets.

Fig. 17 shows a comparison of the specific energy absorption E_m obtained for the investigated structure with the one of different types of structures found in the literature, in terms of structures' density. For the same specific energy absorption (aprox. 1 kJ/kg), the density of the all-PET 2nd order hierarchical sandwich structure is five times lower compared to the one of the lattice structures made by steel through additive manufacturing [22] and seven times lower when compared to the micro-trusses made out of Nichrome alloy [21]. It can also be observed that, for the same density value (~40 kg m^{-3}), the all-PET 2nd order hierarchical sandwich structure can reach a three times higher specific energy absorption capacity compared to the lattice structures made out of CFRP [10]. However, a better behavior at the same weight is observed for a hybrid structure that contains Aluminum, PET foam and GFRP reinforcements [11] and for a type of pyramidal structure made out of CFRP [8].

5. Conclusions

Based on a validated numerical model, a parametric study was done in order to investigate the specific energy absorption in quasi-static loading conditions for a hierarchical sandwich structure. The investigated all-PET 2nd order hierarchical sandwich structure proves to be a competitive constructive solution with respect to energy absorption capacity when compared to other existing cellular configurations which are made through more complicated manufacturing routes. The herein proved characteristics are coming both from the ductile behavior of the SrPET material, combined with the PET foam, and from the geometric arrangement of the investigated cellular structure. This competitive behavior represents an added value for the investigated 2nd order hierarchical sandwich structure in addition to the already proved advantages, such as mechanical performance in out-of-plane compression and a lower life cycle environmental impact through a high degree of recyclability.

Acknowledgements

The financial support from Transilvania University of Brasov is gratefully acknowledged as well as the support received from Christof Schneider, KTH – Royal Institute of Technology, for helping with the specimens.

References

[1] L.J. Gibson, M.F. Ashby, Cellular Solids. Structure and Properties, 2nd ed., Cambridge University Press, 1999.
[2] M. Ashby, A.G. Evans, N.A. Fleck, L. Gibson, J.W. Hutchinson, H. Wadley, Metal Foams - A Design Guide, Butterworth-Heinemann, 2000.
[3] S. Kazemahvazi, B.P. Russell, D. Zenkert, Impact of carbon fibre/epoxy corrugated cores, Compos. Struct. 94 (11) (2012) 3300–3308.
[4] F. Sun, C. Lai, H. Fan, D. Fang, Crushing mechanism of hierarchical lattice structure, Mech. Mater. 97 (2016) 164–183.
[5] F. Cote, V.S. Deshpande, N.A. Fleck, A.G. Evans, The out-of-plane compressive behavior of metallic honeycombs, Mater. Sci. Eng. A 380 (2004) 272–280.
[6] M. Smith, W. Cantwell, Z. Guan, S. Tsopanos, M. Theobald, G. Nurick, G. Langdon, The quasi-static and blast response of steel lattice structures, J. Sandw. Struct. Mater. 13 (4) (2011) 479–501.
[7] J. Xiong, A. Vaziri, L. Ma, J. Papadopoulos, L. Wu, Compression and impact testing of two-layer composite pyramidal-core sandwich panels, Compos. Struct. 94 (2) (2012) 793–801.
[8] G. Zhang, B. Wang, L. Ma, J. Xiong, L. Wu, Response of sandwich structures with pyramidal truss cores under the compression and impact loading, Compos. Struct. 100 (2013) 451–463.
[9] S. Kazemahvazi, D. Tanner, D. Zenkert, Corrugated all-composite sandwich structures. Part 2: failure mechanisms and experimental programme, Compos. Sci. Technol. 69 (7–8) (2009) 920–925.
[10] T.A. Sebaey, E. Mahdi, Crushing behavior of a unit cell of CFRP lattice core for sandwich structures' application, Thin-Walled Struct. 116 (2017) 91–95.
[11] M. Costas, D. Morin, M. Langseth, L. Romera, J. Díaz, Axial crushing of aluminum extrusions filled with PET foam and GFRP. An experimental investigation, Thin-Walled Struct. 99 (2016) 45–57.
[12] M. Costas, D. Morin, M. Langseth, J. Díaz, L. Romera, Static crushing of aluminium tubes filled with PET foam and a GFRP skeleton. Numerical modelling and multi-objective optimization, Int. J. Mech. Sci. 131–132 (2017) 205–217.
[13] K.B. Shin, J.Y. Lee, S.H. Cho, An experimental study of low-velocity impact responses of sandwich panels for korean low floor bus, Compos. Struct. 84 (2008) 228–240.
[14] Mijia Yang, Pizhong Qiao, Quasi-static crushing behavior of aluminum honeycomb materials, J. Sandw. Struct. Mater. 10 (2) (2008) 133–160.
[15] L. Xiao, W. Song, Additively-manufactured functionally graded Ti-6Al-4V lattice structures with high strength under static and dynamic loading: experiments, Int. J. Impact Eng. 111 (2018) 255–272.
[16] X. Wang, J. Shen, Z.H. Zuo, X. Huang, S. Zhou, Y.M. Xie, Numerical investigation of compressive behaviour of luffa-filled tubes, Compos. Part B: Eng. 73 (2015) 149–157.
[17] J. Fang, G. Sun, N. Qiu, T. Pang, S. Li, Q. Li, On hierarchical honeycombs under out-of-plane crushing, Int. J. Solids Struct. 135 (2018) 1–13.
[18] I. Ullah, M. Brandt, S. Feih, Failure and energy absorption characteristics of advanced 3D truss core structures, Mater. Des. 92 (2016) 937–948.
[19] G. Sun, H. Jiang, J. Fang, G. Li, Q. Li, Crashworthiness of vertex based hierarchical honeycombs in out-of-plane impact, Mater. Des. 110 (2016) 705–719.
[20] X. An, H. Fan, Hybrid design and energy absorption of luffa-sponge-like hierarchical cellular structures, Mater. Des. 106 (2016) 247–257.
[21] D.J. Sypeck, H.N.G. Wadley, Multifunctional microtruss laminates: textile synthesis and properties, J. Mater. Res. 16 (3) (2001).
[22] S. McKown, Y. Shen, W.K. Brookes, C.J. Sutcliffe, W.J. Cantwell, G.S. Langdon, G.N. Nurick, M.D. Theobald, The quasi-static and blast loading response of lattice structures, Int. J. Impact Eng. 35 (8) (2008) 795–810.
[23] A. Baroutaji, M. Sajjia, A.-G. Olabi, On the crashworthiness performance of thin-walled energy absorbers: recent advances and future developments, Thin-Walled Struct. 118 (2017) 137–163.
[24] F. Barthelat, Architectured materials in engineering and biology: fabrication, structure, mechanics and performance, Int. Mater. Rev. 60 (8) (2015) 413–430.
[25] C. Schneider, S. Kazemahvazi, M. Åkermo, D. Zenkert, Compression and tensile properties of self-reinforced poly(ethylene terephthalate)-composites, Polym. Test. 32 (2) (2013) 221–230.
[26] J.M. Zhang, T. Peijs, Self-reinforced poly(ethylene terephthalate) composites by hot consolidation of Bi-component PET yarns, Compos. Part A: Appl. Sci. Manuf. 41 (8) (2010) 964–972.
[27] J.M. Zhang, C.T. Reynolds, T. Peijs, All-poly(ethylene terephthalate) composites by

film stacking of oriented tapes, Compos. Part A: Appl. Sci. Manuf. 40 (11) (2009) 1747–1755.
[28] C. Schneider, M.N. Velea, S. Kazemahvazi, D. Zenkert, Compression properties of novel thermoplastic carbon fibre and poly-ethylene terephthalate fibre composite lattice structures, Mater. Des. 65 (0) (2015) 1110–1120.
[29] M.N. Velea, C. Schneider, S. Lache, Second order hierarchical sandwich structure made of self-reinforced polymers by means of a continuous folding process, Mater. Des. 102 (2016) 313–320.
[30] S. Kazemahvazi, C. Schneider, V.S. Deshpande, A constitutive model for self-reinforced ductile polymer composites, Compos. Part A: Appl. Sci. Manuf. 71 (2015) 32–39.
[31] C. Schneider, S. Kazemahvazi, B.P. Russell, D. Zenkert, V.S. Deshpande, Impact response of ductile self-reinforced composite corrugated sandwich beams, Compos. Part B: Eng. 99 (2016) 121–131.
[32] C. Schneider, S. Kazemahvazi, D. Zenkert, V.S. Deshpande, Dynamic compression response of selfreinforced poly(ethylene terephthalate) composites and corrugated sandwich cores, Compos. Part A: Appl. Sci. Manuf. 77 (96–105) (2015).
[33] S. Poulikidou, C. Schneider, A. Björklund, S. Kazemahvazi, P. Wennhage, D. Zenkert, A material selection approach to evaluate material substitution for minimizing the life cycle environmental impact of vehicles, Mater. Des. 83 (2015) 704–712.
[34] S. Kazemahvazi, C. Schneider, V.S. Deshpande, A constitutive model for self-reinforced ductile polymer composites, Compos. Part A: Appl. Sci. Manuf. 71 (0) (2015) 32–39.
[35] Armacell Benelux. ArmaFORM PET/AC Technical data, Rue de Trois Entities 9-B-4890 Thimister Clermont. ⟨www.armacell.com⟩. (Accessed 2 April 2014).
[36] Prescribed Conditions, Constraints & Interactions, Abaqus Analysis User's Manual, Dassault Systèmes, 6.14.
[37] J.A. Harris, R.E. Winter, G.J. McShane, Impact response of additively manufactured metallic hybrid lattice materials, Int. J. Impact Eng. 104 (2017) 177–191.
[38] G. Nagel, Impact and Energy Absorption of Straight and Tapered Rectangular Tubes, Queensland University of Technology, 2005.
[39] S. Lee, F. Barthelat, J.W. Hutchinson, H.D. Espinosa, Dynamic failure of metallic pyramidal truss core materials - experiments and modelling, Int. J. Plast. 22 (2006) 2118–2145.
[40] T. Tancogne-Dejean, A.B. Spierings, D. Mohr, Additively-manufactured metallic micro-lattice materials for high specific energy absorption under static and dynamic loading, Acta Mater. 116 (2016) 14–28.

Materials and Design 102 (2016) 313–320

Contents lists available at ScienceDirect

Materials and Design

journal homepage: www.elsevier.com/locate/matdes

Second order hierarchical sandwich structure made of self-reinforced polymers by means of a continuous folding process

M.N. Velea [a], C. Schneider [b,c], S. Lache [a,*]

[a] Transilvania University of Brasov, Department of Mechanical Engineering, Romania
[b] KTH, Department of Aeronautical and Vehicle Engineering, Stockholm, Sweden
[c] Swerea Swedish Research, Kista, Sweden

ARTICLE INFO

Article history:
Received 30 November 2015
Received in revised form 11 April 2016
Accepted 15 April 2016
Available online 16 April 2016

Keywords:
Hierarchical sandwich structure
Thermoplastic composites
Self-reinforced polymers
Folded structure
Optimization

ABSTRACT

One typical way to obtain higher stiffness and strength to weight ratios within structural applications is to use sandwich structures containing lightweight cellular cores. In this study a novel second order hierarchical sandwich structure and its manufacturing principle are described. The whole hierarchical structure is made of a fully recyclable material – different forms of poly-ethylene terephthalate (PET): PET matrix, reinforced with PET fibres (Self reinforced - SrPET) and PET foam resulting in a recyclable structure. The manufacturing path is developed such that it can be implemented within a continuous production line. Out-of-plane compression test are carried out in order to determine the stiffness and strength properties of the proposed structure. An analytical model is developed for evaluating the out-of-plane stiffness and strength properties and used for investigating the influence of the geometric parameters on the structural performance of the proposed hierarchical sandwich structure.

© 2016 Elsevier Ltd. All rights reserved.

1. Introduction

One way to reduce the vehicles' parts weight is to use materials that provide higher specific stiffness and strength to weight ratios. Therefore, material (re)selection represents an important weight optimization criterion and composite materials having improved mechanical properties are usually searched [1]. However, apart from material type, shape criterion is also important and it may represent an added advantage [2,3]. An example of a near optimal use of material is given by the sandwich concept [22]where the bending stiffness of the structure is increased by placing a lightweight and thicker core between two thin and stiff face sheets while the weight is negligibly increased. The continuing research on improving the overall mechanical performance of sandwich structures focuses also on developing novel core configurations, made of composite materials, in order to gain an improved mechanical behaviour of the core. Examples of such efforts include composite corrugated cores [21], square honeycomb cores [23], rhombic and kagome honeycombs [24], pyramidal lattice truss cores [13,19,25–28] or novel expanded cores [29,30]. Although many of these structures provide competitive weight specific strength and stiffness, their main drawback is related to manufacturing steps which are often complicated and difficult to be integrated within a continuous production line. The more recent development of additive manufacturing technologies allows generating complicated and efficient cellular shapes but on a limited scale yet [7,20].The hierarchical sandwich concept has been introduced as a solution to increase the in-plane shear and the out of plane compression performance [9–11,15,31]. The up to date developed hierarchical sandwich structures are obtained by assembling at least three separate components through a specific joining method, the contact area being placed within geometric planes that are parallel to the middle surface of the structure. This configuration leads to a disadvantageous way of transferring loads between components because the in-plane shear behaviour of the structure is influenced by the shear properties of the joint.

Moreover, the recycling capability represents another important issue which is currently difficult to deal with as typical hierarchical sandwich structures consist of several different materials.

This article presents a novel constructive solution for corrugated second order hierarchical sandwich structures made of self-reinforced thermoplastic composites and a thermoplastic structural foam core resulting in a recyclable structure. A manufacturing process for hierarchical sandwich structures suitable for continuous line production is presented. The proposed manufacturing process can be used for materials that can suffer plastic deformations at room temperature or under heat influence. The stiffness properties in out-of-plane compression of the proposed hierarchical sandwich structure are determined experimentally. A theoretical model is further on used in order to

* Corresponding author at: 29 Eroilor Blvd, 500036, Brasov, Romania.
E-mail address: slache@unitbv.ro (S. Lache).

http://dx.doi.org/10.1016/j.matdes.2016.04.049
0264-1275/© 2016 Elsevier Ltd. All rights reserved.

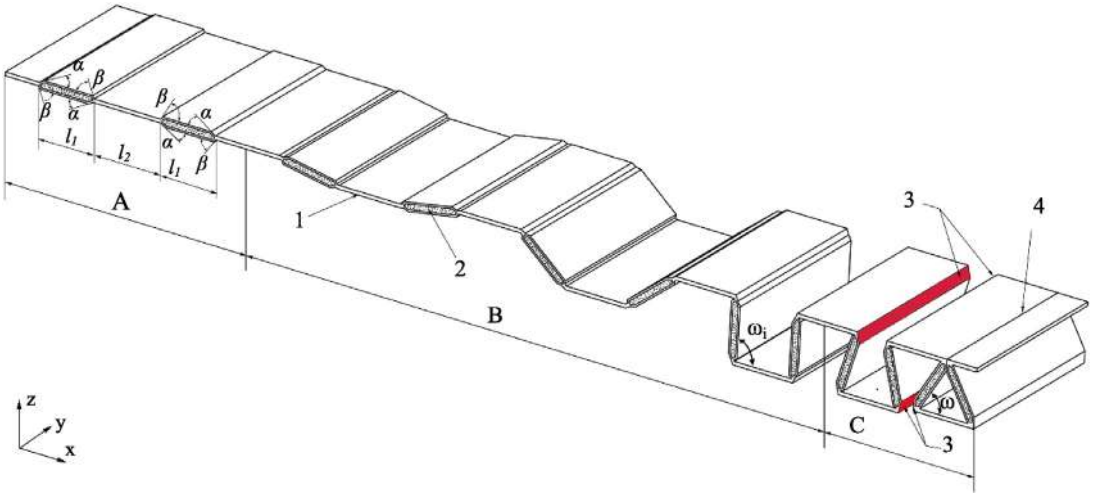

Fig. 1. Schematic illustration of the manufacturing principle for the second order hierarchical sandwich structure.

study the influence of the geometric configuration on the structural performance of the proposed structure.

2. Design and fabrication

2.1. Manufacturing principle

The second order hierarchical sandwich structure is obtained through a continuous flow of operations described further on, related to Fig. 1:

The process starts with the first phase (A) from a single sheet material which contains monolithic (1) and sandwich sections (2) arranged in an alternative way; the folding begins within the second phase (B) where the sandwich sections (2) are rotated along their edges with an angle equal to $90 + \omega\text{-}\alpha$. The joining (4) of the sandwich sections is made within phase (C) through the contact areas (3) which are placed perpendicular to the neutral plane of the structure and which are obtained by the definition of the α and β angles in terms of the desired final angle ω and of the sandwich sections length l_2.

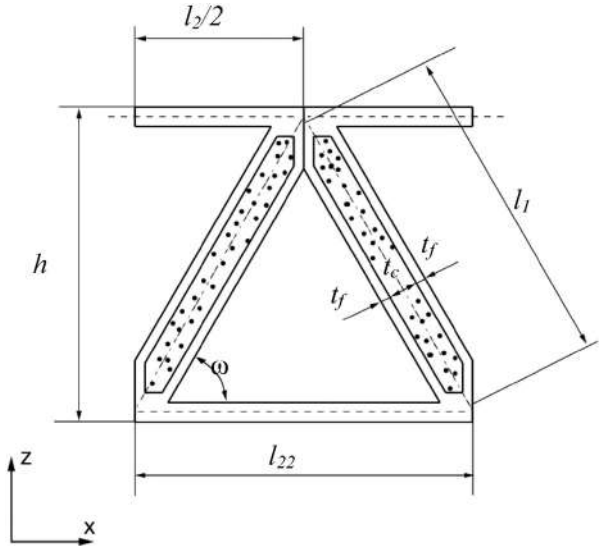

Fig. 2. Unit cell and its geometric parameters. The dotted area is representing the structural foam.

2.2. Constituent materials

The materials used in this study for the hierarchical corrugated folded structure are poly-ethylene terephthalate matrix reinforced with poly-ethylene terephthalate fibres (SrPET) and poly-ethylene terephthalate foam (PET).The SrPET composite material proves to be a good alternative with respect to lightweight design but also considering its lower life cycle environmental impact [17] an high impact energy absorption capacity [32].

The used SrPET composite consists of a low melting temperature matrix PET (termed LPET) and a high tenacity PET (termed HTPET) as fibre material. The LPET is chemically modified to melt at approximately 170 °C whereas the HTPET melts at 260 °C. During consolidation, the temperature should be as high enough to melt the LPET and wet the fibres but not too high so that the HTPET fibres degrade and lose their reinforcing properties. A previous study showed that laminates with good mechanical properties can be consolidated at 220 °C for 20 min under a pressure of 1.5 bar above ambient pressure [33].The SrPET material used in this study is a commingled balanced 2/2 twill fabric with an areal weight of 0.75 kg m^{-2} and 50% reinforcement fibres measured by weight (supplied by Comfil®APS [19]). Using the above mentioned process parameters, one layer of woven fabric results in a lamina with a thickness of 0.45 mm and a material density of 1380 k gm^{-3}.

The compression modulus and ultimate compression strength for the SrPET composite is 5.3 ± 0.2G Pa and 94.7 ± 0.7 MPa, respectively. A material yield point is observed at 35 MPa after which the stiffness of the material reduces and results in softening. For details on test procedures and specimens dimension readers are referred to previous work performed by Schneider et al. [12,33].

The foam used is an ArmaForm PET AC with a density of 100 kg m^{-3}.According to the manufacturer reference, the compression modulus is 105 MPa, the shear modulus is 25 MPa while the compression strength is 1.5 MPa and the shear strength is 0.9 MPa [4].

No additional materials are used for joining.

2.3. Manufacturing steps for the unfolded structure

A hot-press is used for consolidating the fabric and at the same time joining it with the foam, thus the unfolded plate containing the alternative monolithic and sandwich sections results. Firstly, the bottom aluminum profiles (see Fig. 3) are arranged parallel to each other at a specific offset in such way to allow the profiled PET foam and the layer(s) of fabric to fit in between. Secondly, the top aluminum profiles are aligned correspondingly, being guided by the edges of the profiled foam covered

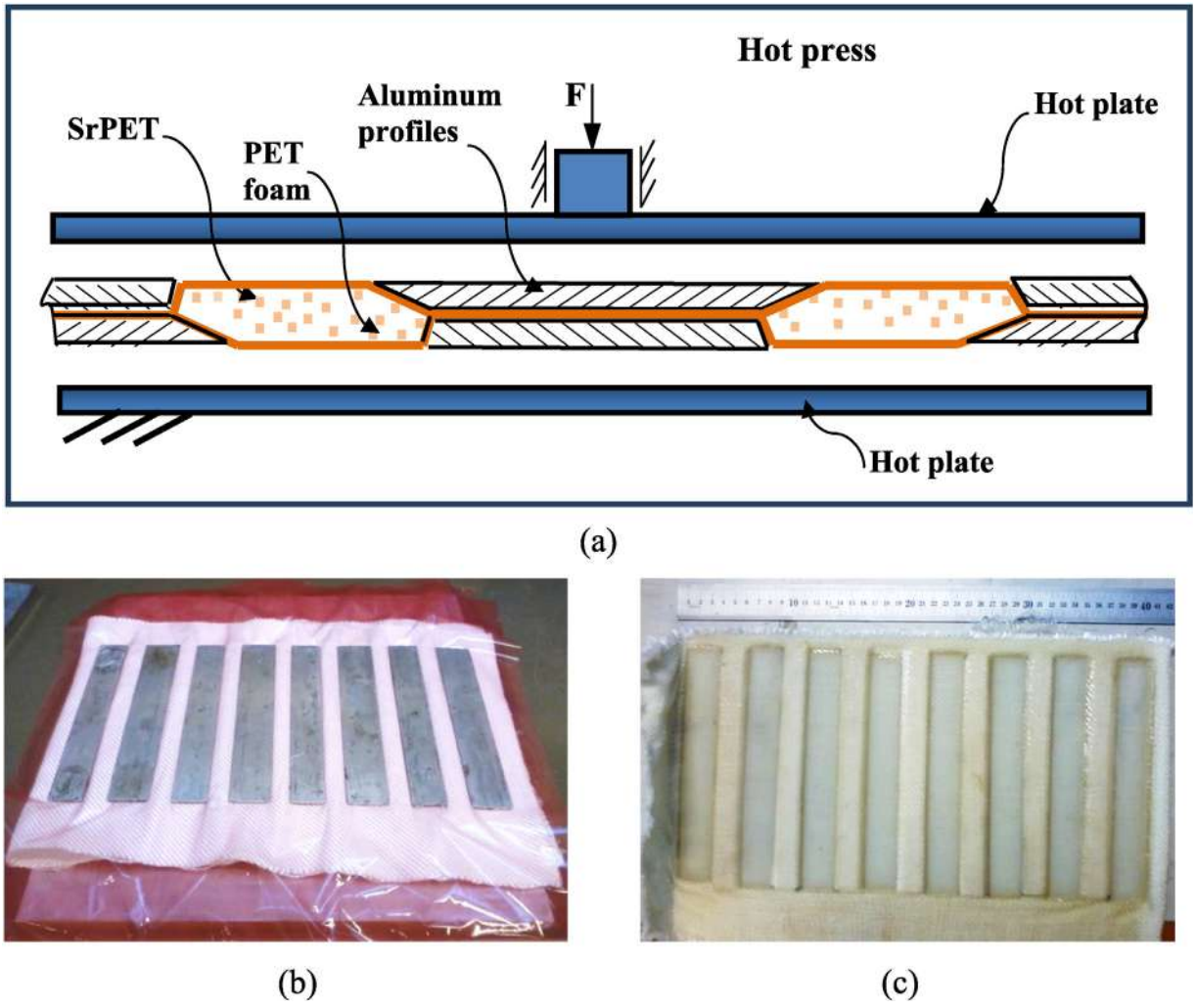

Fig. 3. (a) Schematic illustration for the manufacturing of the unfolded structure; (b) positioning the foam profiles and the fabric between the aluminum profiles; (c) consolidated plate with alternative monolithic and sandwich sections.

with the fabric. A release film is used between the aluminum profiles and the fabric. The previously described package is placed in the hot-press where it is heated up to 220 °C within a heating rate of 20 °C min^{-1}, it is hold at 220 °C under a pressure of 1.5 bar above the ambient pressure for 20 min and cooled to room temperature. The resulted consolidated plate is extracted from the hot-press; cross-section within the resulted consolidated plate with alternative monolithic and sandwich sections is presented within Fig. 4.

Different values for the geometric parameters l_1 and l_2 are possible to be obtained by arranging the aluminum profiles having the same shape and same cross-section as shown within Fig. 5.

2.4. Folding process and the resulted structure

The resulted second order hierarchical corrugated sandwich structure results by simply folding the consolidated plate described in

Fig. 4. Cross-section within the resulted consolidated plate with alternative monolithic and sandwich sections.

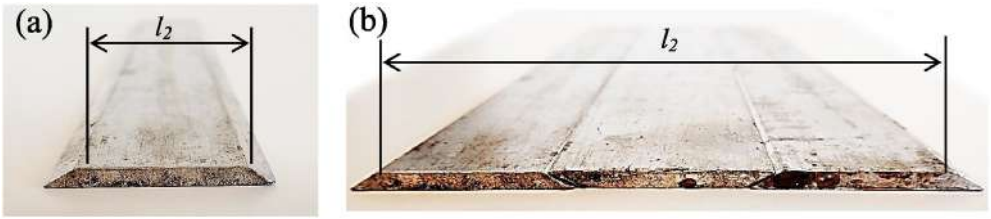

Fig. 5. (a) Single aluminum profile – l_2; (a) grouped aluminum profiles – $3l_2$.

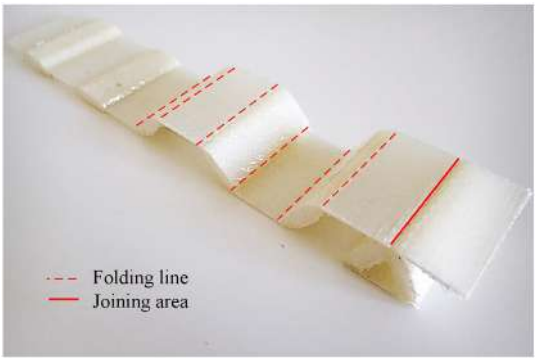

Fig. 6. Folding the consolidated laminate with foam inserts to a hierarchical sandwich structure.

Section 2.3. Starting from the consolidated plate (see Fig. 6), the folding edges are locally heated until the PET matrix is softened. The sandwich sections are then bended around the folding lines until they close the triangle and form the unit cell. The joining between the folded sections is formed with no additional material (see Fig. 6), just by means of the melted PET matrix.

Fig. 7(a) illustrates the resulted hierarchical sandwich structure after the folding process is finished. A more detailed image of the joining area is given in Fig. 7(b). Apart from the material joining, there is a mechanical interlocking between the sandwich sections that contributes on a better load transfer within the structure. In terms of a specific application, the resulted structure might be used as it is, meaning that the thickness of the monolithic sections can play the role of the structural face sheets or, if required, additional structural face sheets can be added.

2.5. Unit-cell geometry

The parameterized topology of the unit cell is shown in Fig. 2, where: l_1 – length of the sandwich section, l_2 – length of the monolithic section, h – height of the sandwich unit cell, t_c – thickness of the foam, t_f – thickness of the face sheets, ω – folding angle.

The relative density of the sandwich ρ_r is defined with:

$$\rho_r = \frac{l_1(t_c + 2t_f + 4t_f\cos\omega) + 4{t_f}^2}{(t_f + l_1\cos\omega)(4t_f + l_1\sin\omega)}. \quad (1)$$

The density of the structure, including the monolithic elements (e.g. face sheets), can be derived further on by:

$$\rho = \rho_r\left(\rho_{solid}\frac{V_{solid}}{V_{structure}} + \rho_{foam}\frac{V_{foam}}{V_{structure}}\right) \quad (2)$$

where

ρ_{solid} – represents the density of the solid material
ρ_{foam}– represents the density of the foam.
$V_{solid} = (4t_f(l_1 + l_2) + t_c(t_f/2\cos\omega + t_f/2\sin\omega))b$; $V_{foam} = 2\,l_1\,t_c b$; $V_{structure} = bhl_2$, where b is the unit cell width and V comes from *Volume*.

3. Experimental setup

The out-of-plane compression properties are evaluated through experimental tests using a hydraulic Walter + Bai testing machine with a load cell of 63 kN. The tests were displacement driven with a constant crosshead speed of 2 mm min^{-1}.

The experimental investigation is done on unit cells. However, in order to avoid the edge effects, each specimen is glued using epoxy based glue - Araldite®- on a metal block having a U shape thus simulating the continuity of the structure (see Fig. 8).

The effective elastic modulus E_z and the ultimate strength σ_z are determined based on the measured reaction force correlated with the imposed displacement and the specimens' geometric dimensions.

Four geometric configurations were tested by varying the value of foam thickness t_f and length l_1, (see Table 1). These configurations were possible to be made with the same shape for the aluminum profiles as shown in Fig. 5. Three specimens have been tested for each geometric configuration.

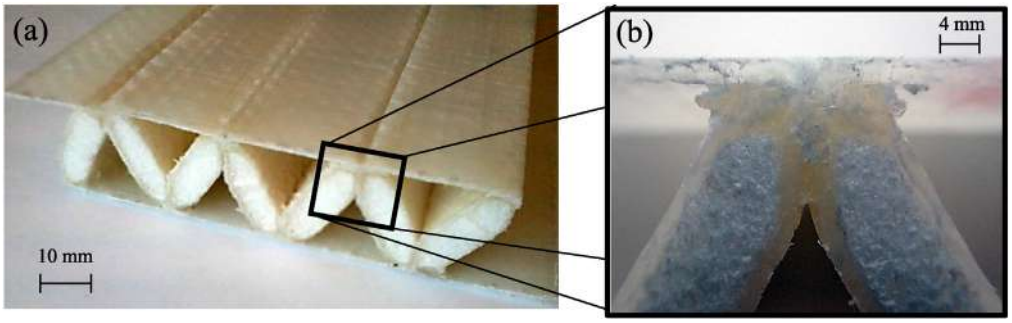

Fig. 7. (a) The resulted hierarchical sandwich structure. (b) Cross section within the joining area.

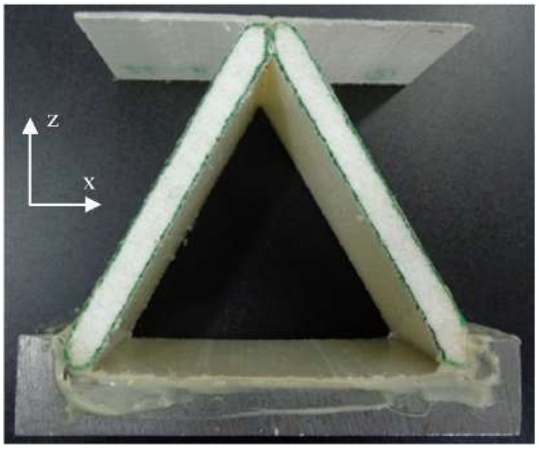

Fig. 8. Specimen used for mechanical testing in out of plane compression.

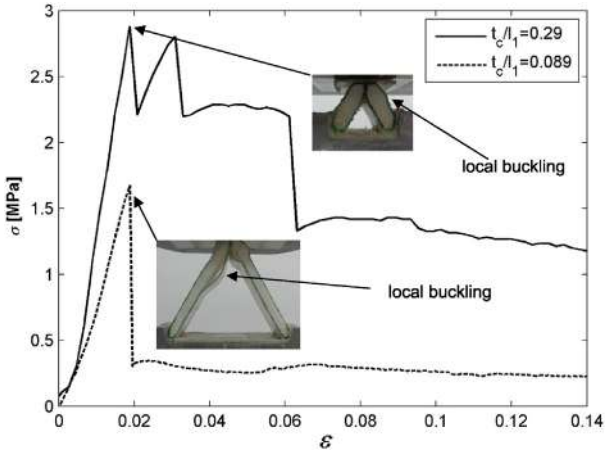

Fig. 10. Out-of-plane compression stress –compression strain response fort he investigated geometric configurations I and III, Table 1.

4. Theoretical study

4.1. Stiffness

The effective compressive elastic modulus is theoretically obtained by means of an analytical model based on elementary sandwich beam theory. Similar investigations were carried by Kazemahvazi et al. [10] for corrugated cores and by Yin et al. [31] for pyramidal cores with sandwich core members.

Assuming an unit imposed displacement δ_z applied on the unit cell a total reaction force F_z results (see Fig. 9). Due to the structures' symmetry the analytical model can be built by analysing the deformation of a single sandwich strut. When looking at the right hand side sandwich strut the reaction force F_z can be decomposed in the two components: F_N – representing the force acting along the sandwich strut and F_T – representing the force acting perpendicular to the sandwich strut, where $F_z = F_N\sin\omega + F_T\cos\omega$.

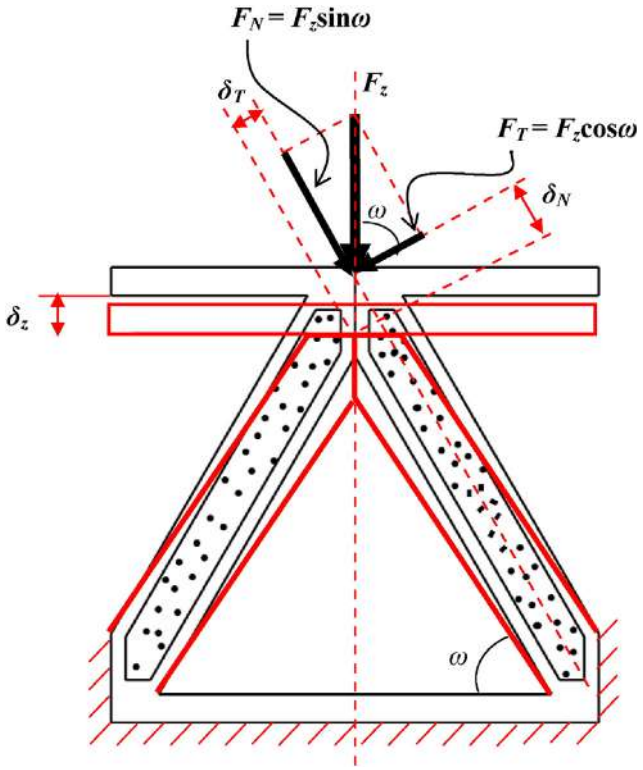

Fig. 9. Unit cell under out-of-plane compression loading.

Based on the sandwich beam theory [22], the resulted forces F_N and F_T may be calculated according to Eqs. (3) and (4):

$$F_T = \frac{\delta_T}{\frac{l_1^3}{3D} + \frac{l_1}{S}} \tag{3}$$

$$F_N = \frac{A\delta_N}{l_1} \tag{4}$$

where:

$\delta_N = \delta_z\sin\omega$; $\delta_T = \delta_z\cos\omega$
$A = 2t_f E_f$, represents the extensional stiffness
$D = \frac{E_f t_f (t_c + t_f)^2}{2}$, represents the bending stiffness
$S = \frac{G_c (t_c + t_f)^2}{t_c}$, represents the shear stiffness
l_1 represents the length of the strut (see Fig. 2).

The nominal stress that occurs within the investigated structure is

$$\sigma_z = \frac{F_z}{2l_1\cos\omega}. \tag{5}$$

The nominal strain within the structure is defined as:

$$\varepsilon_z = \frac{\delta_z}{h}. \tag{6}$$

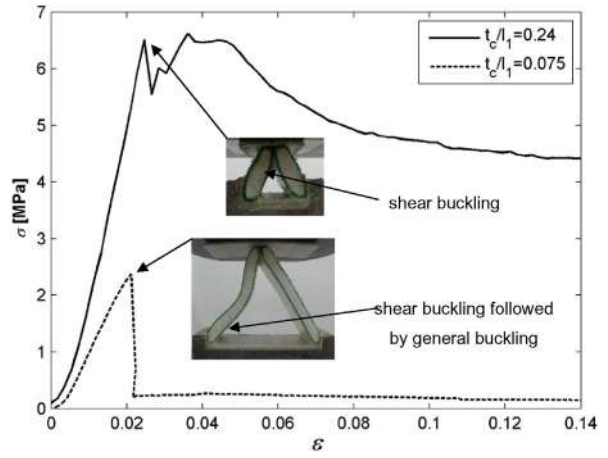

Fig. 11. Out-of-plane compression stress – compression strain response for the investigated geometric configurations II and IV (see Table 1).

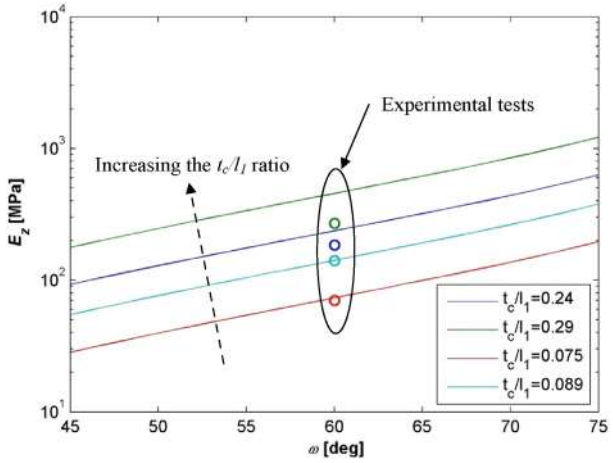

Fig. 12. Influence of the out-of-plane compression stiffness of the ω angle and t_c/l_1 ratio.

The effective elastic modulus in out of plane compression E_z is defined as:

$$E_z = \frac{\sigma_z}{\varepsilon_z}. \tag{7}$$

Eventually, from Eqs. (3)–(6), E_z becomes:

$$E_z = \frac{\sin\ \omega\left(\dfrac{\cos\omega^2}{\dfrac{2l_1^3}{3E_f t_f (t_c+t_f)^2}+\dfrac{l_1 t_c}{G_c(t_c+t_f)^2}}+\dfrac{2E_f t_f \sin\omega^2}{l_1}\right)}{\cos\ \omega}. \tag{8}$$

4.2. Strength

The out-of-plane compressive strength of the hierarchical sandwich structure made of self-reinforced polymers is determined here based on the previous work of Yin et al. [31,34] and Kazemahvazi et al. [10]. Four failure modes are considered when calculating the theoretical strength: local buckling, general buckling, core shear buckling and shear failure of the core.

4.2.1. Local buckling

The face sheets of the sandwich core element can buckle when they are relatively thinner due to the existing in-plane loads. When such a failure mode occurs, the out-of-plane strength of the structure can be determined through Eq. (9):

$$\sigma_z = \frac{\sqrt[3]{E_f E_c G_c} t_f \sin\ \omega\left(\dfrac{\cos\omega^2}{\dfrac{l_1^2 \sin\omega^2}{3(t_c+t_f)^2}+\dfrac{t_c}{G_c(t_c+t_f)^2}}+1\right)}{\cos\ \omega(l_1+2t_f)}. \tag{9}$$

4.2.2. General buckling of sandwich struts

For longer sandwich struts and lower core thicknesses, the expected failure mode is general buckling. The compressive strength of the hierarchical structure is therefore determined by Eq. (10):

$$\sigma_z = \frac{2E_f \pi^2 t_f \sin\ \omega (t_c+t_f)^2\left(\dfrac{\cos\omega^2}{\dfrac{l_1^2 \sin\omega^2}{3(t_c+t_f)^2}+\dfrac{t_c}{G_c(t_c+t_f)^2}}+1\right)}{l_1^2 \cos\ \omega(l_1+2t_f)}. \tag{10}$$

4.2.3. Core shear buckling

The compressive strength of the hierarchical structure in case when the shear buckling failure of the sandwich struts occur can be determined by Eq. (11):

$$\sigma_z = \frac{G_c t_c \tan\ \omega\left(\dfrac{\cos\omega^2}{\dfrac{l_1^2 \sin\omega^2}{3(t_c+t_f)^2}+\dfrac{t_c}{G_c(t_c+t_f)^2}}+1\right)}{l_1+2t_f}. \tag{11}$$

4.2.4. Shear failure of core

This failure mode occurs when the shear stress in the core equals the shear strength of the core material [10]. The compressive strength of the

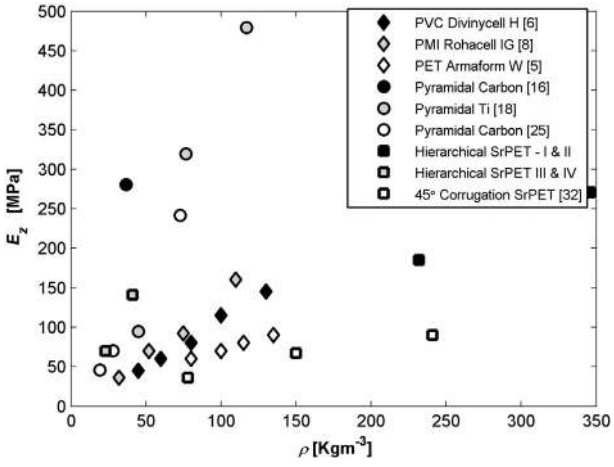

Fig. 13. Stiffness properties as a function of structures' density.

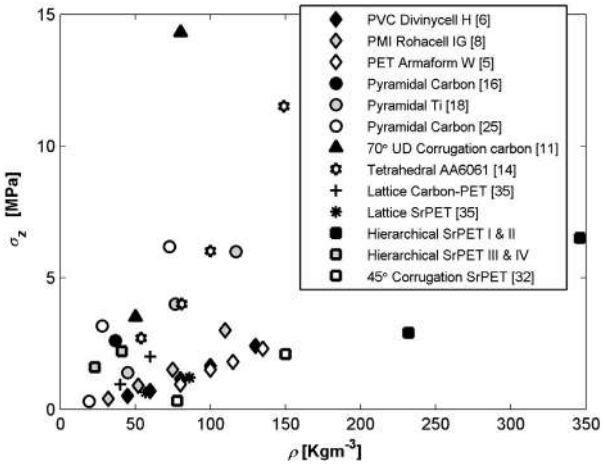

Fig. 14. Strength properties as a function of structures' density.

Table 1
Geometric configurations investigated experimentally.

Configuration	t_f [mm]	l_1 [mm]	t_c [mm]	ρ_r [−]	ρ [kg m^{-3}]
I	0.45	24	7.1	0.738	232
II	0.90	25	6.2	0.715	346
III	0.45	81	7.1	0.245	23
IV	0.90	82	6.2	0.259	41

hierarchical structure can be calculated using Eq. (12):

$$\sigma_z = \frac{\tau_c t_c \left(t_c - \frac{G_c l_1^2 (cos\omega^2 - 1)}{3} \over G_c cos\omega^2 (t_c + t_f)^2 + 1 \right)}{l_1 + 2t_f}. \quad (12)$$

5. Results

Fig. 10 shows the experimental compressive stress-strain response for the configuration I and III where $t_f = 0.45$ mm, Table 1; this value for t_f corresponds to a single layer of SrPET material. As expected, lower values for the t_c/l_1 ratio will provide higher ultimate strength, 2.9 MPa vs. 1.6 MPa. However, the resulted specific strength indicates approximately the same performance for both I and III geometric configurations, see Table 2. Local buckling failure mode is found when testing both configuration I and III. The determined out-of-plane compression stiffness values E_z indicates a more than two times increase for configuration I with respect to configuration III. However, this ratio is inversed when it comes to the specific stiffness, and it has a value of 3.8 (see Table 2), meaning that a higher stiffness performance with respect to weight is offered by configuration III.

The experimental results obtained for the investigated geometric configurations II and IV where t_f = 0.9mmare presented within Fig. 11.The strength behaviour is similar with the one for configurations I and III only that the recorded magnitudes are higher for II and IV (6.5 MPa and 2.2 MPa respectively), as expected. The shear buckling failure mode is found for both configurations II and IV. However, for a lower t_c/l_1 ratio, the general buckling of the sandwich strut was recorded as a post-failure mode (see Fig. 11).

The obtained stiffness is approximately two times higher for configuration II compared to configuration IV. When it comes to the weight specific stiffness, the value is four times higher for the configuration IV compared to configuration II, see Table 2.

Fig. 12 illustrates, based on the developed analytical model, the way the out-off plane stiffness is influenced by ω angle and by the t_c/l_1 ratio, where t_c = 8-2t_f with t_f = 0.45 forgeometric configurations I and III and t_f = 0.9 mm for geometric configurations II and IV (see Fig. 10).As expected, E_z is increasing with the increase of ω angle. Moreover, higher values for the t_c/l_1 provide higher stiffness properties but also higher densities.

A good agreement was found between the analytical model and the experimental results for geometric configurations III and IV (longer sandwich core elements). However, differences were found between the analytical model and the experimental results for geometric configurations I and II, mainly due to manufacturing of the specimens with higher t_c/l_1 ratios (shorter sandwich core elements). One issue is the misalignment of folding edges during the folding process which was difficult to control for higher t_c/l_1 ratios. The misalignment is causing a not even distribution of the load on the sandwich struts during testing of the specimens. Another issue is related to the obtained ω angle for the specimens that vary from 55° to 60°. Apart from the geometric imperfections, material imperfections also occur with an important contribution to the structure's behaviour: the foam core degrades during manufacturing and the resulted bonding is not perfect at the sides which can initiate a premature failure.

6. Discussion

The out-of-plane stiffness of the investigated structure is compared as function of density with several cellular structures in Fig. 13. The investigated configurations III and IV shows a higher stiffness compared with the commercially available foam structures [5,6,8]and also with the pyramidal cores made of Titanium alloy [18] and carbon fibre composite [25] at similar densities. However, another pyramidal carbon fibre composite structure proposed by Li, M. et al. [16] indicates a significantly higher stiffness at approximately the same density. The configurations I and II reach higher stiffness values but also higher densities.

The out-of-plane strength of the investigated structure is compared as function of density with several cellular structures in Fig. 14. At lower densities, configuration III and IV indicates higher strength than the Titanium lattice structures [18] and similar strength compared to the tetrahedral structure made from aluminum [14]. Higher strength performance is found at lower densities compared with the commercial foam structures [5,6,8]. As expected, a better strength behavior is found for the hierarchical concepts made out of SrPET compared to the pyramidal lattice structures made out of the same material [35]. A small increase in strength is found at higher densities for configuration III and IV resulting in a worse strength performance compared to the other type of structures.

Table 2
Stiffness and strength results.

Config	Experimental results				Analytical predictions	
	E_z [MPa]	σ_z [MPa] /Failure mode	E_z/ρ [MPa/kg m^{-3}]	σ_z/ρ [MPa/kg m^{-3}]	E_z [MPa]	σ_z [MPa] /Failure mode
I	185	2.9/local buckling	0.79	0.012	236.9	6.2/local buckling 419/general buckling 10.3/shear buckling 24.6/core shear
II	271	6.5/shear buckling	0.78	0.019	455	11.4/local buckling 336/general buckling 8.3/shear buckling 20/core shear
III	70	1.6/local buckling	3.02	0.069	73	1.9/local buckling 11.8/general buckling 3.1/shear buckling 7.5/core shear
IV	141	2.2/shear buckling	3.42	0.054	142	3.7/local buckling 11/general buckling 2.6/shear buckling 6.4/core shear

7. Conclusions

A novel second order hierarchical sandwich structure is proposed and analysed and its continuously manufacturing process is described. The whole structure is made of a single base material which is polyethylene terephthalate – PET, but used in three distinct forms: matrix, fibres and foam. These PET forms are arranged in a specific manner in order to increase the structural performance of the structure. No additional materials are used, resulting in a fully recyclable structure. An analytical model is developed based on which the effective out-of-plane compression stiffness and strength are evaluated. For long sandwich core elements (configurations III and IV) the model is correlated well with the experiments. Due to manufacturing issues for structures with shorter sandwich core elements (configurations I and II), the agreement with the experiments is poor. However, the influence of the folding angle and of the t_c/l_1 ratio to the out-of-plane compression stiffness of the structure is consistent.

The experimental investigations indicate that the best performance with respect to the weight specific stiffness is offered by configuration IV. When it comes to weight specific strength, the best performance is given by the geometric configuration III. It results that the investigated structure is very competitive at lower densities.

As shown by other authors, the SrPET material is suitable for impact energy absorption applications due to a high ductility characteristic; the herein proposed arrangement of the material may be an added advantage with respect to impact performance.

Acknowledgements

This work was partially supported by the strategic grant POSDRU/159/1.5/S/137070 (2014) of the Ministry of Labour, Family and Social Protection, Romania, co-financed by the European Social Fund – Investing in People, within the Sectorial Operational Programme Human Resources Development 2007-2013. Christof Schneider was partly financed by the Centre of ECO2 Vehicle Design at the Department of Aeronautical and Vehicle Engineering, Royal Institute of Technology, KTH Sweden.

References

[1] M.F. Ashby, Materials Selection in Mechanical Design, fourth ed. Elsevier Butterworth-Heinemann, Oxford, 2011.
[2] M.F. Ashby, Designing architectured materials, Scr. Mater. 68 (1) (2013) 4–7.
[3] M.F. Ashby, Y.J.M. Bréchet, Designing hybrid materials, Acta Mater. 51 (19) (2003) 5801–5821.
[4] Armacell Benelux. ArmaFORM PET/AC Technical data, Rue de Trois Entities 9-B-4890 Thimister Clermont. <www.armacell.com> (accessed 02.04.2014).
[5] Armacell Benelux. ArmaFORM PET/W Technical data, Rue de Trois Entities 9-B-4890 Thimister Clermont. <www.armacell.com> (accessed 02.04.2014).
[6] DIAB Group. Divinycell® H Technical data, SE-31222 Laholm, Sweden, <www.diabgroup.com> (accesed 21.11.2013).
[7] E. Dragoni, Optimal mechanical design of tetrahedral truss cores for sandwich constructions, J. Sandw. Struct. Mater. 15 (4) (2013) 464–484.
[8] Evonik Industries AG, ROHACELL® IG/IG-F Properties, 64293 Darmstadt, Germany. <www.rohacell.com> (accesed 21.11.2013).
[9] H. Fan, et al., Designing and compression behaviors of ductile hierarchical pyramidal lattice composites, Mater. Des. 58 (0) (2014) 363–367.
[10] S. Kazemahvazi, D. Zenkert, Corrugated all-composite sandwich structures. Part 1: modeling, Compos. Sci. Technol. 69 (7–8) (2009) 913–919.
[11] S. Kazemahvazi, D. Tanner, D. Zenkert, Corrugated all-composite sandwich structures. Part 2: failure mechanisms and experimental programme, Compos. Sci. Technol. 69 (7–8) (2009) 920–925.
[12] S. Kazemahvazi, C. Schneider, V.S. Deshpande, A constitutive model for self-reinforced ductile polymer composites, Compos. A: Appl. Sci. Manuf. 71 (0) (2015) 32–39.
[13] G.W. Kooistra, H.N.G. Wadley, Lattice truss structures from expanded metal sheet, Mater. Des. 28 (2) (2007) 507–514.
[14] G.W. Kooistra, V.S. Deshpande, H.N.G. Wadley, Compressive behaviour of age hardenable tetrahedral lattice truss structures made from aluminium, Acta Mater. 52 (2004) 4229–4237.
[15] G.W. Kooistra, V. Deshpande, H.N.G. Wadley, Hierarchical corrugated core sandwich panel concepts, J. Appl. Mech. 74 (2) (2007) 259–268.
[16] M. Li, et al., Mechanical response of all-composite pyramidal lattice truss core sandwich structures, J. Mater. Sci. Technol. 27 (6) (2011) 570–576.
[17] S. Poulikidou, et al., A material selection approach to evaluate material substitution for minimizing the life cycle environmental impact of vehicles, Mater. Des. 83 (2015) 704–712.
[18] D.T. Queheillalt, H.N.G. Wadley, Titanium alloy lattice truss structures, Mater. Des. 30 (6) (2009) 1966–1975.
[19] D.T. Queheillalt, Y. Murty, H.N.G. Wadley, Mechanical properties of an exdruded pyramidal lattice truss sandwich structure, Scr. Mater. 58 (2008) 76–79.
[20] R. Rezaei, et al., Mechanical characterization and finite element modeling of polylactic acid BCC-Z cellular lattice structures fabricated by fused deposition modeling. Proceedings of the Institution of Mechanical Engineers, Part C: Journal of Mechanical Engineering Science (2016).
[21] B.P. Russell, et al., Dynamic compressive response of composite corrugated cores, J. Mech. Mater. Struct. **5** (3) (2010).
[22] D. Zenkert, The Handbook of Sandwich Construction, EMAS LTD, 1997.
[23] B.P. Russell, et al., Quasi-static three-point bending of carbon fiber sandwich beams with square honeycomb cores, J. Appl. Mech., Transactions ASME (2011) 78.
[24] X. Zhang, H. Zhang, Theoretical and numerical investigation on the crush resistance of rhombic and kagome honeycombs, Compos. Struct. 96 (0) (2013) 143–152.
[25] J. Xiong, et al., Fabrication and crushing behavior of low density carbon fiber composite pyramidal truss structures, Compos. Struct. 92 (11) (2010) 2695–2702.
[26] G. Zhang, et al., Response of sandwich structures with pyramidal truss cores under the compression and impact loading, Compos. Struct. 100 (0) (2013) 451–463.
[27] Wadley, H.N.G. and G.W. Kooistra. Cellular Lattice Structures With Multiplicity of Cell Sizes and Related Method of Use 2009; US2009274865 (A1), USA.
[28] Y. Sun, L. Gao, Structural responses of all-composite improved-pyramidal truss sandwich cores, Mater. Des. 43 (0) (2013) 50–58.
[29] M.N. Velea, P. Wennhage, S. Lache, Out-of-plane effective shear elastic properties of a novel cellular core for sandwich structures, Mater. Des. 36 (2012) 679–686.
[30] M.N. Velea, S. Lache, In-plane effective elastic properties of a novel cellular core for sandwich structures, Mech. Mater. 43 (7) (2011) 377–388.
[31] S. Yin, L. Wu, S. Nutt, Stretch–bend-hybrid hierarchical composite pyramidal lattice cores, Compos. Struct. 98 (0) (2013) 153–159.
[32] C. Schneider, et al., Dynamic compression response of selfreinforced poly(ethylene terephthalate) composites and corrugated sandwich cores, Compos. A: Appl. Sci. Manuf. 77 (2015) 96–105.
[33] C. Schneider, et al., Compression and tensile properties of self-reinforced poly(ethylene terephthalate)-composites, Polym. Test. 32 (2) (2013) 221–230.
[34] S. Yin, L. Wu, S.R. Nutt, Compressive efficiency of stretch–stretch-hybrid hierarchical composite lattice cores, Mater. Des. 56 (2014) 731–739.
[35] C. Schneider, et al., Compression properties of novel thermoplastic carbon fibreand poly–ethylene terephthalate fibre composite lattice structures, Mater. Des. 65 (2015) 1110–1120.

Materials and Design xxx (2014) xxx–xxx

Contents lists available at ScienceDirect

Materials and Design

journal homepage: www.elsevier.com/locate/matdes

Compression properties of novel thermoplastic carbon fibre and poly-ethylene terephthalate fibre composite lattice structures

C. Schneider [a], M.N. Velea [a,b,*], S. Kazemahvazi [c], D. Zenkert [a]

[a] KTH, Department of Aeronautical and Vehicle Engineering, Stockholm, Sweden
[b] Transilvania University of Brasov, Department of Mechanical Engineering, Romania
[c] University of Cambridge, Department of Engineering, Cambridge, United Kingdom

ARTICLE INFO

Article history:
Received 5 July 2014
Accepted 12 August 2014
Available online xxxx

Keywords:
Lattice structures
Self-reinforced polymers
Thermoplastic composites

ABSTRACT

A novel manufacturing route to efficiently produce fibre composite lattice structures has been developed. By using thermoplastic composite materials, flat sheets have been continuously folded, cut into a lattice shape and joined into a sandwich structure. Carbon fibre reinforced poly-ethylene terephthalate (CPET) and poly-ethylene terephthalate fibre reinforced poly-ethylene terephthalate (SrPET) materials have been used to explore two different core options; a carbon fibre option which gives high performance but low recyclability and a single polymer PET option which gives lower performance but full recyclability. Parametric numerical simulations have been used to investigate how the various manufacturing parameters affect the mechanical performance of the core. The carbon fibre composite cores have mechanical performance on-par or better than existing metallic and composite lattice cores presented in literature. Single polymer PET cores show better performance compared to high-end foam cores but have considerable lower performance than carbon fibre lattice cores.

© 2014 Elsevier Ltd. All rights reserved.

1. Introduction

Usage of composite materials and sandwich structures have become a common approach to reduce weight of structures in the aerospace and, more recently, in the automotive industry. While the relatively low-volume production of aerospace industry has its main focus on performance and quality, the high volume automotive industry puts more focus on manufacturing lead times and costs. In addition, the automotive industry is currently operating under stringent legislation on CO_2-emissions and recyclability of materials. Thus, although composite materials and sandwich structures can significantly contribute in reducing structural weight and thereby in-service emissions, they still need to prove themselves as "high volume manufacturing materials" with recycling potential.

Numerous studies have focused on further enhancing the weight specific mechanical properties of composite sandwich structures by arranging the material in a more geometrically efficient way. Such efforts include all-composite corrugated cores [1,2], square honeycomb [3] cores and pyramidal lattice truss cores [4–8]. Although many of these novel structures show exceptional weight specific strength and stiffness, they are often complicated to manufacture and more suitable for laboratory scale production. There are currently a number of different routes to manufacture composite lattice truss cores. Xiong et al. [7] used an approach where small manually cut carbon fibre/epoxy pre-preg strips where placed into a mould to create each of the four struts of a pyramidal lattice truss. Yin et al. [9] used an approach where a corrugated carbon fibre reinforced epoxy plate was manufactured in a mould and then small strips were cut in the transverse direction of the corrugation. The strips where subsequently assembled and bonded together perpendicularly to form a pyramidal lattice truss structure. George et al. [10] used a similar approach where small strips were water-jet cut out from a flat carbon fibre reinforced epoxy sheet in a corrugated type shape. These were then assembled and bonded together perpendicularly in the same manner to form a pyramidal lattice truss structure. Although these examples of manufacturing methods for carbon fibre lattice truss cores are innovative, they do not lend themselves for high volume and low-cost production.

In the present paper fibre reinforced thermoplastic materials are used to develop a novel continuous (and potentially high volume) manufacturing method for composite lattice truss structures. The manufacturing process is reminiscent of that developed for metal structures by Velea et al. [11,12]. Two different material concepts are considered; Carbon fibre reinforced PET for high

* Corresponding author. Address: 1 Politehnicii Street, NP1, 500024 Brasov, Romania. Tel.: +40 723676387.
E-mail address: marian.velea@unitbv.ro (M.N. Velea).

http://dx.doi.org/10.1016/j.matdes.2014.08.032
0261-3069/© 2014 Elsevier Ltd. All rights reserved.

Please cite this article in press as: Schneider C et al. Compression properties of novel thermoplastic carbon fibre and poly-ethylene terephthalate fibre composite lattice structures. J Mater Design (2014), http://dx.doi.org/10.1016/j.matdes.2014.08.032

mechanical performance and PET fibre reinforced PET (self-reinforced composite) for low material cost and full recyclability.

The aims of the study are as follows.

1. Demonstrate a continuous and potential high volume manufacturing method to produce composite lattice truss cores.
2. Investigate how different geometrical parameters of the manufacturing method affect the mechanical properties of the core.
3. Investigate the potential of using a low-performance material (self-reinforced PET) in a geometrically efficient design to enhance overall structural performance.

The paper starts by describing the constituent materials and provide an in-depth description of the novel manufacturing method. This is followed by a summary of the results from the experimental programme and a parametric investigation of properties using finite element analysis. The paper will be finalized by comparing the performance of the novel lattice truss cores with currently available commercial materials and selected lattice truss structures available in literature.

2. Materials and manufacturing route

2.1. Description of constituent materials

Two different materials are used in this study; poly-ethylene terephthalate fibre reinforced poly-ethylene terephthalate (SrPET) and carbon fibre reinforced poly-ethylene terephthalate (CPET).

The SrPET composite consists of a low melting temperature matrix PET (termed LPET) and a high tenacity PET (termed HTPET) as fibre material. The melting temperature of the LPET is approximately 170 °C whereas the HTPET melts at 260 °C. During consolidation the temperature should be as high enough to melt the LPET and wet the fibres but not too high so that the HTPET fibres degrade and lose their reinforcing properties. A previous study showed that laminates with good mechanical properties can be consolidated at 220 °C for 20 min under a pressure of 1.5 bar [14].

The SrPET material used in this study is a commingled balanced 2/2 twill fabric with an areal weight of 0.75 kg m^{-2} and 50% reinforcement fibres measured by weight (supplied by Comfil®APS [13]). Using the above mentioned process parameters, one layer of woven fabric results in a lamina with a thickness of 0.5 mm and a material density of 1380 kg m^{-3}.

The second material is a carbon fibre composite where LPET fibres are commingled with carbon fibres to produce yarns. The commingled yarns are then woven into a balanced 2/2 twill fabric with an areal weight of 0.50 kg m^{-2} and 54% carbon fibres measured by weight (supplied by Comfil®APS [13]). The fabric was consolidated using the same processing parameters as for the SrPET composite. One layer of carbon fibre/LPET weave produces a lamina with a thickness of 0.3 mm and a density of 1600 kg m^{-3}.

2.2. Quasi-static response of the constituent materials

The quasi-static in-plane compression stress–strain histories for the CPET and SrPET are presented in Fig. 1. For details on test procedures and specimens dimension readers are referred to previous work performed by Schneider et al. [14]. The compression modulus and ultimate compression strength for the SrPET composite is 5.3 ± 0.2 GPa and 94.7 ± 0.7 MPa respectively. A material yield point is observed at 35 MPa after which the stiffness of the material reduces and results in softening. For the CPET composite the compression modulus is 48.9 ± 3 GPa and the compressive strength 285.3 ± 9 MPa. The strain-to-failure for the CPET is 0.7 ± 0.1%

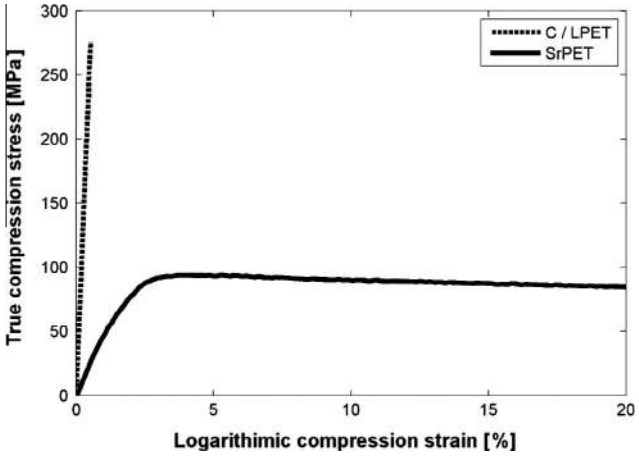

Fig. 1. Compression stress strain diagram for CPET and SrPET [14].

whereas the more ductile SrPET show failure strains of more than 20% [14].

2.3. Manufacturing route for lattice truss core material

The manufacturing route for the composite lattice truss core material consists of three steps as depicted schematically in Fig. 2 and shown for a CPET material in Fig. 3. The first step (I) is to form a corrugated plate shape. In a mass production setting this would be performed using a continuous process such as hot-roll forming of the thermoplastic sheet material but in this laboratory setting the material was hot formed using machined corrugated aluminium moulds (using the same process as described in Section 2.1). In the second step (II), slots with a width, c, are machined out with a distance, d, from each other. For this laboratory scale setup a miniature circular saw (blade diameter = 80 mm and blade thickness = 1.6 mm) was used to cut each slot manually. In a mass production setup one could easily replace this cutting method by using a computer numerical controlled mill to machine out each slot automatically. In the third and final step (III), the core is heated and expanded into its final shape with the desired longitudinal truss angle β (in the y-direction). Assuming a relatively constant distribution of the heat over the folding lines of the structure, the expanding process will take place close to uniform. If the beta angle is not uniform for each fold, it will be corrected in the following step where the folded core is consolidated to the face sheet stringers which have an accurate pre-cut beta angle. These three steps can all be performed simultaneously while the core is expanded in the y-direction. The final result of an expanded CPET lattice truss core is shown in Fig. 3.

2.4. Manufacturing of face sheets and complete sandwich structure

In order to enhance the bonding between the core and face structures, an approach is presented where the face sheets have stringers which provide support for the lattice truss core as shown in Fig. 4a. This both increases the surface area of the bonding between the lattice truss core and face sheets but it also changes the load introduction so that axial loads in the core struts translate into compressive or tension forces on the stringers.

The face sheets used in this laboratory set-up have been made using 4 layers of the fabric for the SrPET structure and 4 layers of fabric in the CPET structure. This results in a face sheet thickness of 1.8 mm and 1.1 mm for the SrPET and CPET structure respectively. The face sheets with stringers were manufacture in two steps as shown in Fig. 5. Firstly, triangular sections where

Please cite this article in press as: Schneider C et al. Compression properties of novel thermoplastic carbon fibre and poly-ethylene terephthalate fibre composite lattice structures. J Mater Design (2014), http://dx.doi.org/10.1016/j.matdes.2014.08.032

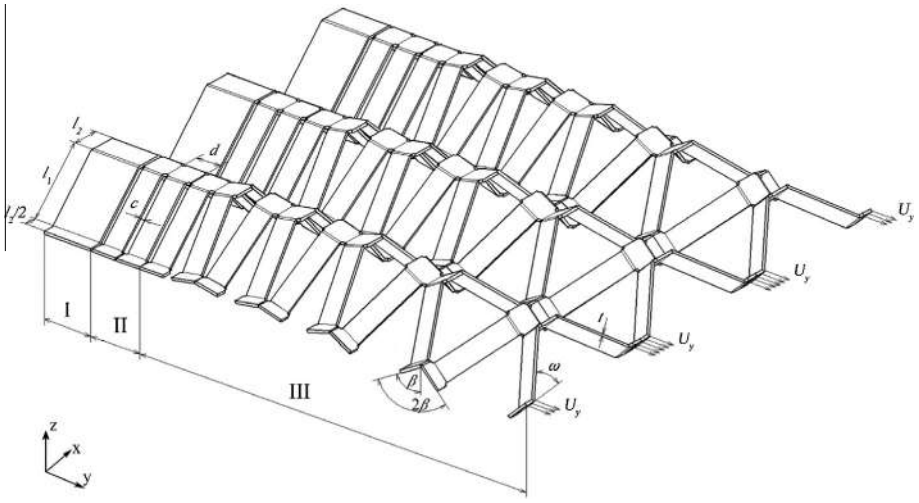

Fig. 2. Three key steps in manufacturing the novel expanded lattice truss structure.

Fig. 3. CPET material in the process of expansion from a corrugation to a lattice truss structure (left) and final result of an expanded lattice truss core structure made of CPET with $\beta = \omega = 45°$, $l_1 = 28.28$ mm, $l_2 = 10$ mm, $t = 1.8$ mm, $d = 9.7$ mm and $c = 2$ mm (right).

machined out from a pre-consolidated plate of 10 mm thickness. After this, each triangular stringer was placed between 4 layers of fabric. An aluminium tool was used to consolidate the stringers to the face sheet in order to obtain high geometrical accuracy. An alternative to adding triangles of SrPET or CPET material is to instead fill the stringers with polymer foam in order to not add significant weight to the face sheets, this has however not been investigated further in the present study.

When the face sheets have been pressed into their final shape they are bonded to the core using a hot-plate bonding method. In this method, the bond surfaces are heated to about 200 °C instantly (which is above the matrix melting temperature) using pre-heated aluminium plates. When both surfaces have been heated, they are pressed together for a few seconds, with a pressure of approximately 0.014 bar, until the material has cooled down and solidified. This method allows for a rapid and strong bond of the material.

The final lattice truss sandwich plate, shown in Fig. 4b, was then cut into individual unit cells in order to perform the out-of-plane compression experiments. A detailed description of the unit cell geometry is given in proceeding section.

3. Experimental protocol

3.1. Selection of lattice truss core geometrical parameters

The manufacturing route for the lattice truss core presented in this study provides the possibility of selecting seven independent geometrical variables as shown in Fig. 2. By altering these geometrical variables, different core relative densities can be achieved with different resulting mechanical properties. The relative density of the core, defined as the density of the core normalised by the density of the constituent material, is defined as,

$$\rho_r = \frac{t[2c(l_1+l_2)-b(2l_1+l_2)]}{(l_2+l_1\cos\alpha)[(t+2l_1\sin\alpha)\cos\beta+2c\sin\beta][(c-b)\cos\beta+(t+l_1\sin\alpha)\sin\beta]} \quad (1)$$

where each individual variable is depicted in Fig. 2. Eq. (1) has its minimum (i.e. lowest relative density) for core configurations where the expanding angle, β, is 45° and the corrugation angle, ω, is 56°. In order to manufacture a core with a low relative density but yet keep the laboratory scale manufacturing straight forward, these two parameters have been fixed to 45° in the experimental part of this study. In order to simplify manufacturing of the cores, a fixed l_1/d ratio of 2.9 was chosen where the strut length $l_1 = 28.3$ mm and the cut distance $d = 9.7$ mm.

3.2. Unit-cell geometry for out-of-plane compression experiments

In order to investigate the out-of-plane compression properties of the sandwich structure, individual unit cells of dimensions $L = 42$ mm and $W = 60$ mm were cut-out from plates, see Fig. 6a. After being cut-out, the unit cell face sheets where then bonded to 5 mm CPET plates in order to minimize face sheet deformation during testing and therefore characterize the core properties only.

Please cite this article in press as: Schneider C et al. Compression properties of novel thermoplastic carbon fibre and poly-ethylene terephthalate fibre composite lattice structures. J Mater Design (2014), http://dx.doi.org/10.1016/j.matdes.2014.08.032

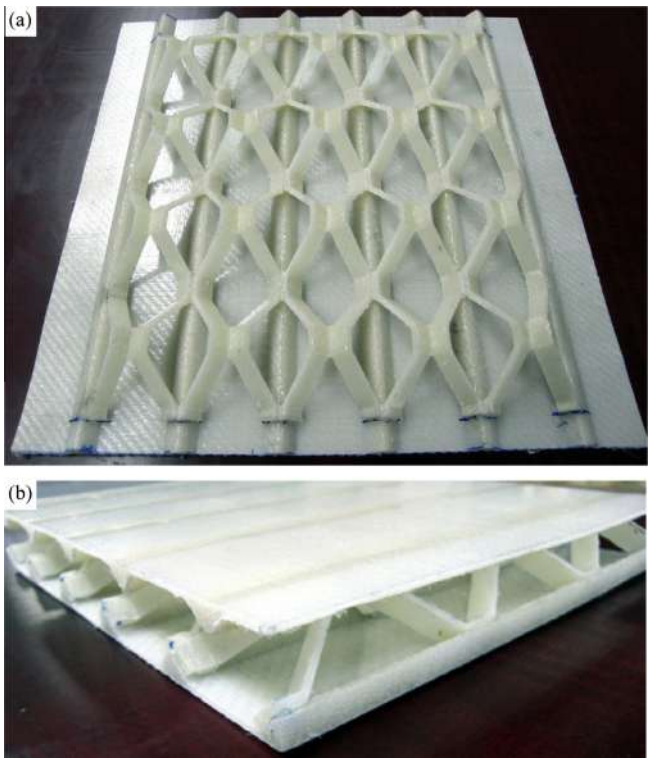

Fig. 4. (a) SrPET lattice truss core which has been hot-plate bonded to one face sheet with reinforcing stringers and (b) final sandwich plate with stringer reinforced face sheets and a lattice truss core.

For each material configuration, two types of strut slenderness ratios (t/l_1) were investigated as summarized in Table 1.

3.3. Compression experiment apparatus

All experiments where performed in a screw-driven Instron 5567 testing machine at a constant compression velocity of 1 mm per minute resulting in a compressive strain rate of 10^{-3} per second over the core thickness. Load was measured using a 30 kN load cell and compressive displacements were measured using a clip-gauge extensometer mounted between the steel loading platens. Compressive stress over the specimen was calculated by dividing the measured load by the surface area of the unit cell ($42 \times 60\ mm^2$ in Fig. 6a). Compressive strain was calculated by dividing the measured displacement by the core height under the assumption that the face sheets exhibit small out-of-plane displacements compared to the core.

4. Description of finite element model

4.1. Model geometry and loading conditions

A unit cell finite element model has been developed in the commercial finite element software Hypermesh [20] to investigate how different geometrical parameters affect the mechanical properties of the lattice truss core. Fig. 6b shows the theoretical unit-cell used to model the specimens. The only difference between the manufactured specimens and the theoretical unit-cell is the size of the face stringers. In order to reduce the amount of elements in the finite element model, the part of the stringers that do not contribute as support for the core struts have been removed. This does, however, not affect the out-of-plane compressive response of the unit cell. The modelled unit cell and the applied boundary conditions are shown in Fig. 7. At each boundary (where core struts meet the face stringers), a tie condition has been employed using the assumption that core struts are perfectly bonded to the face stringers. The tie condition imply that all translational and rotational degrees of freedom are the same as for the face sheet stringers. The bottom face sheet stringers have been assumed to be in a clamped condition so that translational degrees of freedom of the solid brick elements are restricted. An evenly distributed pressure has then been applied to the upper face sheet stringer to simulate a compressive force on the unit cell. Each core configuration was modelled using both a linear elastic buckling analysis and a non-linear implicit analysis in order to capture both instability and material failure

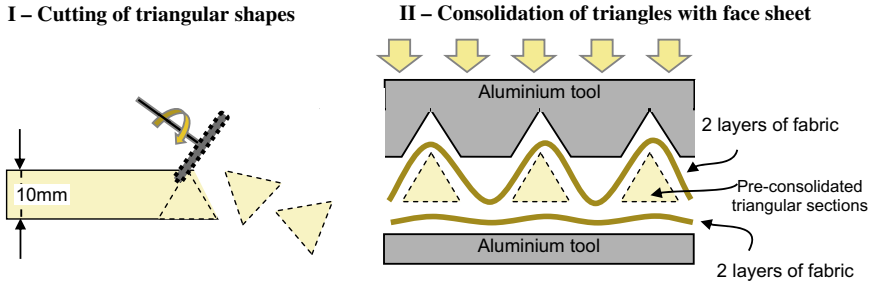

Fig. 5. Steps in manufacturing the face sheets with stringers.

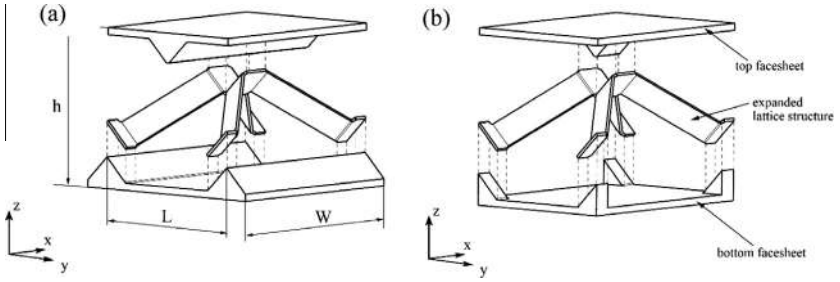

Fig. 6. (a) Unit-cell specimen geometry used to perform out-of-plane compression experiments and (b) theoretical unit-cell used in finite element model.

Please cite this article in press as: Schneider C et al. Compression properties of novel thermoplastic carbon fibre and poly-ethylene terephthalate fibre composite lattice structures. J Mater Design (2014), http://dx.doi.org/10.1016/j.matdes.2014.08.032

Table 1
Four different core configurations tested in the experimental program. All geometries have $\beta = \omega = 45°$, $l_2 = 10$ mm, $d = 9.7$ mm and $c = 2$ mm.

Name	Material	Strut thickness t (mm)	Strut length l_1 (mm)	Relative core density (–)	Core density (kg m^{-3})
SrPET-1	HTPET/LPET	1.8	28.28	0.041	57
SrPET-2	HTPET/LPET	2.7	28.28	0.062	86
CPET-1	Carbon/LPET	1.1	28.28	0.024	40
CPET-2	Carbon/LPET	1.6	28.28	0.037	60

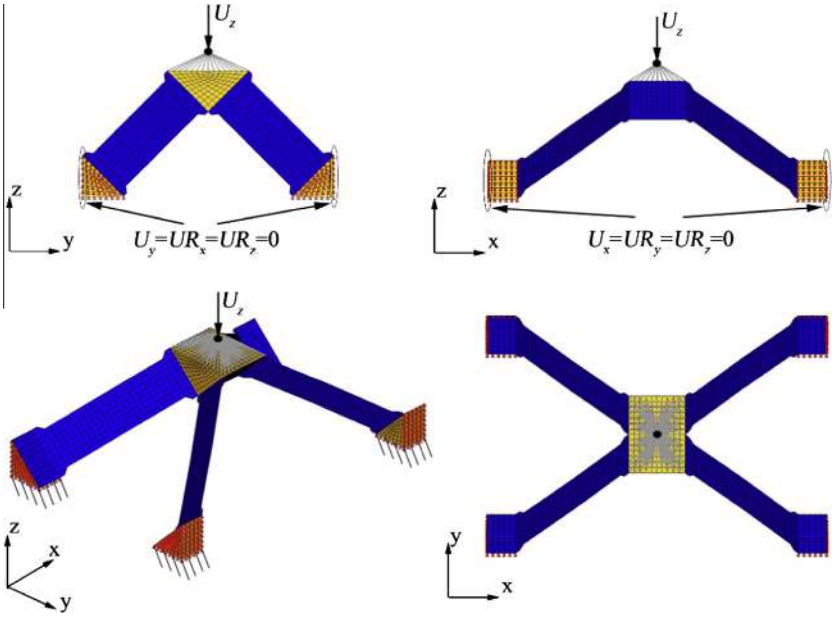

Fig. 7. Finite element model unit cell showing boundary conditions and applied loads from 4 different viewing angles.

mechanisms. Solid brick elements of type CHEXA was used to model the face sheet stringers and composite shell elements of type CQUAD4 were used to model the individual core member struts.

4.2. Initial geometrical imperfections

To simulate the structural imperfections caused during the manufacturing process of the core material, initial geometrical imperfections have been applied to the core. It has been assumed that the geometrical imperfections of each core member have the shape of its first eigenmode. To introduce this imperfection a linear buckling analysis was performed in Hypermesh and the first eigenmode was computed. The deformed core member geometry, in the shape of the first eigenmode, was then used as the initial geometry of the non-linear implicit analysis. As CPET is more sensitive to geometric imperfections than SrPET, the magnitude of the deformed shape was scaled differently, by trying to reach the best correlation with the experiments, so that the maximum initial transverse deflection was 10% and 5% of the core member thickness for SrPET and CPET respectively.

4.3. Material models

The SrPET material was modelled as an elastic–plastic material (using the MAT1 card and its extension – MATS1, in Hypermesh). The material modulus, yield point and stress–strain history measured experimentally were used as input data for the FE model.

The CPET material was modelled using the in-built orthotropic material model in Hypermesh (MAT8 card and its extension – MATX43) where the experimentally measured value for the both the longitudinal and the transversal moduli was used. The transverse shear moduli G_{13} and G_{23} and the in-plane shear modulus were assumed to be the same, having a value of 2000 MPa. It is assumed that the CPET material fails when the maximum longitudinal strain attains the experimentally measured quasi-static failure strain of 0.7%. This relatively straight forward failure modelling approach has previously been proven successful by Tagarielli et al. [15].

5. Summary and discussion of experimental results and FE predictions

In order to validate the accuracy of the FE model a comparison is given between the experimentally measured stress–strain responses and the different failure mechanisms to the predictions made by the FE model.

5.1. Summary of results for SrPET lattice cores

The stress–strain response and the corresponding *in-situ* photographs for the slender SrPET-1 core configuration is shown in Fig. 8. The overall stress–strain response predicted by the FE model shows good agreement with experimental findings. At low compressive strains (<2.5%, point 1 in Fig. 8a), a linear elastic loading behaviour is observed experimentally and in the numerical FE model. There is minimal out-of-plane deformation of the core struts and no plastic deformation is recorded in the FE model. At a compressive strain of ~4.5% (point 2 in Fig. 8a), the core members buckle into a shape similar to a half sinus wave which is followed by a rapid drop in stress level. This drop in load level occurs while the material is still in its elastic range. Shortly after the

Please cite this article in press as: Schneider C et al. Compression properties of novel thermoplastic carbon fibre and poly-ethylene terephthalate fibre composite lattice structures. J Mater Design (2014), http://dx.doi.org/10.1016/j.matdes.2014.08.032

immediate load drop, the stress strain curve starts to flatten out. At this strain point (around point 3 in Fig. 8a), onset of plastic deformations is observed in the FE model which results in a less dramatic load drop and a more controlled softening type of deformation (point 3–4 in Fig. 8a). The FE-model predicts a lower post buckling load drop (~20%) as compared to the experimental findings where a somewhat higher post buckling load drop is observed (~35%). As the specimen is compressed further, a mid-span plastic hinge is formed on the core members and eventually they fold and come into contact with the face sheets which results in increased load levels and core densification.

Turning to the more stubby SrPET-2 core (Fig. 9), a similar stress–strain response can be observed but with a less pronounced immediate load drop after the peak load. In this case, the onset of plastic deformation in the FE model occurs directly at the peak load (point 2 in Fig. 9a) causing the less pronounced load drop. This is an effect of the higher core member thickness which provides better resistance to buckling (higher bending stiffness) causing the core members to yield first prior to onset of buckling. After a plastic hinge has formed, approximately mid-span of the core member, the load however continues to drop beyond compressive strains above 40%.

It is noted that the FE model is able predict the stiffness of the slender core structures with adequate accuracy (typically within 10%) but larger discrepancy is found for the stubby cores (up to 23%). No apparent explanation could be found for this discrepancy.

5.2. Summary of results for CPET lattice cores

The measured and predicted stress–strain history of the slender CPET-1 core is shown in Fig. 10. A linear elastic loading behaviour is observed up to ~2% compressive strain (close to point 2 in Fig. 10a) both in the experiments and the numerical model after which a sudden load drop is observed. Core member compressive material failure is noted in both the experimental measurements and numerical predictions as indicated by the black arrow in Fig. 10b. A considerable variation in stiffness is noted between the experimental measurements elucidating the sensitivity to manufacturing imperfections.

(a)

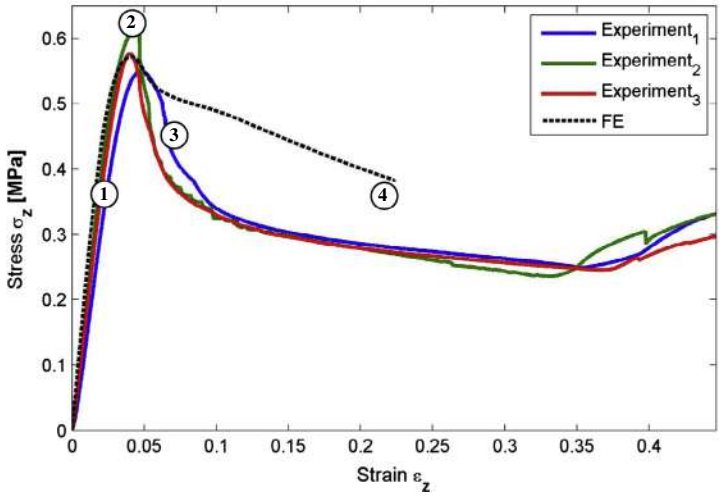

(b)

Position	Experiment	FE-model
1	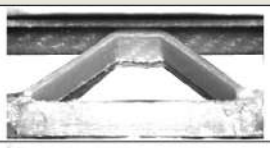	
2	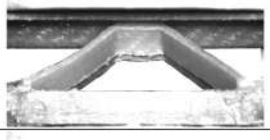	
3		
4	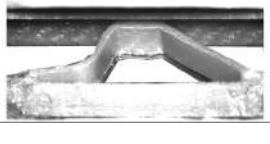	

Fig. 8. (a) Stress–strain response of SrPET-1 as measured experimentally and predicted by finite element model. (b) Deformation mechanism at various strain levels.

Please cite this article in press as: Schneider C et al. Compression properties of novel thermoplastic carbon fibre and poly-ethylene terephthalate fibre composite lattice structures. J Mater Design (2014), http://dx.doi.org/10.1016/j.matdes.2014.08.032

(a)

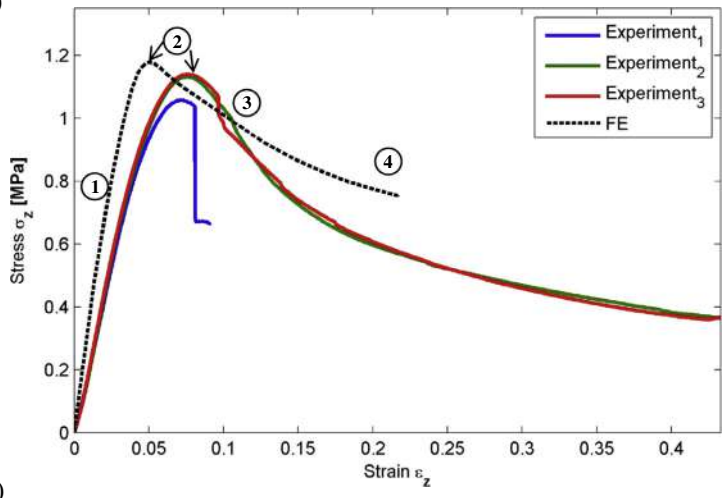

(b)

Position	Experiment	FE-model
1		
2		
3		
4		

Fig. 9. (a) Stress–strain response of SrPET-2 as measured experimentally and predicted by finite element model. (b) Deformation mechanism at various strain levels.

The measured and predicted stress–strain history for the stubbier CPET-2 core is shown in Fig. 11. The peak stress of 2 MPa occurs at a compressive strain of about 2.7% (point 2 in Fig. 11a). At 2.7% core compressive strain, the strain in each core member strut is approximately 0.7% which is close to the measured material failure strain. Compressive material failure of the core members could be observed in the experiments and FE model resulting in a catastrophic failure mode with sudden drop in stress.

The peak stress and loading stiffness is predicted with good accuracy for both the CPET-1 and CPET-2 configuration.

6. Parametric investigation and comparisons to existing core materials

In the previous section it was shown that the FE model developed herein is able to predict stress–strain response and failure mechanism of most core configurations with good accuracy. The only exception is the core stiffness prediction for the stubby SrPET cores where discrepancies up to 20% were found. For the purpose of providing an approximation of the core performance, this level of accuracy is adequate and comparable to commonly used theoretical models. In this section the FE model is used to investigate how the different manufacturing parameters, depicted in Fig. 2, affects the out-of-plane stiffness and strength of the core material.

6.1. Effect of core strut cross-section geometry on out-of-plane compressive response

The effect of core strut cross-section geometry on the weight normalized compressive strength and stiffness of the core is firstly investigated. The strut cross-section geometry is defined by the two variables d and t which describe the cross section width and thickness respectively.

In Fig. 12 it is illustrated the effect of core strut slenderness by keeping all variables fixed ($\omega = 45°$, $\beta = 45°$, $d = 7.7$ mm, $c = 2$ mm, $l_1 = 22.3$ mm, $l_2 = 10$ mm) while changing the strut thickness, t.

Starting with the SrPET core, a major and linear increase of the weight normalized strength up to $t/l_1 = 0.09$ and a minor one further on is observed. This is the point where the failure mode switches from buckling to material compression failure. When the failure is governed by strut buckling, the core strength increases approximately in cube to the strut thickness while the

Please cite this article in press as: Schneider C et al. Compression properties of novel thermoplastic carbon fibre and poly-ethylene terephthalate fibre composite lattice structures. J Mater Design (2014), http://dx.doi.org/10.1016/j.matdes.2014.08.032

(a)

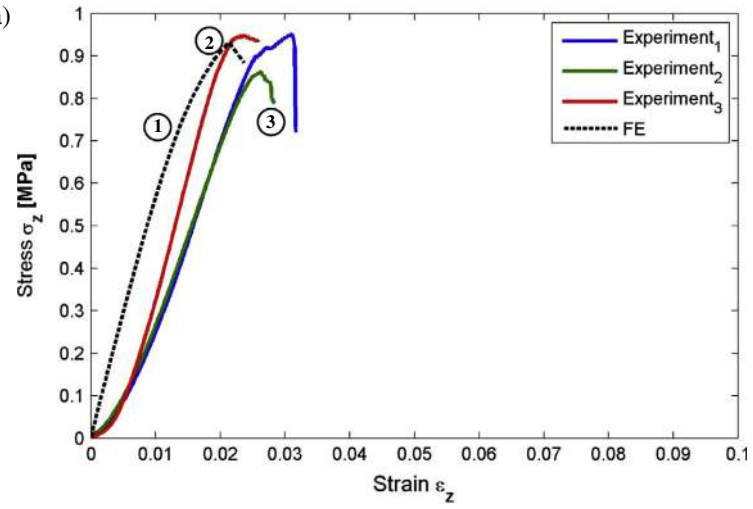

(b)

Position	Experiment	FE-model
1	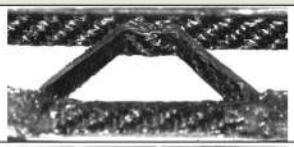	
2		
3	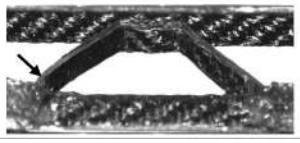	

Fig. 10. (a) Stress–strain response of CPET-1 as measured experimentally and predicted by finite element model. (b) Deformation mechanism at various strain levels.

density increases linearly with the strut thickness resulting in an overall increase in normalized core strength. When the governing failure mode is material compression failure, strength and density increase linearly with thickness resulting in a plateau for the weight normalized strength. The stiffness of the core is constant with changing strut thickness with one exception: At very low strut slenderness ratios, the effect of initial imperfection on core stiffness becomes significant as the core struts have very low bending stiffness.

The CPET core shows the same stiffness and strength behaviour as the SrPET core with the difference that the major increase in normalized strength is up to $t/l_1 = 0.05$ instead of $t/l_1 = 0.09$. This is since the ratio between material strength and material stiffness is an order of magnitude smaller for the CPET material compared to the SrPET material. The effect of this is that the switch in failure mode from buckling to material compression failure will occur at a lower strut slenderness ratio.

Turning to the strut width, d, its effect on the mechanical behaviour is explained as it follows. When the struts are stocky enough so that failure is governed by material compression failure, the compressive strength of the core will change linearly with the increased strut cross section area (t times d). As the core density changes linearly with the strut cross section area, the density normalized core strength will be constant when t/d changes. In the case where failure is governed by strut buckling a different behaviour can be noticed: The core strut will always buckle in the direction of the lowest second moment of inertia meaning that the smaller of the two dimensions, t and d, will define the direction where buckling occurs. For low core relative densities where failure is governed by core strut buckling, the optimal width to thickness ratio, t/d, will thus be 1.

6.2. Effect of expansion and corrugation angle on out-of-plane compressive response

The effect of core expansion angle, β, and corrugation angle, ω, on the weight normalized compressive strength and stiffness of the core is investigated further on.

6.2.1. Effect of expansion angle

In Fig. 13a it is showed the effect of expansion angle on the weight normalized stiffness and strength of the core. The expansion angle is varied within the interval of 45–80° while keeping all other variables fixed. An expansion angle of 90° would result in the structure in stage II of the manufacturing process (see Fig. 2); i.e. a corrugated structure with slots at a distance d from each other.

An increasing weight specific stiffness and strength is observed for both CPET and SrPET cores as the expansion angle increases. For the weight specific stiffness, this increase continues towards 75–80° where a plateau is reached. Looking at the core strength, a similar increase in weight specific strength is noticed but the peak

Please cite this article in press as: Schneider C et al. Compression properties of novel thermoplastic carbon fibre and poly-ethylene terephthalate fibre composite lattice structures. J Mater Design (2014), http://dx.doi.org/10.1016/j.matdes.2014.08.032

(a)

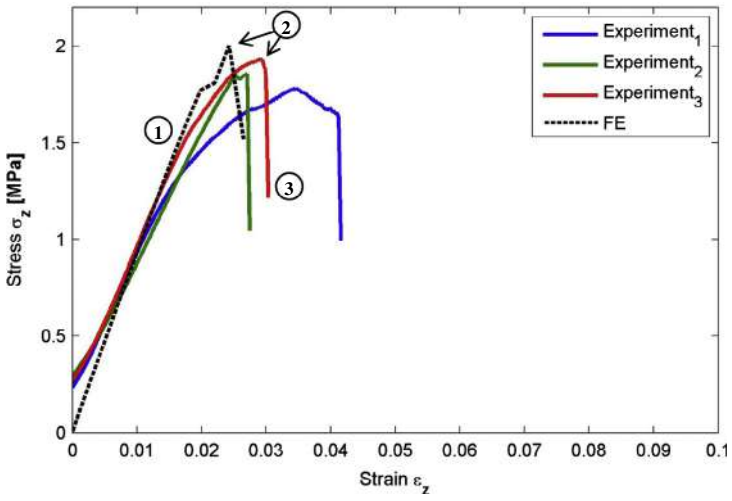

(b)

Position	Experiment	FE-model
1	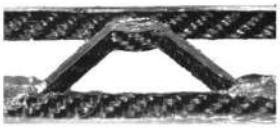	
2	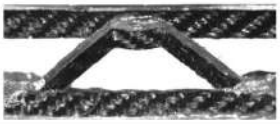	
3	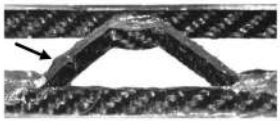	

Fig. 11. (a) Stress–strain response of CPET-2 as measured experimentally and predicted by finite element model. (b) Deformation mechanism at various strain levels.

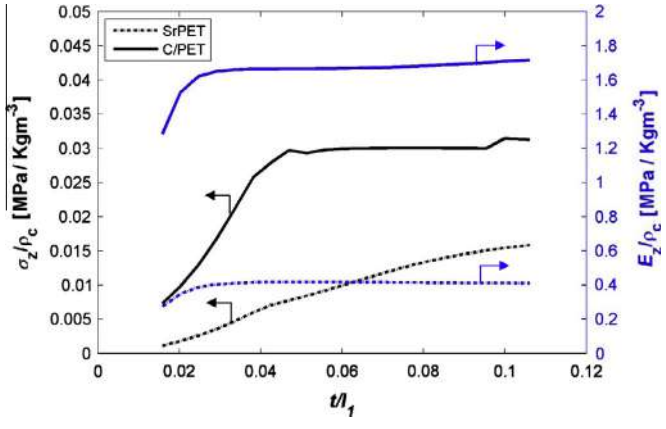

Fig. 12. Effect of strut slenderness ratio (t/l_1) on out-of-plane compressive stiffness and strength.

weight specific strength is found for an expansion angle of approximately 60° after which the weight specific strength starts to drop again. Although the stiffness and strength increases continuously with the expansion angle the core density increases more rapidly for $\beta > 60°$, which causes the plateau and the drop in weight specific stiffness and strength.

6.2.2. Effect of corrugation angle

Fig. 13b shows the effect of corrugation angle, ω, on the weight specific strength and stiffness of the core. Similar to the core expansion angle, an increasing weight specific strength as function of corrugation angle is noticed. The weight specific stiffness of both the CPET and SrPET increase up to the maximum corrugation angle of 90° while the weight specific strength shows a peak at a corrugation angle of approximately 75°. The drop in weight specific strength is caused by the rapidly increasing core density as the corrugation angle increases beyond 70° as can be derived from Eq. (1).

It is worth emphasising that the optimum expansion and corrugation angle for cores subjected to shear load, is likely to be different from the one found for out-of-plane compression.

6.3. Comparisons with existing core materials

Based on the parametric studies described above, the manufacturing parameters for the expanded lattice core are chosen so that a close to optimal geometry is created for out-of-plane compressive loading. The core strut cross-section ratio, t/d, is chosen as close to unity as possible. The expansion angle, β, is chosen to be fixed at 60° and the corrugation angle, ω, is chosen to be fixed at 75°. Further on, the core density is varied by changing the core strut thickness, t, while keeping the core strut length, l_1, fixed.

Please cite this article in press as: Schneider C et al. Compression properties of novel thermoplastic carbon fibre and poly-ethylene terephthalate fibre composite lattice structures. J Mater Design (2014), http://dx.doi.org/10.1016/j.matdes.2014.08.032

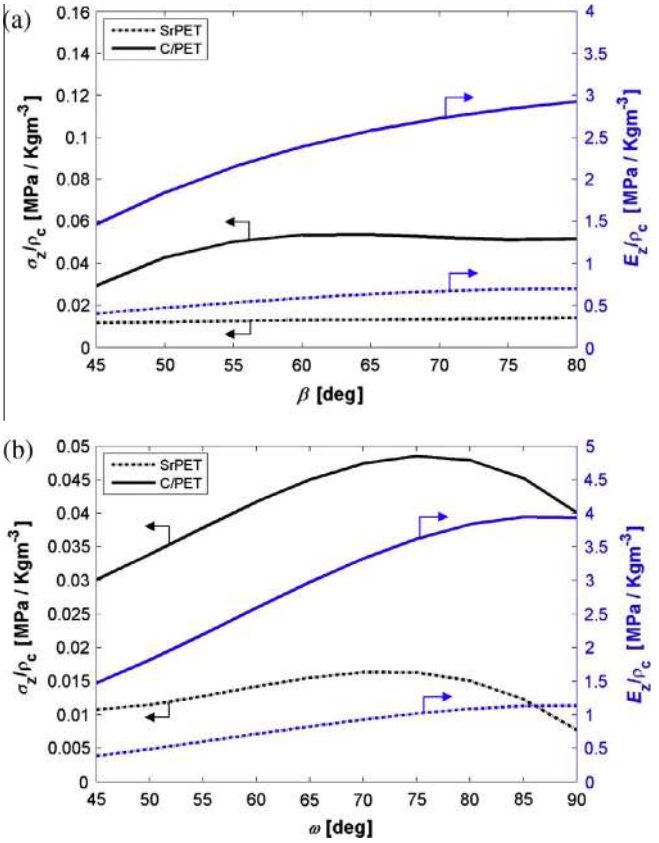

Fig. 13. (a) Effect of expansion angle (β) on out-of-plane compressive stiffness and strength and (b) effect of corrugation angle (ω) on out-of-plane compressive stiffness and strength.

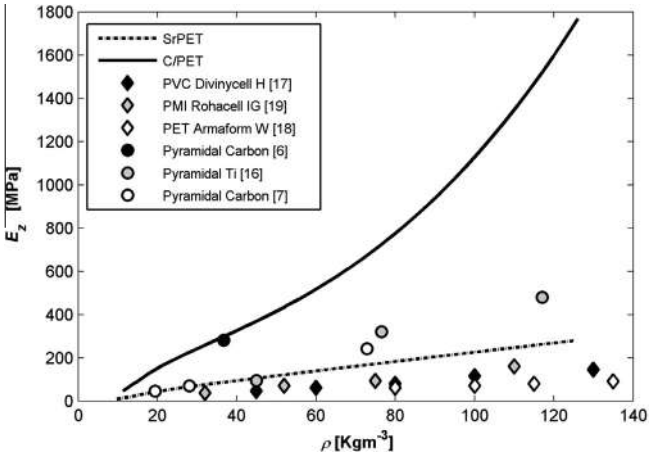

Fig. 14. Core stiffness as function of core density for a range of different sandwich core materials. (See above-mentioned references for further information.)

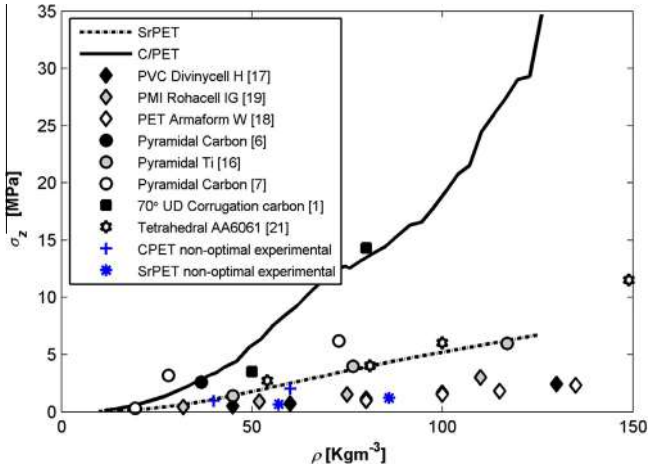

Fig. 15. Core strength as function of core density for a range of different sandwich core materials. (See above-mentioned references for further information.)

Although not all previous studies report stiffness properties, the out-of-plane stiffness as function of density is plotted for a selected number of sandwich core materials in Fig. 14. The CPET lattice cores shows very competitive stiffness compared to both traditional foam cores and to recently developed pyramidal lattice cores [6]. At higher core densities, the CPET core have considerably higher out-of-plane compressive stiffness than both pyramidal titanium [16] and carbon fibre cores [6,7]. The SrPET lattice cores show stiffness similar to high-end PMI Rohacell cores but perform considerable worse than carbon fibre composite lattice cores at densities above 20 kg m^{-3}.

The out-of-plane compressive strength as function of density, for a selection of different core types, is plotted in Fig. 15. At low core densities (<40 kg m^{-3}), the CPET lattice cores have a strength comparable to the pyramidal carbon fibre structures presented in [6,7]. At these low core densities no competing metallic cores exist. The pyramidal composite cores developed by Li et al. [6] have a density of 37 kg m^{-3} and an out-of-plane compressive strength of 2.6 MPa which is slightly lower than the near-optimal CPET lattice core presented in this study. Xiong et al. [7] reports a pyramidal carbon fibre composite core at three different densities. The two configurations at low density show very good performance and outperform the CPET lattice core developed in this study. The pyramidal core at intermediate density (~70 kg m^{-3}), however, shows lower strength than the CPET lattice core presented here. The strength of the CPET structures increases rapidly with increasing density as the core members become more resistant to buckling failure. Similar trend is seen for the pyramidal cores presented by Li et al. [6] which have relatively low strength at very low densities (20 kg m^{-3}) and then increase rapidly. At higher densities, the CPET lattice core outperform other core materials except for the corrugated carbon fibre core presented in [1]. Two metallic lattice cores have also been included for comparison, one based on 6061 aluminium alloy [21] and one based on titanium alloy [16]. Both of these metallic lattice cores show lower out-of-plane compressive performance than the carbon fibre based cores of similar density. Worth noting is that the non-optimal CPET lattice core, which have been tested experimentally in this study, shows similar performance as the two metallic cores, tetrahedral AA6061 [21] and the pyramidal titanium core [16]. The near-optimal CPET lattice core however shows considerably higher out-of-plane strength than the metallic cores of same density.

The performance of the SrPET lattice core is competitive at very low densities. This is mainly since SrPET has lower density than CPET and the core members are therefore thicker and more buckling resistant at low densities. At intermediate densities, the SrPET cores have strength performance which is better than the high-end foam cores Rohacell and Divinycell. The strength of the SrPET core is however considerably lower than the high performing pyramidal carbon fibre cores presented by Xiong et al. [7] and Li et al. [6]. When compared to the titanium alloy pyramidal [16] and aluminium alloy tetrahedral [21] lattice cores, the near-optimal SrPET core configuration shows approximately the same out-of-plane strength performance. The non-optimal SrPET cores, which have been tested experimentally within this study, shows relatively

Please cite this article in press as: Schneider C et al. Compression properties of novel thermoplastic carbon fibre and poly-ethylene terephthalate fibre composite lattice structures. J Mater Design (2014), http://dx.doi.org/10.1016/j.matdes.2014.08.032

poor performance on par with commercially available polymeric foams.

7. Conclusions

It has been demonstrated that thermoplastic composite materials can be used to create lattice structures using an efficient and scalable manufacturing method. The following conclusions can be made regarding the mechanical performance of these lattice materials:

1. The lattice structures manufactured from carbon fibre reinforced PET show both competitive strength and stiffness at a range of densities. The experimentally tested non-optimal configurations shows mechanical properties that are on par with high end metallic cores. It has however been demonstrated that a significant improvement in mechanical properties can be achieved by changing the geometrical properties of the cores so they are more suited for out-of-plane compressive loading.
2. The lattice structures manufactured from PET fibre reinforced PET show similar stiffness and strength performance as high-end polymeric foams but perform considerably worse than metallic and carbon fibre composite lattice structures, especially in terms of stiffness. If a more optimal core geometry is chosen, performance similar to metallic lattice cores can be achieved. Further, the SrPET lattice cores show non-catastrophic and ductile failure modes (as opposed to the carbon fibre based cores) which is beneficial from an energy absorption point of view.

Although the SrPET lattice structures show limited benefits over traditional foam structures when it comes to stiffness, they can still be interesting for strength dimensioned designs where low weight and high energy absorption is important. Further, SrPET lattice structures are fully recyclable as opposed to PVC and PMI foam cores which is key for e.g. automotive applications (such as car bumper beams).

Acknowledgements

The financial support for this investigation has been provided by the Centre of ECO2 Vehicle Design at the Department of Aeronautical and Vehicle Engineering, Royal Institute of Technology, KTH Sweden and the Swedish Agency for Innovation Systems (VINNOVA). Dan Zenkert was partly funded by Vinnova SIO Lighter. We acknowledge the support from Comfil in providing material.

References

[1] Kazemahvazi S, Tanner D, Zenkert D. Corrugated all-composite sandwich structures. Part 2: Failure mechanisms and experimental programme. Compos Sci Technol 2009;69:920–5.
[2] Kazemahvazi S, Zenkert D. Corrugated all-composite sandwich structures. Part 1: Modeling. Compos Sci Technol 2009;69:913–9.
[3] Russell BP, Liu T, Fleck NA, Deshpande VS. Quasi-static three-point bending of carbon fiber sandwich beams with square honeycomb cores. J Appl Mech, Trans ASME 2011;78.
[4] Finnegan K, Kooistraa G, Wadley HNG, Deshpande VS. The compressive response of carbon fiber composite pyramidal truss sandwich cores. Int J Mater Res 2007;98.
[5] Wang Bing, Zhang Guoqi, He Qilin, Ma Li, Linzhi Wu, Feng Jicai. Mechanical behavior of carbon fiber reinforced polymer composite sandwich panels with 2-D lattice truss cores. Mater Des 2014;55:591–6.
[6] Li M, Wu LZ, Ma L, Wang B, Guan ZX. Mechanical response of all-composite pyramidal lattice truss core sandwich structures. J Mater Sci Technol 2011;27:570–6.
[7] Xiong J, Ma L, Wu LZ, Wang B, Vaziri A. Fabrication and crushing behavior of low density carbon fiber composite pyramidal truss structures. Compos Struct 2010;92:2695–702.
[8] Xiong J, Ma L, Pan S, Wu L, Papadopoulos J, Vaziri A. Shear and bending performance of carbon fiber composite sandwich panels with pyramidal truss cores. Acta Mater 2012;60:1455–66.
[9] Yin Sha, Wua Linzhi, Nutt Steven. Stretch–bend-hybrid hierarchical composite pyramidal lattice cores. Compos Struct 2013;98:153–9.
[10] George Tochukwu, Deshpande Vikram S, Wadley Haydn NG. Mechanical response of carbon fiber composite sandwich panels with pyramidal truss cores. Composites: Part A 2013;47:31–40.
[11] Velea MN, Wennhage P, Lache S. Out-of-plane effective shear elastic properties of a novel cellular core for sandwich structures. Mater Des 2012;36:679–86.
[12] Velea MN, Lache S. In-plane effective elastic properties of a novel cellular core for sandwich structures. Mech Mater 2012;43:377–88.
[13] Comfil® APS. Thermoplastic Composites, DK 8883 Gjer, Denmark, 08.2013, <www.comfil.biz> [accessed 18.07.2013].
[14] Schneider C, Kazemahvazi S, Åkermo M, Zenkert D. Compression and tensile properties of self-reinforced poly(ethylene terephthalate)-composites. Polym Testing 2013;32(2):221–30.
[15] Tagarielli VL, Deshpande VS, Fleck NA. Prediction of the dynamic response of composite sandwich beams under shock loading. Int J Impact Eng 2010;37:854–64.
[16] Queheillalt DT, Wadley HNG. Titanium alloy lattice truss structures. Mater Des 2009;30:1966–75.
[17] DIAB Group. Divinycell® H Technical data, SE-312 22 Laholm, Sweden. <www.diabgroup.com> [accessed 21.11.2013].
[18] Armacell Benelux. ArmaFORM PET/W Technical data, Rue de Trois Entites 9-B-4890 Thimister Clermont. <www.armacell.com> [accessed 02.04.2014].
[19] Evonik Industries AG, ROHACELL® IG/IG-F Properties, 64293 Darmstadt, Germany. <www.rohacell.com> [accessed 21.11.2013].
[20] Altair HyperWorks 12. Online Help and Documentation. <http://www.altairhyperworks.com>; 2013 [accessed 14.06.2013].
[21] Kooistra Gregory W, Deshpande Vikram S, Wadley Haydn NG. Compressive behavior of age hardenable tetrahedral lattice truss structures made from aluminium. Acta Mater 2004;52:4229–37.

Composite Structures 111 (2014) 75–84

Contents lists available at ScienceDirect

Composite Structures

journal homepage: www.elsevier.com/locate/compstruct

Multi-objective optimisation of vehicle bodies made of FRP sandwich structures

Marian N. Velea [b,*], Per Wennhage [a], Dan Zenkert [a]

[a] Department of Aeronautical and Vehicle Engineering, Royal Institute of Technology (KTH), SE-100 44 Stockholm, Sweden
[b] Department of Mechanical Engineering, Transilvania University of Braşov, 500024 Braşov, Romania

ARTICLE INFO

Article history:
Available online 3 January 2014

Keywords:
Composite structures
FRP sandwich
Multi-objective optimisation

ABSTRACT

An optimisation methodology is developed and applied on a FRP sandwich body of an electric vehicle – ZBee, where single-objective and multi-objective optimisation studies are performed stepwise using a commercially available software package. The single-objective optimisation allows the identification of the load paths within the composite body, according to the loading conditions previously defined. Within the multi-objective optimisation, the optimum thickness and distribution for each of the layers that form the composite body are searched within the design space so as to obtain the best performance with respect to weight, material cost, global and local stiffness. Strength requirements are also considered as constraints within the optimisation. A conflict situation appears when several objectives are considered within the optimisation, meaning that an increased performance in one objective may often lead to a decreased performance for the others. Therefore, a trade-off between objectives is needed. The interpretation of results is partially made by using trade-off plots, the so-called Pareto frontiers. A method for the overall selection of the most beneficial solutions is proposed and applied in order to choose between the best obtained solutions according to the importance of the objectives.

© 2013 Elsevier Ltd. All rights reserved.

1. Introduction

An extensive interest within vehicles industries to develop and make use of lightweight composite materials and structures has been generated by the need of reducing energy consumption within the vehicles' use-phase. Clear benefits of using composites especially with respect to weight reduction have been reported within aeronautical, rail, naval and automotive industries. Especially for electric vehicles, the use of fibre reinforced polymers (FRP) represents a salient approach to increase their range. Such a demonstration is given by the ZBee vehicle which represents the materialized vision of a Swedish company – Clean Motion AB – regarding energy efficient electric vehicles. This urban vehicle, classified as scooter according to EU regulations, has been designed for short distance transportation of up to three people and smaller goods. Fig. 1 shows the 2nd generation of the ZBee vehicle. The body in white was entirely made of FRP composites. Certain sections within the body were made of FRP sandwich structure for an increased bending stiffness, having PVC foams and polymer honeycombs as cores. The composite body was made of 9 parts which were adhesively bonded together to form a whole.

A new generation of the ZBee – the 3rd generation –, Fig. 2, aims at an increased performance in terms of weight, material costs, local and global stiffness behaviour compared to the 2nd generation.

Space for even more increased performance exists due to the fact that overall properties of FRP composites may be tailored to satisfy specific design requirements by changing the values of the constituents' specific parameters [1]. This goal can be attained if appropriate advanced optimisation tools are used.

An optimisation problem is most often formulated when trying to improve the vehicles' performance by weight reduction. An optimal solution of the objective function (e.g. mass) is searched within a design space defined by the upper and lower limits of the design variables (e.g. materials' properties) and by certain imposed constraints (e.g. required stiffness, strength etc.) [2].

However, lowering the weight of a vehicle will most often imply a reduction of other performance criteria such as the stiffness and strength properties, material cost or the safety performance. Therefore, there are cases where several objectives need to be defined and considered within the optimisation procedure in which case a conflict situation appears between objectives, meaning that an increased performance in one objective leads to a decreased performance for the others [3]. Several complex optimisation techniques and algorithms have been proposed for solving such multi-objective problems [1,4–9].

* Corresponding author: Department of Mechanical Engineering, Transilvania University of Braşov, 1 Politehnicii Street, 500024 Braşov, Romania. Tel.: +40 723676387; fax: +40 268476172.

E-mail addresses: velea@kth.se, marian.velea@unitbv.ro (M.N. Velea), wennhage@kth.se (P. Wennhage), danz@kth.se (D. Zenkert).

0263-8223/$ - see front matter © 2013 Elsevier Ltd. All rights reserved.
http://dx.doi.org/10.1016/j.compstruct.2013.12.030

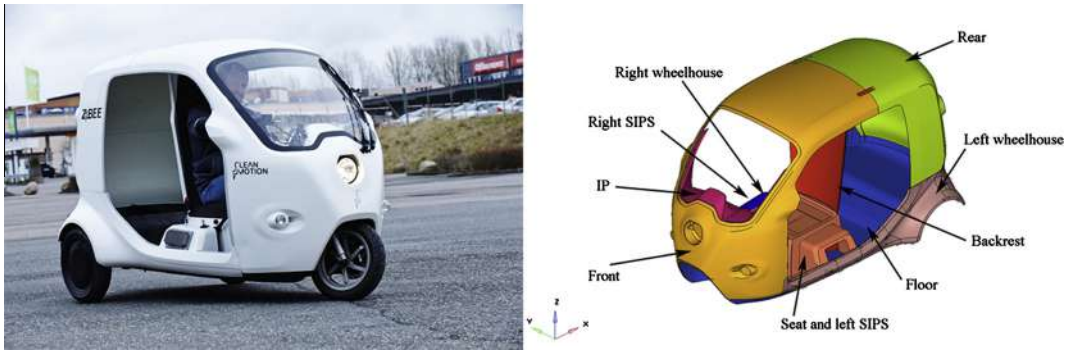

Fig. 1. The 2nd generation of ZBee vehicle.

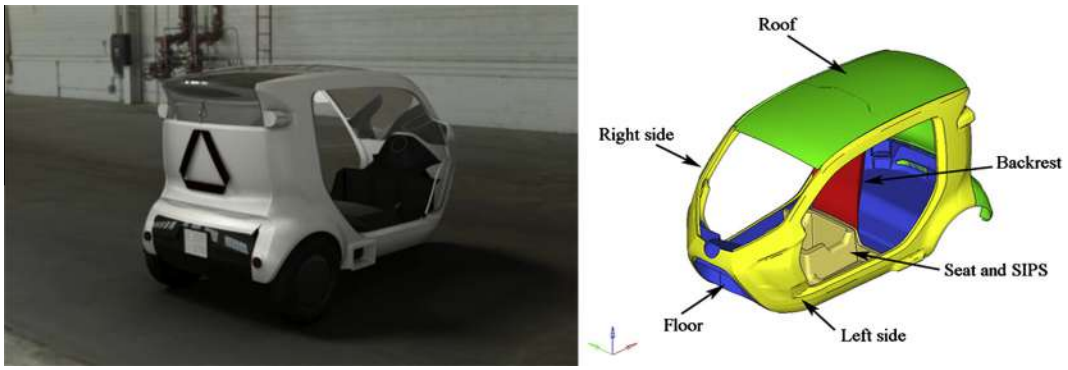

Fig. 2. The 3rd generation of ZBee vehicle – new composite body design.

The weighted sum approach has been used as an attempt to simplify the problem complexity of finding solutions within multi-objective optimisation problems, where all the objectives functions are summed into a single objective function, giving weight penalties for each of them [1]. Then, a solution may be obtained by running one of the many existing single-objective optimisation algorithms. The main drawback regarding the weighted sum method is the quantification of weight penalties because the results are strongly dependent on them [10], although methods for dealing with this issue have been studied and proposed [11].

Therefore, in order to obtain a large spectrum of solutions, dedicated multi-objective optimisation algorithms remain here of interest [12,13]. One of the most spread algorithms within the current available commercial FE packages is the so-called MOGA (Multi-objective Optimisation Genetic Algorithm) [14]. Instead of providing one single solution, MOGA produces a set of solutions by searching within the design space for a set of Pareto optimal solutions [15]. The interpretation of results in the case of a multi-objective optimisation study is partially made with the help of the trade-off curves, the so-called Pareto frontiers [16]. The obtained Pareto frontiers only indicate the set of solutions that gives the best compromise between objectives, but there is a further need for choosing one single solution from the set. This can be done either by intuition or by reformulating the objectives as constraints, except one of them, or by using a composite objective function [3].

This article firstly addresses the problem of optimizing the FRP sandwich body of the new ZBee with respect to weight, stiffness, strength and material costs. Secondly, a selection method of the most beneficial design solutions is developed and applied in order to deal with the difficulties of interpreting the multi-objective optimisation results generated by MOGA.

All the values of the results characterizing the performance of the 3rd generation are normalized to the ones that characterize the 2nd generation, in order to evaluate the gained improvements.

2. Numerical model

All the analyses and optimisation studies have been performed within the Hyperworks 11 software package. Hypermesh facilities were used to simplify the geometry, to generate the mesh, to define material properties and to assign load cases. Optistruct solver was used for FE analyses and single-objective optimisation studies. Hyperstudy and RADIOSS solver was used for multi-objective optimisation studies.

The FE mesh is generated on the outer surface of the body parts. The target finite element size was set to 10 mm. Quad and

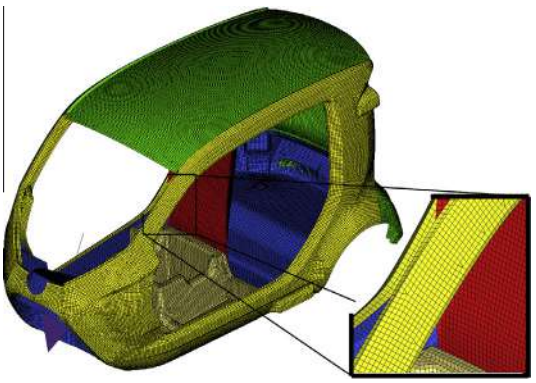

Fig. 3. Meshed body.

Table 1
The materials properties used within the optimisation studies.

Material type	Material characteristics					
	$E_1 = E_2$ [MPa]	G_{12} [MPa]	ρ [kg/m^3]	$X_t = X_c$ [MPa]	$Y_t = Y_c$ [MPa]	S [MPa]
GF-weave	16,740	2237	1704	241	241	7
GF-csm	8462	1712	1432	129	129	9
PUR foam	55	21	150	1.8	1.8	1.18
PVC foam	130	35	100	2	2	1.6
SORIC	800	35	1160	4	4	3
Gelcoat	3800	1387	1200	–	–	–

triangular shell elements were used to realize an initial automated mesh of the body parts.

The generated finite elements have been checked and refined where needed, according to the HyperMesh quality indexes default values [17]. The resulted mesh has 688,638 degrees of freedom, Fig. 3. The connection between body parts (i.e. the adhesive) has been modelled using rigid elements in order to simplify the model.

2.1. Material properties

The composite structures the body parts are made of are modelled in HyperMesh as laminates, each laminate being composed by several plies (layers). The material properties were thus defined individually for each of the layers within the software. Table 1 shows the types of layers that were used within the body structure of the ZBee-Generation 3 and their corresponding material characteristics. The acronyms GF-weave and GF-csm represent a bi-directional weave and glass fibre chopped strands mats respectively. SORIC represents a polymer honeycomb core material.

2.2. Loading conditions

Within the analysis and optimisation of the ZBee composite body there have been considered 6 loading conditions. The corresponding loads and constraints are illustrated in Fig. 4.

2.2.1. Global torsion

This load case has the purpose to evaluate the torsion stiffness of the whole composite body. Fig. 4(a) shows the considered boundary conditions, where node B has all the degrees of freedom retained. The torsion stiffness K_t is thus determined using Eq. (1), where M_{xA} is the moment applied along X-axis at point A and θ_{xA} represents the rotation measured around X-axis at point A.

$$K_t = \frac{M_{x_A}}{\theta_{x_A}} \quad \left[\frac{\text{Nm}}{\text{deg}}\right] \tag{1}$$

2.2.2. Global bending

The bending stiffness K_b of the composite body is determined using Eq. (2), where F_{zC} is the force applied along Z-axis at point C and δ_{zC} represents the displacement measured along Z-axis at point C. The node B has all degrees of freedom retained while node A is allowed to slide along X-direction, Fig. 4(b).

$$K_b = \frac{F_{z_C}}{\delta_{z_C}} \quad \left[\frac{\text{N}}{\text{mm}}\right] \tag{2}$$

2.2.3. Front wheel brake

This load case has been introduced in order to evaluate the local stiffness of the composite body around the front wheel, Fig. 4(c). It is assumed that the vehicle is travelling on a downhill gradient of 15° and only the front wheel is braking (worst case). Taking into consideration the legal requirements that the vehicle needs to stop with an average deceleration of 2.7 m/s, a braking force F and a braking moment M are determined and both are applied on point B (centre of the front wheel); the displacement of point C (the headstock top point) is then determined using Eq. (3), where δ_x, δ_y and δ_z represent the displacements of point C evaluated within the analyses along the three orthogonal axes.

$$\delta = \sqrt{\delta_x^2 + \delta_y^2 + \delta_z^2} \quad [\text{mm}] \tag{3}$$

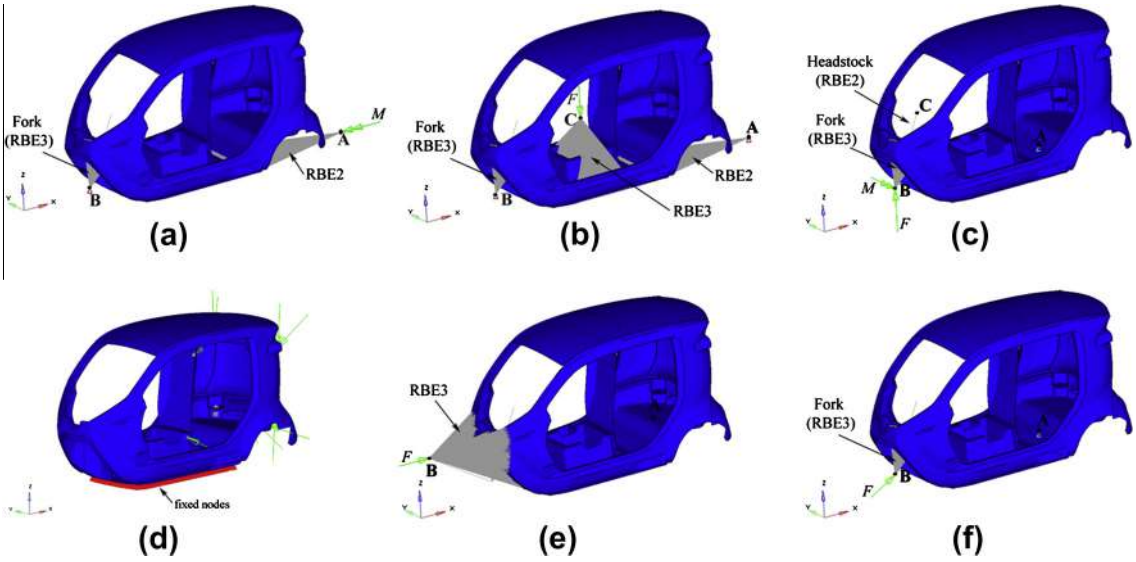

Fig. 4. The applied loads and constraints.

Within this load scenario, inertia relief is used to obtain the load equilibrium of the model [18]. Thus, the applied loads F and M are balanced by inertial accelerations that automatically provide forces distributed over the body in such a way that the sum of the applied forces is equal to zero. However, all the degrees of freedom of node A, Fig. 4(c), are constrained in order to restrain the rigid body motion, but the reaction forces on this node are zero [17].

2.2.4. Belt points forces

Specific local stiffness at belt points is also required. Within this load case, static forces are applied at belt points and their displacements are evaluated and used as constraints within the optimisation study. The degrees of freedom are restrained for all the bottom nodes, Fig. 4(d).

2.2.5. Front impact

For the homologation of the vehicle, several safety requirements need to be fulfilled and therefore equivalent load scenarios also need to be included within the simulations. Dynamic non-linear FE analyses are usually considered for investigating this type of crash scenarios [19] but these imply a high computational time, especially in the case of a multi-objective optimisation. For this reason, an equivalent static load case is here approximated, Fig. 4(e), where a force F is applied on the depended node B and distributed within interpolation constraint elements – RBE3 [17] on an estimated impact area from the composite body. The magnitude of the force F equals M 10g, where M is the full vehicle mass and g is the gravitational acceleration. The displacement of point B is then evaluated and used within the optimisation studies as a constraint or objective in the form of Eq. (3).

As in the case of the Front wheel brake load case, the inertia relief is used here too for obtaining the load equilibrium of the model. The degrees of freedom of node A, Fig. 4(e), are constrained in order to restrain the rigid body motion.

Although this is a roughly simplified way to simulate a front impact scenario, it is anyway expected that the applied static force will unveil the load paths by increasing the thickness of specific layers as required in order to satisfy the displacement constraint of point B. Other authors have used the same approach for single-objective topology optimisation [20].

2.2.6. Curb strike

This load case allows the effect of the load distributed within the composite body to be considered when the front wheel hits a curb. The force F, Fig. 4(f), is calculated as M 3g, where M is the full vehicle mass and g is the gravitational acceleration. It is assumed that the curb has a height of 100 mm and the wheel radius is 230 mm. The force is then applied in the centre of the wheel represented by the point B, Fig. 4(f), at an angle of 34° from Ox axis, within the xOy plane, and it is transferred to the composite body by the interpolation constraint elements – RBE3 [17], that represent the fork.

The displacement of point B is evaluated and used within the optimisation studies as a constraint or objective in the form of Eq. (3).

3. Optimisation methodology

The proposed optimisation methodology consists of three main steps, Fig. 5.

First, a single-objective *free size* optimisation is performed on the composite body modelled as described at Section 2. Within the second step, the area covered by each layer is redefined according to the obtained distribution of thicknesses from the free size optimisation results. The last step consists of performing a multi-objective *size* optimisation to the redefined patches.

A detailed description of these three steps is given further on.

3.1. Free size optimisation

When referring to composite laminates, the mathematical formulation of the single-objective *free size* optimisation problem may be described as it follows (adapted from [21]):

$$\begin{aligned} &\text{Minimize} \quad f(x) = f(x_{11}, \ldots, x_{ij}) \\ &\text{Subject to} \quad x_{ij}^L \leqslant x_{ij} \leqslant x_{ij}^U, \quad i = 1, \ldots, Nl;\ j = 1, \ldots, Ne \end{aligned}$$

where $f(x)$ is the objective function, x_{ij} represents the thickness of the ith layer of the jth finite element, $g_k(x)$ and g_k^U are the kth constraint response and its upper bound, Nl and Ne represent the number of layers and the number of elements, m is the number of constraints.

The goal at this stage is to identify the load paths through the composite body for the given loading conditions. The initial structure of the parts is considered to be made of six layers all over the body, according to the section illustrated in Fig. 6.

The initial thicknesses of the GF-weave and GF-csm layers, Table 2, have been predicted using Eq. (4):

$$h = \frac{W_f}{\rho_f} + \frac{W_m}{\rho_m}, \tag{4}$$

where W_f and W_m represent the weight of the fibres and of the matrix per unit area; W_f is given in Table 2. W_m is calculated for each as $W_m = (W_f/w_f) - W_f$, where $w_f = \rho_f v_f/(\rho_f v_f + \rho_m v_m)$, v_f represents the fibre volume fraction and it is equal to 0.4 for GF-weave and 0.2 for GF-csm. The matrix volume fraction v_m is equal to $1 - v_f$. ρ_f and ρ_m are the densities of the glass fibres and of the polyester matrix, and they are equal to 2520 kg/m^3 and 1160 kg/m^3 respectively, [22].

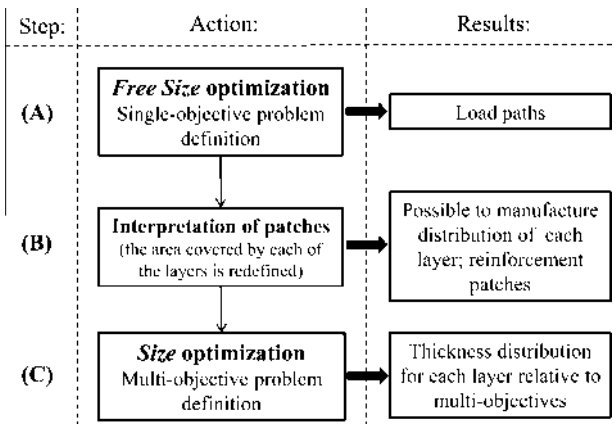

Fig. 5. Optimisation methodology applied on the composite body.

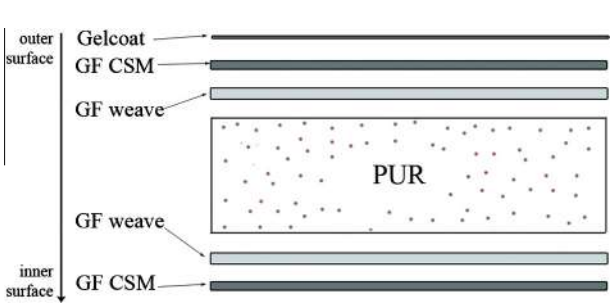

Fig. 6. Section within the composite body structure.

Table 2
Initial thickness and layers' distribution within the composite body.

Layer type	Placement	W_f [g/m^2]	Initial thickness [mm]
Gelcoat	Complete layer	–	0.600
Outer GF-csm	Complete layer	300	0.595
Outer GF-weave	Complete layer	600	0.595
PUR	Complete layer	–	30
Inner GF-weave	Complete layer	600	0.595
Inner GF-csm	Complete layer	300	0.595

Table 3
Design variables within the *free size* optimisation step.

Layer	Thickness [mm]	
	Lower limit	Upper limit
Outer GF-csm	0.2	1.2
Outer GF-weave	0	1.2
PUR	0	30
Inner GF-weave	0	1.2
Inner GF-csm	0.2	1.2

3.1.1. Design variables

Within the *free size* optimisation, the thickness value of the layers shown in Fig. 6 is allowed to vary freely within a predefined interval for each finite element. These thicknesses represent the design variables and their upper and lower limits are shown in Table 3. The thickness of the Gelcoat layer is kept constant.

3.1.2. Constraints

The imposed design constraints within the *free size* optimisation may be interpreted as performance targets that should be met, for each of the considered load cases. The applied constraints are described in Table 4.

The values for the objective functions K_{t3} and K_{b3} are constrained to be at least equal to two times the corresponding values for the 2nd generation in order to force the PUR layer to grow in a more realistic shape instead of a scattered distribution.

3.1.3. Objective

The single-objective is to minimize the mass of the composite body by varying the defined design variables, Table 3, while satisfying the imposed design constraints, Table 4.

3.1.4. Results

The contour plot representing the thickness distribution of the PUR layer, Fig. 7, shows a thickness distribution up to 60 mm around the bucket region, although the upper limit of the corresponding design variable has been set to 30 mm, Table 3. This happens because a T-joint exists around the bucket and therefore the model implies two layers of PUR foam that are concurring within that region.

A feasible solution has been reached within this optimisation step, where the mass has been decreased by 29.9% compared to the 2nd generation, at the same time by satisfying all the constraints defined in Table 4.

Although a theoretical feasible solution was obtained within the free-size optimisation, the resulted thickness distribution of each layer within the composite body is hard to reproduce in reality, especially the layer that represents the core, Fig. 7. For this reason, the interpretation of patches has been considered as a next step.

3.2. Interpretation of patches

The area covered by each layer is interpreted following the free size optimisation results, and redefined in order to reach a shape

Table 4
Constraints applied within the free size optimisation.

Load case	Constraint	Description
Torsion Stiffness	$K_{t3} \geqslant 2K_{t2}$	Torsion Stiffness of the 3rd generation, Eq. (1), should be at least equal to two times the one of the 2nd generation
Bending stiffness	$K_{b3} \geqslant 2K_{b2}$	Bending stiffness of the 3rd generation, Eq. (2), should be at least equal to two times the one of the 2nd generation
Front wheel brake	$\delta_{C3} \leqslant \delta_{C2}$	Displacement of point C, Fig. 4(c) of the 3rd generation should be less than or equal to the one of the 2nd generation
Belt points stiffness	$\delta_{belt\_points\_3} \leqslant \delta_{belt\_points\_2}$	Displacements of belt points, Fig. 4(d) on the 3rd generation should be less than or equal to the ones of the 2nd generation
Front impact	$\delta_{B3} \leqslant \delta_{B2}$	Displacement of point B, Fig. 4(e) of the 3rd generation should be less than or equal to the one of the 2nd generation
Curb strike	$\delta_{B3} \leqslant \delta_{B2}$	Displacement of point B, Fig. 4(f) of the 3rd generation should be less than or equal to the one of the 2nd generation

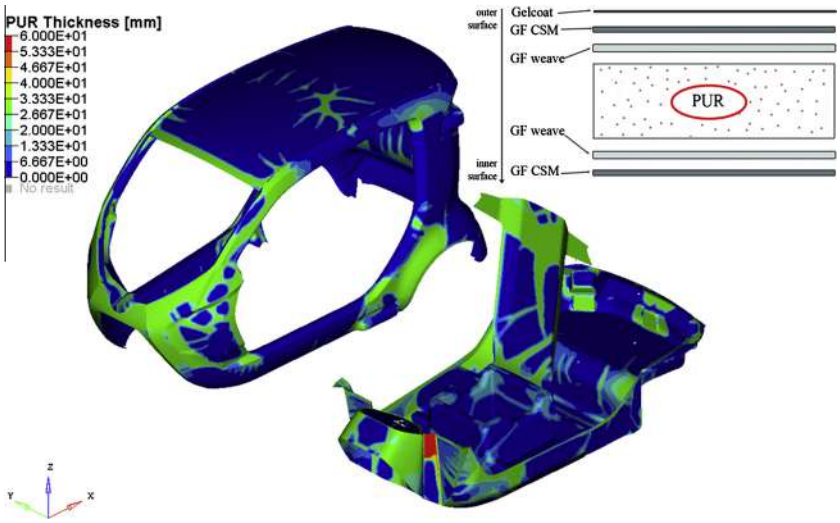

Fig. 7. Thickness distribution of the PUR foam layer.

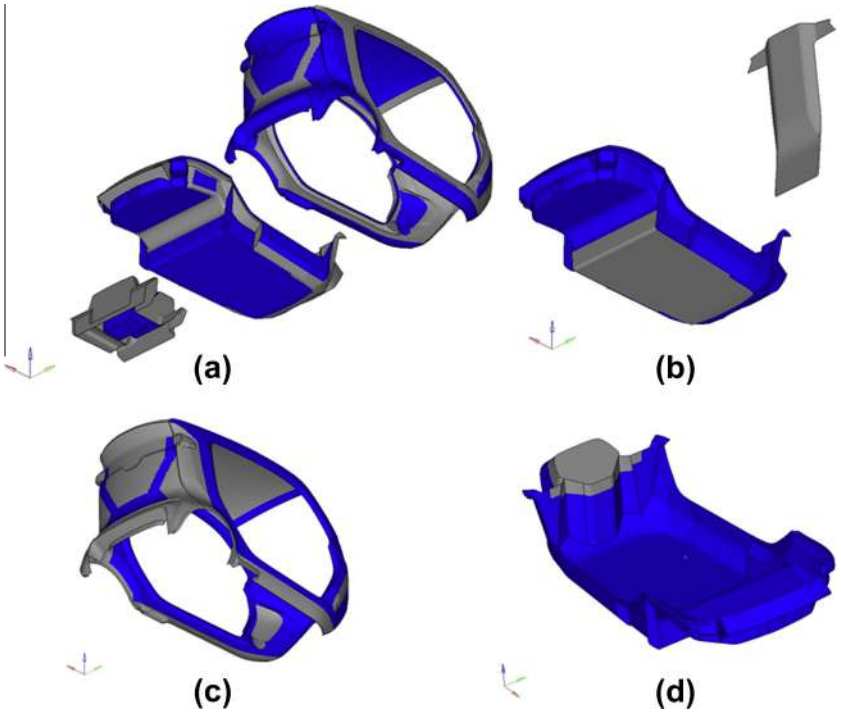

Fig. 8. Interpretation of the layers' distribution within the composite body following the free size results: (a) PUR foam; (b) PVC foam; (c) SORIC honeycomb; and (d) GF weave reinforcement.

Table 5
Objective functions defined within the size optimisation.

Objective	Function	Description
Minimize	Mass of the composite body	Evaluated within the simulation
Minimize	Material Cost	Defined by Eq. (5)
Maximize	Torsion Stiffness	Defined by Eq. (1)
Maximize	Bending Stiffness	Defined by Eq. (2)
Minimize	Headstock displacement	Defined by Eq. (3)
Minimize	Front impact penetration	Defined by Eq. (3)
Minimize	Front wheel centre displacement	Defined by Eq. (3)

that is possible to manufacture. This step requires the assistance of experts on manufacturing technologies of composites.

Fig. 8(a) shows the distribution of the PUR foam within the composite body (gray areas) as it was interpreted based on the information provided by the free size optimisation results, Fig. 7, and by the recommendations coming from manufacturing experts. One of the benefits of using PUR as a core within the composite body is that it may be extruded by using moulds into complex shapes that can better follow the load paths indicated by the analysis.

However, there are regions within the composite body where higher local bending stiffness is required; PVC foam has higher stiffness properties comparing to PUR foam, Table 1, and therefore it may provide a better behaviour. Still, milling the PVC foam into complex shapes may be an expensive process and thus this solution is acceptable only on relatively flat regions within the body. Such areas are shown in Fig. 8(b): the backrest and the bottom area of the floor. The backrest part allows the transfer of loads between floor, sides, seat and roof and therefore its contribution to the global behaviour of the body is important. Also, the bottom area of the floor requires higher bending stiffness due to the loads coming from the road within the connection of the wheels to the body, and from the seat and the backrest.

There are regions within the model where no PUR was required following the considered loading conditions, Fig. 7. However, in order to avoid stability issues [23], a 3 mm SORIC honeycomb [24] is required to be placed where no PUR is located – within the roof and the sides, Fig. 8(c).

Reinforcement patches consisting of glass fibre weaves have been considered within the floor region where the front wheel fork is connected to composite body, Fig. 8(d).

3.3. Size optimisation

The size optimisation is performed by considering multiple objectives. In the context of composite laminates, the mathematical description of the multi-objective *size* optimisation problem may be formulated as it follows:

$$\begin{aligned} &\text{Minimize} \quad F(x_{ij}) = [f_1(x_{ij}), \quad f_2(x_{ij}), \ldots, f_n(x_{ij})]^T \\ &\text{Subject to} \quad x_{ij}^L \leqslant x_{ij} \leqslant x_{ij}^U, \quad i = 1, \ldots, Nl; \quad j = 1, \ldots, Ns \end{aligned}$$

where n is the number of objective functions, x_{ij} represents a vector of design variables; it may be formed by thicknesses and fibre orientation angles for each of the ith layer placed within the jth set of elements, $g_k(x)$ and g_k^U are the kth constraint response and its upper bound, Nl and Ns represent the number of layers and the number of the elements sets the composite body is divided in, m is the number of constraints.

Table 6
Assumptions regarding the costs per kg of the materials used within the composite body.

Material	Cost per kg [SEK/kg]
PVC	500
PUR	200
GF-weave-poly	28
GF-csm	20
SORIC	100
Gelcoat	15

Table 7
Design variables within the *size* optimisation step.

Layer	Placement	Thickness [mm]		
		Lower limit	Initial value	Upper limit
Outer GF-csm	Complete layer	0.2	0.595	1.2
Outer GF-weave - reinforcement	See Fig. 8(d)	0	2.38	2.975
Outer GF-weave	Complete layer	0.2	0.595	1.2
PUR	See Fig. 8(a)	0	30	40
PVC	See Fig. 8(b)	0	15	20
Inner GF-weave	Complete layer	0.2	0.595	1.2
Inner GF-weave - reinforcement	See Fig. 8(d)	0	2.38	2.975
Inner GF-csm	Complete layer	0.2	0.595	1.2

Table 8
Constraints applied within the multi-objective optimisation.

Load case	Constraint	Description
Torsion Stiffness	$K_{t3} \geqslant 0.5K_{t2}$	Torsion Stiffness of the 3rd generation, Eq. (1), should be at least equal to half of the one of the 2nd generation
Bending stiffness	$K_{b3} \geqslant 0.5K_{b2}$	Bending stiffness of the 3rd generation, Eq. (2), should be at least equal to half of the one of the 2nd generation
Failure index	$F \leqslant 0.2$	The failure index F gives the failure condition of the laminate and it is determined using the Tsai–Hill criterion, Eq. (6)

Within the present study, a multi-objective genetic algorithm (MOGA) that is implemented in HyperStudy is used to perform the *size* optimisation by considering multiple objective functions.

3.3.1. Objectives

A number of 7 objectives functions have been defined within the size optimisation stage, Table 5.

The objective function representing the material cost is modelled according to Eq. (5) and considering the assumptions made in Table 6.

$$C = \sum_{i=1}^{n}\sum_{j=1}^{m}(C_{kg} \times A_{ij} \times \rho_{ij} \times T_{ij}) \tag{5}$$

where n is the number of body parts; m, the number of layers within body part; C_{kg}, the material cost per kg; A_{ij}, the area covered by j layer within i part; ρ_{ij}, the material density of j layer within i part; and T_{ij} is the thickness of j layer within i part.

3.3.2. Design variables

The considered design variables represent the thicknesses of the layers redefined in step B (interpretation of patches) and they are shown in Table 7. Because the layers that form the composite laminates are considered to have equal in-plane properties, Table 1, the fibre orientation angle is not included in the optimisation.

According to the defined sections within the body and by considering the number of layers, Table 7, it resulted a total number of 42 variables.

3.3.3. Constraints

Three constraints were considered within this optimisation step, Table 8.

The values for the objective functions K_{t3} and K_{b3} are allowed within this optimisation step to decrease up to half the values of the 2nd generation in order to increase the trade-off space with the conflicting objectives, by adding more solutions. Thus, low performance values for K_{t3} and K_{b3} will allow reaching high performance values for the conflicting objectives, as it will be shown further on.

Tsai–Hill criterion was used in order to predict failure in the composite body assuming equal values for compressive and tensile strength. However, Tsai–Wu failure criterion may be used when different behaviour in compression and tension must be taken into account [25].

Thus, according to Tsai–Hill failure criterion, a value below 1 for the failure index given by Eq. (6) indicates that the stress is within the allowable limits [26]. However, within the optimisation, this failure index is constrained to have a value below or equal to 0.2. This constraint is applied on certain finite elements that were identified as critical within a single run analysis considering the layers shown in Fig. 8 and their initial thickness value shown in Table 7.

$$F = \frac{\sigma_1^2}{X^2} + \frac{\sigma_1\sigma_2}{X^2} + \frac{\sigma_2^2}{Y^2} + \frac{\tau_{12}^2}{S^2} \tag{6}$$

where σ_1 and σ_2 are the in-plane stresses along longitudinal and transverse direction, τ_{12} represents the shear stress, X and Y represent the allowable stress in longitudinal and transverse direction, and S is the allowable shear stress.

3.3.4. Results

The obtained values for the objective functions from the multi-objective size optimisation are graphically presented from Figs. 9–14 and arranged in a tabular form within Table 9, as normalized values to the ones characterizing the 2nd generation of the ZBee; the *Mass* objective is plotted against all the other considered objectives. For the objectives to be minimized, improvements are observed if their normalized value is below 1, while a value above 1 indicates improvements of the objectives to be maximized.

The plots shown, Figs. 9–14, are also divided into four regions (I–IV) in order to clearly show and classify the performance offered by each of the design solutions. The performance is increased for both of the objectives if the solution comes from region I or it is decreased for both of the objectives if the solution comes from region IV. Region II and III contain those solutions where only one of the objectives has an increased performance.

The trade-off between two objectives may be then realized by choosing the solution preferably from those placed within region I, Figs. 9–14, by identifying the Pareto front (red line[1]), and by making the trade-off between the points that define the Pareto front, in terms of the objective importance. However, when it comes to multiple objectives, difficulties with using the Pareto front arise from the fact that the best compromise between two objectives does not necessarily represent the best one between some other two objectives. Therefore, an overall performance of the objectives is needed, that

[1] For interpretation of color in Figs. 9–14, the reader is referred to the web version of this article.

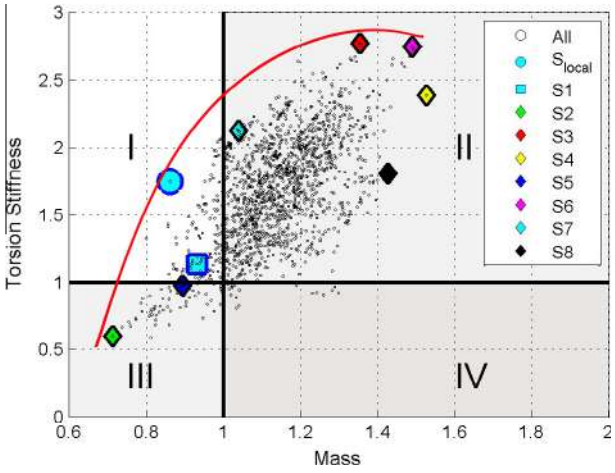

Fig. 9. Mass vs. Torsion Stiffness.

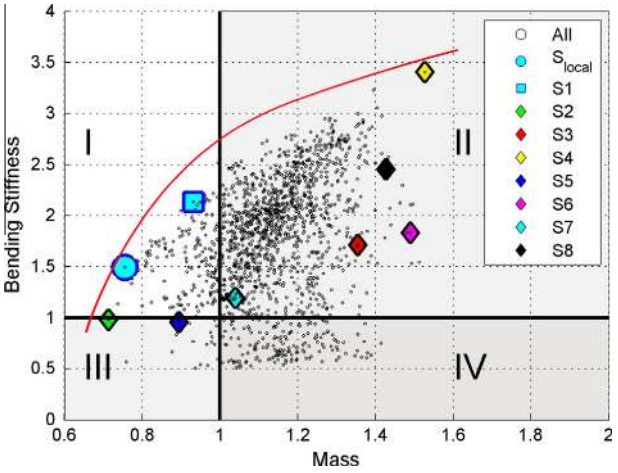

Fig. 10. Mass vs. Bending Stiffness.

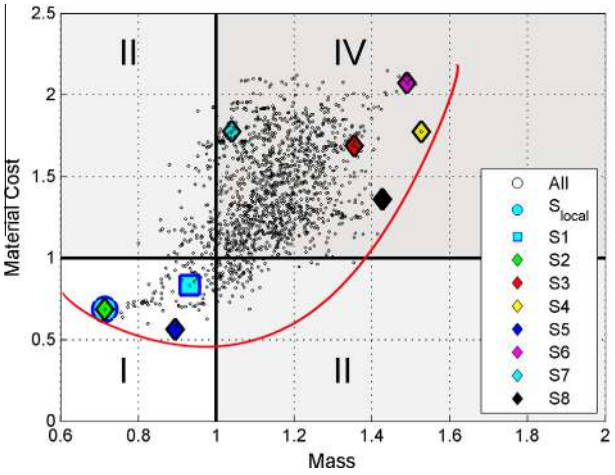

Fig. 11. Mass vs. Material Cost.

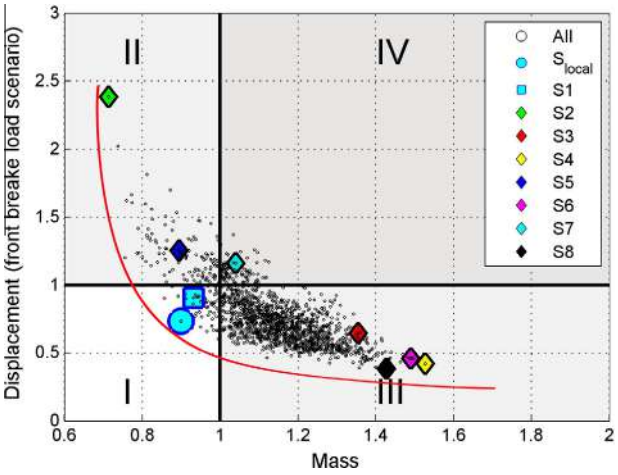

Fig. 12. Mass vs. Displacement of point C from Fig. 4(c).

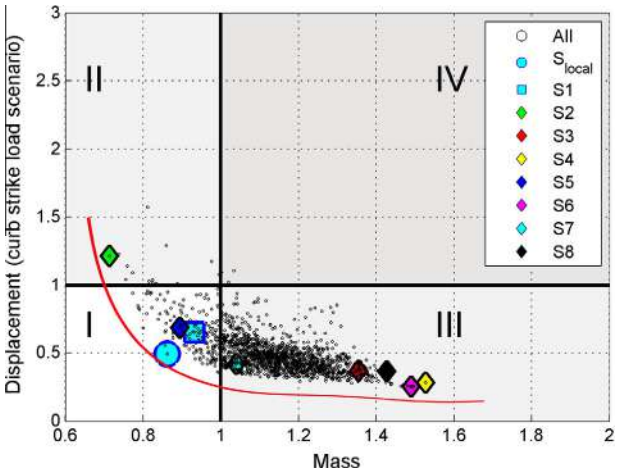

Fig. 13. Mass vs. Displacement of point B from Fig. 4(f).

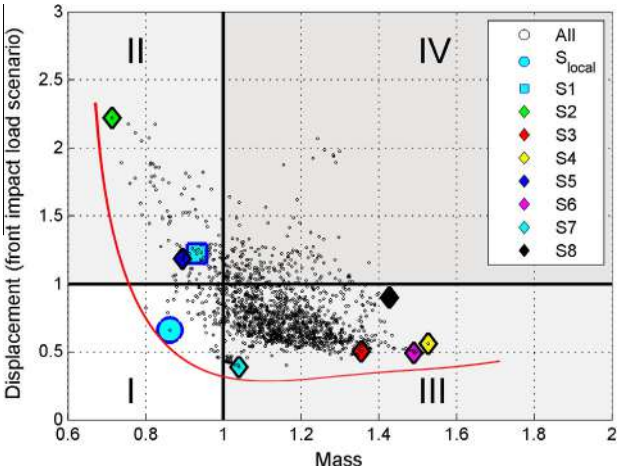

Fig. 14. Mass vs. Displacement of point B from Fig. 4(e).

relates the contribution of each objective when searching the most beneficial overall solution. Such an overall performance function is adapted here from [3], where proportion factors are applied to relate the contribution of the objectives, Eq. (7).

$$P_S = \frac{\sum_{i=1}^{n} p_i \times \bar{O}_i - \sum_{j=1}^{m} p_j \times \bar{O}_j}{100} \tag{7}$$

where P_s represents the overall performance function, $\bar{O}_i$ represents the normalized value of the ith objective to be minimized $i = 1,\ldots,n$;

Table 9
Responses' values and their corresponding proportion factors for different design solutions.

Responses	Selected solutions															
	S1		S2		S3		S4		S5		S6		S7		S8	
	Obj	p%	Obj	p%	Obj	p%	Obj	p%	Obj	p%	Obj	p%	Obj	p%	Obj	p%
Mass	**1.05**	**25**	**0.80**	**94**	1.52	1	1.72	1	1.01	1	1.68	1	1.17	1	1.61	1
Material Cost	0.83	20	0.69	1	1.69	1	1.77	1	**0.56**	**94**	2.07	1	1.78	1	1.36	1
Torsion Stiffness	1.14	−20	0.61	−1	**2.79**	**−94**	2.40	−1	0.98	−1	2.76	1	2.14	1	1.82	1
Bending Stiffness	2.10	−20	0.97	−1	1.68	−1	**3.35**	**−94**	0.94	−1	1.80	1	1.17	1	2.41	1
Displacement (front brake)	0.91	5	2.38	1	0.65	1	0.42	1	1.25	1	0.46	1	1.16	1	**0.38**	**94**
Displacement (front impact)	1.22	5	2.22	1	0.50	1	0.56	1	1.18	1	0.49	1	**0.39**	**94**	0.90	1
Displacement (curb strike)	0.65	5	1.21	1	0.37	1	0.28	1	0.69	1	**0.26**	**94**	0.42	1	0.37	1
Hill Failure Index – F	0.03	–	0.03	–	0.02	–	0.04	–	0.02	–	0.03	–	0.02	–	0.04	–
P_s	−0.010		0.0264		−0.9264		−0.9293		0.0109		0.0057		0.0074		0.0051	

Bold text indicates the objective that dominates each of the considered design solutions.

$\bar{O}_i = \xi(O_{i_{max}} - O_{i_{min}}) + O_{i_{min}}, \xi \in [0,1]$, $\bar{O}_j$ represents the normalized value of the jth objective to be maximized, $j = 1,\ldots,m$; $\bar{O}_j = \xi(O_{j_{max}} - O_{j_{min}}) + O_{j_{min}}, \xi \in [0,1]$, p_i represents the proportion to which the value of the ith objective contributes to the overall performance function P, in percents, p_j represents the proportion to which the value of the jth objective contributes to the overall performance function P, in percents, $\sum_{i=1}^{n} p_i + \sum_{j=1}^{m} p_j = 100\%$.

The minimum value of the overall performance function P_s gives the best compromise between the considered objectives while taking into account the desired value for the proportions p_i and p_j.

Table 9, correlated with the graphical representations shown within Figs. 9–14, shows a selection of eight possible solutions obtained by varying the proportion factor p in such a way to give different contributions of the objective functions to the obtained design solution. Within Table 9, *Obj* columns show the resulted values of the objective functions, for each of the possible solutions.

The solutions denoted S_{local} which are shown only within Figs. 9–14, are obtained by defining equal proportion factors (both having a value of 50%) for each of the plotted objective functions, on each graph. This is a simple verification that the selection method used here gives the best compromise between two selected objectives.

Within the solution denoted *S1*, the contribution of the *Mass* objective function has a proportion of 25%, the *Material Cost* 20%, both *Torsion Stiffness* and *Bending Stiffness* objectives represent 20%, while all the remain objectives only 5% each. This case shows a tied trade-off between objectives, where the *Mass* objective has the most important influence on the solution, followed by *Material Cost*, *Torsion Stiffness* and *Bending Stiffness* with equal importance. The solution *S1* gives improvements for all the objective functions except the one corresponding to the front impact load scenario, Fig. 14. This can be further on fine-tuned as required by redefining the proportion factors p.

The negative sign on the proportion factor applied to *Torsion Stiffness* and *Bending Stiffness* indicates that these objectives are to be maximized. The minimum value obtained for the overall performance function P_s is in this case equal to −0.010, which allows further on the identification of the solution number that gives the best overall performance, Fig. 15.

In the same manner, *S2–S8* represent solutions where different proportion factors are defined, Table 9, in order to look for extreme dominated solutions and also to demonstrate the utility of the proposed selection method. Thus, *S2* represents *Mass* dominated solution ($p = 94\%$). *S3* and *S4* represent *Torsion Stiffness* dominated solution ($p = -94\%$) and *Bending Stiffness* dominated solution ($p = -94\%$) respectively. As it was previously described, the negative sign indicates that the objective that dominates the solution needs to be maximized. Further on, *S5–S8* are solutions dominated by objectives which are to be minimized, all of these objectives having the proportion factor p equal to 94%. The Failure Index

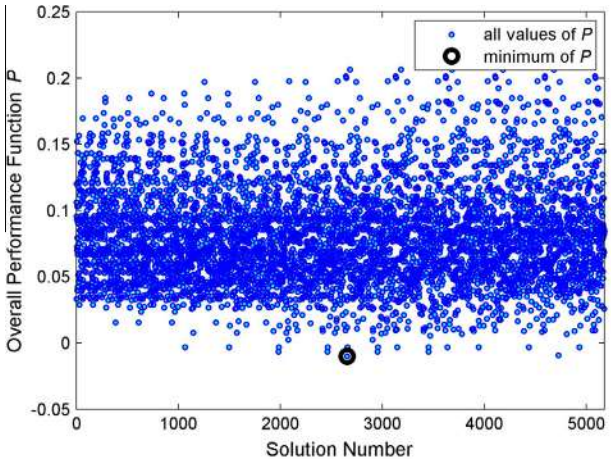

Fig. 15. The complete set of solutions vs. Overall performance function P_s obtained within *S1*.

constraint, Table 8, has been found to be active for seldom design solutions; however, it was not active for the selected solutions *S1–S8*, Table 9.

In order to produce such kind of overall optimum solutions by using the herein proposed method there is a need to first define the proportion factors p. With other words, one should be able to answer the question: what is the proportion with which each objective should contribute to the chosen design solution?

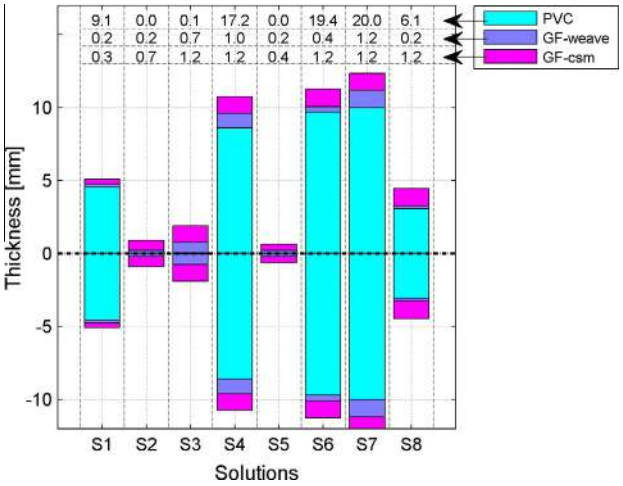

Fig. 16. Values of the layers' thicknesses obtained for the Backrest body part, for the selected design solutions.

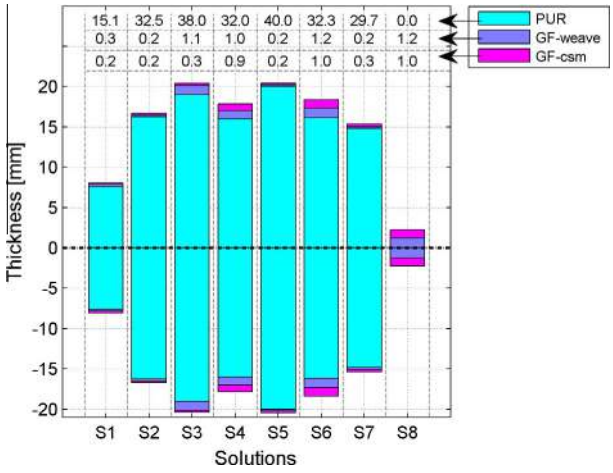

Fig. 17. Values of the layers' thicknesses obtained for the Roof body part, for the selected design solutions.

Each design solution corresponds to a distinct set of values for the design variables (layers' thickness); within the optimisation, the design variables vary between the predefined limits.

The obtained values of the design variables are shown within Figs. 16 and 17, for each of the selected solutions, *S1–S8*, for the Backrest and Roof sections. These plots represent sections within the composite parts, showing the thickness value for each of the layers. The symmetric distribution of the layers comes from the fact that symmetry constraints were considered within the optimisation problem definition.

Similar plots may be generated for each part and used for extracting the thickness that has to be used for each layer, for all body parts, within the manufacturing process.

4. Conclusions

The composite body of a new electric vehicle – ZBee has been optimized with respect to weight, material costs, stiffness and strength, within an optimisation methodology that consists of three main steps. The second step of the described optimisation methodology (the identification of patches), implies knowledge input from manufacturing experts, for which reason a fully automated methodology could not be implemented here. Future research is required for dealing with this issue.

The proposed optimisation methodology allows generating multiple design solutions at its end, from which the most beneficial ones are searched by following the importance allocated for each of the objectives, using the so-called proportion factors.

Acknowledgement

This research has been conducted within the OptFRPBody project funded by *Mistra Innovation* – The foundation for Strategic Environmental Research, Sweden. The funding is gratefully acknowledged. The authors thank all the project partners for their collaboration.

References

[1] Walker M, Smith RE. A technique for the multiobjective optimisation of laminated composite structures using genetic algorithms and finite element analysis. Compos Struct 2003;62:123–8.
[2] Harte AM, McNamara JF, Roddy ID. A multilevel approach to the optimisation of a composite light rail vehicle bodyshell. Compos Struct 2004;63:447–53.
[3] Ashby MF. Multi-objective optimization in material design and selection. Acta Mater 2000;48:359–69.
[4] Marler RT, Arora JS. Survey of multi-objective optimization methods for engineering. Struct Multidiscip Optim 2004;26:369–95.
[5] Badalló P, Trias D, Marín L, Mayugo JA. A comparative study of genetic algorithms for the multi-objective optimization of composite stringers under compression loads. Compos B Eng 2013;47:130–6.
[6] Wang K, Kelly D, Dutton S. Multi-objective optimisation of composite aerospace structures. Compos Struct 2002;57:141–8.
[7] Pohlak M, Majak J, Karjust K, Küttner R. Multi-criteria optimization of large composite parts. Compos Struct 2010;92:2146–52.
[8] Herranen H, Pabut O, Eerme M, Majak J, Pohlak M, Kers J, et al. Design and testing of sandwich structures with different core materials. Mater Sci (Medziagotyra) 2012;18:45–50.
[9] Kers J, Majak J, Goljandin D, Gregor A, Malmstein M, Vilsaar K. Extremes of apparent and tap densities of recovered GFRP filler materials. Compos Struct 2010;92:2097–101.
[10] Kaufmann M, Zenkert D, Wennhage P. Integrated cost/weight optimization of aircraft structures. Struct Multidiscip Optim 2010;41:325–34.
[11] Marler RT, Arora J. The weighted sum method for multi-objective optimization: new insights. Struct Multidiscip Optim 2010;41:853–62.
[12] Lee DS, Morillo C, Bugeda G, Oller S, Onate E. Multilayered composite structure design optimisation using distributed/parallel multi-objective evolutionary algorithms. Compos Struct 2012;94:1087–96.
[13] Almeida FS, Awruch AM. Design optimization of composite laminated structures using genetic algorithms and finite element analysis. Compos Struct 2009;88:443–54.
[14] Fonseca CM, Fleming PJ. Genetic algorithms for multiobjective optimization: formulation, discussion and generalization. In: 5th int conf on genetic algorithms; 1993, p. 416–23.
[15] Konak A, Coit DW, Smith AE. Multi-objective optimization using genetic algorithms: a tutorial. Reliab Eng Syst Saf 2006;91:992–1007.
[16] Deb K. Multi-objective optimisation using evolutionary algorithms: an introduction. In: Wang L, Ng AHC, Deb K, editors. Multi-objective evolutionary optimisation for product design and manufacturing. London: Springer; 2011.
[17] Altair. HyperWorks 11, Online Help and Documentation; 2012.
[18] Christensen J, Bastien C, Blundell M, Gittens A, Tomlin O. Lightweight hybrid electrical vehicle structural topology optimisation investigation focusing on crashworthiness. Int J Vehicle Struct Syst 2011;3:113–22.
[19] Duddeck F. Multidisciplinary optimization of car bodies. Struct Multidiscip Optim 2008;35:375–89.
[20] Cavazzuti M, Baldini A, Bertocchi E, Costi D, Torricelli E, Moruzzi P. High performance automotive chassis design: a topology optimization based approach. Struct Multidiscip Optim 2011;44:45–56.
[21] Zhou M. A comprehensive process for composite design optimisation. In: The 6th Altair CAE technology conference; 2009.
[22] Åström BT. Manufacturing of polymer composites. Nelson Thornes Ltd.; 2002.
[23] Cervellera P, Zhou M, Schram U. Optimization driven design of shell structures under stiffness, strength and stability requirements. In: 6th World congress of structural and multidisciplinary optimization. Rio de Janeiro; 2005.
[24] LANTOR. Data Sheet – Lantor Soric XF Lantor BV2011.
[25] Majak J, Hannus S. Orientational design of anisotropic materials using the HILL and TSAI–WU strength criteria. Mech Compos Mater 2003;39:509–20.
[26] Groenwold AA, Haftka RT. Optimization with non-homogeneous failure criteria like Tsai–Wu for composite laminates. Struct Multidisc Optim 2006;32:183–90.

Provided for non-commercial research and education use.
Not for reproduction, distribution or commercial use.

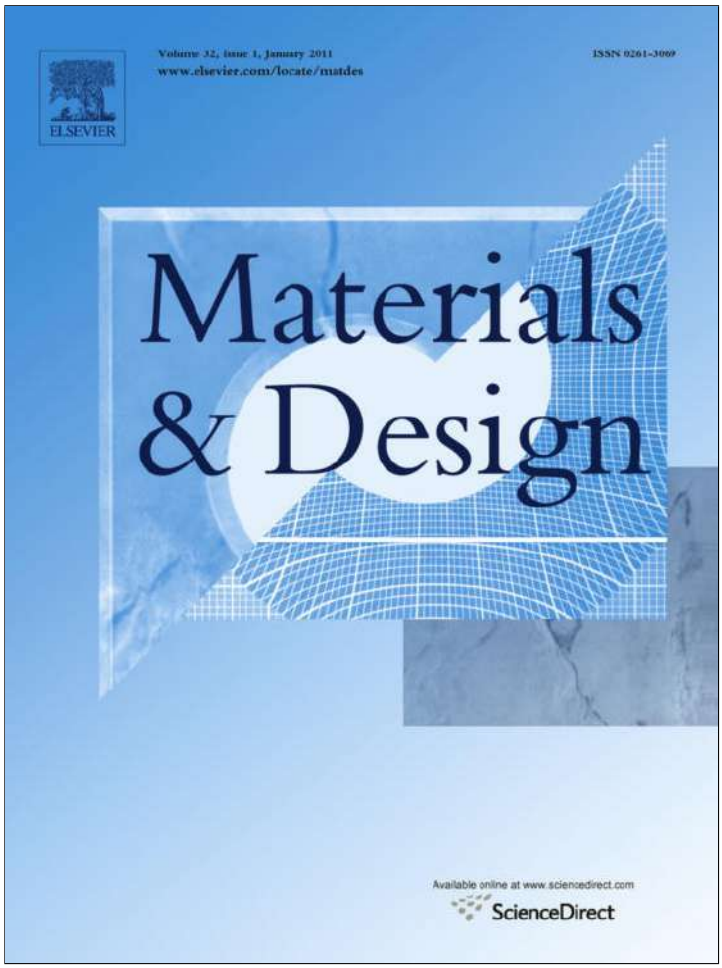

(This is a sample cover image for this issue. The actual cover is not yet available at this time.)

This article appeared in a journal published by Elsevier. The attached copy is furnished to the author for internal non-commercial research and education use, including for instruction at the authors institution and sharing with colleagues.

Other uses, including reproduction and distribution, or selling or licensing copies, or posting to personal, institutional or third party websites are prohibited.

In most cases authors are permitted to post their version of the article (e.g. in Word or Tex form) to their personal website or institutional repository. Authors requiring further information regarding Elsevier's archiving and manuscript policies are encouraged to visit:

http://www.elsevier.com/copyright

Author's personal copy

Materials and Design 36 (2012) 679–686

Contents lists available at SciVerse ScienceDirect

Materials and Design

journal homepage: www.elsevier.com/locate/matdes

Out-of-plane effective shear elastic properties of a novel cellular core for sandwich structures

Marian N. Velea [a], Per Wennhage [b], Simona Lache [a,*]

[a] Department of Product Design, Mechatronics and Environment, Transilvania University of Braşov, 29 Eroilor Blv., 500036 Braşov, Romania
[b] Department of Aeronautical and Vehicle Engineering, Royal Institute of Technology (KTH), SE-100 44 Stockholm, Sweden

ARTICLE INFO

Article history:
Received 5 September 2011
Accepted 8 December 2011
Available online 16 December 2011

Keywords:
B. Sandwich structures
E. Mechanical
F. Elastic behaviour

ABSTRACT

When designing sandwich structures, different types of periodic cellular cores have been considered trying to achieve higher overall bending stiffness and strength to weight ratios as a main objective. Although most of them have proved to offer advantages in certain specific applications, there is a common drawback for all: complexity of the manufacturing process reflected in higher manufacturing costs. This article aims at investigating the out-of-plane shear elastic properties G_{xz} and G_{yz} of a novel cellular core named ExpaAsym, produced by a potentially simple manufacturing method: sheet material expansion. Numerical analyses are carried out in order to study the way in which the out-of-plane shear elastic properties modify in terms of several geometric parameters that define the topology of the structure. The numerical results are validated through experimental tests.

© 2011 Elsevier Ltd. All rights reserved.

1. Introduction

Due to its special characteristics, the sandwich concept applied to different industrial domains allows the designers to increase the performances of their engineering constructions. The most important advantage when using sandwich structures refers to high bending stiffness and strength to weight ratios [1]. Reducing the weight while still having the desired rigidity and strength it is a main concern in different types of vehicle constructions (land, sea, air or space vehicles). This will allow the reduction of the energy consumption necessary for producing the needed mechanical work.

A typical sandwich structure consists of two face sheets with a cellular core placed between them; this assembly is forced to act as a unit by means of a joint method (i.e. adhesive bonding, welding, mechanical fastening) between the face sheets and the core. While for the exterior face sheets the selection process is mainly a matter of the physical and mechanical properties of the material, when choosing the cellular core one must take into consideration also the geometric characteristics that will offer the desired mechanical properties and a low relative density. Thus, different types of periodic cellular topologies have been proposed trying to achieve higher overall bending stiffness and strength to weight ratios. Among these, the most known are the hexagonal honeycombs which are also considered state of the art in aerospace applications. However, one major drawback when using this kind of cellular cores is the high production costs. Another disadvantage may be, in terms of the application, the fact that the cells are closed; in the case of open-cell topologies other functionalities can be implemented in a sandwich assembly, thus allowing using a single sandwich assembly to carry different types of loads: mechanical (static or dynamic), acoustical or thermal loads [2]. Other proposed periodic cellular architectures are lattice-truss structures [3,4], corrugated structures [5,6], egg-box materials [7], hollow tubes cores [8] or folded cores [9]. In order to increase the weight specific strength, Kazemahvazi et al. proposed a novel corrugation concept where the core members consist in a sandwich configuration resulting a hierarchical sandwich structures [10]. Special cellular topologies that possess a zero Poisson's ratio were also developed [11,12]. Although each of these cellular topologies may be successfully used as cores materials in certain applications, there still is a main interest in finding new simple manufacturing methods and new cellular topologies in order to reduce the costs and thus to allow the spread of the sandwich structure use.

The main motivation for proposing a novel type of cellular core concept is to obtain an open-cell structure having a low relative density using a potentially simple manufacturing method.

The purpose of this paper is to numerically evaluate the out-of-plane shear elastic properties G_{xz} and G_{yz} of the novel cellular core and to study how they modify when several geometric parameters that define the topology of the structure are varied. This would facilitate the design of sandwich structures using homogenized models, which is common practice. Experimental tests are conducted in order to validate the numerical results.

* Corresponding author. Tel.: +40 727867447; fax: +40 268 476172.
E-mail addresses: marian.velea@unitbv.ro (M.N. Velea), wennhage@kth.se (P. Wennhage), slache@unitbv.ro (S. Lache).

0261-3069/$ - see front matter © 2011 Elsevier Ltd. All rights reserved.
doi:10.1016/j.matdes.2011.12.017

Author's personal copy

2. Novel cellular core

The novel cellular core named ExpaAsym is proposed as a simpler produced alternative to the already known and used cellular cores for sandwich structures mentioned in Section 1. Its topology is illustrated in Fig. 1 where the notations represent: 1 – the expanded cellular core, 2 – the contact areas with the top exterior face sheet, 3 – the contact areas with the bottom exterior face sheet. G denotes the expansion angle.

ExpaAsym's main advantage is related to the simple manufacturing process that may be shortly described, in relation to Fig. 2, as follows: on a continuous sheet material (zone I) a specific pattern of perforations, numbered 4, and cuts, numbered 5, (zone II) are applied; in order to create the contact areas with the exterior face sheets of the sandwich panel, the edges numbered 2 and 3, resulted after having created the perforations, are bent at an angle equal to the desired expansion angle G (zone III); the mechanical expansion process (zone IV) is realized by applying a displacement U_y in the plane of the sheet material and oriented to a direction perpendicular to the already created transversal cuts and perforations (Y-direction). Due to the stresses that appear in the sheet material and also due to the way in which the transversal cuts are positioned, the material starts to deform progressively in space by local bending and thus resulting in the expanded cellular core.

In order to study its topology, a parameterized unit cell is identified, Fig. 3, where the following geometric parameters have been defined: G – expansion angle, A – internal angle, l – length of the cell wall, c – distance between two transversal cuts, w – width of the unit cell, t – length of the unit cell, h – core height, g – thickness of the sheet material.

The relative density ρ_r of the discussed cellular structure, defined as the density of the cellular material ρ, divided by the density of the solid the cell walls are made of, ρ_s [13] will depend on the geometric parameters defined in Fig. 3, according to Eq. (1):

$$\rho_r = \frac{\rho}{\rho_s} = \frac{g}{l(1+\cos A)\sin A} \tag{1}$$

This topology allows obtaining a very low relative density compared to the already known cellular cores used in sandwich constructions. Its value will decrease while the expansion degree G increases, Fig. 4. However, for each of the studied l/c ratios, Fig. 4, the relative density reaches a minimum when the internal angle A takes a value of 60° and will start to increase slowly when $A > 60°$. It should be noted that for $l = 2c$ and $A = 60°$ the expansion degree $G = 60°$, the cells take the hexagonal shape and the value of the relative density is 0.015.

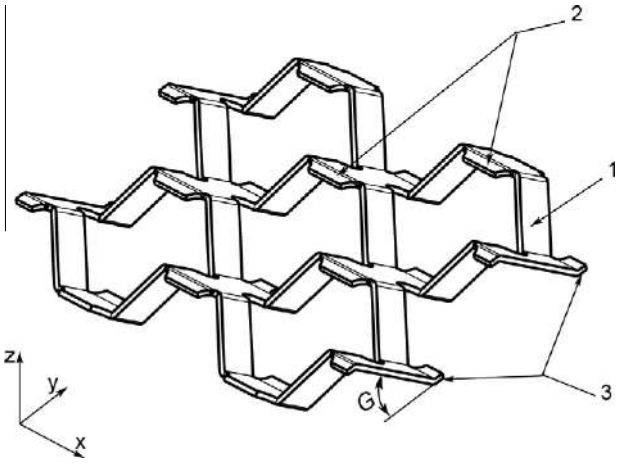

Fig. 1. Novel cellular core.

In addition to a low relative density that may be obtained and to the simplicity of the manufacturing method, the expanded cellular core benefits of the advantages of an open-cell structure. Thus, the intracellular space offers the designer the opportunity to implement additional functionalities to the sandwich structure, as for example thermal and acoustic insulation, by filling it with low density polymeric materials or using the volume for fluid flow.

3. Effective shear elastic properties of cellular structures

Most of the periodic cellular structures used as cores in sandwich assemblies are generally orthotropic meaning that the elastic properties depend on the load direction. From the structural point of view, the main function of a cellular structure used as core in a sandwich assembly is to stabilize the lateral face sheets in order to avoid buckling and wrinkling and to carry shear forces over its thickness. Thus, assuming a perfect joint between the sandwich elements, the shear elastic properties of the core will have an important influence on the stiffness of the sandwich assembly [1]. The novel cellular core analyzed within this paper has the possibility to easily change its shape and properties in the design process, due to its simple manufacturing process, by modifying the expansion angle G and implicitly the internal angle A or by changing the l/c ratio. Thus, it is important to know the way in which the effective shear elastic properties may be modified in the design process by choosing the shape of the structure that responds accordingly to the needs of a specific application.

According to Hooke's law, the shear elastic modulus of a material represents the ratio between the shear stress and the shear strain ($G = \tau/\gamma$). In relation with Fig. 5, the out-of-plane elastic shear modulus G_{xz} is determined using Eq. (2) where Δ_x represents the displacement measured in terms of the applied force F_x and b, l, h, represent the width, the length and the height of the analyzed specimen. This is valid for very small displacements Δ_x so that the height h of the material will remain constant. The same procedure is used for determining the value of G_{yz} by applying the force and measuring the displacement along the Y-direction.

$$G_{xz} = \frac{\tau_{xz}}{\gamma_{xz}} = \frac{F_x h}{\Delta_x b l} \tag{2}$$

4. Numerical analysis

Quasi-static numerical analyses have been performed using the ABAQUS/Standard software in order to evaluate the effective out-of-plane elastic properties G_{xz} and G_{yz}. Twenty geometric cases of the ExpaAsym structure have been considered for this investigation by varying the l/c ratio and the internal angle A. The geometric analyzed cases are obtained by giving to the internal angle A the following values: 30°, 45°, 60°, 75° and 90°, each for $l/c = 0.5$, 1, 1.75, 2. The resulted topology corresponding to the cases when $A = 60°$ are being illustrated in Fig. 6 for all mentioned l/c ratios.

The geometric models have been meshed using linear tetrahedral solid elements of type C3D4 in order to achieve an accurate geometry of the FE model. For each of the analyzed cases, the applied boundary condition may be described, in relation to Fig. 7, as follows: the structure presents a symmetry plane having its normal along X-direction and an asymmetric plane having its normal along Y-direction and thus symmetry conditions have been applied at the end nodes of the unit cell within X-direction and asymmetry conditions at the end nodes within Y-direction; in order to better achieve the experimental test conditions, the amount of adhesive applied for fixing the core within the experiments is taken into consideration in the FE model by applying the displacement Δy on the top set of nodes defined by t_a – adhesive thickness, which

Author's personal copy

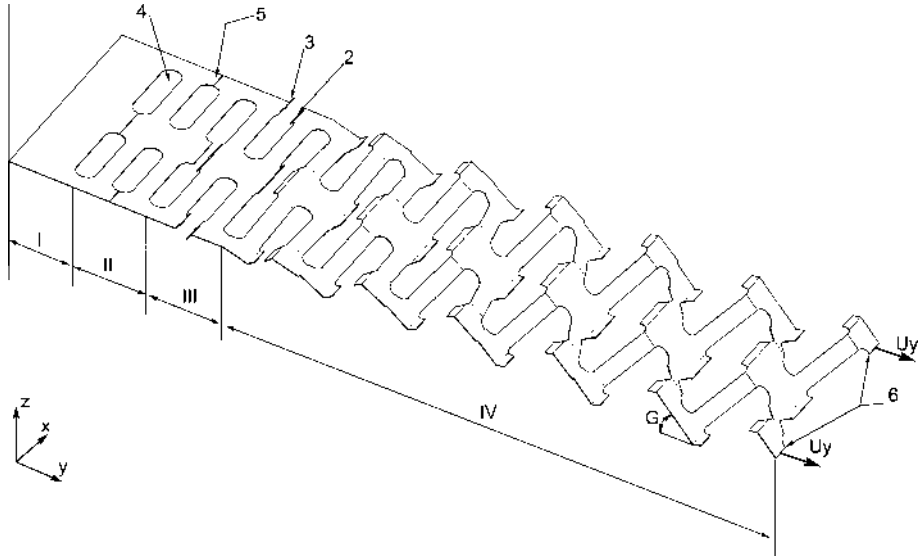

Fig. 2. The manufacturing principle of the proposed novel cellular core: sheet material expansion.

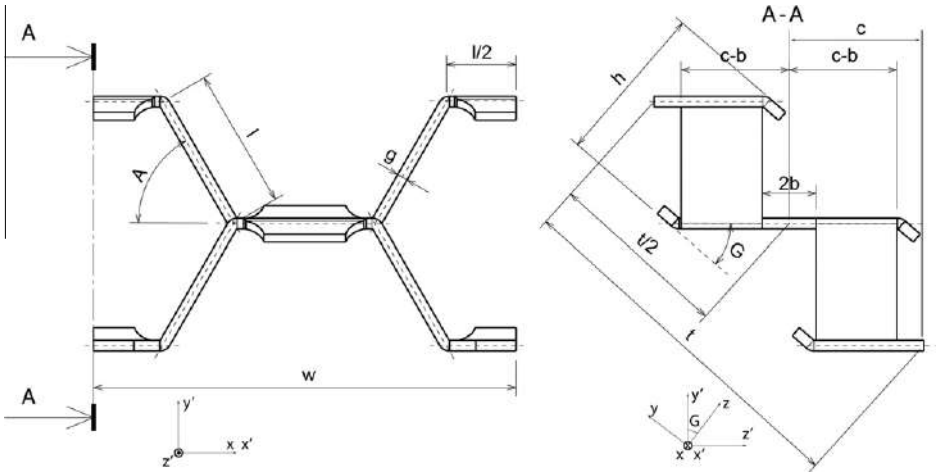

Fig. 3. Parameterized unit cell of the ExpaAsym cellular core.

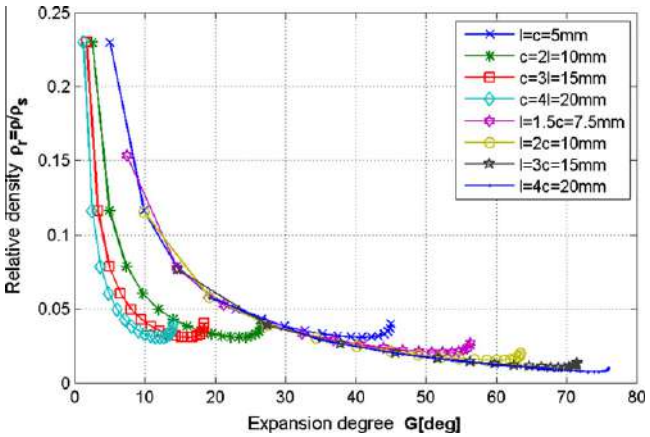

Fig. 4. Relative density of the novel cellular core in terms of the expansion degree G, calculated for $g = 0.2$ mm.

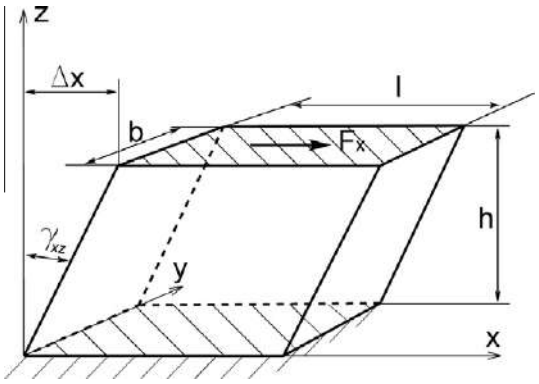

Fig. 5. Pure shear loading.

is approximated to 1 mm based on observations of test specimens; the fixed nodes on the opposite side are treated in the same way.

While the displacement Δ_y, having a value of 0.05 mm, was applied on the top nodes, the reaction force F_y was measured on the fixed bottom nodes. The same procedure was used for the X-direction, and the effective shear modulus was evaluated as previously described.

Author's personal copy

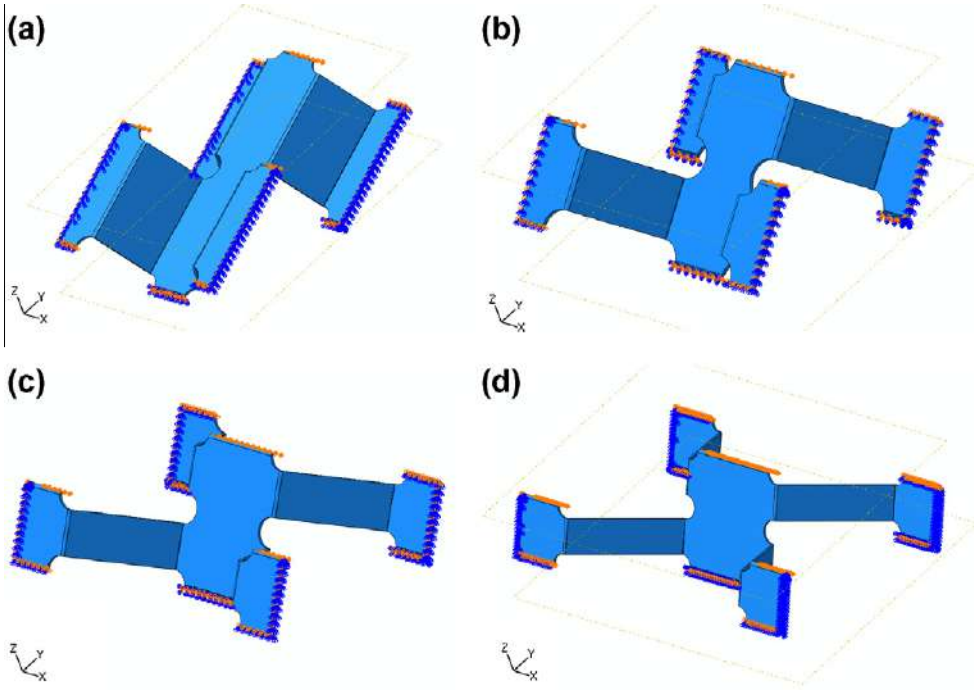

Fig. 6. The FE-representation of the unit cell for $A = 60°$: (a) $2l = c$; $G = 23.41°$; (b) $l = c$; $G = 40.89°$; (c) $l = 1.5c$; $G = 52.41°$; (d) $l = 2c$; $G = 60°$.

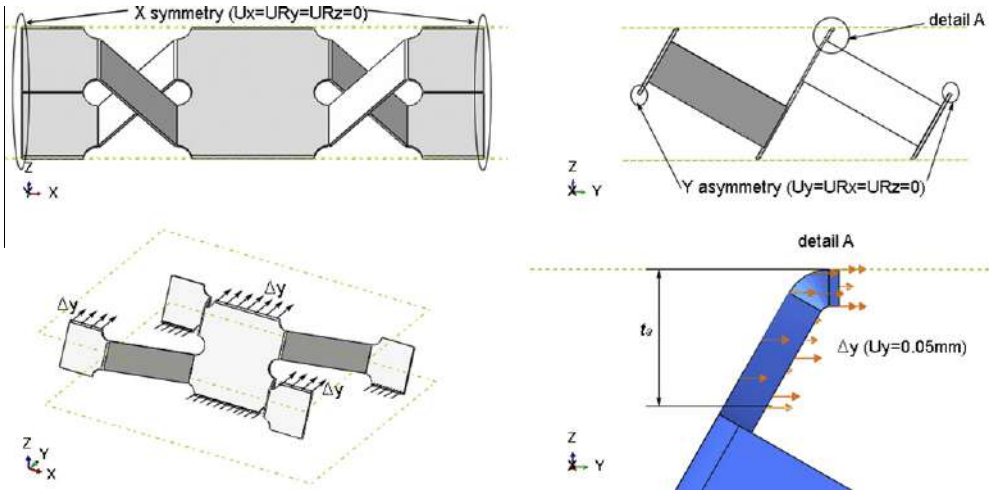

Fig. 7. Boundary conditions defined within the FE model.

The elastic and plastic material properties introduced in the FE model correspond to a 304 type stainless steel: $E_s = 187$ GPa, $v = 0.29$, $\sigma_{yield} = 181.5$ MPa for $\varepsilon_p = 0\%$ and $\sigma_{yield} = 645$ MPa for $\varepsilon_p = 0.4\%$ [14].

5. Experimental analysis

The experimental tests for determining the effective shear elastic properties G_{xz} and G_{yz} have been conducted according to the C273 ASTM standard specifications [15], using an *Instron 4505* testing machine, with a load cell of 100 KN. Within the experiments, a controlled displacement was applied while the reaction force and the relative displacement between the rigid steel blocks Δ_y was measured simultaneously using an *Instron 2630-032* type extensometer, Fig. 8. The applied crosshead speed was 1 mm/min such that the imposed strain rate was about 0.002/s.

Three geometric cases have been taken into consideration, for both X and Y directions, corresponding to three different values for the internal angle A (45°, 60° and 75°) For all this cases l/c ratio remains constant, having a value of 2 ($l = 2c = 10$ mm).

The specimens were manufactured from a 304 type stainless steel sheet material with a thickness of 0.2 mm, Fig. 9. The measured dimensions of the specimens are presented in Table 1, where a comparison is made with the theoretical ones calculated in relation with Figs. 3 and 9, using Eq. (3) for the height h, Eq. (4) for the length t and Eq. (5) for the width w of the core:

$$h = 2(c - b)\sin G \tag{3}$$

$$t = \frac{2c}{\cos G}m \tag{4}$$

$$h = 2l(1 + \cos A)n \tag{5}$$

Author's personal copy

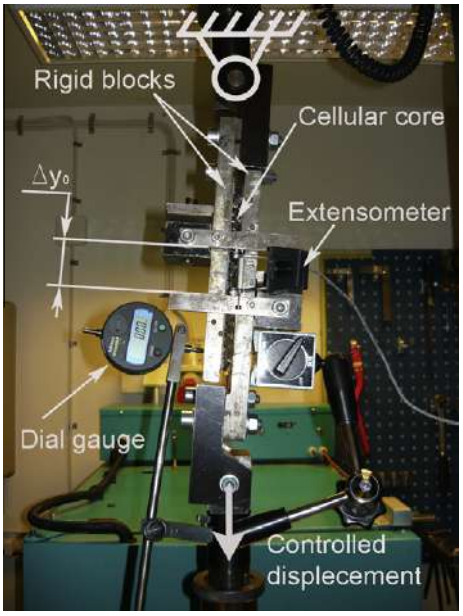

Fig. 8. Experimental setup.

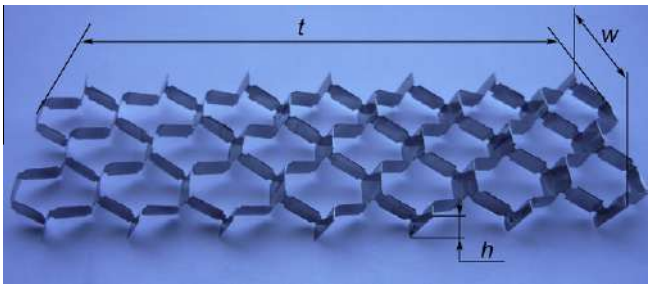

Fig. 9. Specimen dimensions.

where n and m represent the number of cells along X-direction and Y-direction respectively.

The specimens were created having a zero value for the b parameter, Fig. 3, and thus it was considered the same for using Eq. (3).

The core was bonded on two rigid steel blocks using Araldite® 2015, an epoxy based adhesive. It is approximated that the thickness of the glue in the Z direction is 1 mm, Fig. 10.

Based on the registered load–relative displacement data, Figs. 11 and 12, the two out-of-plane effective shear properties G_{xz} and G_{yz} have been obtained using Eq. (2), by introducing the measured values for the reaction force F_x and F_y and for the corresponding relative displacement between the rigid steel blocks Δ_x and Δ_y.

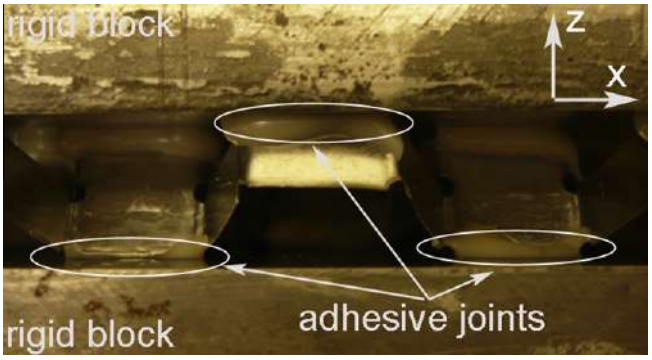

Fig. 10. The joints between the core and the rigid steel blocks.

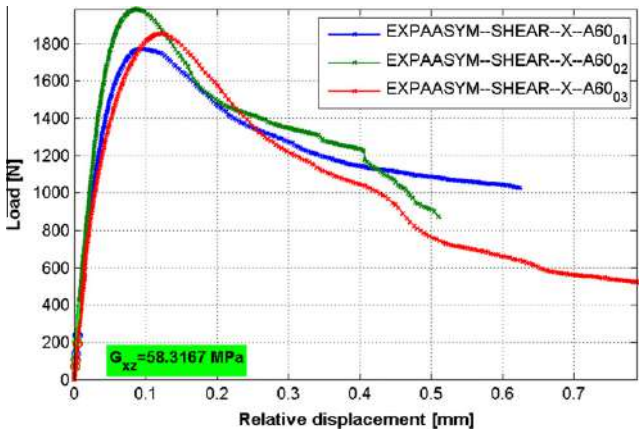

Fig. 11. Load–relative displacement curve for the case when $A = 60°$, $G = 60°$, $l = 2c$, tested along X direction.

During the tests, a digital dial gauge was used in order to observe possible variations of the core height, Fig. 8. It was observed that the height of the core was not affected when the relative displacement was less than 0.2 mm in neither of the tested cases. Thus, the data used for calculations was taken from the very beginning of the tests, at a value of 0.004 mm for the relative displacement, thus assuring a linear elastic deformation of the structure and avoiding core height variations. The dimensions of the specimens used within the calculations correspond to the measured ones, given in Table 1, which represent the average of the three specimens tested for each case and direction.

6. Results and discussion

The values of G_{xz} obtained experimentally show a close correlation with the numerical results, Table 2. The out-of-plane stiffness,

Table 1
Measured specimen's dimensions compared to the theoretical ones.

Direction	Case	Geometric parameters				w (mm)		t (mm)		h (mm)	
		l (mm)	c (mm)	A (°)	G (°)	Theoretical	Measured	Theoretical	Measured	Theoretical	Measured
X	1	10	5	45	57.74	204.84	209	34.64	36	8.16	7.6
	2	10	5	60	60	180	182	40	41	8.66	8.2
	3	10	5	75	62.63	151.08	152	43.5	47	8.88	8.5
Y	1	10	5	45	57.74	68.28	70.5	138.56	145	8.16	8
	2	10	5	60	60	60	60	140	142	8.66	8.4
	3	10	5	75	62.63	50.36	50	152.25	160	8.88	9.1

Author's personal copy

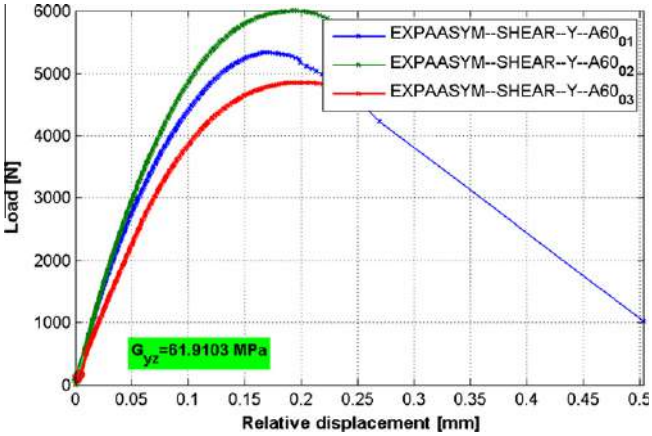

Fig. 12. Load–relative displacement curve for the case when $A = 60°$, $G = 60°$, $l = 2c$, tested along Y direction.

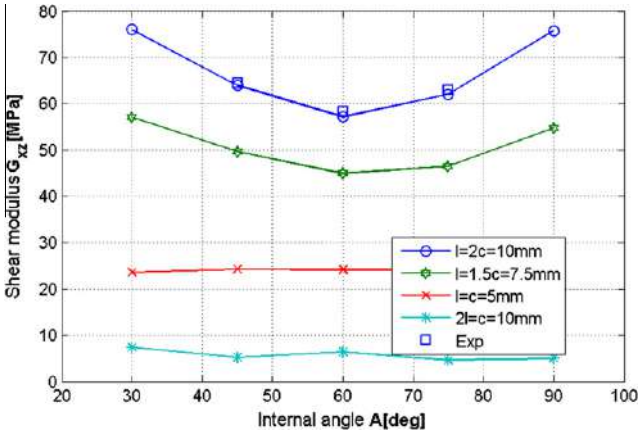

Fig. 13. Shear modulus G_{xz} in terms of the internal angle A.

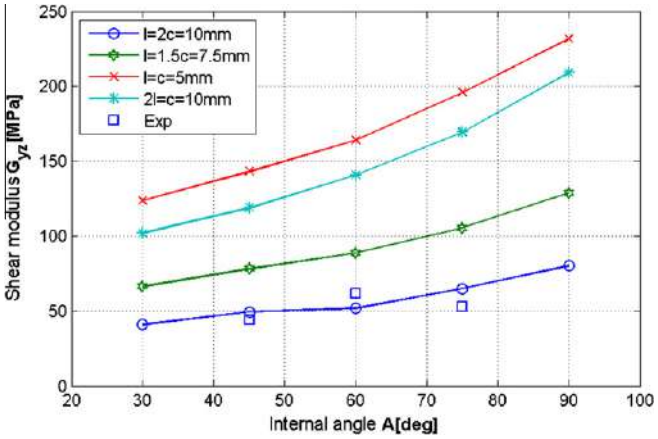

Fig. 14. Shear modulus G_{yz} in terms of the internal angle A.

when loading within XY-plane, will increase while the l/c ratio increases, Fig. 13. While for $l/c > 1$, G_{xz} reaches a minimum value when $A = 60°$ and increases for both $A > 60°$ and $A < 60°$ cases, for $l/c \leqslant 1$ the value of G_{xz} is no more influenced by the variations of the internal angle A, Fig. 13.

Although small differences are observed between the numerical and experimental obtained values for G_{yz}, Table 2, the experimental ones still follow the path given by the numerical model, Fig. 14: for all l/c ratios considered in the numerical analysis, the value of G_{yz} increases at the same time with the internal angle A. Based on the developed numerical model, a higher out-of-plane shear stiffness, when loading within YZ-plane, is obtained when $l/c = 1$.

Within the manufacturing process of the specimens, the amount of glue could not be controlled to be exactly the same for all the contact zones between the core and the rigid steel blocks. Due to the orientation of the cell walls, the variations of the applied adhesive amount did not present an important influence on the shear stiffness for the case when the load is applied within the XZ-plane, Fig 10. However, when the load is applied within YZ-plane, the stiffness may be artificially increased or decreased if a "too much" or "not enough" quantity of glue is applied. This fact could be an explanation for the differences between the obtained numerical and experimental results for the case of G_{yz}. Another reason for this disagreement may be the possible influence of the specimens' size relative to the cells size, on the mechanical response of the whole cellular structure (size effects). Thus, considering the specific distribution of the elements that form the cells of the ExpaAsym structure, an important influence of the size effect is expected to appear in the case when the load is applied within the YZ-plane, Fig. 15. The specimens analyzed within this article are of the same scale and thus it was not possible to clearly observe and quantify the size effects; however, it is expected that smaller cells or an increased number of cells will normally conduct to stronger boundary conditions and implicitly to higher stiffness values. As the influence of size effects on the response of periodic cellular structures have been proved to be important for tetrahedral truss cores [16] or honeycombs [17], further research should be carried out in order to address this issue when analyzing ExpaAsym structure mechanical properties.

Although bonding the core to the rigid steel blocks allowed us to extract the out-of-plane elastic shear stiffness, cracks within the bonded areas appeared immediately after the beginning of the plastic deformations, Fig. 15.

Fig. 16 illustrates the G_{xz} and G_{yz} shear elastic properties obtained using the validated FE model, for different geometric cases. The cases 2 and 3 from Table 2 have been identified to give approximately equal shear stiffness when the load is applied to both XZ and YZ planes.

The specific shear elastic moduli $G_{xz}/G_s/\rho_r$ and $G_{yz}/G_s/\rho_r$ are calculated and represented in Figs. 17 and 18, respectively, in terms of the internal angle A, where $G_s = 86$ GPa represents the value of the shear modulus for the material the cellular structure is made of and ρ_r represents the relative density of the cellular structure, defined by Eq. (1). This representation allows making a comparison

Table 2
Analyzed geometric cases and correlation between the numerical and experimental results.

Case	Geometric parameters				G_{xz} (MPa)		G_{yz} (MPa)	
	l (mm)	c (mm)	A (°)	G (°)	Numerical	Experimental	Numerical	Experimental
1	$10 = 2 \times c$	5	45	57.74	63.98	64.50	49.53	44.17
2	$10 = 2 \times c$	5	60	60	57.22	58.31	51.99	61.91
3	$10 = 2 \times c$	5	75	62.63	62.06	63.04	65.1	53.16

Author's personal copy

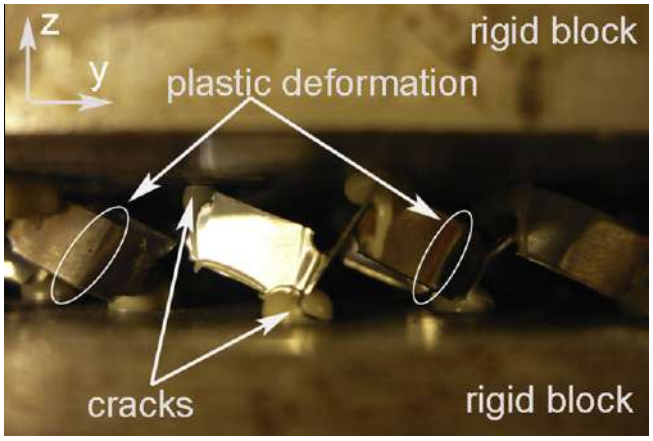

Fig. 15. Cracks and plastic deformation appearance.

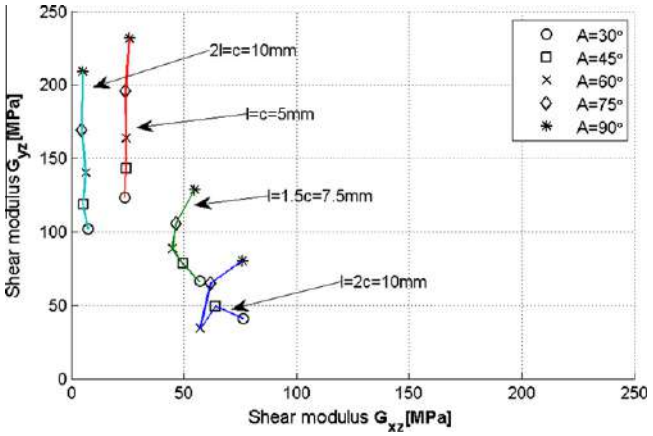

Fig. 16. G_{xz} vs. G_{yz}.

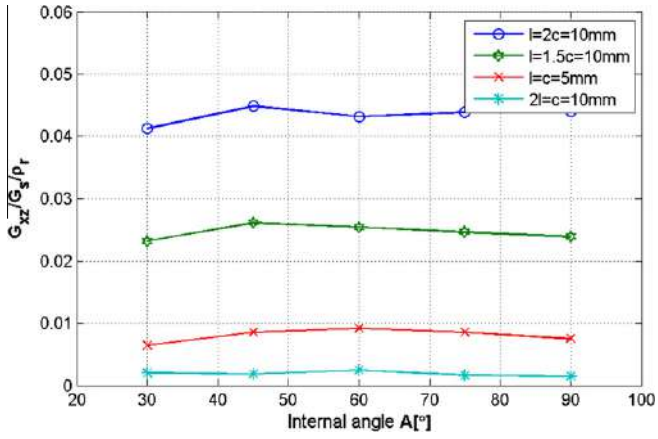

Fig. 17. Specific shear elastic modulus in terms of the internal angle A when loading is applied along X direction.

between the out-of-plane shear elastic behaviour of several types of cores discussed in [12] and the ones of ExpaAsym cellular structure determined here. It is mentioned that, in order to have a consistent comparison of the results, the thickness ratio $\beta = 0.05$, defined in [12] as the ratio between the thickness of the base material and the length of the cell wall, has been omitted within the calculations performed for determining the specific shear elastic moduli of ExpaAsym. Thus, when reading the data from [12] and

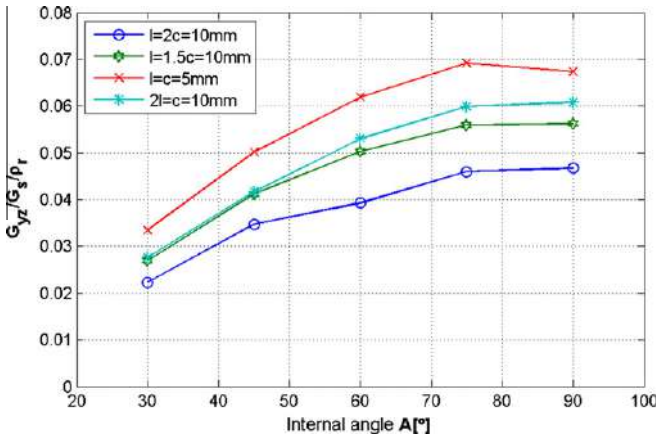

Fig. 18. Specific shear elastic modulus in terms of the internal angle A when loading is applied along Y direction.

comparing them with the ones presented here, the results should be multiplied by 0.05, the value of β. The literature shows that the specific shear elastic moduli $G_{xz}/G_s/\rho_r$ and $G_{yz}/G_s/\rho_r$ vary between 0.0175 and 0.034 for honeycombs, while for the Silicomb structure these properties vary between 0.014 and 0.032 [12]. When looking to the ExpaAsym cellular structure, the specific shear elastic moduli vary between 0.0016 and 0.045 when loading is applied within XZ plane, Fig. 17, while when the shear loads are applied within YZ plane, the values obtained vary between 0.022 and 0.069, Fig. 18. The comparison of these results leads to the conclusion that, for certain geometric configurations, the ExpaAsym cellular structure may give comparable performance in shear to the most known and used cellular cores – the honeycombs. When shear forces are applied within the YZ plane, the specific shear elastic modulus rises its value while the value of the internal angle A increases; the maximum reached value corresponds to the case when $l/c = 1$ and $A = 75°$, Fig. 18. The internal angle presents a small influence on the specific shear elastic modulus for the case when the loads are applied within the XZ plane; however, a value of 2 for the l/c ratio seems to give the most favourable results.

7. Conclusions

A novel cellular topology has been developed to be used as core in sandwich structures. Its main advantages come from a very low relative density and a simple manufacturing process: expanding a single sheet material. Numerical and experimental analyses of the novel cellular core have been carried out in order to determine the effective out-of-plane shear elastic properties G_{xz} and G_{yz}. Good agreement was found between the numerical and experimental results, the FE model being validated. However, due to the way in which the cell walls are distributed in space, an important influence of the joint method used for fixing the core on the rigid blocks (adhesive bonding) has been observed on the results when analyzing G_{yz}. Although the out-of-plane elastic shear properties have been possible to be extracted using the adhesive bonding joint method, further research should be carried out by using other types of joining methods (laser welding or mechanical fastening) for creating sandwich specimens. This will also allow studying the plastic deformations and the collapse of the cellular structure. The influence of the l/c ratio and of the internal angle A on the out-of-plane shear elastic properties has been studied using the validated FE model. An increased out-of-plane shear stiffness may be obtained in the YZ-plane if the internal angle A increases and the maximum rigidity is reached when $l/c = 1$. When looking at the XZ-plane, the out-of-plane shear stiffness increases once the l/c ra-

Author's personal copy

tio increases. It is shown that, for certain specific geometric cases, the ExpaAsym cellular structure may offer out-of-plane shear elastic properties comparable to the ones of the honeycombs cores.

Acknowledgements

This paper is supported by the Sectoral Operational Programme Human Resources Development (SOP HRD), financed from the European Social Fund and by the Romanian Government under Contract No. POSDRU/6/1.5/S/6. The authors express their gratitude for the support of the staff from the laboratory of the Department of Aeronautical and Vehicle Engineering, Royal Institute of Technology – Sweden, where the experiments have been carried out.

References

[1] Zenkert D. The handbook of sandwich construction. EMAS Ltd.; 1997.
[2] Wadley HNG. Multifunctional periodic cellular metals. Philos Trans R Soc A: Math, Phys Eng Sci 2006;364:31–68.
[3] Queheillalt DT, Wadley HNG. Cellular metal lattices with hollow trusses. Acta Mater 2005;53:303–13.
[4] Joo J-H, Kang K-J. Modified metallic octet truss cellular cores for sandwich structures fabricated by an expanded metal forming process. J Sandwich Struct Mater 2010;12:327–49.
[5] Valdevit L, Wei Z, Mercer C, Zok FW, Evans AG. Structural performance of near-optimal sandwich panels with corrugated cores. Int J Solids Struct 2005;43:4888–905.
[6] Leekitwattana M, Boyd SW, Shenoi RA. Evaluation of the transverse shear stiffness of a steel bi-directional corrugated-strip-core sandwich beam. J Construct Steel Res 2011;67:248–54.
[7] Deshpande VS, Fleck NA. Energy absorption of an egg-box material. J Mech Phys Solids 2003;51:187–208.
[8] Xiong J, Ma L, Wu L, Li M, Vaziri A. Mechanical behavior of sandwich panels with hollow al–si tubes core construction. Mater Des 2011;32:592–7.
[9] Fischer S, Heimbs S, Kilchert S, Klaus M, Cluzel C. Sandwich structures with folded core: manufacturing and mechanical behavior. SAMPE EUROPE 30th 2009. p. 256-263.
[10] Kazemahvazi S, Tanner D, Zenkert D. Corrugated all-composite sandwich structures. Part 2: failure mechanisms and experimental programme. Compos Sci Technol 2009;69:920–5.
[11] Olympio KR, Gandhi F. Zero Poisson's ratio cellular honeycombs for flex skins undergoing one-dimensional morphing. J Intell Mater Syst Struct 2010;21:1737–53.
[12] Lira C, Scarpa F, Tai YH, Yates JR. Transverse shear modulus of SILICOMB cellular structures. Compos Sci Technol 2011.
[13] Gibson LJ, Ashby MF. Cellular solids: structure and properties. 2nd ed. Cambridge University Press; 1999.
[14] Chen J, Young B. Stress–strain curves for stainless steel at elevated temperatures. Eng Struct 2006;28:229–39.
[15] ASTM. C 273 Standard Test Method for Shear Properties of Sandwich Core Materials. ASTM C273. West Conshohocken: ASTM International; 2000.
[16] Bouwhuis B, Bele E, Hibbard G. Edge effects in compression testing periodic cellular metal sandwich cores. J Mater Sci 2008;43:3267–73.
[17] Foo CC, Chai GB, Seah LK. Mechanical properties of Nomex material and Nomex honeycomb structure. Compos Struct 2007;80:588–94.

Provided for non-commercial research and education use.
Not for reproduction, distribution or commercial use.

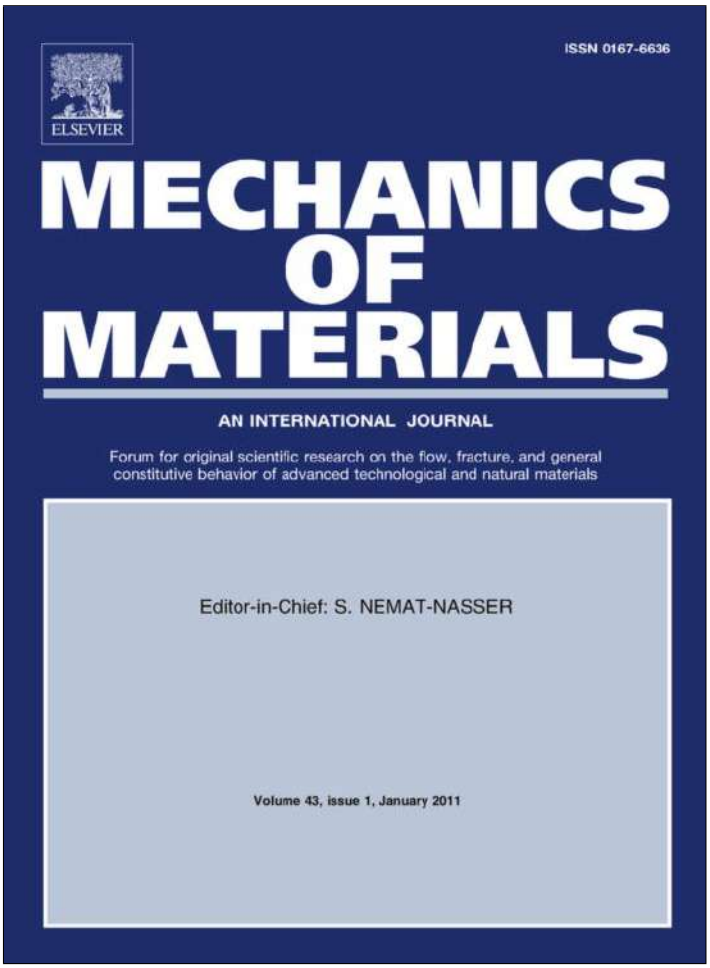

(This is a sample cover image for this issue. The actual cover is not yet available at this time.)

This article appeared in a journal published by Elsevier. The attached copy is furnished to the author for internal non-commercial research and education use, including for instruction at the authors institution and sharing with colleagues.

Other uses, including reproduction and distribution, or selling or licensing copies, or posting to personal, institutional or third party websites are prohibited.

In most cases authors are permitted to post their version of the article (e.g. in Word or Tex form) to their personal website or institutional repository. Authors requiring further information regarding Elsevier's archiving and manuscript policies are encouraged to visit:

http://www.elsevier.com/copyright

Author's personal copy

Mechanics of Materials 43 (2011) 377–388

Contents lists available at ScienceDirect

Mechanics of Materials

journal homepage: www.elsevier.com/locate/mechmat

In-plane effective elastic properties of a novel cellular core for sandwich structures

Marian N. Velea *, Simona Lache

Department of Precision Mechanics and Mechatronics, Transilvania University of Braşov, 29 B-dul Eroilor, 500036 Braşov, Romania

ARTICLE INFO

Article history:
Received 9 April 2010
Received in revised form 27 November 2010
Available online 27 April 2011

Keywords:
Sandwich structure
Cellular core
Elastic properties
Analytical model

ABSTRACT

Within this paper an analytical model is presented for the calculation of the in-plane effective elastic properties E_x and E_y of a novel cellular structure which is proposed to be used as a core in sandwich structures. The proposed cellular core may represent a less expensive and easily to produce alternative to the already known cellular structures used for the construction of sandwich structures. The developed analytical model is validated through experimental tests. The results obtained by analyzing the theoretical model show a good agreement with the tests. The structure topology is studied using a parameterized unit cell and it is shown the way in which the in-plane stiffness depends on the geometric parameters and relative density of the core.

© 2011 Elsevier Ltd. All rights reserved.

1. Introduction

The sandwich concept (Zenkert, 1997) plays an important role in the development of efficient engineering systems, due to the special characteristics and advantages that it may offer. Among these, the most important are: high bending stiffness to weight ratio, high bending strength to weight ratio, high shock and vibration absorption rate, good acoustic and thermal insulation properties. Each of these properties are prone to improvements in terms of the application, in terms of the type of the used cellular structure, the manufacturing methods and the properties of each separate material which is part of the assembly. The word core is often used to describe a cellular structure in sandwich theory, due to its middle position between the exterior face sheets. Many types of periodic cellular cores have been proposed, among which the most known being the honeycombs (Wadley, 2006). Other proposed periodic cellular architectures are lattice truss structures (Sypeck and Wadley, 2004; Wang et al., 2003).

Analytical models for the evaluation of the effective mechanical properties of the cellular structures are of interest, on one hand because they allow to study the way in which these properties are influenced by the structure topology and by different geometric parameters. Models of this kind have been developed for the existing cellular structures, such as honeycombs (Bezazi et al., 2005; Chung and Waas, 2000; Gibson, 1981; Gibson and Ashby, 1999; Gibson et al., 1982; Goswami, 2006) or lattice structures (Deshpande et al., 2001). On the other hand, having determined the effective mechanical properties of a cellular structure, it allows using plate and shell theory in order to analyze the sandwich panel with finite elements, where the core material is replaced with an equivalent single layer material of a homogenized solid. This reduces the effort of detailed modeling and implicitly the computational cost when simulating large structural components made of sandwich material, as for instance a complete fuselage of an airplane (Goswami, 2006; Sue and Whitcomb, 2008).

However, there are still limits in using sandwich structures at a large scale, mainly due to the high price coming from the manufacturing technology of the already known cellular cores. This is the main motivation for the present study initiation: to propose new alternative cellular cores to be used in the construction of sandwich structures,

* Corresponding author. Fax: +40 268 476172.
E-mail addresses: marian.velea@unitbv.ro (M.N. Velea), slache@unitbv.ro (S. Lache).

0167-6636/$ - see front matter © 2011 Elsevier Ltd. All rights reserved.
doi:10.1016/j.mechmat.2011.04.006

Author's personal copy

having geometries that allow the reduction of the base material consumption and less expensive manufacturing technologies.

As a result, a novel periodic cellular structure numbered 2, Fig. 1, is proposed at Transilvania University of Braşov, in order to be used as a core in sandwich structures. This cellular structure is produced by the expansion of a continuous sheet material that previously suffered intercalated cuts and perforations in such a way that a pattern of opened cells is formed. Due to this simple fabrication principle and the reduction of the base material consumption, this type of core may represent a much less expensive and easily to produce alternative to the already known cellular structures.

In addition, the cells are formed by a continuous material, without any bonded areas between the cells, as the honeycombs have. As it will be shown further on, the relative density that may be obtained is very low, compared to the honeycombs, allowing for designing ultra-light sandwich structures. Being a structure with open cells, the intercellular space gives to the designer the opportunity to implement additional functionalities to the sandwich structure.

The proposed cellular structure presents some contact areas, noted 4, which the two exterior face sheets numbered 1 and 3 will be in contact with, Fig. 1. As shown in Fig. 2, the contact area will vary in terms of the cell wall length l and the value of b which represents half of the width of the perforation.

The aim of this paper is to analytically evaluate the in-plane effective elasticity E_x and E_y of the proposed cellular core as a unit. This will further allow studying the influence of the cellular topology on these effective properties. The results obtained through analytical calculations are compared with the ones of experimental tests and thus the proposed analytical model is validated.

2. Cellular structure topology

Fig. 2 depicts a representative unit cell of the structure where g is the thickness of the base material, c is the distance between two transversal cuts and l is the length of the cell wall.

The expansion degree, denoted as G, is the geometrical parameter on which the topology of the proposed cellular core is primarily dependent and it is derived as:

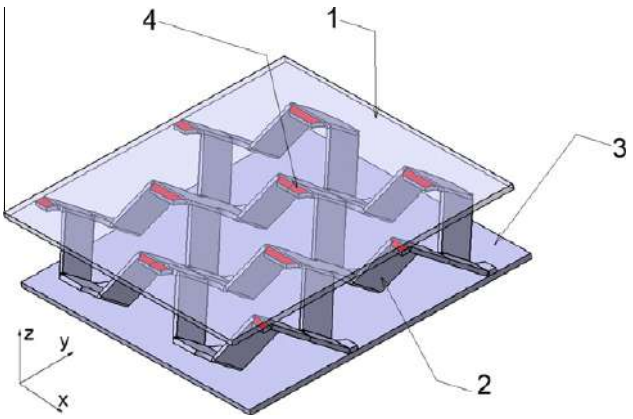

Fig. 1. Sandwich panel consists of two face sheets (1–3) and the proposed cellular core (2).

$$G = \tan^{-1}\left(\frac{l\sin(A)}{c}\right) \tag{1}$$

Fig. 3 shows the way in which the internal angle A modifies in terms of the expansion degree G at different l/c ratios. It should be noted that at a value of 60° for G and when $l = 2c$, the internal angle A will be 60°, which will give a hexagonal shape to the cells. Nevertheless, considering the sandwich effect, in order to obtain a high second moment of inertia, the expansion degree G should be large, resulting in a greater height of the core.

Depending on the internal angle A and expansion degree G, the height h, the length t and the width w of the unit cell can be calculated as:

$$h = 2(c - b)\sin(G) \tag{2}$$

$$t = \frac{2c}{\cos G} \tag{3}$$

$$w = 2l(1 + \cos(A)) \tag{4}$$

An important characteristic of a cellular structure is the relative density ρ_r, defined as the density of the cellular material ρ, divided by the density of the solid the cell walls are made of, ρ_s (Gibson and Ashby, 1999). In the case of the discussed cellular structure, the relative density will depend on the geometric parameters according to Eq. (5):

$$\rho_r = \frac{\rho}{\rho_s} = \frac{g}{(1 + \cos A)l\sin A} \tag{5}$$

Fig. 4 shows the manner in which the relative density varies in terms of the internal angle A, considering also different values for the l/c ratio and a value of 0.2 mm for g, the thickness of the base material. It may be observed that the lowest relative density is obtained when the internal angle A equals 60°.

According to this cellular topology, the consumed base material is significantly diminished when compared to the hexagonal honeycombs. This difference becomes obvious when looking at the quantity of the base material necessary for producing 1 m^2 of cellular material, Fig. 5 for the hexagonal honeycomb and Fig. 6 for the proposed cellular core, considering different values for the l/c ratio and for the internal angle A, the geometrical parameters for the hexagonal honeycomb being identified on a unit cell, Fig. 7.

3. Analytical modeling

The analytical relations for the calculation of the two in-plane Young's moduli, E_x and E_y are derived with the help of Castigliano's second theorem, an approach based on energy methods, used to determine the displacements in linearly elastic structures.

The strain potential energy stored in a volume V of a body in equilibrium conditions can be expressed as (Reddy, 2002):

$$U = \int_V \frac{\sigma\varepsilon}{2} dV + \int_V \frac{\tau\gamma}{2} dV \tag{6}$$

where σ is the normal stress, τ is the shear stress, ε is the normal strain and γ is the shear strain.

Author's personal copy

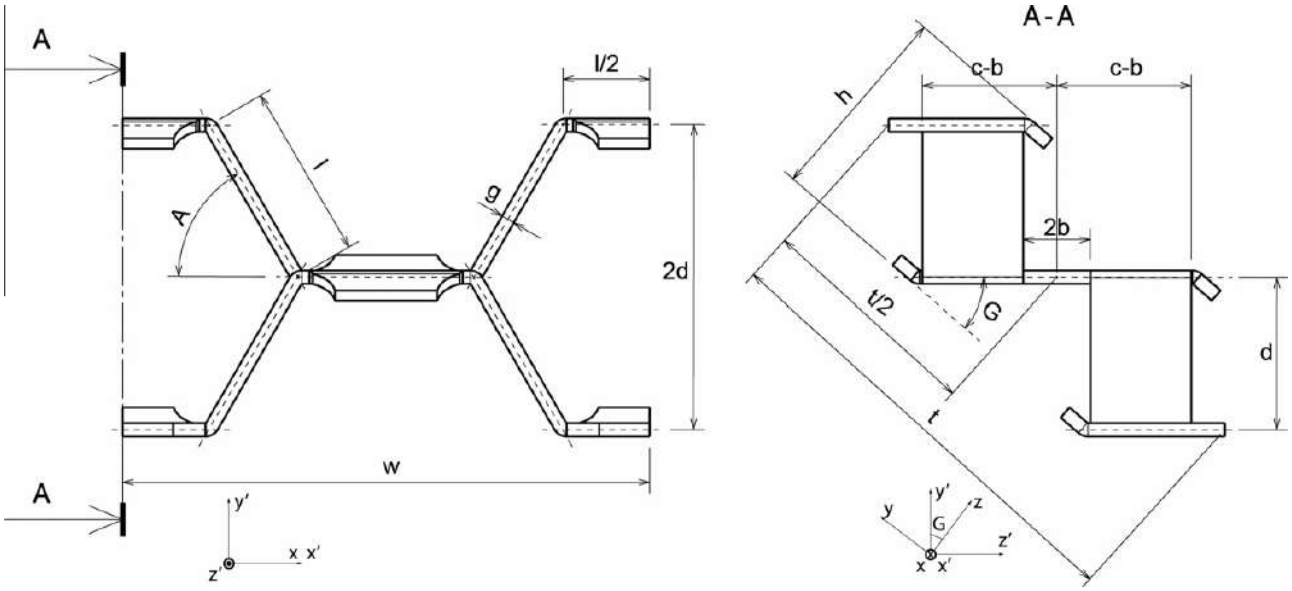

Fig. 2. Representative unit cell of the proposed cellular core.

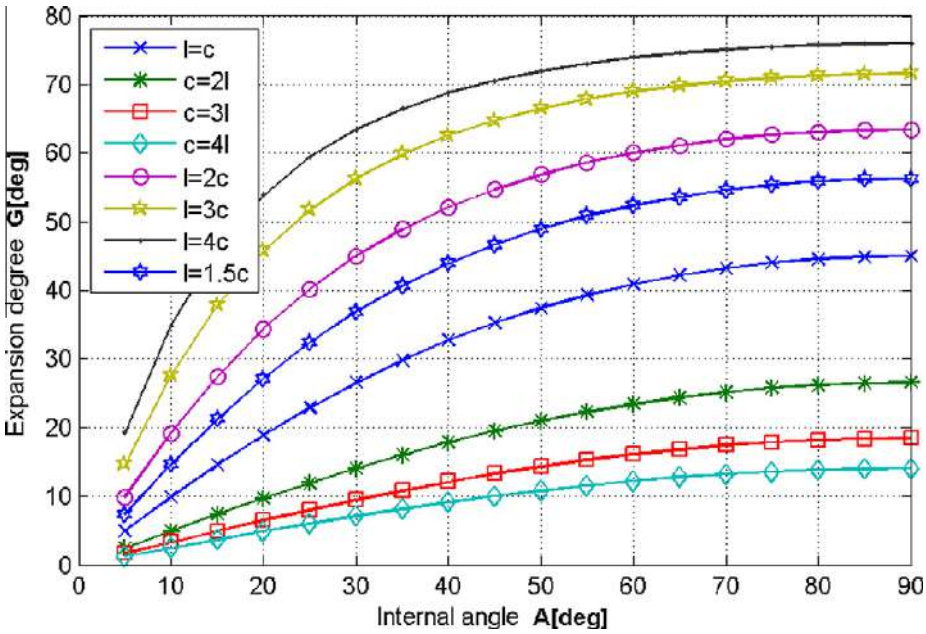

Fig. 3. Relation between the internal angle A and the expansion degree G.

If a loading composed of bending and torsional moments is considered and the material complies with Hooke's law ($\sigma = E\varepsilon$ and $\tau = G\gamma$), the above equation becomes:

$$U = \int_V \frac{\sigma^2}{2E} dV + \int_V \frac{\tau^2}{2G} dV \tag{7}$$

In case of an Euler beam of length l, Eq. (7) may be rewritten as:

$$U = \int_l \frac{M^2}{2EI} dx + \int_l \frac{T^2}{2GJ} dx \tag{8}$$

where M is the bending moment and T is the torsional moment.

According to Castigliano's second theorem, assuming linear elastic deformations, the displacement δ_j of the point of application j of the force F_j in the direction of F_j can be determined as (Reddy, 2002):

$$\delta_j = \frac{\partial U}{\partial F_j} \tag{9}$$

where U is the strain potential energy.

By replacing U from the above relation with Eq. (8), Eq. (9) becomes:

$$\begin{aligned} \partial_j &= \frac{\partial}{\partial F_j} \int_l \frac{M^2}{2EI} dx + \frac{\partial}{\partial F_j} \int_l \frac{T^2}{2GJ} dx \\ &= \frac{1}{EI} \int_l M \frac{\partial M}{\partial F_j} dx + \frac{1}{GJ} \int_l T \frac{\partial T}{\partial F_j} dx \end{aligned} \tag{10}$$

Author's personal copy

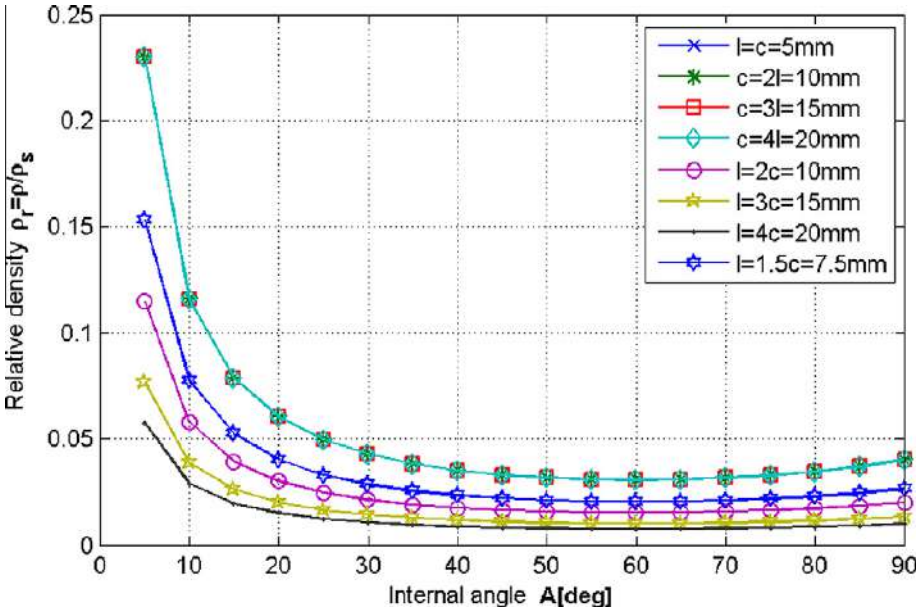

Fig. 4. Relative density in terms of the internal angle *A*.

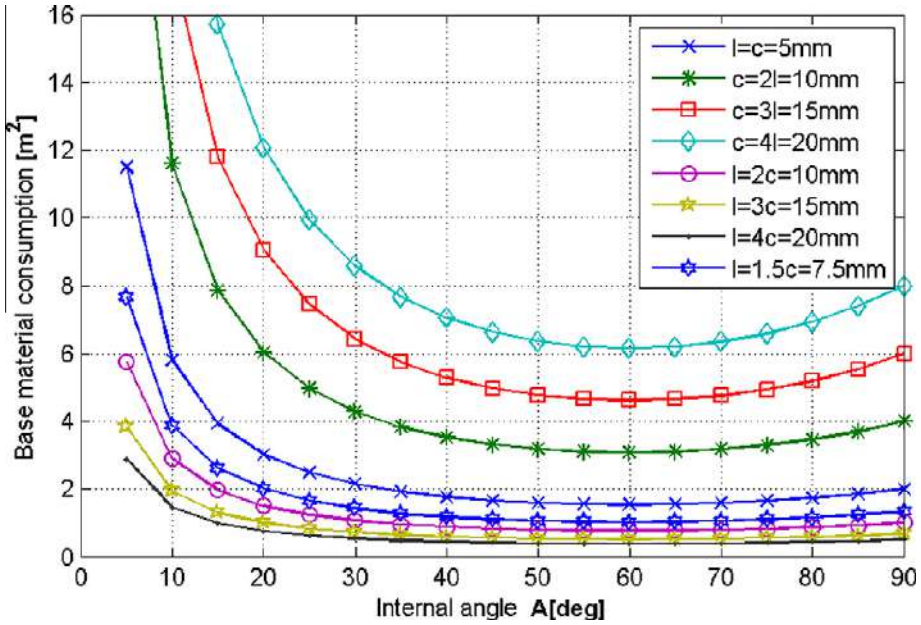

Fig. 5. The consumption of the base material necessary for producing 1 m^2 of hexagonal honeycomb structure.

The displacements determined using the above relation will be further on used to obtain the analytical relations for the calculation of the in-plane effective mechanical properties E_x and E_y.

3.1. Effective Young's modulus E_x

Once the displacements are determined with the help of Eq. (10), the effective strain is calculated as the ratio between the displacement and the initial height of the structure. The effective in-plane stress introduced in the structure will be obtained as the ratio between the applied force and the theoretical area. Finally, the effective elastic moduli of the structure will be determined as the ratio between the calculated stress and strain.

Thus, E_x of the proposed cellular structure is obtained considering a quarter of a unit cell formed by three straight elements, Fig. 8. The loading consists of a force F_x and an end moment $M_{Z'}$ which is related to F_x by $M_{Z'} = (F_x l \sin(A))/2$; both are applied to the node denoted **A**, Fig. 8. On the other side, the node named **D** has been clamped. As long as these three beam elements represent a quarter of the unit cell, the width of the element numbered 3 has the value of *c*, Fig. 2; this means that one edge of the element 3, along its length, is not actually free, as it was assumed in this model. In reality, this beam is linked

Author's personal copy

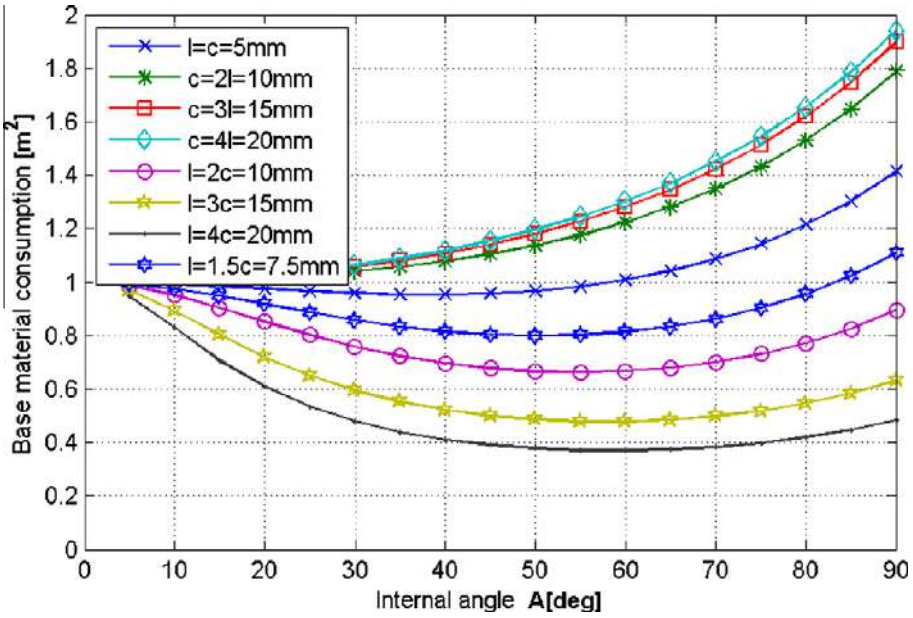

Fig. 6. The consumption of the base material necessary for producing 1 m^2 of the proposed cellular structure.

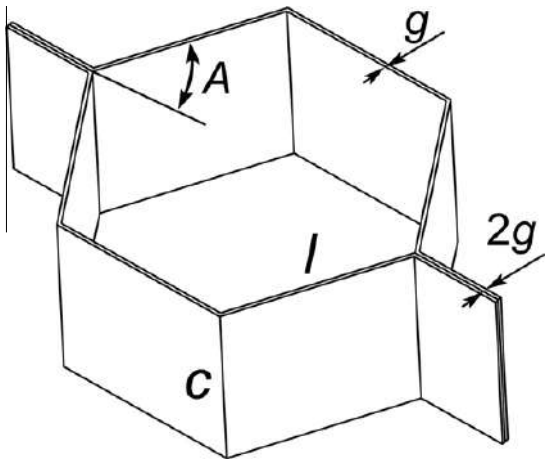

Fig. 7. Unit cell of a hexagonal honeycomb.

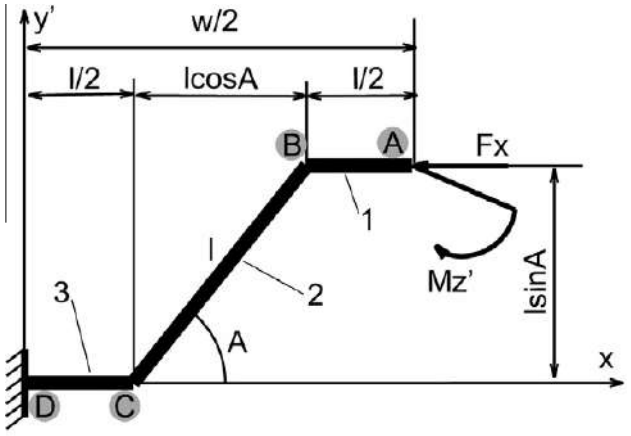

Fig. 8. Loading of a quarter unit cell along X direction.

with a similar one from another quarter of the unit cell. However, it is expected that this assumption will not significantly affect the results as long as the important deformations will be recorded in the elements numbered 1 and 2, Fig. 8.

Following Eq. (10) and considering a pure bending moment loading, the displacement of the point of application of F_x along the X direction is determined as:

$$\delta_x = \sum_{i=1}^{n} \frac{1}{E_i I_{z_i'}} \int_{l_i} M \frac{\partial M_i}{\partial F_x} dx \tag{11}$$

where $i = 1\ldots3$ represents the number of straight elements the analyzed structure is made of.

Table 1 presents the distribution of the moments along the 3 elements, as well as the partial derivative of the moment, in terms of the load applied F_x and the rigidities for each element. Thus, according to Eq. (11), the displacement will be:

$$\delta_x = \frac{F_x l^3 \sin(A)^2}{3 I_{z'} E_s} \tag{12}$$

The effective strain ϵ_x will be therefore calculated as:

$$\epsilon_x = \frac{2\delta_x}{w} = \frac{F_x l^2 \sin(A)^2}{3 E_s l_{z'} (1+\cos(A))} \tag{13}$$

The effective in-plane stress σ_x introduced in the structure is:

$$\sigma_x = \frac{F_x}{2cl\sin(A)} \tag{14}$$

If the elements have a rectangular cross section, with $I_{z'} = cg^3/12$, the effective Young's modulus E_x is further obtained as the ratio between σ_x and ε_x given by Eqs. (13) and (14):

$$E_x = \frac{g^3 E_s (1+\cos(A))}{8 l^3 \sin(A)^3} \tag{15}$$

Author's personal copy

Table 1
Bending moments distribution through the straight elements when applying a force F_x along X-direction.

Interval	Bending moment M	$\frac{\partial M}{\partial F_x}$	Rigidity	Limits of integration
A–B	$-\frac{F_x l \sin(A)}{2}$	$-\frac{l \sin(A)}{2}$	$EI_{z'}$	$0-\frac{l}{2}$
B–C	$-\frac{F_x l \sin(A)}{2}+F_x x \sin(A)$	$-\frac{l \sin(A)}{2}+x \sin(A)$	$EI_{z'}$	$0-l$
C–D	$\frac{F_x l \sin(A)}{2}$	$\frac{l \sin(A)}{2}$	$EI_{z'}$	$0-\frac{l}{2}$

3.2. Effective Young's modulus E_y

E_y of the proposed cellular structure is obtained through almost the same procedure as E_x, but when taking into consideration the tri-dimensional distribution of the structure, Fig. 9, for the calculation of the displacement δ_y, the problem is reduced to two bi-dimensional loading cases, Fig. 10(a) and (b), and respectively to the calculation of two displacements $\delta_{y'}$ and $\delta_{z'}$. The displacement δ_y will be therefore determined using Eq. (16):

$$\delta_y = \sqrt{\delta_{y'}^2 + \delta_{z'}^2} \tag{16}$$

In the first case, Fig. 10(a), the loading consists of a force $F_{y'}$ and an end moment $M_{z'}$ which is related to $F_{y'}$ by $M_{z'} = (F_{y'} l(\cos(A)+1))/2$; both are applied to the node denoted **A**. In the same way as described at Section 3.1, the node named **D** has been clamped and it was also assumed that the element numbered 3 has free edges over its length. Following Eq. (10) and considering a pure bending moment loading, the displacement of point of the application of $F_{y'}$ along Y' direction is determined as:

$$\delta_{y'} = \sum_{i=1}^{n} \frac{1}{E_i I_{z'_i}} \int_{l_i} M_i \frac{\partial M_i}{\partial F_{y'}} dx \tag{17}$$

where i is the number of the straight elements the analyzed structure is made of.

Considering Table 2 and Eq. (17), the displacement $\delta_{y'}$ is obtained as:

$$\delta_{y'} = \frac{F_{y'} l^3 (3 + 3\cos(A) + 2\cos(2A))}{12 I_{z'} E_s} \tag{18}$$

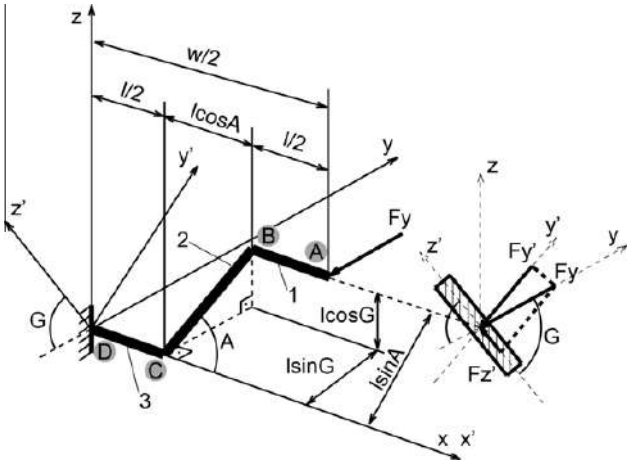

Fig. 9. Loading of a quarter unit cell along Y direction.

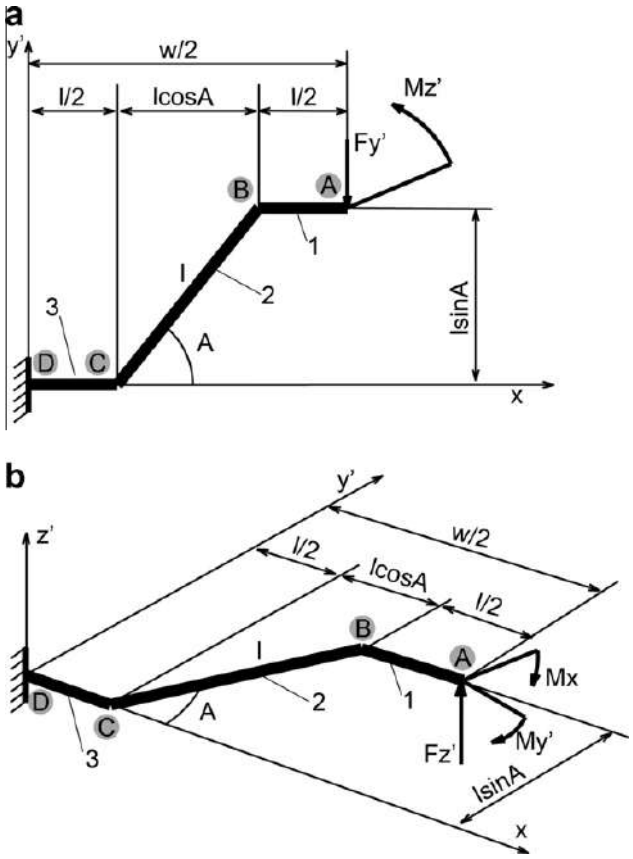

Fig. 10. Loading cases for the calculation of E_y: (a) loading along y', (b) loading along z'.

In the second case, Fig. 10(b), the loading consists of a force $F_{z'}$, an end bending moment $M_{y'}$ which is related to $F_{z'}$ by $M_{y'} = (F_{z'} l(1+\cos(A)))/2$ and an end torsional moment $T = M_x$ which is related to $F_{z'}$ by $M_x = (F_{z'} l \sin(A))/2$. Both force and moments were applied to node **A**. Following Eq. (10) and considering both bending and torsional moment deformations, the displacement of point of the application of $F_{z'}$ along Z' direction is determined as:

$$\delta_{z'} = \sum_{i=1}^{n} \frac{1}{E_i I_{y'_i}} \int_{l_i} M_i \frac{\partial M_i}{\partial F_{z'}} dx + \sum_{i=1}^{n} \frac{1}{G_i J_i} \int_{l_i} T_i \frac{\partial T_i}{\partial F_{z'}} dx \tag{19}$$

where i is the number of the straight beams the analyzed structure is made of.

Considering Table 3 and Eq. (19), the displacement $\delta_{z'}$ is obtained as:

$$\delta_{z'} = \frac{F_{z'} l^3 (6 I_{y'} \sin(A)^2 E_s + 4J(3 + 3\cos(A) + 2\cos(2A)) G_s))}{48 J I_{y'} E_s G_s} \tag{20}$$

Author's personal copy

Table 2
Bending moments distribution through the straight elements when applying a force $F_{y'}$ along Y'-direction.

Interval	Bending moment M	$\frac{\partial M}{\partial F_y}$	Rigidity	Limits of integration
A–B	$\frac{F_{y'}l(\cos(A)+1)}{2} - F_{y'}x$	$\frac{l\cos(A)+1}{2} - x$	$EI_{z'}$	$0 - \frac{l}{2}$
B–C	$\frac{F_{y'}l(\cos(A)+1)}{2} - F_{y'}\frac{l}{2} - F_{y'}x\cos(A)$	$\frac{l\cos(A)+1}{2} - \frac{l}{2} - x\cos(A)$	$EI_{z'}$	$0 - l$
C–D	$\frac{F_{y'}l(\cos(A)+1)}{2} - F_{y'}\frac{l}{2} - F_{y}l\cos(A) - F_{y'}x$	$\frac{l\cos(A)+1}{2} - \frac{l}{2} - l\cos(A) - x$	$EI_{z'}$	$0 - \frac{l}{2}$

Table 3
Bending and torsion moments distribution through the straight elements when applying a force $F_{z'}$ along Z'-direction.

Interval	Bending moment M, torsional moment T	$\frac{\partial M}{\partial F_{z'}}, \frac{\partial T}{\partial F_{z'}}$	Rigidity	Limits of integration
A – B	$M = -\frac{F_{z'}l(\cos(A)+1)}{2} + F_{z'}x$	$\frac{\partial M}{\partial F_{z'}} = -\frac{l(\cos(A)+1)}{2} + x$	$EI_{y'}$	$0 - \frac{l}{2}$
B – C	$M = -\frac{F_{z'}l(\cos(A)+1)}{2} + F_{z'}\frac{l}{2} + F_{z'}x\cos(A)$	$\frac{\partial M}{\partial F_{z'}} = -\frac{l\cos(A)+1)}{2} + \frac{l}{2} + x\cos(A)$	$EI_{y'}$	$0 - l$
C – D	$M = -\frac{F_{z'}(l\cos(A)+1)}{2} + F_{z'}\frac{l}{2} + F_{z'}l\cos(A) + F_{z'}x$	$\frac{\partial M}{\partial F_{z'}} = -\frac{l\cos(A)+1)}{2} + \frac{l}{2} + l\cos(A) + x$	$EI_{y'}$	$0 - \frac{l}{2}$
	$T = -F_{z'}l\sin(A) + \frac{F_{z'}l\sin(A)}{2}$	$\frac{\partial T}{\partial F_{z'}} = -l\sin(A) + \frac{l\sin(A)}{2}$	GJ	

The displacement δ_y is therefore obtained by substituting Eqs. (18) and (20) in Eq. (16):

$$\delta_y = \frac{F_y l^3}{24E_s}\sqrt{\frac{4(3+3\cos(A)+2\cos(2A))^2\sin(G)^2}{l_{z'}^2} + \frac{\cos(G)^2(3I_{y'}\sin(A)^2E_s + 2J(3+3\cos(A)+2\cos(2A))G_s)^2}{J^2I_{y'}^2G_s^2}} \tag{21}$$

The effective strain ϵ_y is further obtained as:

$$\epsilon_y = \frac{\delta_y}{l\sin(G) + c\cos(G)} \tag{22}$$

The effective stress σ_y introduced in the structure is given by Eq. (23):

$$\sigma_y = \frac{2F_y}{wl\cos(G)} = \frac{F_y}{l^2\cos(G)(1+\cos(A))} \tag{23}$$

Finally, considering the elements having a rectangular cross section, with $I_{z'} = cg^3/12$, $I_{y'} = gc^3/12$, and $J = cg(c^2+g^2)/12$, the effective Young's modulus E_y is further obtained as the ratio between σ_y and ε_y given by Eqs. (23) and (22):

$$E_y = \frac{2E_sc^3g^3(c + l\tan(G))}{l^5(1+cos(A))\sqrt{4c^4(3+3\cos(A)+2\cos(2A))^2 \times \sin(G)^2 + \frac{g^4\cos(G)^2(3c^2\sin(A)^2E_s + 2(c^2+g^2)(3+3\cos(A)+2\cos(2A))G_s)^2}{(c^2+g^2)^2G_s^2}}} \tag{24}$$

4. Experimental analysis

In order to verify the above derived analytical expressions, experimental compression tests have been carried out on an *LFPlus* testing machine, produced by Lloyd Instruments, with a load cell of 1KN. At the beginning of the analysis, three geometric cases have been taken into consideration corresponding to cases 1, 3 and 5 from Table 4. The corresponding dimensions of the specimens are: $74.6 \times 28.2 \times 5.6$ mm – for case 1, $60 \times 40 \times 6.9$ mm – for case 3 and $40.5 \times 44.7 \times 7.1$ mm – for case 5. These dimensions may be also checked using Eq. (2)–(4), considering two cells in both X and Y directions. Later on, two additional geometric cases (2 and 4 from Table 4) have been included, because unexpected results have been obtained when determining the value of E_y for the case 1. The structure base material is a 304 type stainless steel with $E_s = 2.01 \times 10^5$ MPa. The applied crosshead speed has been of 5 mm/min. In order to ensure a uniform distribution of the load over the entire loading surface of the specimen, the load has been applied through a spherical bearing block. In addition, in order to ensure that the displacement of the crosshead is applied exactly along the X direction and respectively Y direction of the cellular structure, a right angle has been used to orient de specimen. A very small preload has been applied in order to retain the correct orientation of the specimens. The position of the specimens prepared for the tests is illustrated in Fig. 11.

The two in-plane effective Young's moduli E_x and E_y have been determined as the ratio between the measured

Author's personal copy

Table 4
Analytical and experimental results for the case when $E_s = 2.01 \times 10^5$ MPa, $g = 0.2$ mm.

Case	Geometric parameters				E_x (MPa)		E_y (MPa)	
	l (mm)	c (mm)	A (°)	G (°)	Analytical	Experimental	Analytical	Experimental
1	$10 = 2 \times c$	5	30	45	3.001	2.115	0.128	0.331
2	$10 = 2 \times c$	5	45	57.74	–	–	0.216	0.236
3	$10 = 2 \times c$	5	60	60	0.464	0.477	0.395	0.389
4	$10 = 2 \times c$	5	75	62.63	–	–	0.855	0.885
5	$10 = 2 \times c$	5	90	63.43	0.201	0.203	2.247	2.395

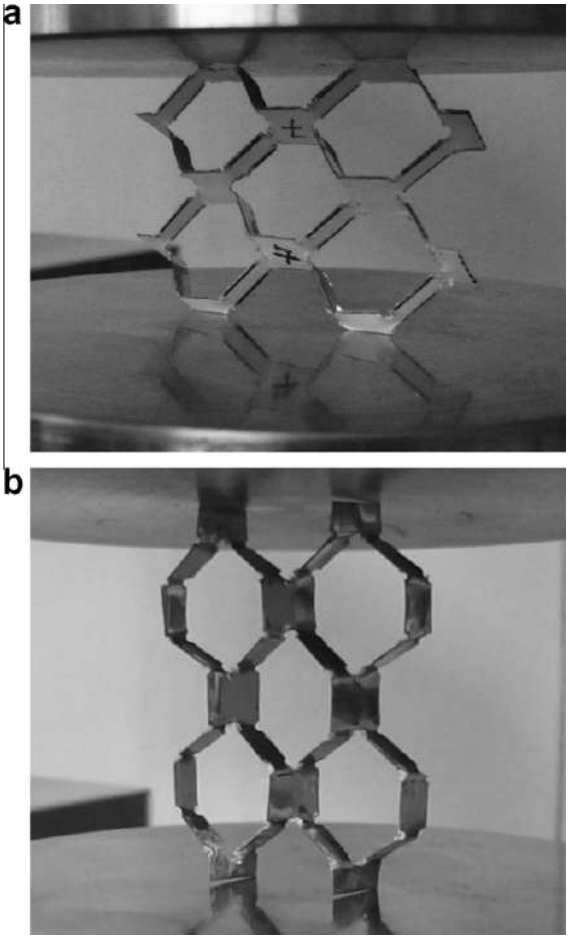

Fig. 11. The position of the specimens prepared for the experimental compression tests: (a) loading along *Y*-direction and (b) loading along *X*-direction.

stress and engineering strain. Both have been calculated at the engineering strain level of 0.01%, thus assuring a linear elastic deformation of the structure and avoiding the out-of-plane deformations. Figs. 12 and 13 show the resulted strain-stress dependencies for the two loading conditions (in-plane compression along *X* and *Y* directions) and the values obtained for E_x and E_y, for the geometry described in case 2.

5. Results

The Young's moduli obtained through the experimental tests are very close to the ones resulted from the analytical model, for the cases when the internal angle $A \geqslant 45°$, Table 4.

The values predicted by the analytical model follow the path given by the experiments: while the value of the internal angle A rises, the value of E_x decreases, Fig. 14, and the value of E_y increases, Fig. 15. However, for the analyzed case 1 ($A = 30°$), the theoretical results slightly differ from the tests: the experimental value of E_y is higher and the one of E_x is lower when being compared to the theoretical value. In order to obtain a more accurate path of the experimental results, two additional geometric cases (2 and 4 from Table 4) have been considered for determining the value of E_y. The obtained results validate the analytical model for the cases when the internal angle A takes values between 45° and 90°. Table 4 shows a comparison between the experimental and theoretical results. The differences may be interpreted as a consequence of the following practical fact: in order to simplify the analytical model, the value of b is assumed to be equal to zero while, in reality, the specimens have a value of 1mm for the b parameter; this value contributes to avoiding the crack propagation during the manufacturing process of the cellular structure, i.e. the expansion of the metal sheet. In addition, the cells walls are not perfectly plane, due to the manufacturing process. They suffer small deformations in the out of plane direction. These imperfections are not taken into account within the developed analytical model. However, the effect of geometric imperfections on the behavior of cellular structures is of high importance, several works being carried out in this direction (Chung and Waas, 2002a,b; Silva et al., 1995). This may be a reason for the fact that the theoretical model, where the geometry is considered to be perfect, predicts higher values than the experiments have shown. The influence of geometric imperfections on the in-plane properties of the expanded cellular core is considered to be addressed in a future research study.

6. Parameter study

Based on the developed analytical model, validated through experimental tests, the effective elastic moduli for the *X* and *Y* direction can be represented in terms of the geometrical parameters of the cellular structure. Fig. 14 shows the manner in which E_x modifies in terms of the internal angle A; E_x decreases with an increase of A. It can be also noticed that E_x diminishes while the length of the cell wall l increases. The distance c between two transversal cuts does not affect the value of E_x.

E_y slightly rises in value while the internal angle A increases its value, Fig. 15. In addition to this, it may be no-

Author's personal copy

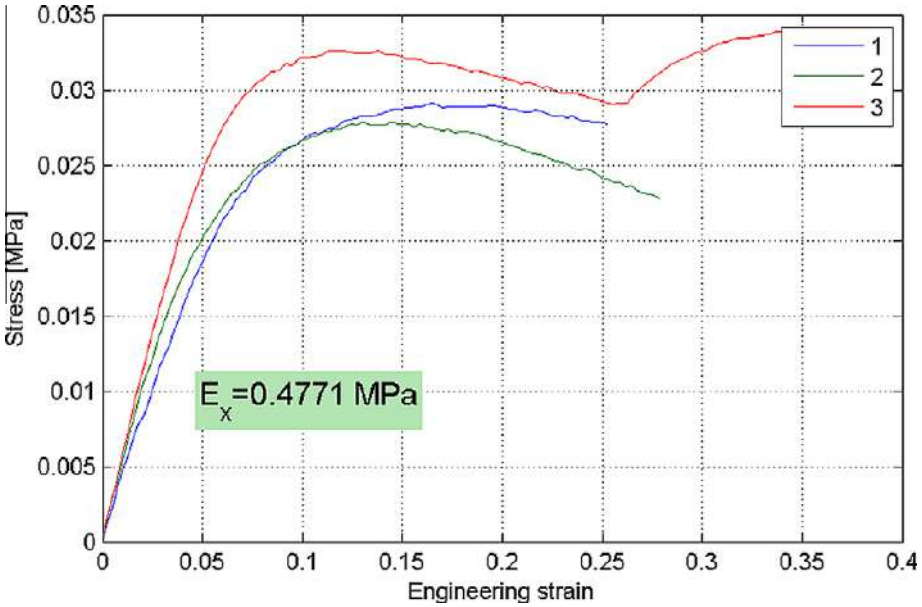

Fig. 12. Compression test results – *X* direction, for the geometry described in case 3.

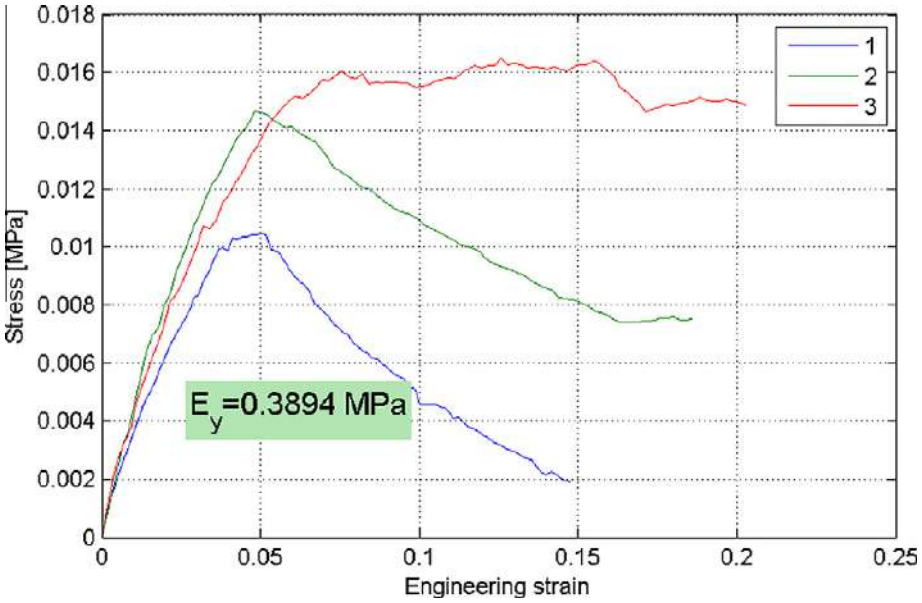

Fig. 13. Compression test results – *Y* direction, for the geometry described in case 3.

ticed that a smaller value for the l/c ratio implicitly increases the value of E_y.

As being expected, while E_x reduces its value with an increase of A, E_y varies in an opposite way. This will force the designer to solve a trade-off problem between the value of E_x and E_y, in terms of the requirements of the application where the cellular structure will be used.

If E_x and E_y are plotted one against the other, Fig. 16, it may be observed that both rise in value while decreasing the l/c ratio. Still, when $l/c \leqslant 1$, the value of E_x is no more affected. For few specific geometric topologies, the cellular structure manifests transverse isotropy of elastic properties in such a way that the value of E_x equals the value of E_y for both X and Y directions. The values for the geometric parameters that give these particular cases are presented in Table 5. These results have been extracted using the validated analytical model, for a number of 8 discrete values taken by the l/c ratio and by the internal angle A, with the corresponding expanding degree G. As the value of the internal angle A increases, the discrete values become denser, Fig. 16, and the difference between the values taken by E_x and E_y becomes smaller. Except these particular geometric cases, the cellular core shows orthotropic behavior.

The normalized effective elastic moduli of the proposed cellular structure, for X and Y direction, are shown in Figs. 17 and 18, while the relative density varies. In Section 2, it has been emphasized that for each of the considered l/c ratio, the lowest relative density is reached when the cells have a hexagonal shape ($A = 60°$). Bearing this in mind,

Author's personal copy

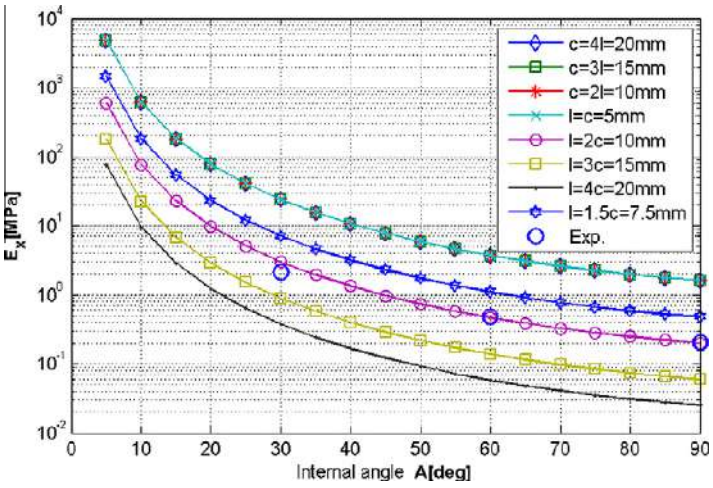

Fig. 14. Effective elastic modulus E_x vs. internal angle A.

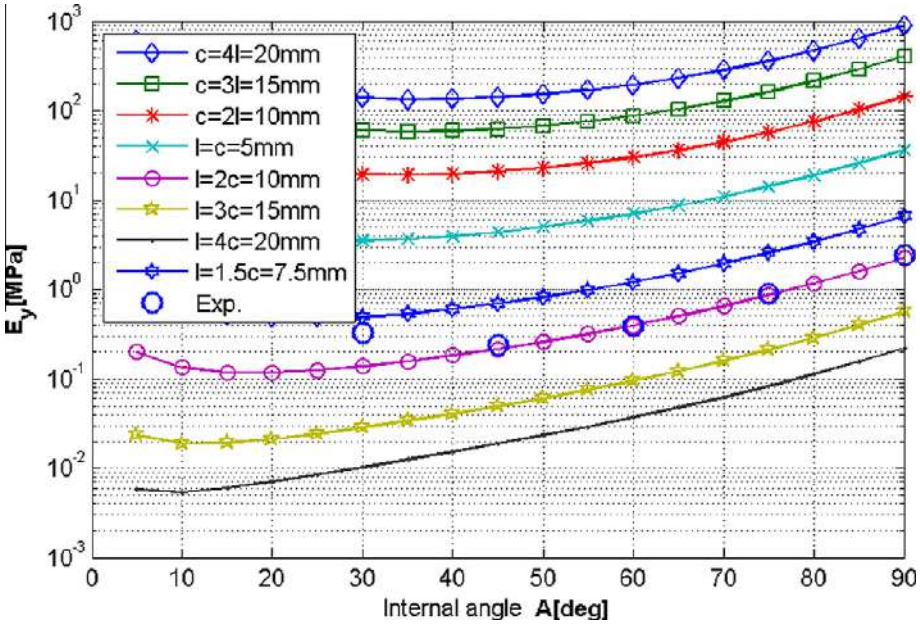

Fig. 15. Effective elastic modulus E_y vs. internal angle A.

one should be able to identify, from Figs. 17 and 18, the l/c ratios that offer higher in-plane stiffness while keeping a low weight of the core.

7. Conclusions

The main motivation for this study is to propose new alternative cellular cores to be used in the construction of sandwich structures, having geometries that allow the reduction of the base material consumption and less expensive manufacturing technologies.

As a result, this paper presents a novel cellular structure that is proposed to be used as a core in sandwich panels. It aims to develop an analytical model for the in-plane effective elastic properties of the proposed cellular structure which is validated through experimental tests. The results obtained through the theoretical model show a close correlation with the tests results when the internal angle A takes values between 45° and 90°. This interval represents the feasible region when designing such a cellular core because, in order to obtain a high second moment of inertia, the height of the core h should be as large as possible, which also implies a higher value of the expansion degree G and implicitly of the internal angle A. The structure topology is analyzed using a parameterized unit cell and the effective Young's moduli are studied in terms of the geometrical parameters of the core, using an original analytical model. It is presented the way in which the values of the geometrical parameters should be chosen in order to increase the in-plane stiffness of the cellular structure.

The lowest relative density is obtained at a value of 60° for the internal angle A. In addition, when l/c ratio equals a value of 2 and A is 60° in value, the expansion degree G will have also a value of 60°; this configuration will give the hexagonal shape of the cells.

Author's personal copy

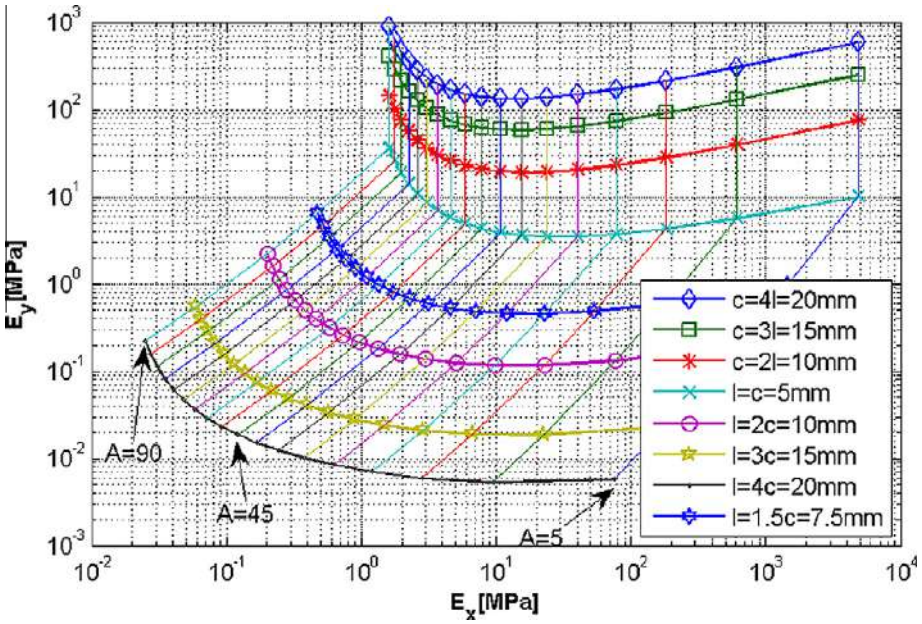

Fig. 16. E_x vs. E_y.

Table 5
The values of the geometrical parameters that gives a transverse isotropic behavior of the cellular core.

Variable parameters				Fixed parameters	E_x (MPa)	E_y (MPa)
l (mm)	c (mm)	A (°)	G (°)			
5	$20 = 4 \times l$	15	3.702	$E_s = 201000$ MPa $g = 0.2$ mm	182.3	216
5	$15 = 3 \times l$	20	6.504		77.96	74.4
5	$10 = 2 \times l$	35	16		15.5	19.1
5	$5 = l$	55	39.32		4.603	5.814
$7.5 = 1.5 \times c$	5	60	52.41		1.1	1.201
$10 = 2 \times c$	5	65	61.11		0.384	0.5
$15 = 3 \times c$	5	65	69.81		0.113	0.122
$20 = 4 \times c$	5	65	74.58		0.048	0.048

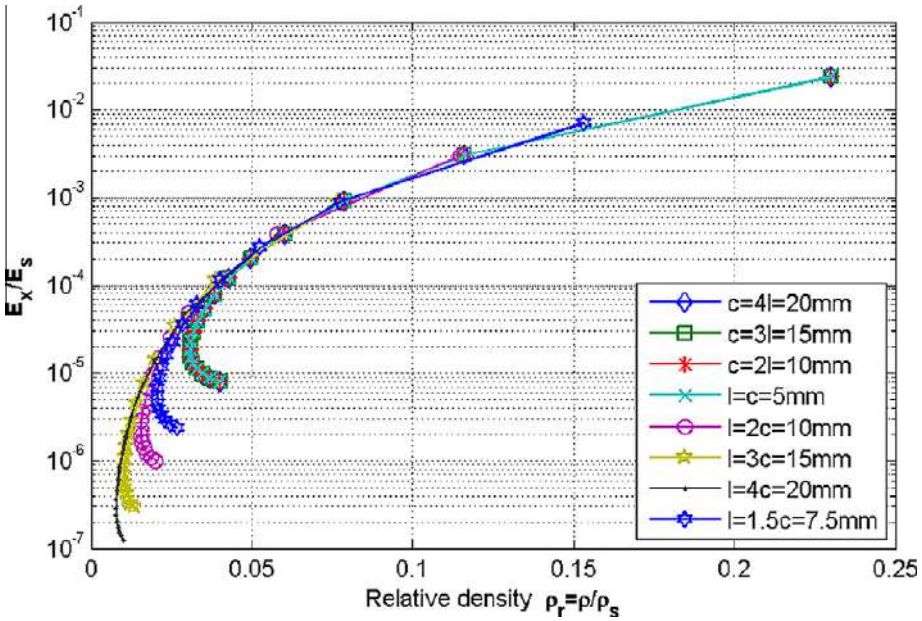

Fig. 17. Normalized elastic modulus – X direction vs. relative density.

Author's personal copy

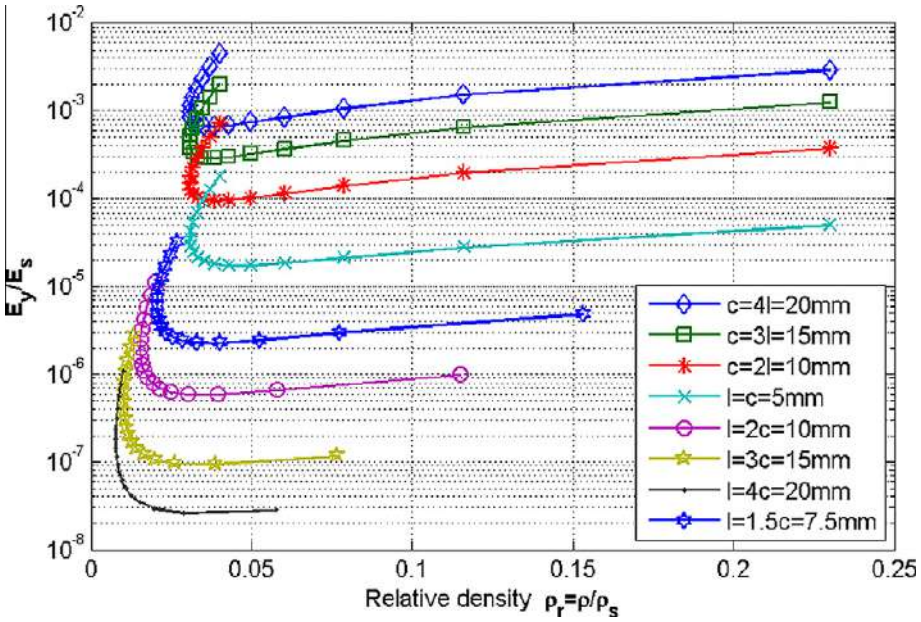

Fig. 18. Normalized elastic modulus – *Y* direction vs. relative density.

The in-plane stiffness increases in both directions while the *l*/*c* ratio decreases. However, a lower value for the *l*/*c* ratio would also add weight to the cellular structure by increasing the relative density.

For some particular geometric cases, the analyzed cellular structure is transversely isotropic, having the *X*–*Y* plane as the plane of isotropy. Due to a high number of parameters that may vary, the in-plane stiffness of the expanded cellular structure can be easily changed during the design process, in terms of the application.

Some of the strengths of this new expanded cellular core are: it represents a less expensive alternative to the already known cellular architectures, due to a reduced quantity of the used base material and due to the simplicity of the manufacturing method; the cells are formed by a continuous material, without any bonded areas as the honeycombs have; the relative density that may be obtained is very low, comparing to honeycombs, allowing to designing ultra-light sandwich structures; it is a cellular structure with open cells, giving the opportunity to implement additional functions to the sandwich structure. These are all arguments for using the proposed structure in the construction of sandwich panels, for applications where these strengths are fully exploited.

Acknowledgements

This paper is supported by the Sectoral Operational Programme Human Resources Development (SOP HRD), financed from the European Social Fund and by the Romanian Government under the Contract No. POSDRU/6/1.5/S/6. The authors are grateful to Dr. Horaţiu Teodorescu, Transilvania University of Brasov – Romania, for his support in carrying on the experiments and to Dr. Per Wennhage, Royal Institute of Technology – Sweden, for his valuable professional advice.

References

Bezazi, A., Scarpa, F., Remillat, C., 2005. A novel centre symmetric honeycomb composite structure. Composite Structures 71, 356–364.

Chung, J., Waas, A.M., 2000. The inplane elastic properties of circular cell and elliptical cell honeycombs. Acta Mechanica 144, 29–42.

Chung, J., Waas, A.M., 2002a. Compressive response of circular cell polycarbonate honeycombs under inplane biaxial static and dynamic loading – Part II: simulations. International Journal of Impact Engineering 27, 1015–1047.

Chung, J., Waas, A.M., 2002b. Compressive response of circular cell polycarbonate honeycombs under inplane biaxial static and dynamic loading. Part I: experiments. International Journal of Impact Engineering 27, 729–754.

Deshpande, V., Fleck, N.A., Ashby, M.F., 2001. Effective properties of the Octet-Truss lattice material. Journal of Mechanics and Physics of Solids 49, 1747–1769.

Gibson, L.J., 1981. The Elastic and Plastic Behaviour of Cellular Materials. Engineering Department, Cambridge University.

Gibson, L.J., Ashby, M.F., 1999. Cellular Solids. Structure and Properties, second ed. Cambridge University Press.

Gibson, L.J., Ashby, M.F., Schajer, G.S., Robertson, C.I., 1982. The mechanics of two-dimensional cellular materials. Proceedings of the Royal Society 382, 25–42.

Goswami, S., 2006. On the prediction of effective material properties of cellular hexagonal honeycomb core. Journal of Reinforced Plastics and Composites 25, 393–405.

Reddy, J.N., 2002. Energy Principles and Variational Methods in Applied Mechanics, second ed. John Wiley & Sons, Inc..

Silva, M.J., Hayes, W.C., Gibson, L.J., 1995. The effects of non-periodic microstructure on the elastic properties of two-dimensional cellular solids. International Journal of Mechanical Sciences 37, 1161–1177.

Sue, J.-W., Whitcomb, J., 2008. Effect of sandwich configuration on behavior of honeycomb core. Journal of Sandwich Structures and Materials 10, 311–329.

Sypeck, D.J., Wadley, H.N.G., 2004. Multifunctional Periodic Cellular Solids and the Method of Making Same. University of Virginia Patent Foundation, USA, p. 34.

Wadley, H.N.G., 2006. Multifunctional periodic cellular metals. Philosophical Transactions of the Royal Society 364, 31–68.

Wang, J., Evans, A.G., Dharmasena, K.P., Wadley, H.N.G., 2003. On the performance of truss panels with Kagome cores. International Journal of Solids and Structures 40, 6981–6988.

Zenkert, D., 1997. The Handbook of Sandwich Construction. EMAS Ltd..

THE PUBLISHING HOUSE
OF THE ROMANIAN ACADEMY

PROCEEDINGS OF THE ROMANIAN ACADEMY, Series A,
Volume 17, Number 4/2016, pp. 336–343

DAMPING CHARACTERISTICS IDENTIFICATION OF SELF-REINFORCED POLY-ETHYLENE TEREPHTHALATE

Marian Nicolae VELEA, Simona LACHE, Ioan Calin ROSCA
"Transilvania" University of Brasov, Department of Mechanical Engineering
Corresponding author: Simona LACHE, E-mail: slache@unitbv.ro

Abstract. Damping material characteristics are important to be considered in dynamic numerical simulations in order to obtain accurate results. The dependency between the critical damping fraction and frequency is experimentally determined within this article for a novel thermoplastic composite material - poly-ethylene terephthalate fiber reinforced poly-ethylene terephthalate (SrPET). The article explains the theoretical background used for obtaining the values of damping ratio. A curve fitting process is applied in order to identify the mathematical function that best fit the experimental data. It is shown that the damping ratio varies with frequency by following an exponential function. The influence of material damping characteristic is evidenced through a case study where a flat plate of SrPET is subjected to an impulse unit force. The results indicate, as expected, a high sensitivity to damping data.

Key words: damping ratio, poly-ethylene terephthalate, self-reinforced-polymer.

1. INTRODUCTION

An intelligent use of composite materials and structures may provide important benefits with respect to different engineering systems' performance criteria. This may refer to lightweight design which is important in order to reduce energy consumption of the system in use and to save material resources [1]. The performance criteria may also refer to mechanical characteristics as high stiffness and strength or high impact performance [2–4], special thermal properties [5, 6] or electric properties [7]. A large spectrum of characteristics is therefore attainable when combining several materials by following a specific way dictated by the application needs [8].

Although the individual characteristics of polymers may not be attractive when looking at mechanical properties, their properties may be improved for example through reinforcements. Novel composite materials related to high specific performance criteria are continuously proposed. Additional benefits as recycling potential is also of high importance nowadays [9]. One category of such novel materials are the self-reinforced polymers: SrPET – self-reinforced poly-ethylene terephthalate [10, 11] or SrPP – self-reinforced polypropylene [12–14]. The SrPET is a poly-ethylene terephthalate matrix reinforced with poly-ethylene terephthalate fibres. However, their melting temperature is different; details about the manufacturing process of the SrPET are given within the 3rd section of this article.

Especially when working with ductile materials, as the case of the SrPET, the dynamic numerical analysis may be inaccurate if the damping characteristic is not considered [15]. However, this type of data is not usually found on the material supplier and must be determined by the user.

The purpose of this article is to determine the dependency between damping ratio and frequency for the SrPET material. This data is usually required in a tabular form within the dynamic FE analyses. The influence of the damping ratio on the dynamic simulations is afterwards investigated within a numerical case study. Conclusions are drawn eventually based on the obtained results.

2. DAMPED RATIO IDENTIFICATION. THEORETICAL BACKGROUND

The modal parameters can be found using the so-called frequency domain methods. These methods are based on estimators that are frequency response functions defined with some frequency dependent functions as: Auto Spectral Density of the force excitation $S_{ff}(\omega)$, Auto Spectral Density of the response $S_{xx}(\omega)$, the Cross Spectral Density between the response and the force excitation $S_{xf}(\omega)$, and the Cross Spectral Density between the force excitation and the response $S_{fx}(\omega)$. According to Heylen, W. *et. al.* [16], the main estimators used in modal analysis are the following:

$$H_1(\omega) = \frac{S_{fx}(\omega)}{S_{ff}(\omega)}, \tag{1}$$

$$H_2(\omega) = \frac{S_{xx}(\omega)}{S_{xf}(\omega)}, \tag{2}$$

$$H_3 = \sqrt{H_1 H_2}\ . \tag{3}$$

The H_3 estimator is used when the signal to noise ratio is approximately the same at the input and at the output. By considering the influence of the noise, the two estimators given by the equations (1) and (2) can be rewritten as:

$$H_1(\omega) = \frac{S_{fx}(\omega)}{S_{ff}(\omega)+S_{nn}(\omega)}, \tag{4}$$

where $S_{nn}(\omega)$ is the Autospectra of the noise on input signal, and

$$H_1(\omega) = \frac{S_{fx}(\omega)}{S_{ff}(\omega)+S_{nn}(\omega)}, \tag{5}$$

where $S_{nm}(\omega)$ represents the Autospectra of the noise on output signal.

By considering the equations (4) and (5) it yields that the estimator H_1 will suffer most at the resonance; therefore, H_2 is a better indicator near resonance. In addition, the estimator H_1 is used in case of a low noise at input, while H_2 is mainly used when it is a low answer on response.

The quality of the data is evaluated by the coherence function:

$$\gamma^2 = \frac{H_1(\omega)}{H_2(\omega)}. \tag{6}$$

In general, the range value of the coherence function is of $0 \le \gamma^2 \le 1$. For $\gamma^2 \to 0$ the signal is pure noise while for $\gamma^2 \to 1$ a signal without noise is obtained. As it is mentioned within the basic theory of modal analysis, the data with a coherence of less than 0.75 are not used in practice [16].

Another method that can be used in damping ratio evaluation is the so called “Power Input Method “ (PIM) that is based on the comparison between the dissipated energy of a system to its maximum total energy under vibration per radians [17]. This method is unbiased at the natural frequencies of the defined modes. In fact, the method allows the loss factors and the damping ratio to be found at different frequencies. The analyzed structure is divided into n areas, each one having a partial mass $m_i \left(i = \overline{1,n}\right)$ [16].

For a structural system, the damping loss factor per cycle, in the frequency band centered at a considered frequency ω, is defined as follows [18]:

$$\eta(\omega) = \frac{E_d}{E_t}\ , \tag{7}$$

where E_d is the dissipated energy by damping, and E_t represents the time averaged total energy of the system (the strain energy).

The dissipated energy E_d can be evaluated using the simultaneous measurements of the force and velocity at the point of energy input with the formula:

$$E_d = \frac{1}{2\omega}\mathrm{Re}\left[H_{xx}(\omega)\right]S_{xx}(\omega), \tag{8}$$

where $H_{xx}(\omega)$ represents the driving point mobility frequency transfer function (input-response in the application point of the force).

Thus, the strain energy cannot be directly found from the measurements of the force; the velocity it is necessary to be replaced with twice the kinetic energy and the system has to be approximated by a summation as opposed to a volume integral [18]:

$$T = \frac{1}{2}\sum_{i=1}^{n} m_i S_{ii}(\omega)\,, \tag{9}$$

where $S_{ii}(\omega)$ is the power spectral density of the velocity response at each measurement location.

By considering that all the n measurement points are uniformly spaced throughout the system and the mass is divided in equal mass ratio, the damping loss factor for the considered system can be found with the relation [18, 19]:

$$\eta(\omega) = \frac{\mathrm{Re}\left[H_{xx}(\omega)\right]}{\omega m \sum_{i=1}^{n}\left|H_{yx}(\omega)\right|^2}\ , \tag{10}$$

where H_{yx} is the frequency transfer function of the mobility between the driving point x and a measuring point y.

Further on, by considering the value of the damping loss factor given by (10), one can calculate the damping ratio from the following relation:

$$\eta(\omega) = 2\zeta(\omega)\,. \tag{11}$$

3. EXPERIMENTAL INVESTIGATION

3.1. The novel material under study

The investigated material is made of poly-ethylene terephthalate reinforced with fibre poly-ethylene terephthalate (SrPET). The SrPET material used in this study was supplied by Comfil®APS and is a commingled balanced 2/2 twill fabric with a weight of 0.75 kgm^{-2} and 50% reinforcement fibers. It is presented as a plate made of 6 layers of fabric, with the plate thickness of 2.7 mm and a material density of 1 380 kg·m^{-3}.

The SrPET composite consists of a low melting temperature poly-ethylene terephthalate (PET) matrix and a high tenacity poly-ethylene terephthalate (PET) fiber material. The melting temperature of the PET matrix is around 170°C while the PET fiber melts at 260°C. A good consolidation is obtained if the temperature is high enough to melt the matrix and wet the fibers but not too high so that the fibers degrade and lose their reinforcing properties. According to a previous study [10] laminates with good mechanical properties can be consolidated at 220°C for 20 min under a pressure of 1.5bar.

3.2. The experimental set-up

The aim of the considered Experimental Modal Analysis (EMA) is to obtain the modal parameters (natural frequencies, damping ratios or damping loss factors and modal constants or modal amplitudes) from measured vibration data. A mathematical relation for the global value of the damping ratio ζ as function of frequency value is searched based on the above theoretical considerations and EMA.

This experimental investigation is carried out in order to determine how the critical damping ratio ζ varies in terms of frequency.

A Brüel & Kjær equipment was used for the modal analysis, consisting of: a shaker type 4810, three accelerometers type 4517-002, PULSE 12 platform connected to a PC. The data acquisition and post processing results were performed using two soft modules type 7709 and type 7770-6.

The dimensions of the tested composite plate were 300 × 300 mm and the plate was supported by a soft polymeric sponge, thus establishing the so-called free-free conditions. A mesh was drawn on the plate (square elements 50 × 50 mm) in order to arrange the accelerometers in the mesh nodes (Fig.1).

The SIMO test was chosen as testing method by considering the shaker fixed in a reference point, the middle of the plate. The applied signal was a true random signal in the range 0–1600 Hz used in parallel with a Hanning window to minimize the leakage. In the same time a spectrum averaging was used in order to excite the non-linearity in the structure.

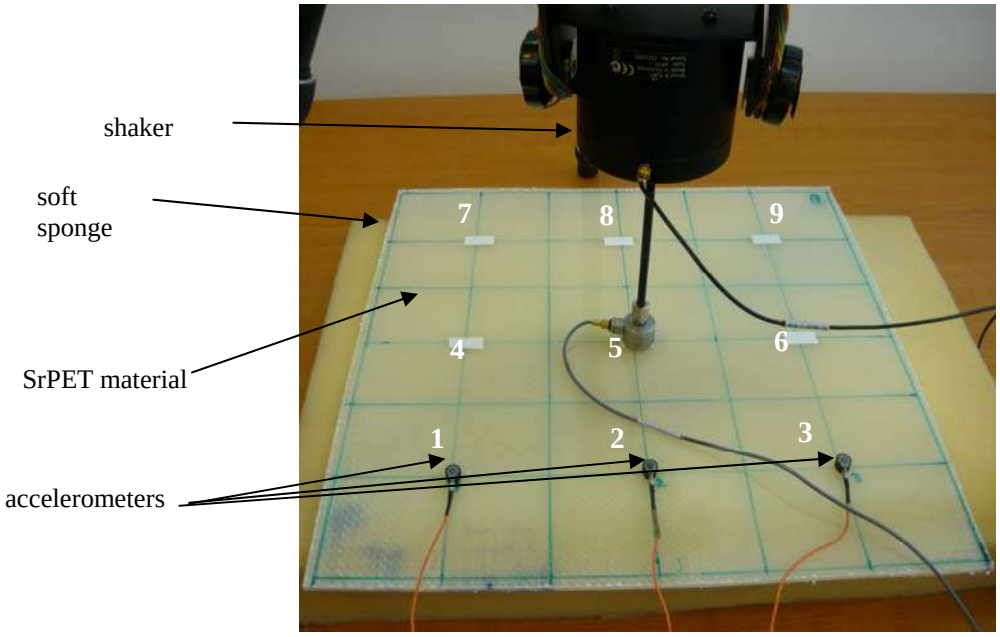

Fig. 2 – Experimental set-up.

The values of interest for modal parameters can be obtained based on the modal analysis identification extraction. The extraction method can be one of the following: the peak amplitude method, the quadrature response method, the maximum quadrature component method, the maximum frequency spacing method, the circle fitting method, or the inverse method. The peak amplitude method was the method used within this investigation. According to this method, at the vicinity of the resonance, the FRF is dominated by the contribution of that vibration mode while the contributions of other vibration modes are negligible. The FRF graph shows the natural frequencies that are the peaks of FRF. By considering the half power method, the modal damping ratios from the sharpness of the peaks are found. The used FRF was the mobility one and the resulted functions and the coherence functions were measured in all 9 nodes of the defined mesh.

3.3. The results

The obtained set of data was further on processed and interpreted in order to determine a mathematical relation between frequency and the critical damping fraction ζ. The Frequency Response Functions (FRFs) were recorded for all nine points (Fig. 1). In Figs. 2a, 3a, and 4a there are presented the mobility FRFs for the points ①, ②, and ③ from Fig. 1. The measured values were read and for each natural frequency the correspondent value of the coherence was analysed (Figs. 2b, 3b, and 4b). From each diagram one can read, in the considered range, the values of natural frequencies and the values of damping ratio. The considered data are validated by correlation to the coherence values (Fig. 2b, 3b, and 4b).

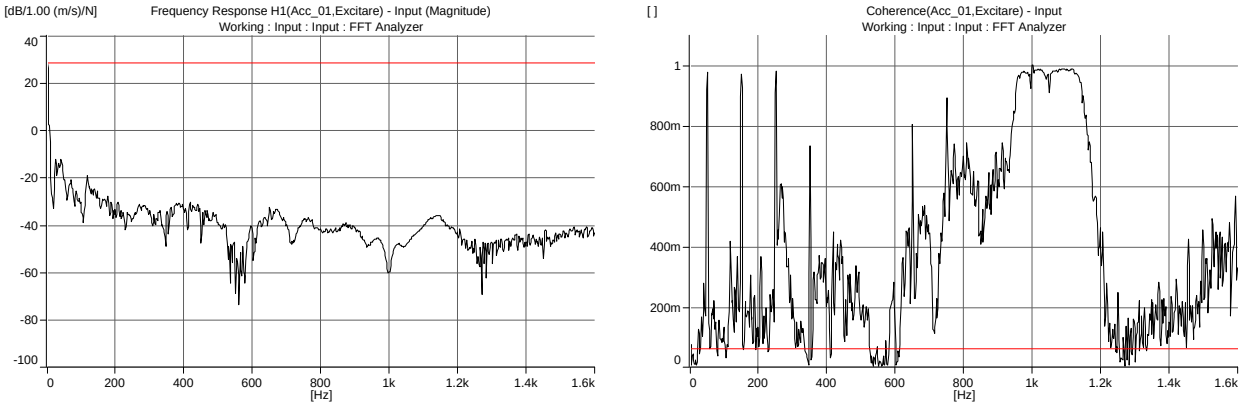

Fig. 2 – Data recorded for the accelerometer 1:
a) frequency response function; b) coherence function.

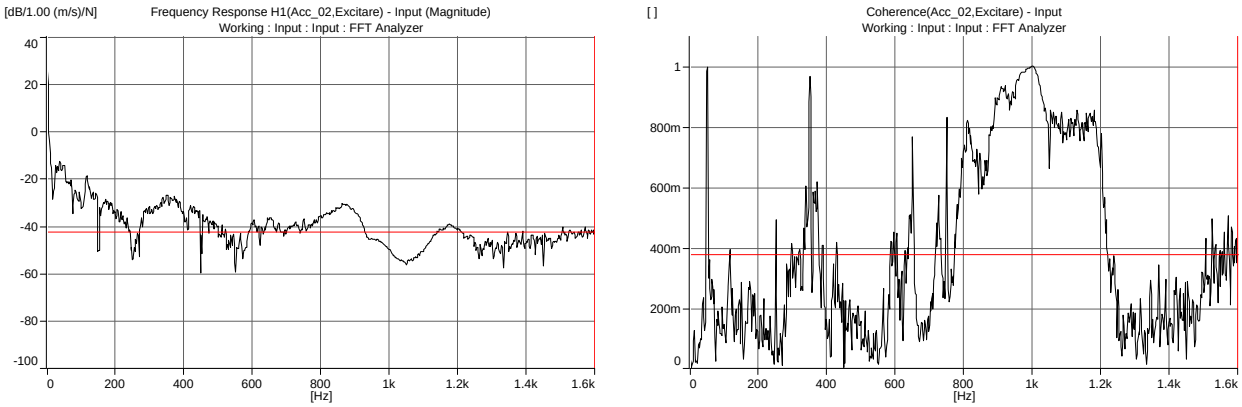

Fig. 3 – Data recorded for the accelerometer 2:
a) frequency response function; b) coherence function.

The proper values of the frequencies and of the damping ratios were chosen by considering the limits of the coherence functions (Fig. 5). A relatively scarce distribution for the measured values of ζ in terms of frequency can be noticed from Fig. 5, i.e. ζ determined on the 9 measured points varies significantly within small intervals of frequencies. This was an expected behavior and it is explained by the structural non-homogeneity of the material. In reality, the tested material is not homogeneous and isotropic, therefore differences in values of the damping ratio measured in different points can be observed.

In order to deal with this problem, an arithmetic mean was calculated for the values of ζ founded within intervals of 20 Hz; the resulted points are illustrated in Fig. 5 as filled circles.

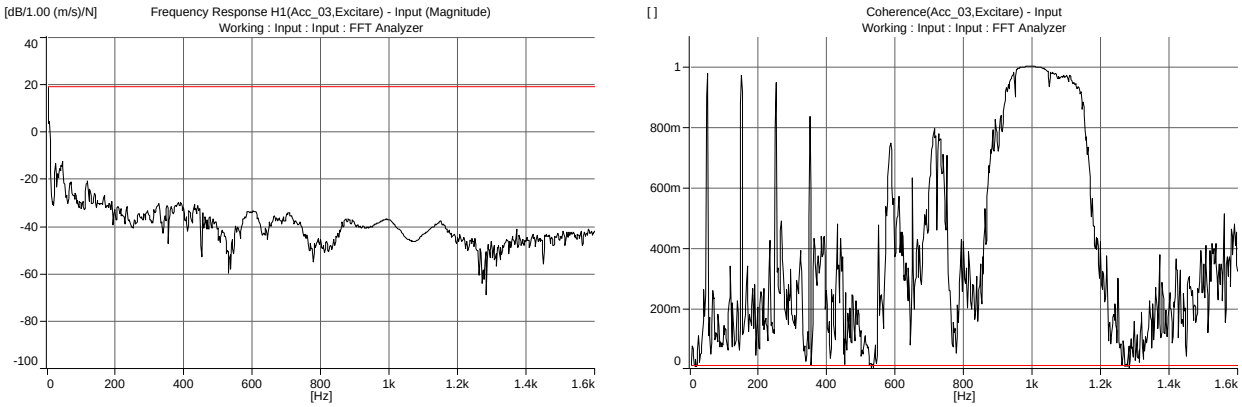

a) b)

Fig. 4 Data recorded for the accelerometer 3:
a) frequency response function; b) coherence function.

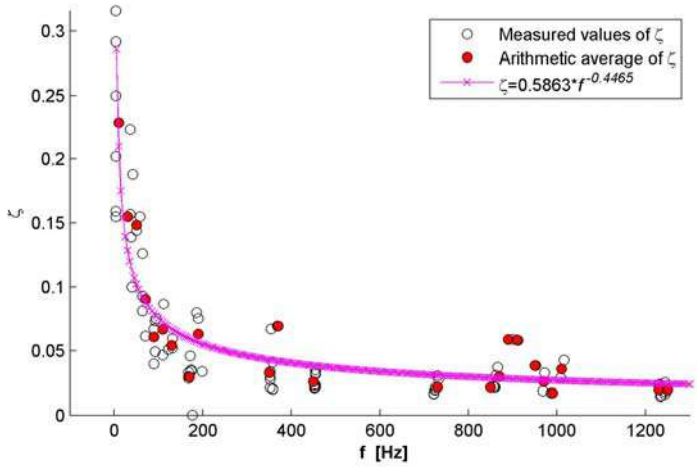

Fig. 5 – Damping ratio as a function of frequency for poly-ethylene terephthalate reinforced with fiber poly-ethylene terephthalate (SrPET).

The mean values are used further on to curve fit data and to find out the mathematical function $\xi(f)$. The best fit is obtained by an exponential function (12):

$$\xi(f) = 0.5863 f^{-0.4465} \quad . \tag{12}$$

This relation will be further on implemented within a numerical simulation

4. CASE STUDY

4.1. Numerical model

A numerical approach is further on used in order to study the influence of the damping data on the dynamic response of a structure. The developed numerical model consists of a flat plate, having a thickness of 2.7 mm, clamped at two opposite edges (Fig. 6).

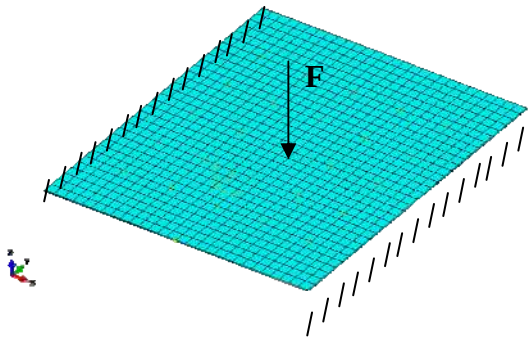

Fig. 6 – Boundary conditions considered within the simulation.

A Dirac delta function is considered to model the excitatory force (unit force). S4R elements are used to create the mesh and the SrPET material is assumed to be isotropic, having the following material properties: $E = 5300$ MPa, $\nu = 0.3$ and $\rho = 1380$ kg/m^3. The analysis is carried out in two steps. Firstly, a frequency step is done, where the first 50 eigenvalues are determined by using the Lanczos eigensolver. Secondly, a modal dynamic step is considered, where the critical damping fraction is defined as a function of frequency using data generated by (12). The model is solved using Abaqus/Standard.

4.2. Results

The vibration response of the plate is recorded over time (for 0.2 seconds), by comparing the displacements of the point where the unit force was previously applied, for both considered cases: damped and un-damped structure (Fig. 7).

As it was expected, while the un-damped structure continuously oscillates, the displacement of the damped structure reduces with time until the structures reach the equilibrium state. The energy generated by the applied unit force is making the plate to oscillate but this energy is lost by intermolecular friction within the material structure. This observation corresponds to the real behavior of structures.

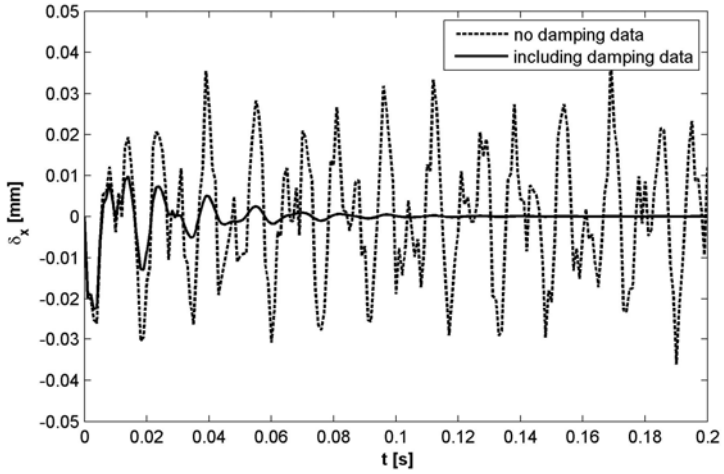

Fig. 7 – Displacement *vs*. time caused by the unit force applied at $t = 0$.

5. CONCLUSION

A novel thermoplastic composite material – poly-ethylene terephthalate fiber reinforced poly-ethylene terephthalate (SrPET) – is analyzed in terms of damping characteristics. The values of the critical damping ratio are found experimentally in terms of frequency. An exponential function is found to best fit the

obtained set of experimental data. A numerical model is presented as a case study where dynamic simulations are carried out separately for damped and un-damped structure. The results demonstrate the important influence the damping properties have on the results within numerical dynamic analyses.

AKNOWLEDGEMENTS

This work was partially supported by the strategic grant POSDRU/159/1.5/S/137070 (2014) of the Ministry of Labour, Family and Social Protection, Romania, co-financed by the European Social Fund – Investing in People, within the Sectorial Operational Programme Human Resources Development 2007-2013. The support received from Christof Schneider, KTH – Royal Institute of Technology, Sweden, is gratefully acknowledged.

REFERENCES

1. González Palencia, J.C., T. Furubayashi and T. Nakata, *Energy use and CO_2 emissions reduction potential in passenger car fleet using zero emission vehicles and lightweight materials*, Energy, **48**, *1*, pp. 548–565, 2012.
2. Xiong, J. *et al*., *Compression and impact testing of two-layer composite pyramidal-core sandwich panels*, Composite Structures, **94**, *2*, pp. 793–801, 2012.
3. Kazemahvazi, S., B.P. Russell and D. Zenkert, *Impact of carbon fibre/epoxy corrugated cores*, Composite Structures, **94**, *11*, pp. 3300–3308 .
4. Burada, C.O. *et al*., *Experimental determinations of some mechanical properties for new types of composite bars with polypropylene honeycomb core*, Proceedings of the Romanian Academy, Series A, **16**, *1*, pp. 70–79, 2015.
5. Sadighi, M., M. Benvidi and M. Eslami, *Improvement of thermo-mechanical properties of transversely flexible sandwich panels by functionally graded skins*, Journal of Sandwich Structures and Materials, **13**, *5*, pp. 539–577, 2011.
6. Marín, L. *et al*., *Optimization of composite stiffened panels under mechanical and hygrothermal loads using neural networks and genetic algorithms*, Composite Structures, **94**, *11*, pp. 3321–3326, 2012.
7. Jung, W.-K. *et al*., *Fabrication of Radar Absorbing Structure and Evaluation of Radar Cross Section: Case Study of Hybrid Shells*, Journal of Composite Materials, **41**, pp. 1375–1387, 2007.
8. Ashby, M.F., *Designing architectured materials*, Scripta Materialia, **68**, *1*, pp. 4–7, 2013.
9. Yang, Y. *et al*., *Recycling of composite materials*, Chemical Engineering and Processing: Process Intensification, **51**, pp. 53–68, 2012.
10. Schneider, C. *et al*., *Compression and tensile properties of self-reinforced poly (ethylene terephthalate)-composites*, Polymer Testing, **32**, *2*, pp. 221–230, 2013.
11. Kazemahvazi, S., C. Schneider and V.S. Deshpande, *A constitutive model for self-reinforced ductile polymer composites*, Composites Part A: Applied Science and Manufacturing, **71**, pp. 32–39, 2015.
12. Swolfs, Y. *et al*., *The influence of weave architecture on the mechanical properties of self-reinforced polypropylene*, Composites Part A: Applied Science and Manufacturing, **53**, pp. 129–136, 2013.
13. Swolfs, Y. *et al*., *The influence of process parameters on the properties of hot compacted self-reinforced polypropylene composites*, Composites Part A: Applied Science and Manufacturing, **65**, pp. 38–46, 2014.
14. Swolfs, Y. *et al*., *Introducing ductility in hybrid carbon fibre/self-reinforced composites through control of the damage mechanisms*, Composite Structures, **131**, pp. 259–265, 2015.
15. Treviso, A. *et al*., *Damping in composite materials: Properties and models*, Composites Part B: Engineering, **78**, pp. 144–152, 2015.
16. Heylen, W., S. Lammens and P. Sas, *Modal Analysis Theory and Testing*, Katholieke Universiteit Leuven, Faculty of Engineering, Department of Mechanical Engineering, 1998.
17. Bratti, G. *et al.*, *Estimation of damping loss factor of fuselage panel by power injection method and impulse response decay method*, in *21st International Congress of Mechanical Engineering*, Proceedings of COBEM 2011.
18. Wanbo, L., *Experimental and Analytical Estimation of Damping in beams and plates with damping treatments*, University of Kansas, 2008.
19. Carfagni, M. and M. Pierini, *Determining the Loss Factor by the Power Input Method (PIM). Part 2: Experimental Investigation with Impact Hammer Excitation*, Transactions of the ASME, **121**, pp. 422–428, 1999.

Received April 16, 2016